PhD program in Mechanical, Fluids and Aerospace Engineering

Numerical Tools for Computational Design of Acoustic Metamaterials

Doctoral thesis by David Roca Cazorla

Thesis advisors Juan Carlos Cante Terán
Oriol Lloberas-Valls

Research promoter Xavier Oliver Olivella

Article-based thesis

Escola Superior d'Enginyeries Industrial, Aeroespacial i Audiovisual de Terrassa

Terrassa, June 2020

To my family and friends

ABSTRACT

The notion of metamaterials as artificially engineered structures designed to obtain specific material properties, typically unachievable in naturally occurring materials, has captured the attention of the scientific and industrial communities. Among the broad range of applications for such kind of materials, in the field of acoustics, the possibility of creating materials capable of efficiently attenuating noise in target frequency ranges is of utmost importance for a lot of industrial areas. In this context, the so-called locally resonant acoustic metamaterials (LRAMs) can play an important role, as their internal topology can be designed to exhibit huge levels of attenuation in specific frequency regions by taking advantage of internal resonance modes. With a proper, optimized topological design, LRAMs can be used, for instance, to build lightweight and thin noise insulation panels that operate in a low-frequency regime, where standard solutions for effectively attenuating the noise sources require dense and thick materials.

Given the importance of the topological structure in obtaining the desired properties in acoustic metamaterials, the use of novel numerical techniques can be exploited to create a set of computational tools aimed at the analysis and design of optimized solutions. These are based on three fundamental pillars: (1) the multiscale homogenization of complex material structures in the microscale to get a set of effective properties capable of describing the material behavior in the macroscale, (2) the model-order reduction techniques, which are used to decrease the computational cost of heavy computations while still maintaining a sufficient degree of accuracy, and (3) the topology optimization methods that can be employed to obtain optimal configurations with a given set of constraints and a target material behavior. This set of computational tools can be applied to design acoustic metamaterials that are both efficient and practical, i.e. they behave according to their design specifications and can be produced easily, for instance, making use of novel additive manufacturing techniques.

RESUM

La concepció dels metamaterials com a estructures dissenyades artificialment amb l'objectiu d'obtenir un conjunt de propietats que no són assolibles en materials de manera natural, ha captat l'atenció de les comunitats científiques i industrials. Dins de l'ampli ventall d'aplicacions que se'ls pot donar als metamaterials, si ens centrem en el camp de l'acústica, la possibilitat de crear un material capaç d'atenuar de manera efectiva sorolls en rangs de freqüència concrets és de gran interès en multitud d'indústries. En aquest context, els anomenats *locally resonant acoustic metamaterials* (LRAMs) destaquen per la possibilitat de dissenyar la seva topologia interna per tal que produeixin elevats nivells d'atenuació en regions concretes de l'espectre de freqüències. Amb un disseny topològic òptim, els LRAMs poden servir, per exemple, per a la construcció de panells lleugers aïllants de soroll, que operin en rangs de freqüències baixos, en els quals la solució clàssica requereix de materials d'elevada densitat i espessor.

Donada la importància de l'estructura topològica dels metamaterials acústics en l'obtenció de les propietats desitjades, resulta convenient l'ús de mètodes numèrics punters per al desenvolupament d'un conjunt d'eines computacionals que tinguin per objectiu l'anàlisi i el disseny de solucions òptimes. Tals eines es fonamenten en tres pilars: (1) la homogeneïtzació multiescala d'estructures de material complexes a una escala micro que derivi en l'obtenció de propietats efectives que permetin descriure el comportament del material a una escala macro, (2) tècniques de reducció per minimitzar l'esforç computacional mantenint nivells de precisió suficients i (3) mètodes d'optimització topològica emprats per a l'obtenció de configuracions òptimes donat un conjunt de restriccions i unes propietats de material objectiu. Aquestes eines computacionals es poden aplicar al disseny de metamaterials acústics que resultin eficients i pràctics a la vegada, és a dir, que es comportin segons les especificacions de disseny i siguin fàcilment fabricables, per exemple, mitjançant tècniques punteres d'impressió 3D.

PREFACI

La meva ment curiosa sempre m'ha portat a voler adquirir més coneixements i és el motiu que em va empènyer a formar-me en l'àmbit de la ciència i tecnologia. Aquesta tesi representa la culminació d'aquest llarg procés, un viatge en el que més enllà de formar-me i adquirir aquests coneixements tan anhelats, he crescut com a persona, m'he conegut a mi mateix i he trobat el camí a seguir. No és estrany sentir dir que fer una tesis doctoral pot resultar una "tortura". La realitat, per mi, ha estat totalment diferent. Si bé és cert que ha suposat un repte, és un repte que he gaudit en tot moment. Inclús les parts més dificultoses m'han aportat beneficis, tant a nivell personal com possibilitant la obertura de nous camins per explorar. I, en general, em sento satisfet amb el resultat final. Tot això no hauria estat possible sense un conjunt de persones que m'agradaria mencionar a continuació, per mostrar-los el meu profund agraïment per haver-me ajudat o acompanyat en aquest viatge i haver-lo fet possible.

En primer lloc, vull agrair-li a Xavier Oliver el fet d'haver-me brindat l'oportunitat de realitzar aquesta tesi. Ell és qui ha estat al capdavant promovent la línia d'investigació en la que s'ha desenvolupat la tesi i, en aquest sentit, és qui l'ha fet possible. Per altra banda, vull agrair també la seva figura com a mentor, per haver-me ajudat i ensenyat què significa ser investigador.

M'agradaria agrair també la tasca dels directors d'aquesta tesi, el Juan Carlos Cante i l'Oriol Lloberas, pel seu ajut i recolzament en els moments que ho he necessitat. En especial, voldria agrair al Juan Carlos haver estat present i recolzant-me en moments de dificultat personals, per haver-me donat valuosos consells per seguir endavant i no defallir en la seva tasca de formar-me com a docent.

Tot seguit vull agrair a les persones que, d'una manera o altra, han fet possible que hagi pogut realitzar aquest treball. D'entrada a Àlex Ferrer, per haver-me convençut a iniciar

aquesta aventura. Al CIMNE, per haver proporcionat l'entorn i els recursos necessaris. També vull mostrar el meu agraïment al professor Mahmoud Hussein, per haver possibilitat la meva estància a la Universitat de Colorado a Boulder i brindar-me l'oportunitat d'explorar noves maneres de seguir explorant la línia d'investigació de la tesis. A la Teresa Pàmies, per haver-me ajudat en les sessions al laboratori d'acústica. Voldria agrair també a HP i, en particular, a Lucas Rotllant, per haver proporcionat el seu ajut en l'adquisició dels prototips emprats en la part experimental de la tesis. Per últim a Oriol Guasch, qui va inspirar la línia d'investigació centrada en els metamaterials acústics.

Per altra banda, voldria fer especial menció a tots els companys i companyes que m'han acompanyat, en un moment o altre, i han compartit amb mi el camí durant aquests anys de doctorat: en Joaquín, l'Àlex, l'Alfredo, en Manuel, en Marcelo, la Lucía, l'Alejandro i el Sergi. En particular també a la Laura i en Daniel, per compartir penúries i alegries durant els mítics dinars al búnquer (i quan el temps acompanyava a la terrassa). I aquest últim també pel seu suport, a nivell de la tesis i a nivell personal.

Per acabar, m'agradaria expressar el meu profund agraïment a tots les meus amics i familiars. En particular als meus pares, la Remei i l'Isidre, per ser els responsables que hagi arribat tan lluny. I al meu pare també per haver fet la seva aportació en la tesis, possibilitant la realització dels experiments. Per últim, vull agrair a la Laura tots els anys que ha passat al meu costat, per haver-me mostrat lo bonica que pot ser la vida i haver cregut sempre en mi i el meu potencial com a persona.

Contents

List of figures

List of tables

Chapter 1

MOTIVATION AND SCOPE

I like to define progress as the ability of making possible what once was impossible. Challenging the limits of nature is a quality of our species that has brought us to an era where we can travel thousands of kilometers in a matter of hours, communicate almost instantly with other people anywhere in the planet or even explore the universe beyond our solar system. The progress of humanity is a proof that we are good at solving problems, but in order to do that, what is most important is for the right questions to be raised first. This is precisely our task, as scientists, and ultimately the driving force that makes us succeed and evolve as a civilization.

This constant questioning is carried out in every existing field of science. However, this work will be focused on what can be considered a very clear example of what it means to surpass the limits of what is possible: *metamaterials*. The notion behind this concept lies on its own etymological meaning, combining the word *material* with the prefix *meta*, which denotes "beyond", to refer to "materials with properties beyond those found naturally". The prospect applications of such kind of materials have attracted the attention of the scientific and industrial communities for the past decades. Technically speaking, metamaterials consist of artificially engineered materials with the ability to manipulate waves for different outcomes. The nature of these waves is what determines the kind of application, offering a wide range of possibilities.

To narrow down the research, this study will focus on acoustic problems. The so-called *acoustic metamaterials* are capable of producing frequency bandgaps, i.e. selected regions in the frequency spectrum where waves' propagation is effectively stopped, due to local resonance phenomena. For practical purposes, this translates in the ability to

attenuate sound pressure waves at targeted frequency ranges, typically in the lower end of the spectrum, where a classical approach would require huge amounts of mass. This is a very interesting property, for instance, for cheap and lightweight sound insulation in many industrial sectors including construction or transport.

With the current and potential growth of manufacturing technologies, including novel techniques such as 3D-printing, practical realizations of metamaterials are getting closer. Furthermore, given the importance of the role their design plays in obtaining the desired properties, there is a need for fast and efficient resources capable of performing this task. In this context, the aim of this work is to develop a set of computational tools for the analysis and design of acoustic metamaterials. These tools are grounded on three fundamental pillars in the field of computational design of materials: (a) multiscale modelling, (b) model-order reduction techniques, and (c) topology optimization.

Additionally, as part of this work, the application of the aforementioned tools for the study, design and characterization of different kinds of acoustic metamaterials is performed. The obtained results and the concept of local resonance as the mechanism responsible for the attenuating capabilities of acoustic metamaterials is assessed through a set of experiments in an impedance tube with 3D-printed prototypes.

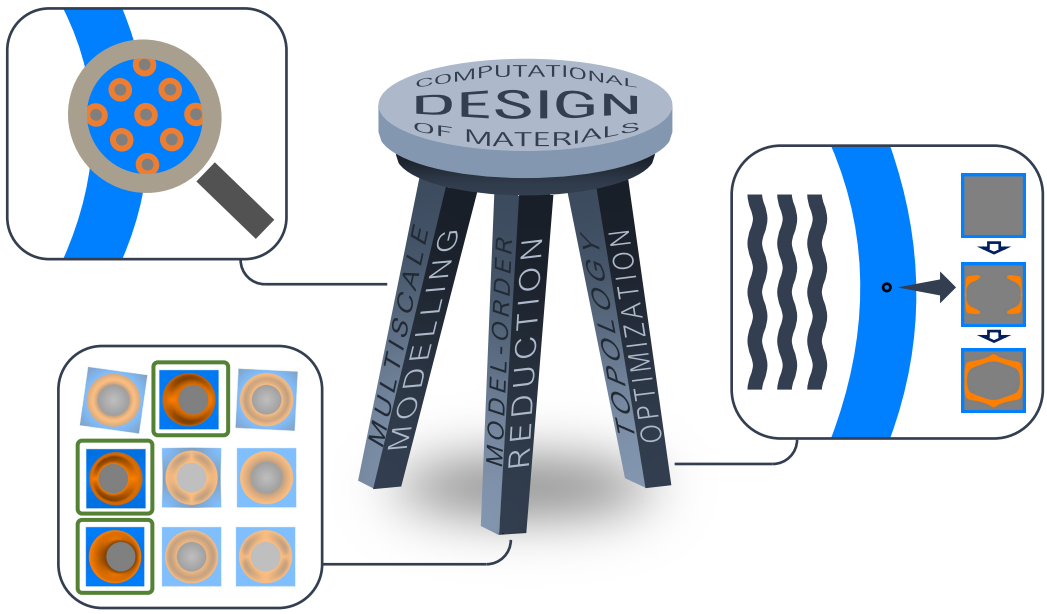

FIG. 1 Computational design of materials paradigm. The multiscale modelling, model-order reduction and topology optimization are the three pillars upon which it is built.

Chapter 2

STATE OF THE ART

2.1 Metamaterials technology

In the previous chapter, the concept of metamaterials has been introduced to describe artificially engineered structures capable of manipulating waves and exhibiting non-conventional behavior as a result. A more general definition is provided by Cui *et al*. (2010) where a metamaterial is considered "a macroscopic composite of periodic or non-periodic structure, whose function is due to both the cellular architecture and the chemical composition" [1]. According to this description, metamaterials gain their properties by combining materials with different chemical compositions and/or by rearranging their internal topology.

2.1.1 Early days of metamaterials

Even though the term metamaterial has been used since the late 1990's, the notion of "artificial" materials had already been explored in the past. For instance, in 1948, Kock managed to manipulate the refractive index of an artificial media created by periodically arranging conducting spheres, disks and strips [2]. However, it was not until 1967, when Veselago conducted the first theoretical study on plane-wave propagation in materials with simultaneously negative permittivity and permeability [3]. With his work, Veselago established the physics behind the metamaterial's ability to manipulate waves, in the context of electromagnetism. Those theoretical findings would not be validated until some decades later, with the first experimental realizations of the so-called double-negative metamaterials. Smith *et al*. (2000) introduced a composite structure based on split rings resonators (SRRs) that exhibited a frequency band over which both the effective permittivity and permeability were negative [4]. The SRRs is a common metamaterial design

that consists of a set of concentric conducting rings with a gap on each. It is used to achieve magnetic resonance in a selected frequency band, which is responsible for the negative refractive index of the metamaterial [5].

2.1.2 Phononic crystals and acoustic metamaterials

While the idea of waves' manipulation to obtain unusual properties was born in the context of electromagnetism, it rapidly extended to other fields where the material response is also governed by waves' propagation mechanisms. In particular, by applying the concept to sound waves manipulation, the notion of acoustic metamaterials was introduced. Analogously to how electromagnetic metamaterials exhibit exotic behavior by showing negative effective permittivity and permeability, in the context of acoustic metamaterials, this translates in negative effective mass density and bulk modulus. In this case, these are the source of certain regions in the frequency spectrum, called frequency bandgaps, where sound waves effectively stop propagating. There are two known mechanisms by which this can be achieved: Bragg scattering and local resonance effects [6].

Bragg scattering occurs in periodic media, typically consisting of a lattice with repeating unit cells, which are known as phononic crystals (PCs). The physics behind Bragg scattering effects is discussed in [7]. An important aspect to notice is that in order for Bragg scattering to manifest, the crystal's dimensions (i.e. the periodicity size) must be larger than the incident wave's wavelength. This means that bandgaps produced by PCs usually appear at frequency ranges higher than those interesting for acoustic applications based on sound insulation. However, PCs are still a topic of active research due to their applications in several areas including: superlensing, for which PCs can be used for medical and non-destructive sensing [8], energy harvesting through the interaction between PCs bandgaps and piezoelectric microstructures [9], thermal control using PCs with nanoscale dimensions [10] and opto-mechanics, where PCs are used in combination with their electromagnetic analogous, photonic crystals, for communication and sensing applications [11], among others. Also in this context, the notion of acoustic black holes (ABHs) [12], which typically operate in the same frequency range as PCs, has recently been proposed for isolating vibrations in plates [13].

The other phenomenon capable of producing frequency bandgaps is local resonance. Metamaterials that employ this mechanism to get their unusual properties are known as locally resonant acoustic metamaterials (LRAMs). As with PCs, the structure of LRAMs

contains a lower scale with a certain topology that triggers the effects causing the appearance of frequency bandgaps. While periodicity is not a requirement in this case, it is still preferable for most cases, as it enables a unit cell-based description of its dynamical properties as well as ease in the process of introducing resonating elements (for manufacturing purposes, for instance). A main difference of LRAMs in contrast to PCs is that the characteristic size of the lower scale needs to be smaller than the incident wave's wavelength [14]. This requirement is important for two reasons: (1) it allows using LRAMs for low-frequency applications (which are interesting especially in sound insulation problems) and, (2) in cases where periodicity is present, it gives the metamaterial the ability to be regarded as an effective medium.

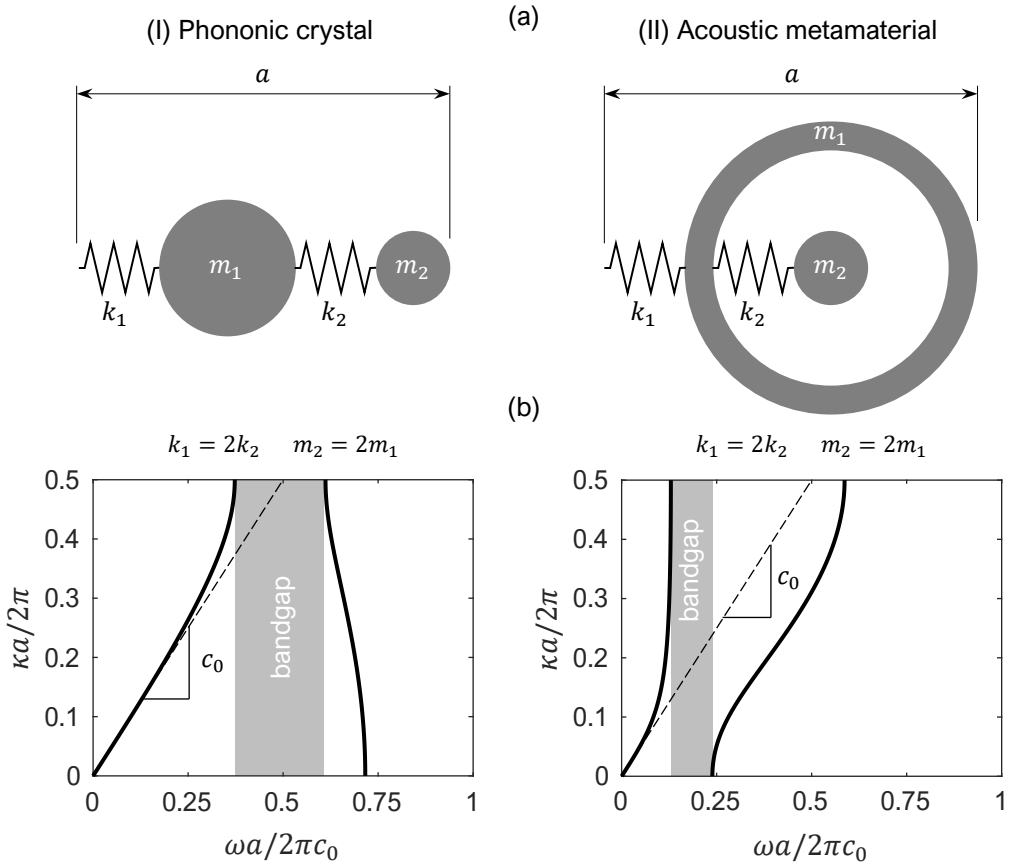

FIG. 2 Concept of phononic crystals (PCs) and acoustic metamaterials (AMs). (a) Rheological models of mass-and-mass (PCs) and mass-in-mass (AMs) unit cells. (b) Characteristic dispersion curves showing the bandgap formation nature of each case. The frequency ω is normalized with a reference frequency $\omega_0 = 2\pi\, c_0/a$, with c_0 being the static wave propagation speed. For comparison, the parameters in both systems are chosen so that they have the same static wave propagation speed, c_0. Notice how the frequency bandgaps are more narrowband in the AM case than in the PC case, but with the latter occurring at higher frequency ranges. These differences are more apparent the higher the contrast between k_1/k_2 and m_2/m_1 becomes.

As the name suggests, local resonance takes advantage of resonating effects in the internal structure of the metamaterial to effectively stop the propagation of waves at a macroscopic scale. In order for it to occur, the lower scale must be composed of certain resonating elements. These resonating elements typically contain a compliant component, the purpose of which is to play the role of a *spring*, and a dense component acting as *mass*, the combination of which resonates at the desired frequencies in order to produce bandgaps. It is important for local resonance effects to manifest that each unit cell vibrates independently of the others. For this reason, these effective spring-mass systems are typically embedded in a stiff matrix or frame.

While LRAMs are especially interesting for sound insulation, shielding and noise blocking purposes [15, 16], there are other kind of application for which they can also be considered. These include subwavelength focusing, where LRAMs allow to break the diffraction limit and can be used as an alternative to conventional imaging technologies [17–19], or cloaking applications, where an object becomes "invisible" to acoustic waves by guiding them around it instead of being scattered [20–23].

2.2 Computational design of materials

Computational modelling is a field that has experienced a significant growth in the last decades and has been infiltrating in a broad range of application areas. In several contexts, experimental validation of a phenomenon or the evaluation of a certain behavior is difficult to reproduce, either because of its complexity or simply due to the lack of resources. In such situations, computational modelling offers the ability to perform a preliminary (and sometimes sufficient) characterization allowing great savings of time and resources. Additionally, it can be used for design purposes, allowing the obtention of desired features and optimal results. In this regard, the field of computational design of materials, which is growing alongside new developments in computer technologies, is progressively getting more attention in several disciplines. The foundation upon which it is based can be synthesized with three main branches: the multiscale modelling, model-order reduction techniques and topology optimization.

2.2.1 Multiscale modelling

Homogenization-based or multiscale techniques offer the possibility of accounting for microstructural physical phenomena and their impact in a macroscopic level at a

relatively inexpensive computational cost compared to direct numerical simulations or concurrent multiscale techniques. In the context of solid mechanics, the first theoretical developments based on the obtention of macroscopic properties from heterogeneous materials were carried out by Hill (1965) [24] and Mandel (1971) [25], among others. Since then, these theories have derived to more sophisticated models, mostly based on finite element methods, allowing their use in a computational context and giving them several practical applications.

For instance, homogenization models in which the constitutive information driving the macroscopic analysis is computed from consecutive interaction between the macro and microscales can be found in Feyel and Chaboche (2000) [26] or Kouznetsova *et al*. (2001) [27]. This approach has been successfully applied to a wide range of quasi-static contexts, including complex material behavior such as softening and localization phenomena [28–30], multi-physics [31] or large deformations [32], among others. However, developments in the context of dynamic problems, where inertial effects are relevant, started to emerge only in more recent years with the works of Karamnejad *et al*. (2013) [33], Pham *et al*. (2013) [34] or De Souza Neto *et al*. (2015) [35, 36], who count among the first to propose a formulation in rigorous variational form based on a generalized Hill-Mandel principle along with kinematic admissibility between scales.

2.2.2 Model-order reduction techniques

Model-order reduction techniques are an effective tool to reduce the computational cost associated to large-scale problems. They are based on retaining the relevant information of the problem by using physical insight and intuition or through statistical correlation between input data and output results. In either case, the so-called projection-based methods have gained prominence in recent years. In projection-based methods a set of solutions is computed in an offline stage and a subspace of a reduced basis is built with the most dominant ones. Then, in the online stage, the governing equations are projected onto this reduced-order subspace, allowing faster computational evaluation while preserving the required accuracy for the problem.

The most popular model-order reduction technique is the proper orthogonal decomposition (POD). In Chatterjee's work, a review on the fundamental idea behind the POD can be found [37]. Furthermore, Krysl *et al*. (2001) provided a rigorous discussion on this method [38]. Other projection-based methods used, more specifically, in the context of

wave propagation in periodic media were firstly proposed by McDevitt *et al*. (2001) [39]. Research in this line was followed by Hussein and Hulbert (2006), who presented a method for fast dispersion curves calculation based on a mode-enriched model, in a multiscale context, by selecting a set of Bloch eigenvectors to build a projection subspace [40].

2.2.3 Topology optimization

Topology optimization techniques have been spreading progressively to a wide range of fields for the past decades. Typically, they are based on computing the gradient of a functional in order to steer the algorithm into gradually improving a certain objective function. The first notions were introduced in the work of Bendsøe *et al*. (1988), which proposed a method that relied on homogenization theory to define a set of macroscopic properties and perform the topology optimization through the parametrization of the microstructure [41]. The solid isotropic material with penalization (SIMP) method was proposed in 1989 also by Bendsøe [42] and has been improved by several works later [43], [44]. Since then, it has become one of the most used techniques and applications can be found in several disciplines, including compliant mechanisms [45], geometrical non-linear structures [46], multi-physics actuators [47], photonic crystal structures [48] or phononic bandgap materials [49], among others.

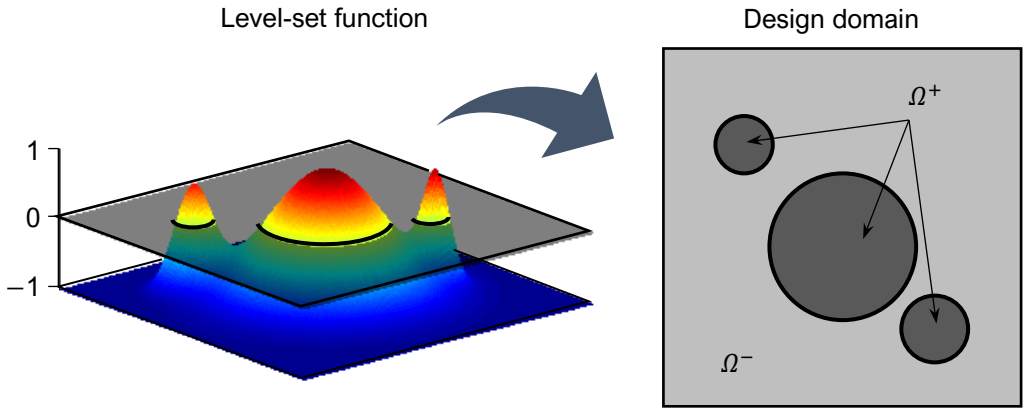

FIG. 3 Graphical idea of the level-set based methods for topology optimization. The level-set function φ sign determines material regions Ω^+ ($\varphi > 0$) and void regions Ω^- ($\varphi < 0$) in the design domain.

Theories based on topological derivative were first suggested by Eschenauer *et al*. (1994) [50] and Sokolowki and Zochowki (1999) [51]. They resort to computing a function evaluating the sensitivity of the specific problem to the appearance of an infinitesimal void in the material domain. In contrast, shape derivative methods are based on computing the sensitivity of the problem when a unit normal deformation is applied on the boundaries of the domain. In this context, level-set methods used in image processing were adapted to work together with the shape derivative [52, 53] and later also with the topological derivative [54, 55] as a tool to update the topology at each optimization step. Alternatively, recent methods combining a 0-level set function and an estimated topological derivative are being developed by Oliver, *et al*. (2019) [56] and Yago, *et al*. (2020) [57] to overcome the high computational cost of the aforementioned techniques.

2.2.4 Computational modelling of acoustic metamaterials

Research on acoustic metamaterials has derived in several approaches that go from simple analytical studies to sophisticated computational models capable of accounting for their intrinsic exotic behavior. For instance, in the work of Xiao et al. (2011), an analytical model of a 1D string with spring-mass resonators is developed to study the bandgap formation mechanisms showed by acoustic metamaterials [58]. In the context of numerical modelling, most of the early works focused on periodically repeated microstructures where Bloch-Floquet boundary conditions can be applied to study the dispersion properties of 2D and 3D unit cells [59, 60]. In this line, Hussein (2009) proposed a Bloch-based model to characterize the local resonance effects in periodic structures [61].

Other approaches have focused on retrieving effective properties from acoustic metamaterials by means of homogenization theory. In this regard, Fokin *et al*. (2007) developed a method to obtain properties from experimental measurements of the reflection and transmission coefficients of LRAMs [62]. Nemat-Nasser *et al*. (2011) presented a homogenization method based on Floquet theory applied to periodically arranged elastic composites [63]. In more recent developments, the use of computational homogenization frameworks based on variational formulations have been successfully applied to acoustic problems and, in particular, for the study and characterization of local resonance effects in LRAMs. For instance, Sridhar *et al*. (2016) proposed a Craig-Bampton mode synthesis substructuring method to reduce the set of degrees of freedom in the microscale accounting only for the relevant resonance modes, leading towards an emergent enriched

continuum [64, 65]. A similar approach is proposed in the present work [66, 67], but by performing a unit cell's system split into a quasi-static and inertial components based on a set of simple hypotheses that do not require to resort to substructuring techniques to identify the relevant resonance modes.

Given the intrinsic narrowband nature of frequency bandgaps caused by local resonance effects, research can be found in the literature aiming at enlarging the attenuating properties of acoustic metamaterials. In this regard, Krushynska *et al*. (2014) presented the first attempts towards the design of acoustic metamaterials by studying the effects of certain parameters in their topology [68]. Additionally, Matsuki *et al*. (2014) proposed a topology optimization-based method to find optimal LRAM configurations with multiple attenuation peaks [69].

Another approach that has been studied consists of exploiting the viscoelastic behavior of certain materials used in typical acoustic metamaterial configurations. In this context, Hussein and Frazier (2013) [70] introduced the concept of *metadamping* referring to the damping emergence phenomenon produced when viscous dissipation is used in combination with local resonance effects [71, 72]. The effects of dissipative behavior in acoustic metamaterials has also been studied analytically by Manimala and Sun (2014) [73]. Furthermore, numerical generalized viscoelastic models have been developed by Krushynska *et al*. (2016) [74] and Lewinska *et al*. (2017) [75] to characterize the attenuation performance of LRAMs.

Other attempts in this endeavor include, for instance, the addition of holes on a plate with resonating pillars. The idea was proposed by Bilal and Hussein (2013), who called this phenomenon the trampoline effect, given the analogy between springboards and recreational trampolines with the holed plate, the increased compliance of which enhances the motion of the pillars at the resonance frequencies [76].

2.3 Acoustic metamaterial designs

The first actual realizations of an acoustic metamaterial came from the work of Liu (2000), who built a composite structure that possessed negative elastic constants and exhibited frequency bandgaps around 400 and 1100 Hz [14]. The material consisted of a 2.1 cm slab with a structure made of an epoxy matrix with randomly dispersed rubber-coated lead spheres. In this case, the elastic properties of the silicone rubber coating made it

act as a spring, which combined with the high density of the lead spheres gave rise to local resonances at lower frequency ranges. The concept of building acoustic metamaterials based on the combination of different material properties was implemented in several other experimental demonstrations [77–81], where typically a polymer-based structure was used to host rubber-coated metal inclusions.

There are several other experimental realizations of acoustic metamaterials exploiting the local resonance phenomenon which are based on different configurations. For instance, the idea of introducing hollow topologies or cavities in the material, acting as Helmholtz resonators capable of producing bandgaps, has been explored [82, 83]. Designs with different kinds of resonators can also be found, including beam resonators [84], pillared plates [85–90] or membranes [91–93], among others. Recent works have also studied the effects of irregularities and random structures in acoustic metamaterials without periodic arrangements [94–97].

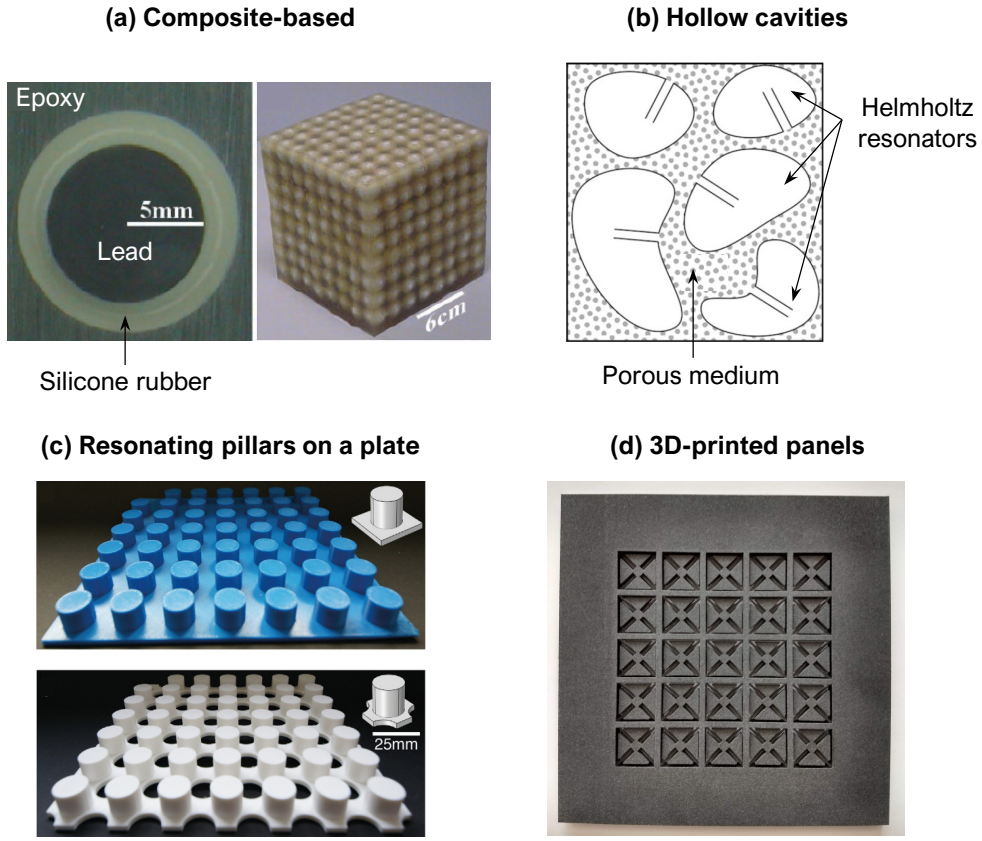

FIG. 4 Examples of different acoustic metamaterial designs. (a) Composite-based concept based on combining materials with different properties [14]. (b) Hollow cavities acting as Helmholtz resonators [83]. (c) Resonating pillars on a plate acting as an acoustic metamaterial [98]. (d) 3D-printed acoustic metamaterial panel [99].

While the idea and properties of acoustic metamaterials have been demonstrated, both theoretically and experimentally, their intrinsic complex nature still make them far from practical realizations. In this regard, new kinds of acoustic metamaterials meant to be built monolithically through an additive manufacturing process have been devised. Since only one material is considered, one cannot resort to the combination of material properties in order to achieve the resonances in the desired frequency range. This highlights the importance of the topology and geometrical features in the design for these kinds of acoustic metamaterials. Experimental implementations of such metamaterials can be found in the work of Claeys *et al*. (2016), in which they demonstrate the attenuating capabilities of acoustic enclosures composed of unit cells with internal resonators that were fully 3D-printed [98]. More recently, Leblanc and Lavie (2017) came up with another 3D-printed configuration based on a resonating membrane [100], while McGee *et al*. (2019) devised a 3D-printed foam with hollow spheres capable of producing low-frequency bandgaps [101]. Finally, as a result of the present work, a 3D-printed prototype LRAM panel has been designed and tested numerically and experimentally to assess its transmission loss capabilities [99].

Chapter 3

SCIENTIFIC CONTRIBUTIONS

3.1 Multiscale homogenization framework

3.1.1 Multiscale virtual power principle

Aiming at characterizing the behavior of LRAMs and to provide a computational framework that can be employed in the design of such metamaterials, a homogenization model has been developed. The multiscale framework is based on the ability to identify a repeating structure (unit cell) in what is considered a macroscopic domain. In the present context, this unit cell configures the metamaterial structure and is treated as the microscale (see Fig. 5).

In this regard, a kinematic relation is established between the macro and microscales in terms of the displacement field and its symmetric gradient (i.e. strain field). Namely,

$$\boldsymbol{u}_{\mu}(\boldsymbol{y},t) = \boldsymbol{u}(\boldsymbol{x},t) + \boldsymbol{\nabla}_{\boldsymbol{x}}\boldsymbol{u}(\boldsymbol{x},t)\cdot(\boldsymbol{y}-\boldsymbol{y}^{(0)}) + \tilde{\boldsymbol{u}}_{\mu}(\boldsymbol{y},t), \tag{1}$$

$$\boldsymbol{\nabla}^{\mathrm{S}}_{\boldsymbol{y}}\boldsymbol{u}_{\mu}(\boldsymbol{y},t) = \boldsymbol{\nabla}^{\mathrm{S}}_{\boldsymbol{x}}\boldsymbol{u}(\boldsymbol{x},t) + \boldsymbol{\nabla}^{\mathrm{S}}_{\boldsymbol{y}}\tilde{\boldsymbol{u}}_{\mu}(\boldsymbol{y},t), \tag{2}$$

where $\boldsymbol{u}$ and $\boldsymbol{u}_{\mu}$ correspond to the displacement fields in the macro and the microscales, respectively, and $\tilde{\boldsymbol{u}}_{\mu}$ is the micro-fluctuation field. Note in Eqs. (1) and (2) the use of $\boldsymbol{x}$ to refer to the spatial coordinates in the macroscopic domain and $\boldsymbol{y}$ to refer to their microscale counterparts ($\boldsymbol{y}^{(0)}$ are the coordinates of the unit cell's geometric center). The symbols $\boldsymbol{\nabla}_{\boldsymbol{x}}$ and $\boldsymbol{\nabla}_{\boldsymbol{y}}$ denote the gradient operators in the macro and microscale contexts and the superscript $(\cdot)^{\mathrm{S}} = ((\cdot)+(\cdot)^{\mathrm{T}})/2$ is used to specify the symmetric component of $(\cdot)$. A specific set of restrictions over the micro-fluctuation field and its symmetric gradient, $\tilde{\boldsymbol{u}}_{\mu}$ and $\boldsymbol{\nabla}^{\mathrm{S}}_{\boldsymbol{y}}\tilde{\boldsymbol{u}}_{\mu}$, need to be considered in order to set the kinematic relation between scales.

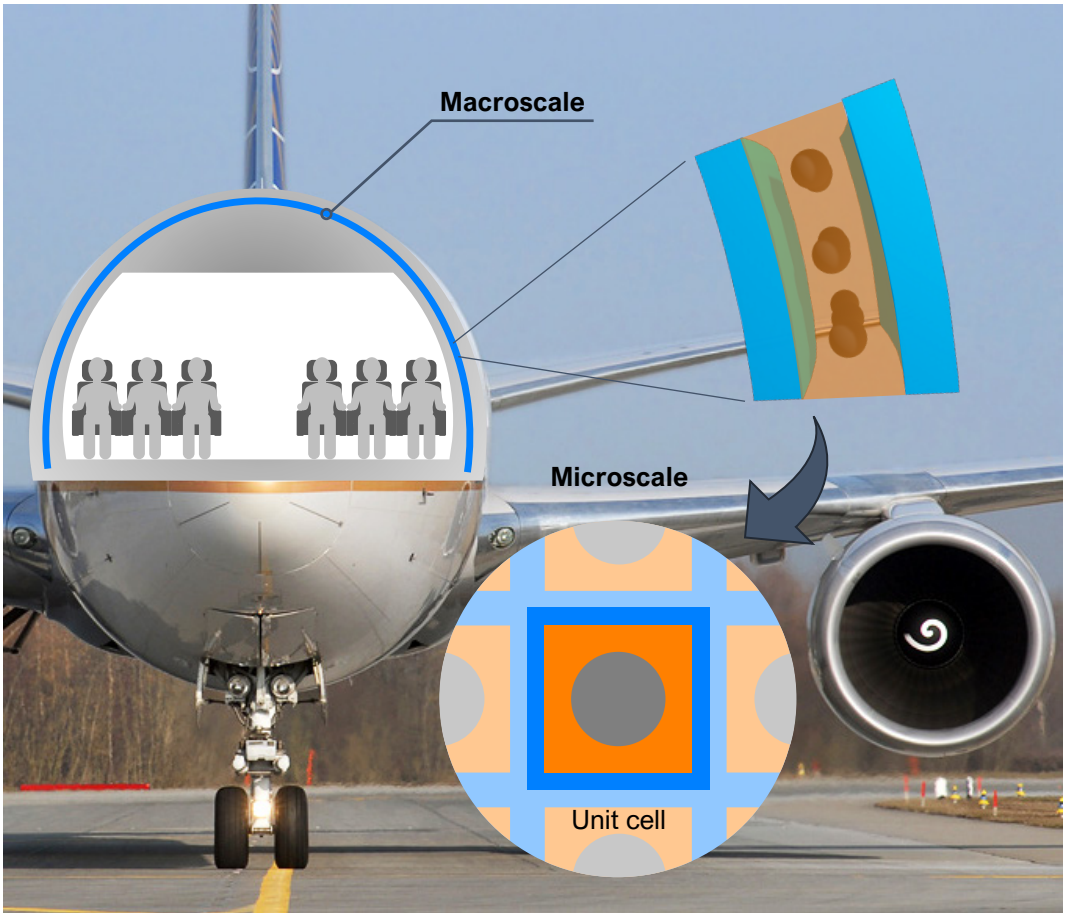

FIG. 5 Multiscale framework setting. The macroscale domain corresponds to some part or structure with a certain internal configuration/topology that is represented by the microscale.

Then, an energetic equivalence between both scales is established by means of an extended version of the classical Hill-Mandel principle, in which inertial effects can be accounted for (also known as *multiscale virtual power principle* [36]). In its variational form, the postulate reads

$$\boldsymbol{\sigma} : \boldsymbol{\nabla}^{\mathrm{S}}_{\boldsymbol{x}} \dot{\boldsymbol{u}} - \boldsymbol{f} \cdot \dot{\boldsymbol{u}} = \langle \boldsymbol{\sigma}_{\mu} : \boldsymbol{\nabla}^{\mathrm{S}}_{\boldsymbol{y}} \dot{\boldsymbol{u}}_{\mu} - \boldsymbol{f}_{\mu} \cdot \dot{\boldsymbol{u}}_{\mu} \rangle_{\Omega_{\mu}}, \tag{3}$$

for all kinematically admissible (i.e. *constrained* by Eqs. (1) and (2)) displacement-rate fields $\dot{\boldsymbol{u}}$ and $\dot{\boldsymbol{u}}_{\mu}$. In Eq. (3), $\boldsymbol{\sigma}$ and $\boldsymbol{\sigma}_{\mu}$ are the macro and microscale stress tensors, respectively, while $\boldsymbol{f}$ and $\boldsymbol{f}_{\mu}$ denote the D'Alembert forces density vectors (which include the inertial effects), also for the macro and microscales. The notation $\langle \cdot \rangle_{\Omega_{\mu}} = \frac{1}{|\Omega_{\mu}|} \int_{\Omega_{\mu}} (\cdot) d\Omega$ is employed here to refer to the average value of $(\cdot)$ over the unit cell domain Ω_{μ}.

3.1.2 Lagrange functional-based reformulation

The problem can be reformulated as a saddle point problem where the specific kinematic restrictions are introduced via Lagrange multipliers. In this context, by associating these Lagrange multipliers to the minimal kinematic restrictions, the problem results in the following system of equations:

$$\langle \boldsymbol{\sigma}_\mu : \boldsymbol{\nabla}^S_{\boldsymbol{y}} \delta \boldsymbol{u}_\mu - \boldsymbol{f}_\mu \cdot \delta \boldsymbol{u}_\mu \rangle_{\Omega_\mu} - \boldsymbol{\beta} \cdot \langle \delta \boldsymbol{u}_\mu \rangle_{\Omega_\mu} - \boldsymbol{\lambda} : \langle \boldsymbol{\nabla}^S_{\boldsymbol{y}} \delta \boldsymbol{u}_\mu \rangle_{\Omega_\mu} = 0, \quad \forall\, \delta \boldsymbol{u}_\mu; \tag{4}$$

$$\langle \boldsymbol{u}_\mu - \boldsymbol{u} \rangle_{\Omega_\mu} \cdot \delta \boldsymbol{\beta} = 0, \quad \forall\, \delta \boldsymbol{\beta}; \tag{5}$$

$$\langle \boldsymbol{\nabla}^S_{\boldsymbol{y}} \boldsymbol{u}_\mu - \boldsymbol{\varepsilon} \rangle_{\Omega_\mu} : \delta \boldsymbol{\lambda} = 0, \quad \forall\, \delta \boldsymbol{\lambda}; \tag{6}$$

where $\boldsymbol{\beta}$ and $\boldsymbol{\lambda}$ are the Lagrange multipliers and the perturbation fields $\delta \boldsymbol{u}_\mu$, $\delta \boldsymbol{\beta}$ and $\delta \boldsymbol{\lambda}$, are totally *unconstrained*. Note that in Eq. (6), the macroscopic strain field is denoted by $\boldsymbol{\varepsilon} \equiv \boldsymbol{\nabla}^S_{\boldsymbol{x}} \boldsymbol{u}$. The key aspect about associating the Lagrange multipliers to the minimal kinematic restrictions (derived from Eqs. (5) and (6)), is that one can give them a *physical* interpretation. This can be seen by appropriately manipulating Eq. (4) to obtain:

$$\boldsymbol{\beta}(\boldsymbol{x}, t) = -\langle \boldsymbol{f}_\mu(\boldsymbol{y}, t) \rangle_{\Omega_\mu} \equiv -\boldsymbol{f}(\boldsymbol{x}, t), \tag{7}$$

$$\boldsymbol{\lambda}(\boldsymbol{x}, t) = \langle \boldsymbol{\sigma}_\mu - \boldsymbol{f}_\mu(\boldsymbol{y}, t) \otimes^{\mathrm{S}} (\boldsymbol{y} - \boldsymbol{y}^{(0)}) \rangle_{\Omega_\mu} \equiv \boldsymbol{\sigma}(\boldsymbol{x}, t), \tag{8}$$

where the operator $\otimes^{\mathrm{S}}$ is used to denote the symmetric outer product between tensors (i.e. $\boldsymbol{a} \otimes^{\mathrm{S}} \boldsymbol{b} = (\boldsymbol{a} \otimes \boldsymbol{b} + \boldsymbol{b} \otimes \boldsymbol{a})/2$). Specific details on the derivation of these results are given in Article I. Note that according to Eqs. (7) and (8), the Lagrange multiplier $\boldsymbol{\beta}$ can be interpreted as the opposite macroscopic D'Alembert force density vector, $\boldsymbol{f}$, while the other Lagrange multiplier, $\boldsymbol{\lambda}$, is directly interpreted as the macroscopic stress tensor, $\boldsymbol{\sigma}$.

Considering a Galerkin-based finite element discretization of Eqs. (4)-(6), the resulting system can be expressed in matrix form as

$$\begin{bmatrix} \mathbb{M}_\mu & \mathbf{0} & \mathbf{0} \\ \mathbf{0} & \mathbf{0} & \mathbf{0} \\ \mathbf{0} & \mathbf{0} & \mathbf{0} \end{bmatrix} \begin{bmatrix} \ddot{\widehat{\boldsymbol{u}}}_\mu \\ \ddot{\boldsymbol{\beta}} \\ \ddot{\boldsymbol{\lambda}} \end{bmatrix} + \begin{bmatrix} \mathbb{K}_\mu & -\mathbb{N}_\mu^{\mathrm{T}} & -\mathbb{B}_\mu^{\mathrm{T}} \\ -\mathbb{N}_\mu & \mathbf{0} & \mathbf{0} \\ -\mathbb{B}_\mu & \mathbf{0} & \mathbf{0} \end{bmatrix} \begin{bmatrix} \widehat{\boldsymbol{u}}_\mu \\ \boldsymbol{\beta} \\ \boldsymbol{\lambda} \end{bmatrix} = \begin{bmatrix} \widehat{\boldsymbol{b}}_\mu \\ -\boldsymbol{u} \\ -\boldsymbol{\varepsilon} \end{bmatrix}, \tag{9}$$

where $\mathbb{K}_\mu$, $\mathbb{M}_\mu$ are the standard stiffness and mass matrices, $\mathbb{N}_\mu$ and $\mathbb{B}_\mu$ are matrices applying the minimal kinematic restrictions, $\widehat{\boldsymbol{u}}_\mu$ is the vector of nodal micro-displacements and $\widehat{\boldsymbol{b}}_\mu$ is another vector containing body forces data. Again, the reader is referred to Article I for a complete derivation of all these terms.

The system in Eq. (9) clearly shows that the microscale gets the information from the displacement and strain fields, $\boldsymbol{u}$ and $\boldsymbol{\varepsilon}$, in the associated macroscopic point (which become *actions* in the microscale system). These, along with the body forces data given by $\widehat{\boldsymbol{b}}_\mu$ (if present), are used to obtain the effective response, the information of which is condensed on the Lagrange multipliers, $\boldsymbol{\beta}$ and $\boldsymbol{\lambda}$, and returned to the macroscale as the D'Alembert force density and stress (acting as *reactions* in the microscale context).

3.1.3 Application to acoustic metamaterials problems

Up to this point, the proposed formulation is general for as long as homogenization theory holds, which means: (a) it exists a separation of scales enough to satisfy $\lambda \gg \ell_\mu$ (i.e. inertial effects or force excitations in the macroscale have a wavelength λ higher than one order of magnitude compared to the characteristic size of the microscale ℓ_μ) and (b) the kinematic relation between both scales reflects the actual material interaction in the microscale. The better these two conditions are satisfied, the better the microscale effects on the macroscale will be captured by the homogenization scheme.

However, in the context of this work, where the goal of the proposed multiscale framework is to characterize the behavior of acoustic metamaterials, additional hypotheses can be considered to further simplify the model. In particular:

(a) Supported by the separation of scales condition, $\lambda \gg \ell_\mu$, the macroscopic strain acceleration field can be neglected, $\ddot{\boldsymbol{\varepsilon}} \approx \mathbf{0}$, because no deformation modes will be excited. Although this condition limits the applicability of the homogenization framework to cases in the low-frequency regime, it is also a requirement for local resonance phenomena to arise. Thus, the model is still capable of characterizing the behavior of LRAMs.

(b) The density distribution on the unit cell satisfies $\langle \rho_\mu (\boldsymbol{y} - \boldsymbol{y}^{(0)}) \rangle_{\Omega_\mu} \approx \mathbf{0}$, i.e. its center of mass lies close to the geometric center $\boldsymbol{y}^{(0)}$. This occurs, for instance, if the unit cell topology is symmetric with respect to its geometric center $\boldsymbol{y}^{(0)}$.

(c) Body forces are neglected, so that the D'Alembert force density vector contains only its inertial component, i.e. $\boldsymbol{f}_\mu \approx -\rho_\mu \ddot{\boldsymbol{u}}_\mu$ and $\boldsymbol{\beta} \equiv -\boldsymbol{f} \approx \dot{\boldsymbol{p}}$ (with ρ_μ being the density distribution on the microscale and $\dot{\boldsymbol{p}}$ denoting the time derivative of the linear momentum in the macroscale).

Furthermore, given the periodic nature of acoustic metamaterial structures, and since the study on the microscale is focused on a unit cell, the appropriate set of kinematic restrictions considered for the micro-fluctuation field consists of: (1) applying periodic boundary conditions and (2) prescribing the value of $\tilde{\boldsymbol{u}}_\mu = \mathbf{0}$ at some point on the unit cell's boundary (in order to avoid rigid body motion). These are used instead of the minimal kinematic conditions as they give more accurate results in the present context. In Fig. 6 a schematic representation of the micro-displacement field is shown. The derivation of the matrices $\mathbb{I}$, $\mathbb{Y}_\theta$, $\mathbb{Y}_\varepsilon$ and $\mathbb{P}$ (from Fig. 6) is given in Article I.

In order to proceed with the unit cell system resolution, in the context of acoustic metamaterials, the system in Eq. (9) will be split into two subsystems. Under the assumptions considered, this split will allow us to isolate the *quasi-static* response from the *inertial* one, simply by dealing with the actions of the system (i.e. the macroscopic displacement and strain fields, $\boldsymbol{u}$ and $\boldsymbol{\varepsilon}$) separately.

The quasi-static subsystem is derived when $\boldsymbol{u} = \mathbf{0}$ is considered, so it represents the system's response to a homogeneous strain action, $\boldsymbol{\varepsilon}$. According to hypothesis (a), by assuming $\ddot{\boldsymbol{\varepsilon}} \approx \mathbf{0}$, the inertial response of this subsystem can be neglected (hence the name quasi-static). In this regard, one can anticipate the resulting displacement field to satisfy $\ddot{\boldsymbol{u}}_\mu^{(1)} \approx \mathbf{0}$ and, according to Eq. (7) and considering $\boldsymbol{f}_\mu^{(1)} = -\rho_\mu \ddot{\boldsymbol{u}}_\mu^{(1)}$, then $\boldsymbol{\beta}^{(1)} \equiv \dot{\boldsymbol{p}}^{(1)} \approx \mathbf{0}$. This subsystem can be solved by means of classical homogenization theory and one is able to obtain a value for the effective macroscopic stress as a result,

$$\boldsymbol{\sigma}^{(1)} \equiv \boldsymbol{\lambda}^{(1)} = \mathbf{C}^{\text{eff}} : \boldsymbol{\varepsilon}, \tag{10}$$

where $\mathbf{C}^{\text{eff}}$ is the resulting effective homogenized constitutive tensor.

On the other hand, the inertial subsystem takes into account the effect of a homogeneous displacement $\boldsymbol{u}$ in the action vector, so in this case $\boldsymbol{\varepsilon} = \mathbf{0}$. Since body forces are being neglected here (according to hypothesis (c)), it should be noted that the sum of both subsystems accounts for the complete action vector, hence giving the full response of the original microscale system. In this case, given the nature of the action for this system (that essentially simulates a homogeneous, rigid body-like displacement of the unit cell) one can anticipate the traction forces appearing as a reaction to be negligible, $\boldsymbol{\sigma}_\mu^{(2)} \cdot \boldsymbol{n} \approx \mathbf{0}$ ($\boldsymbol{n}$ here referring to the outward unit normal vector at the unit cell's boundaries). Furthermore, in virtue of hypothesis (b), it is reasonable to assume that the global contribution

of the resulting moments will also be small, thus the term $\langle \rho_\mu \ddot{\boldsymbol{u}}_\mu^{(2)} \otimes^{\mathrm{S}} (\boldsymbol{y} - \boldsymbol{y}^{(0)}) \rangle_{\Omega_\mu} \approx \mathbf{0}$ can be neglected too. In this regard, according to Eq. (8), one can expect $\boldsymbol{\lambda}^{(2)} \equiv \boldsymbol{\sigma}^{(2)} \approx \mathbf{0}$, and obtain an effective macroscopic inertial force density as a result,

$$\dot{\boldsymbol{p}}^{(2)} \equiv \boldsymbol{\beta}^{(2)} = \bar{\rho} \ddot{\boldsymbol{u}} + \langle \rho_\mu \ddot{\tilde{\boldsymbol{u}}}_\mu^{(2)} \rangle_{\Omega_\mu} = \bar{\rho} \ddot{\boldsymbol{u}} + \mathbb{D} \ddot{\hat{\boldsymbol{u}}}_\mu^{*}, \tag{11}$$

where $\bar{\rho} = \langle \rho_\mu \rangle_{\Omega_\mu}$ is the average density of the unit cell, $\ddot{\hat{\boldsymbol{u}}}_\mu^{*}$ is the nodal vector containing the free degrees of freedom of the micro-fluctuation acceleration field, $\ddot{\tilde{\boldsymbol{u}}}_\mu^{(2)}$, and $\mathbb{D}$ is a *pseudo-density* coupling matrix.

At this point, it is important to remark two key aspects:

(1) By expressing the microscale system in the form of Eq. (9), one gets enough *physical insight* of the problem to properly apply the simplifying hypotheses considered, granting us with the ability to *uncouple* the macroscopic stress from the macroscopic inertial force density and associate the former with the macroscopic strains only (through Eq. (10)), and the latter with the macroscopic acceleration field (through Eq. (11)).

(2) The second component appearing in Eq. (11), $\langle \rho_\mu \ddot{\tilde{\boldsymbol{u}}}_\mu^{(2)} \rangle_{\Omega_\mu} \equiv \mathbb{D} \ddot{\hat{\boldsymbol{u}}}_\mu^{*}$, corresponds to the micro-inertial effects of the metamaterial on the macroscale, thus being the most interesting term in this context. However, it requires a full resolution of the inertial subsystem in order to obtain the resulting micro-fluctuation field, $\ddot{\tilde{\boldsymbol{u}}}_\mu^{(2)}$

$$\mathbb{M}_\mu^{*} \ddot{\hat{\boldsymbol{u}}}_\mu^{*} + \mathbb{K}_\mu^{*} \hat{\boldsymbol{u}}_\mu^{*} = -\mathbb{D}^T \ddot{\boldsymbol{u}}, \tag{12}$$

where $\mathbb{M}_\mu^{*}$ and $\mathbb{K}_\mu^{*}$ are the mass and stiffness matrices obtained after the kinematic restrictions over the micro-fluctuation field have been applied. This is not efficient from a computational point of view, since this system solving needs to be successively carried out *online* and at each point in the macroscale.

3.1.4 Modal-based reduced-order modelling

Aiming at counteracting the issue with the computational efficiency of the formulation involving the micro-inertial effects, a reduced-order methodology is devised. Given the nature of the problem, we want the term $\langle \rho_\mu \ddot{\tilde{\boldsymbol{u}}}_\mu^{(2)} \rangle_{\Omega_\mu} \equiv \mathbb{D} \ddot{\hat{\boldsymbol{u}}}_\mu^{*}$ to capture the local resonance phenomenon characterizing the acoustic metamaterial behavior. To do so, a modal

analysis of Eq. (12) is performed, from which the mass-normalized eigenvectors, $\widehat{\boldsymbol{\phi}}_{\mu}^{*(k)}$, and eigenvalues, $\lambda_{\mu}^{*(k)}$, can be obtained:

$$\left(\mathbb{K}_{\mu}^{*} - \lambda_{\mu}^{*(k)}\mathbb{M}_{\mu}^{*}\right)\widehat{\boldsymbol{\phi}}_{\mu}^{*(k)} = \mathbf{0}, \quad \text{such that} \quad \widehat{\boldsymbol{\phi}}_{\mu}^{*(k)T}\mathbb{M}_{\mu}^{*}\widehat{\boldsymbol{\phi}}_{\mu}^{*(k)} = 1. \tag{13}$$

Then, the solution field can be expressed as

$$\widehat{\boldsymbol{u}}_{\mu}^{*} = \sum_{k} \widehat{\boldsymbol{\phi}}_{\mu}^{*(k)} q_{\mu}^{*(k)}, \tag{14}$$

where $q_{\mu}^{*(k)}$ are the modal amplitudes associated to the k-th eigenvectors, which become the new system unknowns. Furthermore, the system in Eq. (12) can also be projected onto each eigenvector, yielding a set of *uncoupled* equations

$$\omega_{\mu}^{*(k)^2} q_{\mu}^{*(k)} + \ddot{q}_{\mu}^{*(k)} = -\mathbb{Q}^{(k)^T}\ddot{\boldsymbol{u}}, \tag{15}$$

where $\omega_{\mu}^{*(k)^2} = \lambda_{\mu}^{*(k)}$ refer to the natural frequencies and $\mathbb{Q}^{(k)} = \mathbb{D}\widehat{\boldsymbol{\phi}}_{\mu}^{*(k)}$ can be regarded as a coupling vector (or the k-th component of a coupling matrix $\mathbb{Q}$). In this regard, the macroscopic inertial force density expression can be written as

$$\dot{\boldsymbol{p}} \approx \bar{\rho}\ddot{\boldsymbol{u}} + \sum_{k} \mathbb{Q}^{(k)}\ddot{q}_{\mu}^{*(k)}. \tag{16}$$

The actual system reduction here comes from identifying the set of relevant eigenvectors (i.e. vibration modes) responsible for local resonance effects. This selection is performed at two different levels:

(1) The first big truncation comes from the separation of scales condition, that limits the applicability of the proposed formulation to the low-frequency range. In particular, all modes associated to a natural frequency $\omega_{\mu}^{*(k)}$ above a certain limit can be discarded as they will not be excited in the range of application of the model. This limit is typically determined by the first natural frequencies associated to deformation modes of the unit cell.

(2) From the set of remaining modes after the first truncation, only those relevant on the macroscale should be considered. In the proposed model, the criterion to determine whether a particular mode is relevant comes down to the coupling vector $\mathbb{Q}^{(k)}$. A small absolute value of the magnitude of $\mathbb{Q}^{(k)}$ indicates that the vibration

mode $\widehat{\boldsymbol{\phi}}_{\mu}^{*(k)}$ associated to the natural frequency $\omega_{\mu}^{*(k)}$ is poorly coupled with the macroscale, hence its effects can be neglected. In other words, it means that this mode is not responsible for local resonance effects.

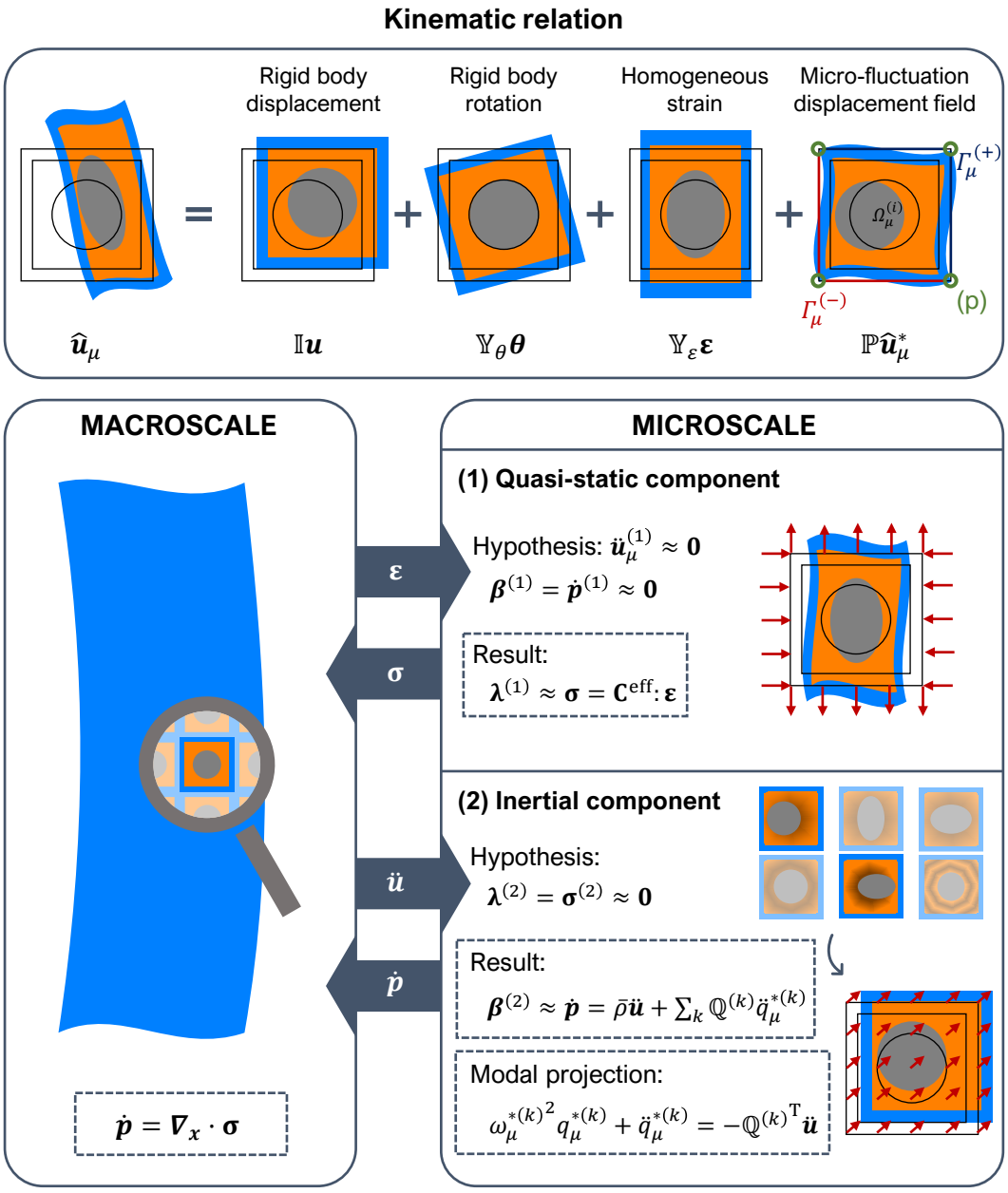

FIG. 6 Global homogenization scheme for characterizing acoustic metamaterials. The wave equation in the macroscale is solved with effective values of the stress and inertial force density terms, $\boldsymbol{\sigma}$ and $\dot{\boldsymbol{p}}$, that come from the resolution of the unit cell system in the microscale under the action of the associated macroscopic strain and acceleration fields, $\boldsymbol{\varepsilon}$ and $\ddot{\boldsymbol{u}}$. This problem is split into a quasi-static component and a reduced inertial subsystem allowing us to uncouple the stress and inertial force density contributions in the macroscale, while still accounting for local resonance effects.

3.1.5 Homogenization framework applications

With Eqs. (10), (15) and (16), we now have all the ingredients to express the set of equations to be solved in the macroscale:

$$\begin{cases} \nabla_x \cdot \left(\mathbf{C}^{\text{eff}} : \nabla_x^{\text{S}} \boldsymbol{u}(\boldsymbol{x}, t) \right) - \bar{\rho} \ddot{\boldsymbol{u}}(\boldsymbol{x}, t) = \displaystyle\sum_k \mathbb{Q}^{(k)} \ddot{q}_\mu^{*(k)}(\boldsymbol{x}, t) \,, \\ \omega_\mu^{*(k)^2} q_\mu^{*(k)}(\boldsymbol{x}, t) + \ddot{q}_\mu^{*(k)}(\boldsymbol{x}, t) = -\mathbb{Q}^{(k)^T} \ddot{\boldsymbol{u}}(\boldsymbol{x}, t). \end{cases} \tag{17}$$

Again, it should be noted that local resonance effects are accounted for by the presence of the coupling vector $\mathbb{Q}^{(k)}$ in the equations. But for this additional term to appear, the unit cell design of the acoustic metamaterial plays an important role. In particular, two key aspects need to be satisfied:

(a) Each unit cell is isolated from the rest in order to trigger internal resonance modes. This is important for the separation of scales condition, $\lambda \gg \ell_\mu$, to be satisfied, which is also required for local resonance effects to arise. To guarantee this, one can rely on employing stiff materials on the unit cell's boundaries, for instance.

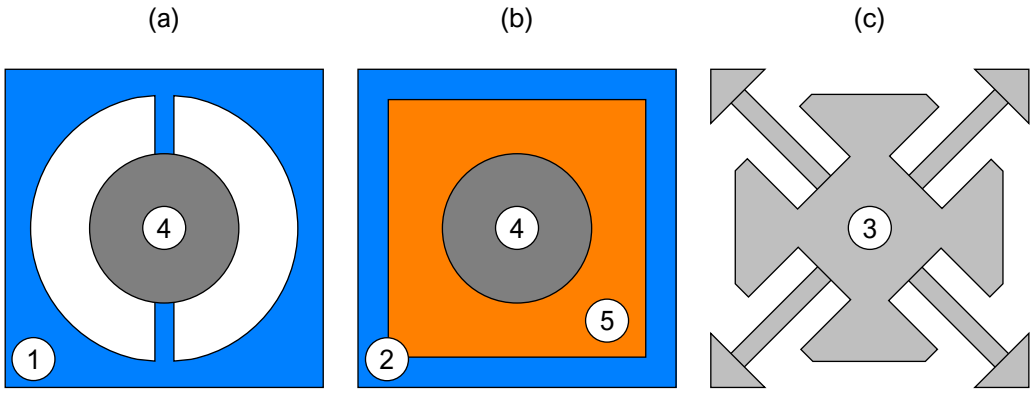

FIG. 7 Different LRAM-based unit cell configurations. All the designs consist of a relatively stiff frame to isolate each unit cell from the rest and a resonating element with components acting as masses and springs. (a) Bi-material design considered in Article I: the steel inclusion is the resonating element, which is attached to a polymer-based frame through thin attachments built with the same material. (b) Three-phase composite configuration used in Article II: in this case, the resonating element is a steel inclusion coated with a silicone rubber embedded in a stiff matrix. (c) Single material unit cell devised for Article III: the support rods on the vertices fix each cell and the combination of the thin attachments with the flower-shaped inclusion allow for out-of-plane local resonance effects in the low-frequency range of interest, despite employing only one material phase. The numbers correspond to materials listed in Tab. 1.

TAB. 1 Material properties considered for the different LRAM designs.

Material	Density (kg/m^3)	Young's Mod. (MPa)	Poisson's ratio
(1) Nylon	1100	2000	0.4
(2) Epoxy	1180	4350	0.368
(3) PA 11	1050	1800	0.405
(4) Steel	7800	180000	0.33
(5) Silicone rubber	1300	0.1175	0.469

(b) The unit cell contains some kind of resonating element. These resonating elements are what cause the internal resonance modes that trigger the local resonance effects at a specified frequency. To achieve this, one can combine materials with different properties (preferably *compliant* materials assuming the role of springs and *dense* inclusions to act as masses) and/or rely on specific topologies that produce the same effects.

In Fig. 7, different LRAM-based unit cell configurations considered in this work are depicted. Each one employs a different strategy to achieve the local resonance effects expected.

3.1.5.1 Homogenized macroscale model to study local resonance effects

In order to analyze the behavior of LRAMs and provide a better understanding of the bandgap formation mechanisms due to local resonance effects, an analytical treatment of Eq. (17) will be performed.

To do so, Eq. (17) will be solved in the frequency domain, for a given frequency ω, allowing us to condense the system by establishing the following relation:

$$\ddot{q}_{\mu}^{*(k)}(\boldsymbol{x},t) = \frac{\omega^2}{\omega_{\mu}^{*(k)^2} - \omega^2} \mathbb{Q}^{(k)^T} \ddot{\boldsymbol{u}}(\boldsymbol{x},t). \tag{18}$$

Substituting Eq. (18) into the expression for the inertial force density (given by Eq. (16)) allows us to determine an effective density tensor,

$$\mathbf{R}^{\text{eff}}(\omega) = \bar{\rho}\mathbf{1} + \sum_k \frac{\omega^2}{\omega_{\mu}^{*(k)^2} - \omega^2} \mathbb{Q}^{(k)} \otimes \mathbb{Q}^{(k)^T}, \tag{19}$$

where $\mathbf{1}$ is the identity tensor.

For the sake of simplicity, let us assume plane wave propagation at a given frequency ω and wavenumber κ. Then

$$\boldsymbol{u}(\boldsymbol{x},t) = \boldsymbol{U}e^{i(\kappa \boldsymbol{n}_\kappa \cdot \boldsymbol{x} - \omega t)}, \tag{20}$$

where $\boldsymbol{U}$ is the wave amplitude and $\boldsymbol{n}_\kappa$ is a unit vector with the wave propagation direction. In this context,

$$\ddot{\boldsymbol{u}}(\boldsymbol{x},t) = -\omega^2 \boldsymbol{U}e^{i(\kappa \boldsymbol{n}_\kappa \cdot \boldsymbol{x} - \omega t)}, \tag{21}$$

$$\boldsymbol{\nabla}_{\boldsymbol{x}}^{S}\boldsymbol{u}(\boldsymbol{x},t) = i\kappa \boldsymbol{n}_\kappa \otimes^{S} \boldsymbol{U}e^{i(\kappa \boldsymbol{n}_\kappa \cdot \boldsymbol{x} - \omega t)}. \tag{22}$$

Upon substitution of Eqs. (21) and (22) into Eq. (17), one gets the following dispersion relation

$$\left(\omega^2 \mathbf{R}^{\text{eff}}(\omega) - \kappa^2 \boldsymbol{n}_\kappa^T \cdot \mathbf{C}^{\text{eff}} \cdot \boldsymbol{n}_\kappa\right)\boldsymbol{U} = \mathbf{0}. \tag{23}$$

To further simplify the analysis, let us consider a wave propagating in the x-direction, i.e. $\boldsymbol{n}_\kappa = \{1,0,0\}^T$, and a single vibration mode arising from the microscale causing local resonance effects only in the direction of the wave propagation, i.e. $\mathbb{Q}^{(1)} = \{Q_1^{(1)},0,0\}^T$. In this regard, assuming the effective metamaterial has a standard linear elastic behavior, one gets three eigenvalues and eigenvectors from Eq. (23), namely

$$\begin{cases} \kappa^{(1)} = \omega\sqrt{\dfrac{\bar{\rho}}{C_{1111}^{\text{eff}}} + \dfrac{\omega^2}{\omega_\mu^{*(1)^2} - \omega^2}\dfrac{Q_1^{(1)^2}}{C_{1111}^{\text{eff}}}}, & \boldsymbol{U}^{(1)} = \{U_1,0,0\}^T; \\ \kappa^{(2)} = \omega\sqrt{\dfrac{\bar{\rho}}{C_{1212}^{\text{eff}}}}, & \boldsymbol{U}^{(2)} = \{0,U_2,0\}^T; \\ \kappa^{(3)} = \omega\sqrt{\dfrac{\bar{\rho}}{C_{1313}^{\text{eff}}}}, & \boldsymbol{U}^{(3)} = \{0,0,U_3\}^T. \end{cases} \tag{24}$$

Note that $\kappa^{(2)}$ and $\kappa^{(3)}$, which are associated to transverse propagation modes ($\boldsymbol{U}^{(2)}$ and $\boldsymbol{U}^{(3)}$ are normal to the wave propagation direction $\boldsymbol{n}_\kappa$), have a standard dispersion relation proportional to the frequency ω through a constant propagation speed. However, for longitudinal waves the material is dispersive, as the relation between $\kappa^{(1)}$ and ω is not linear due to the presence of local resonance effects caused by non-null values of $Q_1^{(1)}$. A close inspection on this expression allows us to realize: (1) as ω approaches the natural frequency $\omega_\mu^{*(1)}$, the corresponding effective density tensor term $R_{11}^{\text{eff}} \to +\infty$ which causes

$\kappa^{(1)} \to +\infty$; and (2) when ω surpasses the value of $\omega_{\mu}^{*(1)}$, then $R_{11}^{\text{eff}} \to -\infty$ (i.e. the metamaterial exhibits *negative density*-like behavior) causing $\kappa^{(1)}$ to be purely imaginary (see Fig. 8 for an illustrative example).

According to Eq. (20), a purely imaginary wavenumber κ causes an effective attenuation of the wave's amplitude as it propagates, producing the so-called *frequency bandgap*. This bandgap region is extended until a frequency that makes the corresponding effective density tensor component become null, $R_{11}^{\text{eff}} = 0$. In Article I, it is demonstrated that these frequencies correspond to resonance frequencies for vibration modes in the *unrestricted* microscale inertial system.

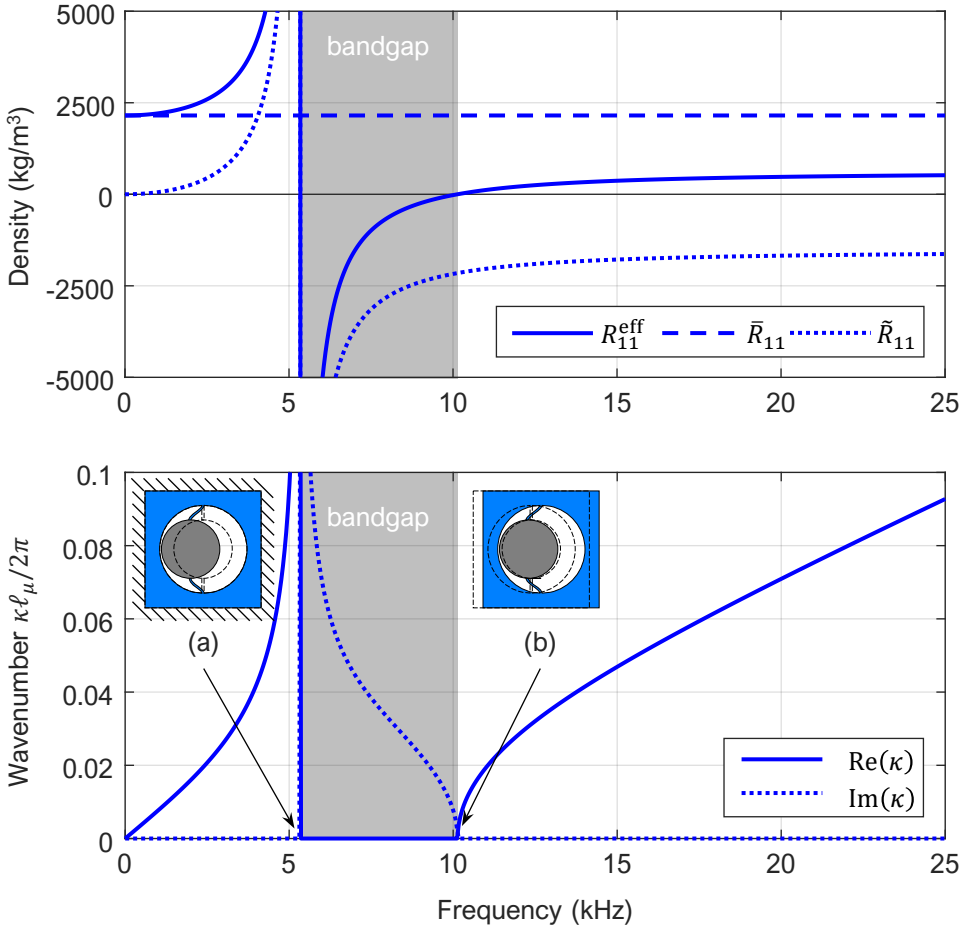

FIG. 8 Illustrative example of the local resonance phenomenon. The bandgap corresponds to a region bounded by the frequencies of the restricted and unrestricted unit cell systems, whose vibration modes are depicted as (a) and (b) (dashed lines indicate the undeformed state). Note that in this region the metamaterial exhibits negative density-like behavior, causing a purely imaginary valued wavenumber. The plots are adapted from the ones provided in Article I considering Fig. 7-(a) unit cell design.

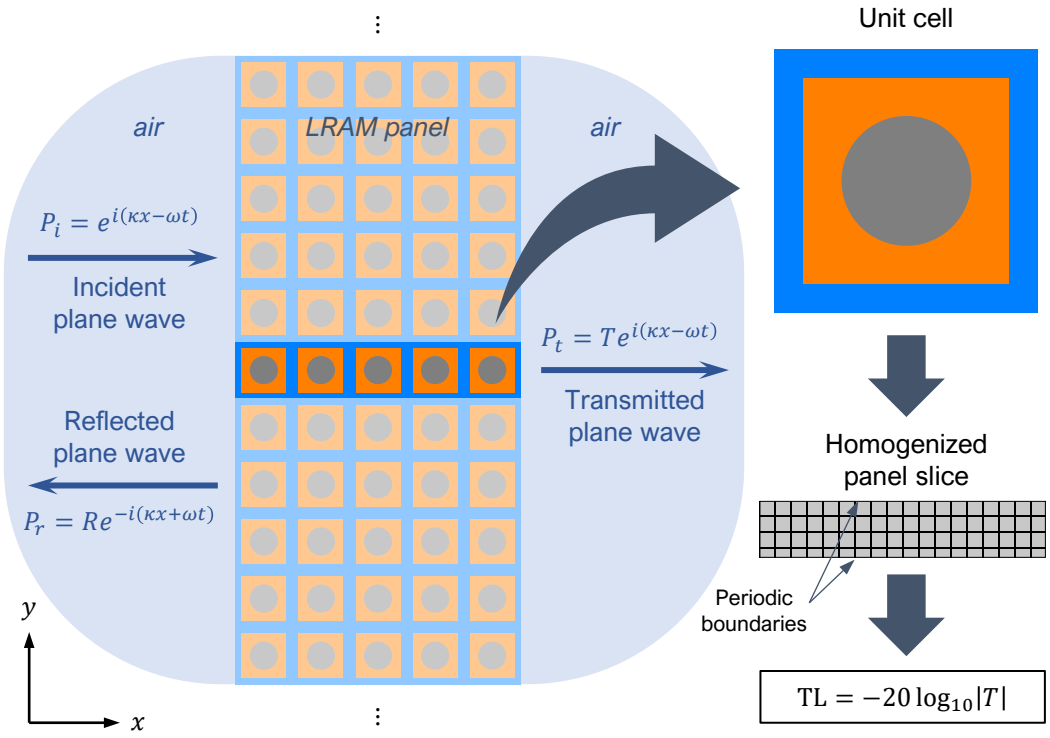

FIG. 9 LRAM-based panel problem setting for computing its transmission loss. The macroscopic domain consists of an infinitely extended panel with a certain thickness. Its microscale is modelled as a periodically repeated unit cell with a given configuration that allows it to produce local resonance effects. In order to compute the transmission loss, acoustic plane waves propagating in the direction normal to the panels' surfaces are considered. On the front side, there are two waves travelling in opposite directions corresponding to the incident and reflected waves, while on the rear side, there is only the transmitted wave propagating away from the panel. The ratios between these waves' amplitudes define the reflection and transmission coefficients, R and T, respectively.

3.1.5.2 Transmission loss in LRAM-based panels

The LRAM application considered throughout this work is the design of noise insulation panels with enhanced attenuating capabilities (due to local resonance effects) in a specified frequency range. These are typically in the low-frequency regime, where standard solutions would require the use of thick panels of dense materials.

The scheme in Fig. 9 is used to characterize the performance of such LRAM-based panels by computing their transmission loss as the ratio of the amplitudes of acoustic plane waves propagating normal to the panels' surfaces on their front and rear sides. Details on this computation are provided in Article II.

This kind of example has also been used in Article I to validate the homogenization model through a comparison of the results obtained with a direct numerical simulation of the panel. The results of this study can be seen in Fig. 10.

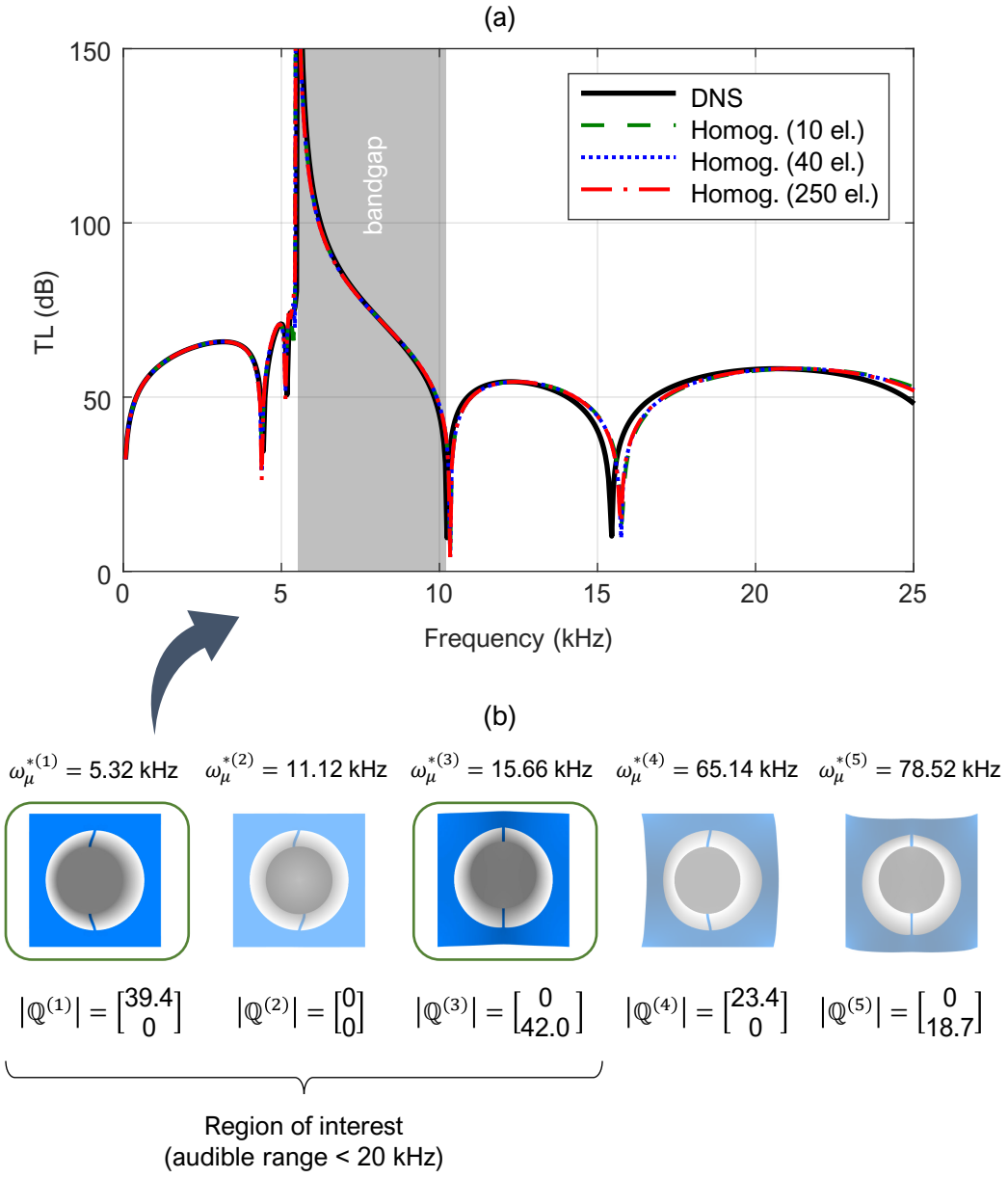

FIG. 10 Validation of the proposed homogenization scheme. (a) The transmission loss of a panel has been computed through a direct numerical simulation and the results are compared with those obtained by the proposed homogenization framework. (b) Internal resonance modes for the unit cell design considered. Notice that only the first 3 modes lie in the audible frequency range, of which only 2 have non-negligible components in the coupling vector and only the first is responsible for causing local resonance effects for waves propagating in the longitudinal direction. Results adapted from Article I.

3.2 Computational design of acoustic metamaterials

The homogenization framework presented can be employed to characterize the behavior of LRAMs. This motivates its use in the design process of such metamaterials aiming, for instance, at enhancing its attenuating capabilities. In this context, the application devised for LRAMs is in the form of noise insulation panels as described in Section 3.1.5.2. Therefore, since the levels of attenuation achieved by local resonance effects are large but very narrowband, the goal is to enlarge the effective frequency bandgap. In this regard, three different strategies have been considered: (1) stacking layers with different LRAM unit cell configurations aiming at overlapping their effective bandgaps, (2) taking advantage of the viscoelastic behavior of certain materials which, in combination with local resonance effects, can give rise to a damping emergence phenomenon called *metadamping* and (3) use topology optimization techniques to obtain unit cell designs with a targeted frequency range of operation and optimal (maximized) bandwidth.

3.2.1 Multi-layer LRAM-based panel design

As a first approach in LRAMs design, the consideration of a multi-layered panel has been studied. The idea in this case is to enlarge the effective attenuation band (defined as the frequency range with transmission loss levels over a certain baseline value) by using different unit cell configurations in each layer, with overlapping frequency bandgaps. This concept has been explored using the proposed homogenization scheme as part of the examples section in Article I. An adaptation of these results (in terms of transmission loss) can be seen in Fig. 11.

First, it should be noted that the two overlapping bandgaps are produced with small changes in the geometrical properties of each unit cell. In this case, a simple reduction of 0.25 mm in the outer hole diameter (see Fig. 7-(a)) is enough to slightly increase the frequency bandgap width and move it to a 2 kHz higher frequency range.

The main drawback observed with this design concept is that, while the corresponding unit cells' bandgaps overlap, the resulting transmission loss curve is not capable of producing a *continuous* effective attenuation band throughout the entire expected enlarged frequency bandgap. This is because by stacking layers with different unit cell configurations, they interact with each other producing undesired transmission (inverted) peaks at frequencies inside the attenuation region.

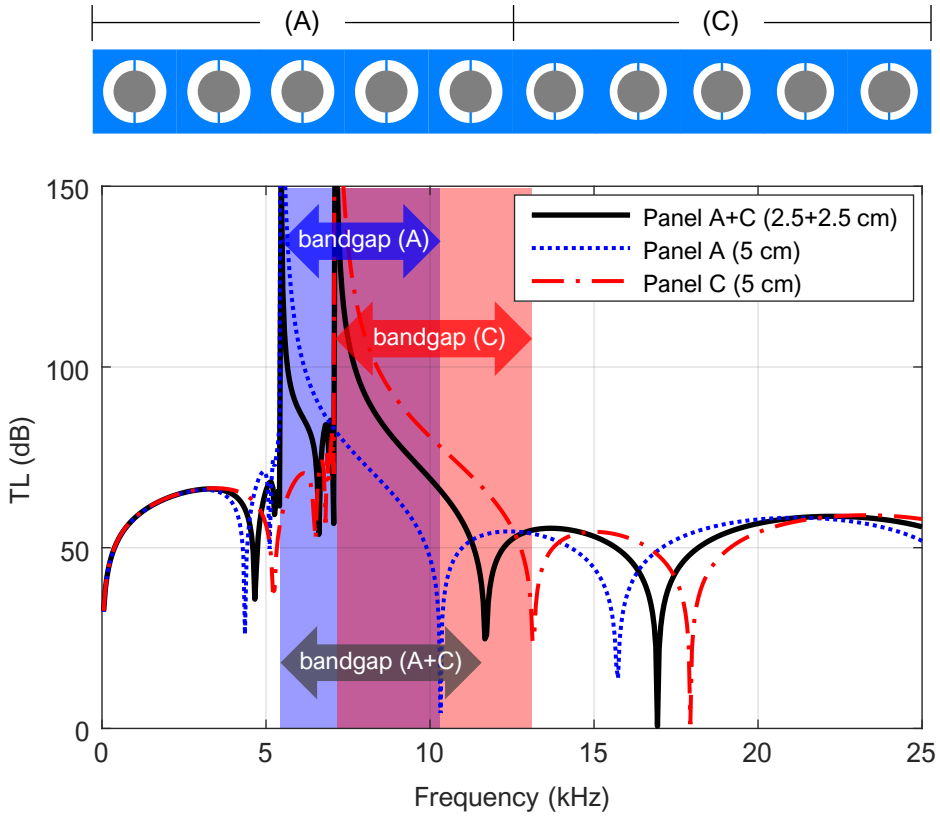

FIG. 11 Transmission loss of a bi-layer LRAM panel. Each layer contains 5 unit cells with variations in the geometric parameters of the configuration in Fig. 7-(a), in order to produce two overlapping frequency bandgaps (shaded areas in the plot). Results adapted from Article I.

3.2.2 Introduction of damping effects

Viscoelastic behavior of materials can be accounted for in the proposed formulation by considering, on the microscale, a stress-strain relation of the form

$$\boldsymbol{\sigma}_\mu = \mathbf{C}_\mu : \boldsymbol{\nabla}_y^{\mathrm{S}} \boldsymbol{u}_\mu + \boldsymbol{\eta}_\mu : \boldsymbol{\nabla}_y^{\mathrm{S}} \dot{\boldsymbol{u}}_\mu, \tag{25}$$

so that the stress tensor gains a strain-rate, $\boldsymbol{\nabla}_y^{\mathrm{S}} \dot{\boldsymbol{u}}_\mu$, dependency through a fourth-order viscous tensor $\boldsymbol{\eta}_\mu$. First, it should be noted that the introduction of this additional term in the formulation does not affect the simplifying hypotheses considered for the application of the model to acoustic metamaterials problems. Details on the whole derivation of the model with viscoelastic effects can be found in Article II. Here, only the major implications of the changes in the results will be discussed:

(a) While the assumption considered for the quasi-static subsystem still holds, some changes need to be applied to accommodate the presence of dissipation terms. Ultimately, this affects the expression obtained for the effective macroscopic stress, that now reads

$$\boldsymbol{\sigma} \approx \mathbf{C}^{\mathrm{eff}}\!:\!\boldsymbol{\varepsilon} + \boldsymbol{\eta}^{\mathrm{eff}}\!:\dot{\boldsymbol{\varepsilon}}. \tag{26}$$

In contrast to the previous definition, given by Eq. (10), in this case a new term arises accounting for an effective viscous tensor, $\boldsymbol{\eta}^{\mathrm{eff}}$, responsible for relating the macroscopic stress with the strain-rate, $\dot{\boldsymbol{\varepsilon}}$.

(b) Another difference appearing as a result of considering viscoelastic effects concerns the inertial subsystem. In this case, the expression for the macroscopic inertial force density remains the same as in Eq. (16), but an additional dissipation term appears in the reduced microscale system:

$$\boldsymbol{\Omega}_{\mu}^{2}\boldsymbol{q}_{\mu} + \boldsymbol{\Omega}_{\mu}^{\mathrm{D}}\dot{\boldsymbol{q}}_{\mu} + \ddot{\boldsymbol{q}}_{\mu} = -\mathbb{Q}^{T}\ddot{\boldsymbol{u}}, \tag{27}$$

where former Eq. (15) in its matrix form has been considered, i.e. with $\boldsymbol{\Omega}_{\mu}^{2} = \mathrm{diag}\{ \dots \ \omega_{\mu}^{*(k)^2} \ \dots \}$ being a diagonal matrix containing all the relevant squared natural frequencies, $\boldsymbol{q}_{\mu} = \{ \dots \ q_{\mu}^{*(k)} \ \dots \}^{T}$ denoting a column vector with the modal amplitudes and $\mathbb{Q} = \{ \dots \mathbb{Q}^{(k)} \dots \}$ referring to a matrix containing the coupling vectors. In Eq. (27), $\boldsymbol{\Omega}_{\mu}^{\mathrm{D}}$ is the new term assuming the role of a damping matrix.

Regarding Eq. (27), it should be noted that the addition of damping counteracts the beneficial effects of local resonance phenomena. However, in a low-frequency regime, depending on the level of viscosity, it can slightly extend the effective attenuation band. Another issue concerning the modal-based reduction is that, unlike the former microscale system from Eq. (15), the new system in Eq. (27) is not necessarily uncoupled, since $\boldsymbol{\Omega}_{\mu}^{\mathrm{D}}$ is not diagonal, in general. This may cause the reduction scheme to not be so efficient, as additional modal amplitudes may be required in order to achieve more accurate results. While this issue is something that needs to be considered, in practice, it has been verified that it does not have a major impact on the overall formulation, because the degree of coupling is so small that good results can still be obtained considering only the relevant modes selected using the criterion established in Section 3.1.4 .

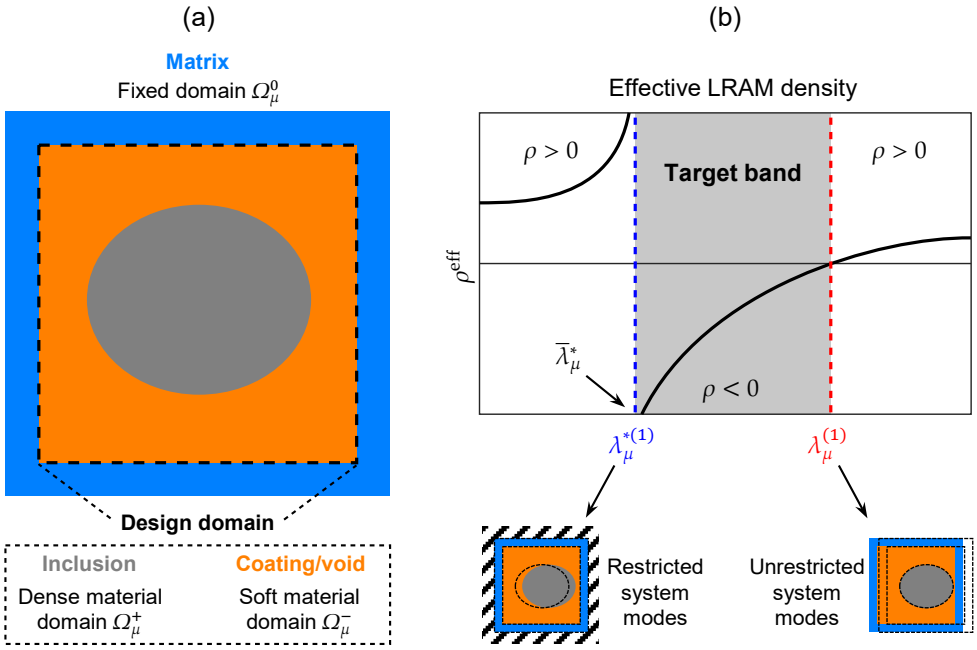

FIG. 12 Problem setting for the topology optimization of acoustic metamaterials. (a) Unit cell configuration showing the fixed stiff material frame and the design domain where the topology of the inclusions (acting as dense material regions) is obtained. (b) Restricted and unrestricted resonance frequencies marking the frequency bandgap limits. Figure extracted from Article II.

3.2.3 *Topology optimization of LRAMs*

A LRAMs computational design methodology based on a level-set topology optimization strategy has been devised. The objectives for this optimization problem are:

(1) Fit the relevant resonance frequency triggering local resonance effects into a targeted range.
(2) Maximize the bandwidth of the frequency bandgap associated to the previous resonance frequency.

To do so, a smooth level-set function $\varphi(\boldsymbol{y})$ is defined to determine the material distribution by means of a characteristic function

$$\chi(\boldsymbol{y}) \coloneqq \mathscr{H}\big(\varphi(\boldsymbol{y})\big) \equiv \begin{cases} 0 & \forall\, \boldsymbol{y} \text{ such that } \varphi(\boldsymbol{y}) < 0 \\ 1 & \forall\, \boldsymbol{y} \text{ such that } \varphi(\boldsymbol{y}) \geq 0 \end{cases}. \tag{28}$$

This characteristic function χ takes values of 1 for *dense* material regions (these will correspond to the resonating elements, i.e. the inclusions) and values of 0 for *compliant* material regions (which will be treated as void or coating materials). In this context, the

level-set function φ becomes the unknown of the problem of minimizing the cost function, given by

$$\Pi\big(\chi(\varphi)\big) := \alpha f^2 + (1-\alpha) g^2 \tag{29}$$

with

$$f = \frac{\ln \lambda_\mu^{*(1)}\big(\chi(\varphi)\big) - \ln \overline{\lambda}_\mu^*}{\ln \lambda_\mu^{*(1)}\big(\chi(\varphi)\big) + \ln \overline{\lambda}_\mu^*}, \tag{30}$$

$$g = \frac{\ln \lambda_\mu^{*(1)}\big(\chi(\varphi)\big)}{\ln \lambda_\mu^{(1)}\big(\chi(\varphi)\big)}, \tag{31}$$

In Eqs. (29)-(31), α is a weighting parameter ($0 \leq \alpha \leq 1$) and $\overline{\lambda}_\mu^* \equiv \overline{\omega}_\mu^{*\,2}$ is the squared target frequency where we expect to obtain local resonance effects. The variables $\lambda_\mu^{*(1)}$ and $\lambda_\mu^{(1)}$ are the first relevant resonance frequencies for the *restricted* and *unrestricted* microscale inertial systems, respectively, which typically determine the lower and upper bounds of the associated frequency bandgap. Thus, at each iteration step, the following equations must be satisfied:

$$\big(\mathbb{K}_\mu^* - \lambda_\mu^{*(1)} \mathbb{M}_\mu^*\big)\widehat{\boldsymbol{\phi}}_\mu^{*(1)} = \mathbf{0}, \tag{32}$$

$$\big(\mathbb{K}_\mu - \lambda_\mu^{(1)} \mathbb{M}_\mu\big)\widehat{\boldsymbol{\phi}}_\mu^{(1)} = \mathbf{0}. \tag{33}$$

It should be noted that the objective function Π is bounded between 0 and 1 and is composed by two subfunctions, f^2 and g^2. The former (see Eq. (30)) reaches its minimum when the squared first relevant resonance frequency of the restricted system $\lambda_\mu^{*(1)}$ (i.e. the one producing local resonance effects) matches the targeted one $\overline{\lambda}_\mu^*$, satisfying the first objective established. As for the latter (see Eq. (31)), its value decreases as the difference between $\lambda_\mu^{(1)}$ and $\lambda_\mu^{*(1)}$ becomes larger (i.e. the frequency bandgap limits extend, which satisfies the second objective set).

To solve the problem, a pseudo-time variable is used to update the solution, starting from an initial state that consist of the design area filled entirely with dense material (i.e. $\varphi > 0$ in the whole domain), until it reaches an appropriate converged solution. A Hamilton-Jacobi approach has been considered, where the updated solution is given by

$$\varphi^{(n+1)}(\boldsymbol{y}) = \varphi^{(n)}(\boldsymbol{y}) - \Delta t\, C_1 \frac{\delta \Pi_t}{\delta \chi}(\boldsymbol{y}), \tag{34}$$

with Δt being a time-step, $C_1 > 0$ is an adjusting parameter and $\delta \Pi_t / \delta \chi$ is the so-called topological sensitivity of the cost function (also known as the variational topological derivative of the functional Π). Details on the derivation of $\delta \Pi_t / \delta \chi$ can be found in Article II.

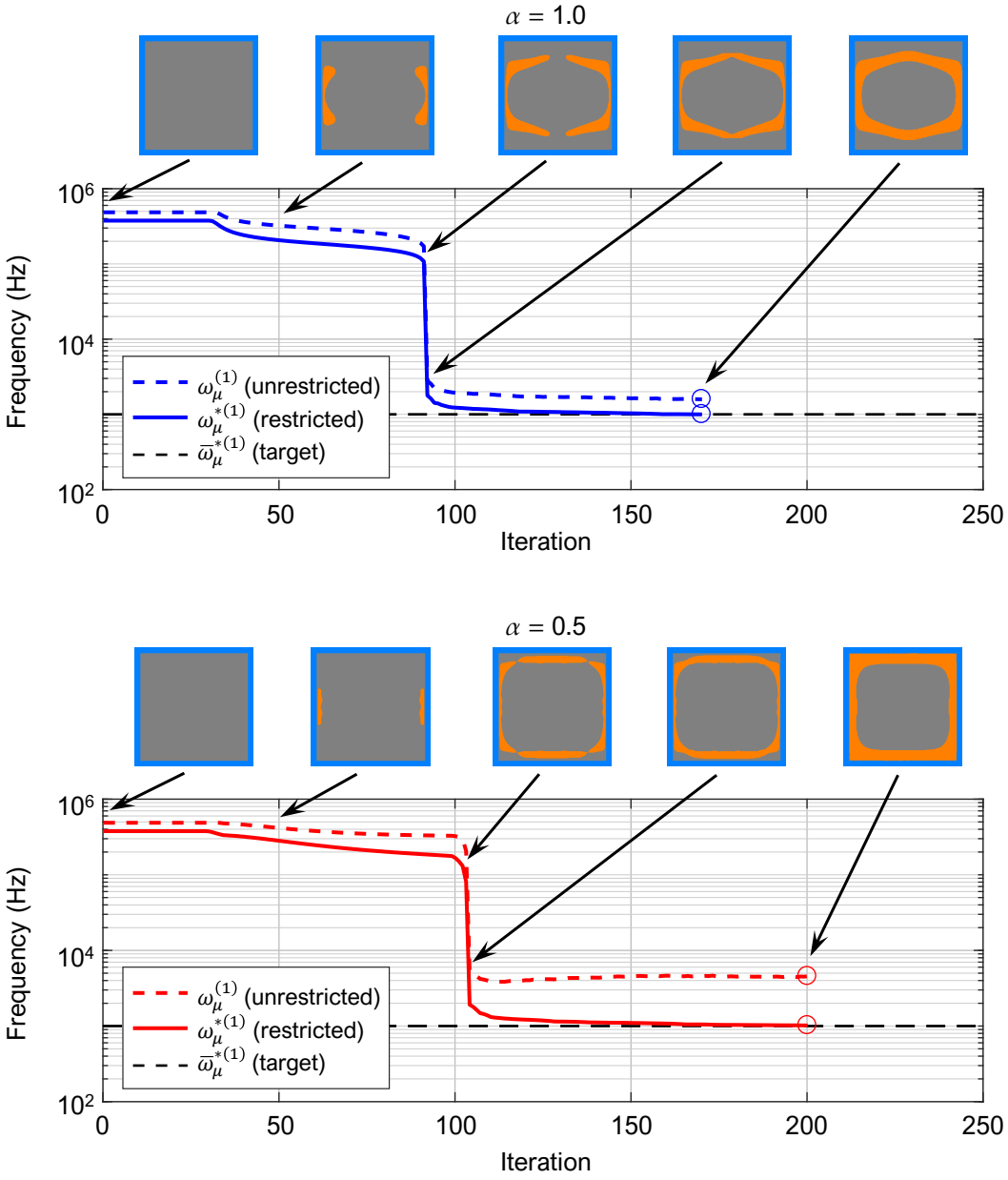

FIG. 13 Evolution plots for the topology optimization of acoustic metamaterials. (a) Frequency fitting case and (b) Frequency fitting paired with bandgap maximization. In Additional media, a link to a video showcasing the topology evolution at each iteration for both cases can be found. Figure extracted from Article II.

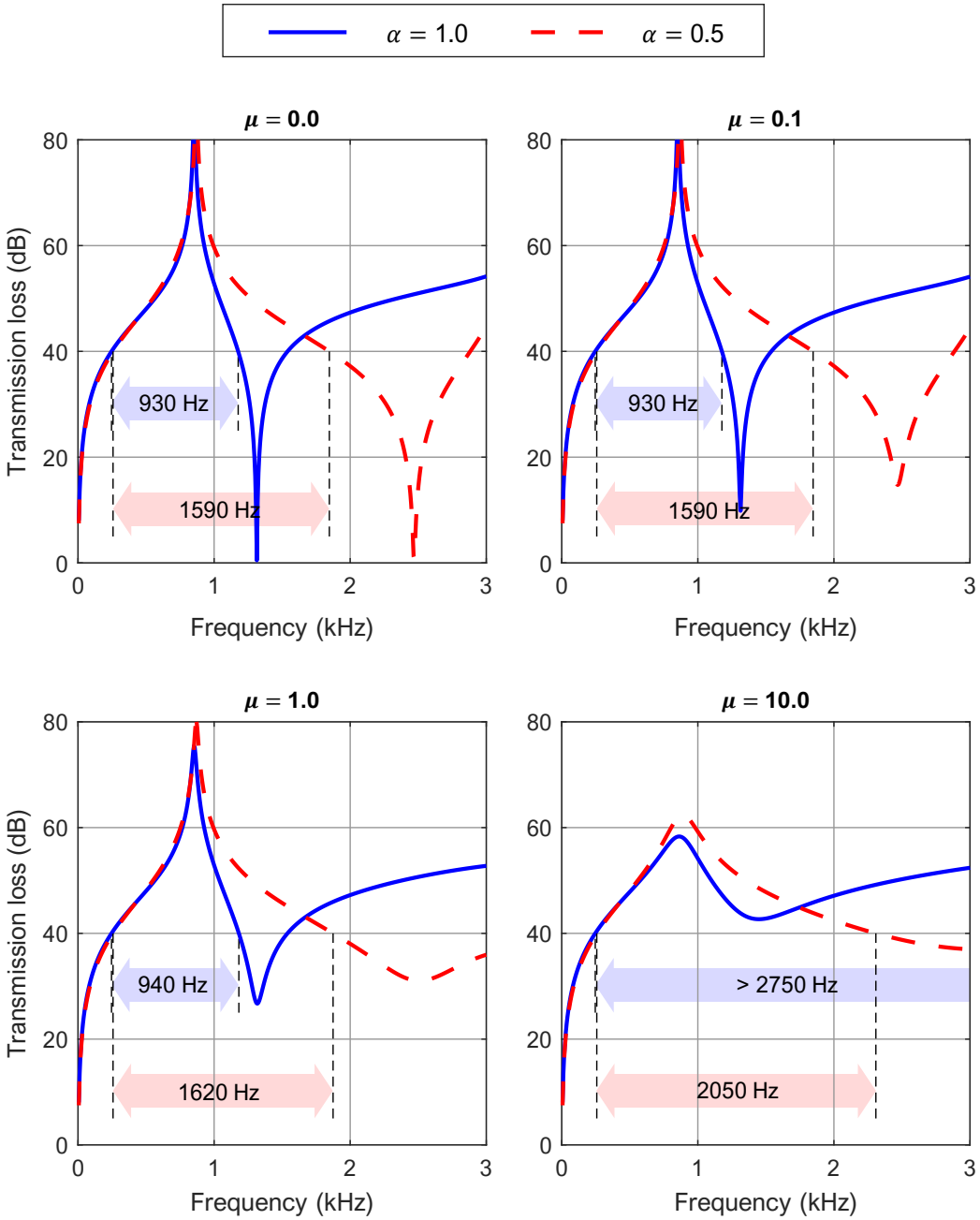

FIG. 14 Transmission loss for the optimized LRAM topologies. Comparison between the frequency fitting design and the frequency fitting paired with the bandgap maximization case. Each plot corresponds to different viscosity parameters to highlight the effect of considering viscoelastic behavior in the design. The effective attenuation bands are defined as the uninterrupted frequency regions with a TL level over 40 dB. Figure extracted from Article II.

Some important aspects concerning the topology optimization problem devised include:

(a) To ensure the appearance of a topological design that triggers local resonance effects, the target squared frequency $\overline{\lambda}_{\mu}^{*}$ needs to be set in a proper region that is typically determined by the dimensions of the unit cell, for a given set of material properties. This also implies that $\alpha > 0$, i.e. the frequency fitting must be part of the objective function always.

(b) The design domain is surrounded by a fixed material frame, which is considered infinitely stiff so that no deformation modes appear in the modal analysis. This is done also to avoid spurious interactions of the matrix with the inclusion/coating materials considered for the topological design area in the early steps of the algorithm.

(c) The mass of the void/coating material is neglected, again, to avoid spurious modes that would difficult the proper identification of the relevant resonance mode. This should not affect the value of the resonance frequency, since the parameters that play a role in its determination are the elastic properties of the coating phase and the mass of the inclusion, both of which remain unaltered with this assumption.

(d) Finally, in order to help the algorithm become more stable, only the degrees of freedom in the direction where one expects local resonance effects to arise are left free (assuming the unit cell will work as a LRAM panel subjected to plane waves propagating in the predefined direction, this simplification is not a cause for important issues from the topological design point of view).

In Fig. 13, an example from Article II of the application of the proposed topological design strategy is shown. For comparison, two cases have been studied: one only accounting for the frequency fitting ($\alpha = 1$) to get a topology with an internal resonance frequency in a target value, and another in which bandgap maximization is also taken into account ($\alpha = 0.5$). Notice the big jump in the resonance frequency scale once the inclusion gets detached from the matrix. The corresponding transmission loss curves for each case are given in Fig. 14, which can be found also in Article II. In this case, one can also see the smoothing effect caused by increasing the viscosity of the coating material upon considering viscoelastic behavior in the model, which translates in slightly wider bandgaps. This, combined with topological optimized designs, lead to big improvements in the attenuation properties of the LRAM panel.

3.3 Experimental validation

The last main contribution of this work involves a series of experimental tests with the following objectives: (1) to demonstrate the concept of local resonance and show its effects on a fully 3D-printed acoustic metamaterial prototype and (2) validate the computational framework developed to characterize them. A detailed description of the experiments carried out and the obtained results can be found in Article III. Here, some important aspects will be highlighted.

3.3.1 Prototypes design

For almost 20 years, there have been plenty of acoustic metamaterials realizations that have been tested experimentally. While most of them are based on local resonance as the mechanism responsible for their attenuating properties, they differ in the way this kind of phenomenon is achieved. For a review on the different concepts and designs found in the literature, the reader is referred to Section 2.3 of this work. Most of the early designs employed composite structures composed of different material phases in order to obtain the desired properties. These designs are effective and capable of exhibiting local resonance effects, but they are not practical, mainly because of manufacturability issues or the dimensions required.

In this context, the prototypes for the devised set of experimental tests are designed with the notion of making them practical. To do so, given the recent growth and potential of new additive manufacturing technologies, the acoustic metamaterials employed as prototypes have been designed so that they can be fully 3D-printed via multi jet fusion (MJF) techniques. The main challenge when choosing 3D-printing as the fabrication method is in the currently available materials. In order to target the interesting frequency range of operation for sound insulation applications (around and below 1000 Hz), the materials employed need to allow internal resonances in this low-frequency regime, which typically implies the combination of highly compliant and dense materials. Since the majority of materials used in 3D-printing are polymers, the aforementioned frequency range is difficult to achieve with a set of dimensions that makes the metamaterial attractive for practical purposes, i.e. thin and lightweight, and at the same time, respect the limits and tolerances set by the manufacturing system. Here is where the unit cell design plays an important role, since it can be exploited to obtain the desired properties, subjected to the material restrictions, and be interesting from a practical point of view.

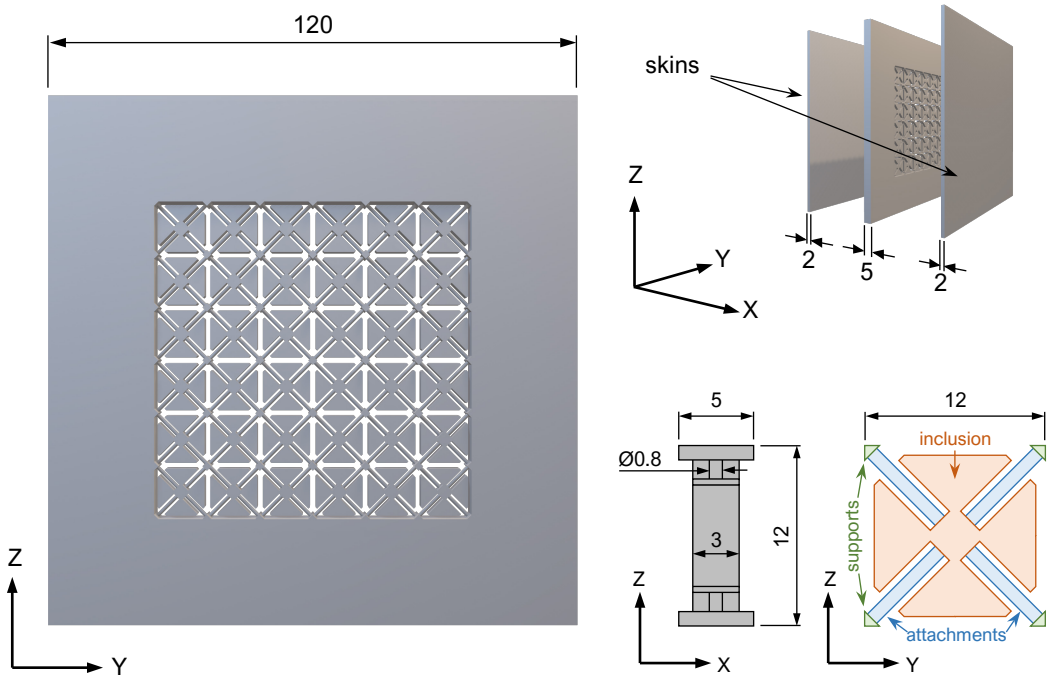

FIG. 15 3D-printed acoustic metamaterial panel design. Two skins are stuck at the panel in order to hold and isolate each unit cell. The flower-like design of the unit cells is depicted in the bottom right corner of the figure. All dimensions are in millimeters. Figure extracted from Article III.

To this end, the prototype built for the experimental tests consists of a panel with a thickness of only 5 mm and composed of unit cells with the design shown in Fig. 13. The material employed is a Polyamide (PA11), with a density of 1050 kg/m^3, a Young's modulus of 1800 MPa and a Poisson's ratio of 0.405. The unit cell design has been carefully chosen so that it can be easily 3D-printed from a single block of material, while still having the required elements for local resonance effects to arise. In particular, (1) the support rods at the unit cell's vertices act as fixing points to isolate each unit cell and trigger the appearance of internal resonance modes; (2) the central inclusion provides the *mass* for the resonating element, and (3) the thin attachments connecting the inclusion to the supports assume the role of *springs*, allowing the unit cell to have relevant resonance modes in the desired frequency range, around 1000 Hz. In fact, in order to achieve this frequency range, the particular *flower-like* topology has been chosen so that the bending stiffness of the attachments is small (which is attained with longer elements) and the resonating mass is as big as possible (by occupying most of the space available).

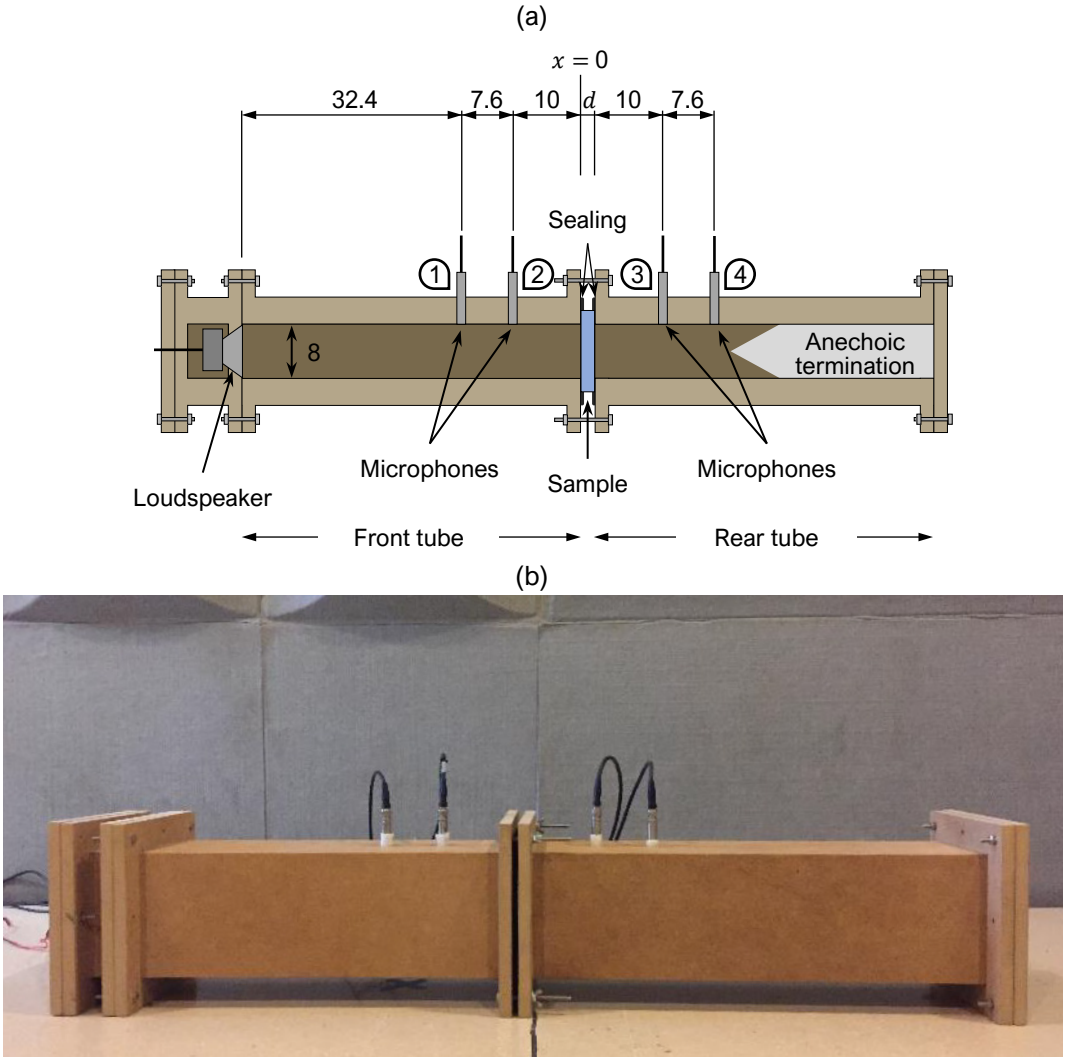

FIG. 16 Experiment setup for normal-incidence transmission loss measurements. (a) Schematic representation showcasing the four microphone positions and holding of the sample panel. (b) Actual impedance tube employed in the experiments. Figure from Article III.

3.3.2 *Impedance tube measurements*

Impedance tubes are used to characterize the acoustic performance of materials, in particular, its transmission and reflection coefficients to normal incidence plane waves. The device employed to carry out such kind of experimental tests in the present work consists of two tube parts built with medium-density fiberboard 4 cm thick, with a squared section of 8 cm x 8 cm. A 3.3 inch loudspeaker (4 Ohm, 30 W) is connected to an amplifier and located on one end of the first tube. The other tube's termination is filled with a polyurethane foam to act as an absorbing material, which guarantees an anechoic condition (no

reflections). Four 1/2 inch prepolarized microphones with an integrated circuit piezoelectric preamplifier are positioned at different tube sections (see Fig. 14).

The guidelines from ASTM E1050-98 have been followed in order to set the section size and microphone separation to guarantee a frequency range of operation between 200 and 2000 Hz. Assuming plane wave propagation in this range, the following expressions can be used to describe the pressure field in the front (f) and rear (r) tube sections in the frequency domain:

$$P_f(x,\omega) = A(\omega)e^{i\kappa x} + B(\omega)e^{-i\kappa x}, \tag{35}$$

$$P_r(x,\omega) = C(\omega)e^{i\kappa x}, \tag{36}$$

where x refers to the longitudinal position in the tube with respect to the sample's incident surface section, ω is the frequency, κ is the wavenumber (which is related to the speed of sound in air, c, by $\kappa = \omega/c$) and A, B and C are the incident, reflected and transmitted wave's amplitude coefficients, respectively.

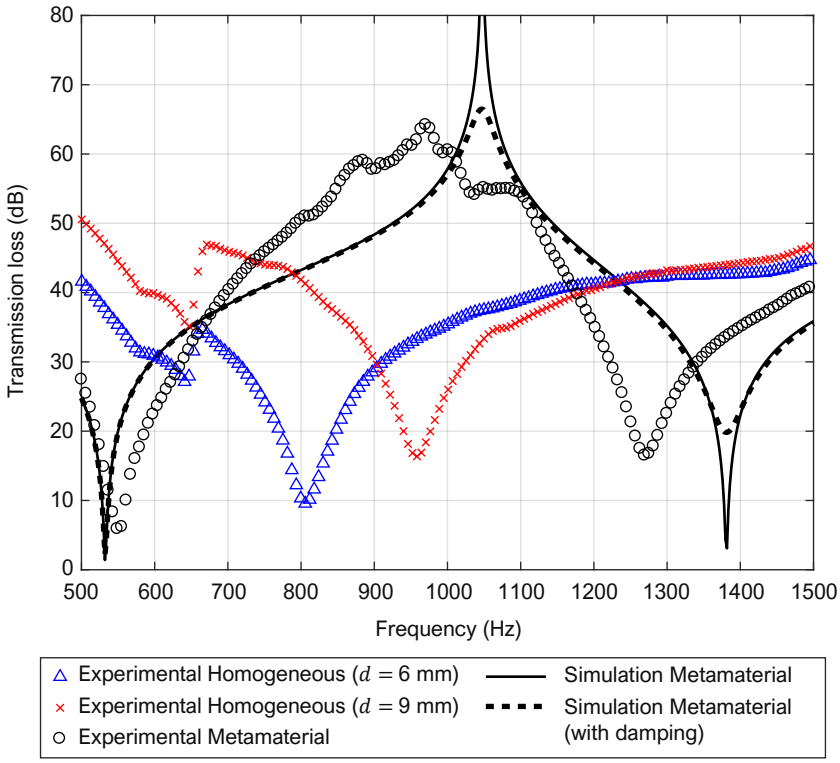

FIG. 17 Comparison between experimental and simulated results. The simulations have been performed using the proposed homogenization framework (further details in Article III). The experimental curves represent the results for the metamaterial panel and two homogeneous panels with an equivalent mass ($d = 6$ mm) and thickness ($d = 9$ mm), for comparison. Figure extracted from Article III.

Note that reflections on the rear sections of the tube are being neglected here because of the anechoic termination. With measurements of the pressure field on the four microphone positions, one can easily obtain the values for these coefficients and compute the transmission loss as

$$\mathrm{TL}(\omega) = 10 \log_{10} \left| \frac{A(\omega)}{C(\omega)} \right|^2 . \tag{37}$$

The results of these measurements for the 3D-printed prototype panel can be observed in Fig. 17 (also in Article III), along with the transmission loss computation from a simulated panel where the proposed homogenization scheme has been applied. The metamaterial case shows increased attenuation around the expected frequency when compared to equivalent homogeneous panels with the same thickness and equivalent mass.

Chapter 4

CONCLUSIONS

4.1 Discussion of the results

By applying the concepts of multiscale homogenization, model-order reduction techniques and topology optimization, a set of computational tools has been developed to study and design acoustic metamaterials. The numerical framework proposed highlights the potential of the computational design of materials and its ability to characterize complex material behavior, such as local resonance effects. The key aspects developed throughout the present thesis are discussed here:

(a) *Multiscale homogenization of acoustic metamaterials*. A general multiscale homogenization framework capable of accounting for inertial effects has been built upon the so-called *multiscale virtual power principle*. The macroscale (part) is linked to the microscale (metamaterial) through a kinematic relation and a *Lagrange-based form* of the energetic equivalence between both scales provides a good setting for solving the problem in the microscale and identifying the Lagrange multipliers as the macroscopic effective stress and inertial force density terms. Based on (a) the separation of scales condition ($\lambda \gg \ell_\mu$) and assuming (b) a density distribution symmetrical with respect to each unit cell's center, along with (c) neglecting body forces, the formulation can be simplified to characterize periodic arrangements of acoustic metamaterials. Namely, the microscale system can be split onto a *quasi-static* component, from which an effective constitutive tensor is obtained, and an *inertial* component, from which the effective inertial force density is derived as a function of the macroscopic acceleration and some micro-inertial terms accounting for local resonance effects.

(b) *Modal-based model-order reduction accounting for internal resonances*. By solving the eigenproblem in the microscale inertial subsystem, one can identify the relevant internal resonance modes responsible for triggering local resonance effects on the macroscale. This is translated in a huge reduction of the computational effort required to solve the coupling between the macro and microscales due to inertial effects, while still allowing the model to properly capture the acoustic metamaterials' behavior.

(c) *Topology optimization for frequency bandgap fitting and maximization*. A level-set optimization algorithm is used to obtain acoustic metamaterial unit cell's designs that allow to (a) set the target frequency range where local resonance effects are expected to arise, and (b) maximize the effective frequency bandgap along with the attenuation performance for panel-based applications subject to normal incident acoustic plane waves.

(d) *Damping phenomena accounting for more realistic material behavior*. The homogenization framework has been enriched with the incorporation of more realistic material behavior in the microscale by accounting for viscoelastic effects. This addition has allowed to study the impacts of damping in acoustic metamaterials and, more specifically, its role when used in combination with local resonance effects.

(e) *Experimental validation with 3D-printed prototypes*. Aiming at experimentally demonstrating the effects of local resonance phenomena of acoustic metamaterials, an impedance tube-based test has been devised to analyze the transmission loss of panels subject to normal-incidence acoustic plane waves. These experiments have been used to both validate the homogenization model and to prove the enhanced attenuating capabilities of acoustic metamaterials based on a fully 3D-printed design.

The model has been successfully applied to simulate the attenuating capabilities of LRAM-based panels subject to normal-incidence acoustic plane waves. Such example has been considered to validate the homogenization framework through comparison with a direct numerical simulation. The results confirm the applicability range of the model within the simplifying hypotheses considered and prove the effectiveness of the modal-based reduction strategy by achieving reductions of up to 0.1% of the total number of degrees of freedom of the problem (in a 2D setting) while still managing to obtain accurate results with $< 1\%$ of relative error in the frequency range of interest.

Using the computational tools developed in this work, early attempts at designing LRAM-based panels for sound insulation in a low-frequency range (around 1 kHz) have been carried out, following different approaches:

(a) In Article I, the idea of combining multiple layers with different unit cell designs (each one providing a frequency bandgap in different overlapping regions) has been explored. The aim is to obtain an extended effective attenuation band by taking advantage of multiple internal resonances. The preliminary study performed reveals that there is still room for improvement in this regard, especially in understanding the interaction between the different layers to get a continuous attenuation band.

(b) In Article II, the topology optimization algorithm has been used to set the local resonance effects in a targeted frequency around 1 kHz. Designs with bandgap maximization as part of the cost function in the optimization algorithm have been obtained and proven to almost double the frequency bandgap compared to non-optimized designs. This translates in an increase of more than 1.5 times the bandwidth of effective continuous attenuation over 40 dB. Furthermore, the consideration of viscoelastic effects in the coating material phase has also shown that this effective bandwidth can be extended an additional 30%.

(c) In Article III, the first attempt at building a practical acoustic metamaterial prototype by employing a currently available 3D-printing technology has been carried out. Its design has been devised to get local resonance effects in a frequency range around 1 kHz with a set of dimensions that make it both interesting for practical applications and manufacturable within the 3D-printing technology limitations. To do so, the design consists of a flower-like shaped inclusion in order to maximize the resonating mass, while still allowing the presence of thin attachments (acting as springs) long enough to produce internal resonances in the frequency range of interest.

4.2 Future research lines

All the developments and results achieved throughout the present work can be regarded as the foundation for further research lines related to the design and characterization of acoustic metamaterials. Some of these possible research topics are discussed here:

(a) Similar to how viscoelastic effects have been introduced in the model in order to account for more realistic behavior, other kind of phenomena can also be added to the present formulation in order to enrich it. In this context, the consideration of non-linear material behavior could be an example. Another possibility would be to extend the range of applicability of the model to higher frequency ranges by incorporating Bloch-Floquet conditions. This would allow the model to be used, for instance, in characterizing the behavior of phononic crystal structures.

(b) The topology optimization algorithm presented is also subject to be updated (for example, with new cost functions or restrictions) to obtain more efficient designs that are feasible and practical in terms of manufacturability. This would also offer the possibility of building prototypes to experimentally test and validate the benefits attained with the design optimization.

(c) Although the proposed model is specifically tailored for the study of acoustic metamaterials, given the similarity between such kind of metamaterials with others (in electromagnetic applications, for instance), another possible research line devised is the adaptation of the framework to these other types of metamaterials.

References

[1] T. J. Cui, D. R. Smith, and R. Liu, “Introduction to Metamaterials,” in *Metamaterials*, Springer, 2010, pp. 1–19.

[2] W. E. Kock, “Metallic Delay Lenses,” *Bell Syst. Tech. J.*, vol. 27, no. 1, pp. 58–82, Jan. 1948, doi: http://dx.doi.org/10.1002/j.1538-7305.1948.tb01331.x.

[3] V. G. Veselago, “The electrodynamics of substances with simultaneously negative values of ϵ and μ,” *Sov. Phys. Uspekhi*, vol. 10, no. 4, pp. 509–514, Apr. 1968, doi: http://dx.doi.org/10.1070/PU1968v010n04ABEH003699.

[4] D. R. Smith, W. J. Padilla, D. C. Vier, S. C. Nemat-Nasser, and S. Schultz, “Composite Medium with Simultaneously Negative Permeability and Permittivity,” *Phys. Rev. Lett.*, vol. 84, no. 18, pp. 4184–4187, May 2000, doi: http://dx.doi.org/10.1103/PhysRevLett.84.4184.

[5] J. B. Pendry, A. J. Holden, D. J. Robbins, and W. J. Stewart, “Magnetism from conductors and enhanced nonlinear phenomena,” *IEEE Trans. Microw. Theory Tech.*, vol. 47, no. 11, pp. 2075–2084, 1999, doi: http://dx.doi.org/10.1109/22.798002.

[6] P. A. Deymier, “Introduction to Phononic Crystals and Acoustic Metamaterials,” in *Acoustic metamaterials and phononic crystals*, vol. 173, Springer Science & Business Media, 2013, pp. 1–12.

[7] M. I. Hussein, M. J. Leamy, and M. Ruzzene, “Dynamics of Phononic Materials and Structures: Historical Origins, Recent Progress, and Future Outlook,” *Appl. Mech. Rev.*, vol. 66, no. 4, p. 040802, Jul. 2014, doi: http://dx.doi.org/10.1115/1.4026911.

[8] T.-T. Wu, Y.-T. Chen, J.-H. Sun, S.-C. S. Lin, and T. J. Huang, “Focusing of the lowest antisymmetric Lamb wave in a gradient-index phononic crystal plate,” *Appl. Phys. Lett.*, vol. 98, no. 17, p. 171911, Apr. 2011, doi: http://dx.doi.org/10.1063/1.3583660.

[9] S. Gonella, A. C. To, and W. K. Liu, “Interplay between phononic bandgaps and piezoelectric microstructures for energy harvesting,” *J. Mech. Phys. Solids*, vol. 57, no. 3, pp. 621–633, Mar. 2009, doi: http://dx.doi.org/10.1016/j.jmps.2008.11.002.

[10] P. E. Hopkins *et al.*, “Reduction in the Thermal Conductivity of Single Crystalline Silicon by Phononic Crystal Patterning,” *Nano Lett.*, vol. 11, no. 1, pp. 107–112, Jan. 2011, doi: http://dx.doi.org/10.1021/nl102918q.

[11] Y. Pennec *et al.*, “Simultaneous existence of phononic and photonic band gaps in periodic crystal slabs,” *Opt. Express*, vol. 18, no. 13, p. 14301, Jun. 2010, doi: http://dx.doi.org/10.1364/OE.18.014301.

[12] O. Guasch, P. Sánchez-Martín, and D. Ghilardi, “Application of the transfer matrix approximation for wave propagation in a metafluid representing an acoustic black hole duct termination,” *Appl. Math. Model.*, vol. 77, pp. 1881–1893, Jan. 2020, doi: http://dx.doi.org/10.1016/j.apm.2019.09.039.

[13] J. Deng, O. Guasch, and L. Zheng, “Ring-shaped acoustic black holes for broadband vibration isolation in plates,” *J. Sound Vib.*, vol. 458, pp. 109–122, Oct. 2019, doi: http://dx.doi.org/10.1016/j.jsv.2019.06.017.

[14] Z. Liu *et al.*, “Locally Resonant Sonic Materials,” *Science (80-.).*, vol. 289, no. 5485, pp. 1734–1736, Sep. 2000, doi: http://dx.doi.org/10.1126/science.289.5485.1734.

[15] K. M. Ho, C. K. Cheng, Z. Yang, X. X. Zhang, and P. Sheng, “Broadband locally resonant sonic shields,” *Appl. Phys. Lett.*, vol. 83, no. 26, pp. 5566–5568, Dec. 2003, doi: http://dx.doi.org/10.1063/1.1637152.

[16] C.-L. Ding and X.-P. Zhao, “Multi-band and broadband acoustic metamaterial with resonant structures,” *J. Phys. D. Appl. Phys.*, vol. 44, no. 21, p. 215402, Jun. 2011, doi: http://dx.doi.org/10.1088/0022-3727/44/21/215402.

[17] M. Ambati, N. Fang, C. Sun, and X. Zhang, “Surface resonant states and superlensing in acoustic metamaterials,” *Phys. Rev. B*, vol. 75, no. 19, p. 195447, May 2007, doi: http://dx.doi.org/10.1103/PhysRevB.75.195447.

[18] S. Guenneau, A. Movchan, G. Pétursson, and S. Anantha Ramakrishna, “Acoustic metamaterials for sound focusing and confinement,” *New J. Phys.*, vol. 9, no. 11, pp. 399–399, Nov. 2007, doi: http://dx.doi.org/10.1088/1367-2630/9/11/399.

[19] J. Zhu *et al.*, “A holey-structured metamaterial for acoustic deep-subwavelength imaging,” *Nat. Phys.*, vol. 7, no. 1, pp. 52–55, Jan. 2011, doi: http://dx.doi.org/10.1038/nphys1804.

[20] J. B. Pendry and J. Li, “An acoustic metafluid: realizing a broadband acoustic cloak,” *New J. Phys.*, vol. 10, no. 11, p. 115032, Nov. 2008, doi: http://dx.doi.org/10.1088/1367-2630/10/11/115032.

[21] S. A. Cummer and D. Schurig, “One path to acoustic cloaking,” *New J. Phys.*, vol. 9, no. 3, pp. 45–45, Mar. 2007, doi: http://dx.doi.org/10.1088/1367-2630/9/3/045.

[22] H. Chen and C. T. Chan, “Acoustic cloaking in three dimensions using acoustic metamaterials,” *Appl. Phys. Lett.*, vol. 91, no. 18, p. 183518, Oct. 2007, doi: http://dx.doi.org/10.1063/1.2803315.

[23] A. N. Norris, “Acoustic metafluids,” *J. Acoust. Soc. Am.*, vol. 125, no. 2, pp. 839–849, Feb. 2009, doi: http://dx.doi.org/10.1121/1.3050288.

[24] R. Hill, “A self-consistent mechanics of composite materials,” *J. Mech. Phys. Solids*, vol. 13, no. 4, pp. 213–222, Aug. 1965, doi: http://dx.doi.org/10.1016/0022-5096(65)90010-4.

[25] J. Mandel, *Plasticite classique et viscoplasticite*. Springer, 1971.

[26] F. Feyel and J.-L. Chaboche, “FE2 multiscale approach for modelling the elastoviscoplastic behaviour of long fibre SiC/Ti composite materials,” *Comput. Methods Appl. Mech. Eng.*, vol. 183, no. 3–4, pp. 309–330, Mar. 2000, doi: http://dx.doi.org/10.1016/S0045-7825(99)00224-8.

[27] V. Kouznetsova, W. A. M. Brekelmans, and F. P. T. Baaijens, “Approach to micro-macro modeling of heterogeneous materials,” *Comput. Mech.*, vol. 27, no. 1, pp. 37–48, 2001, doi: http://dx.doi.org/10.1007/s004660000212.

[28] C. V. Verhoosel, J. J. C. Remmers, and M. A. Gutiérrez, “A partition of unity-based multiscale approach for modelling fracture in piezoelectric ceramics,” *Int. J. Numer. Methods Eng.*, vol. 82, no. 8, pp. 966–994, Dec. 2009, doi: http://dx.doi.org/10.1002/nme.2792.

[29] V. Phu Nguyen, O. Lloberas-Valls, M. Stroeven, and L. Johannes Sluys, “On the existence of representative volumes for softening quasi-brittle materials – A failure zone averaging scheme,” *Comput. Methods Appl. Mech. Eng.*, vol. 199, no. 45–48, pp. 3028–3038, Nov. 2010, doi: http://dx.doi.org/10.1016/j.cma.2010.06.018.

[30] J. Oliver, M. Caicedo, E. Roubin, A. E. Huespe, and J. A. Hernández, “Continuum approach to computational multiscale modeling of propagating fracture,” *Comput. Methods Appl. Mech. Eng.*, vol. 294, pp. 384–427, Sep. 2015, doi: http://dx.doi.org/10.1016/j.cma.2015.05.012.

[31] I. Özdemir, W. A. M. Brekelmans, and M. G. D. Geers, “Computational homogenization for heat conduction in heterogeneous solids,” *Int. J. Numer. Methods Eng.*, vol. 73, no. 2, pp. 185–204, Jan. 2008, doi: http://dx.doi.org/10.1002/nme.2068.

[32] V. Kouznetsova, M. G. D. Geers, and W. A. M. Brekelmans, “Multi-scale constitutive modelling of heterogeneous materials with a gradient-enhanced computational homogenization scheme,” *Int. J. Numer. Methods Eng.*, vol. 54, no. 8, pp. 1235–1260, Jul. 2002, doi: http://dx.doi.org/10.1002/nme.541.

[33] A. Karamnejad, V. P. Nguyen, and L. J. Sluys, “A multi-scale rate dependent crack model for quasi-brittle heterogeneous materials,” *Eng. Fract. Mech.*, vol. 104, pp. 96–113, May 2013, doi: http://dx.doi.org/10.1016/j.engfracmech.2013.03.009.

[34] K. Pham, V. G. Kouznetsova, and M. G. D. Geers, “Transient computational homogenization for heterogeneous materials under dynamic excitation,” *J. Mech. Phys. Solids*, vol. 61, no. 11, pp. 2125–2146, Nov. 2013, doi: http://dx.doi.org/10.1016/j.jmps.2013.07.005.

[35] E. A. de Souza Neto, P. J. Blanco, P. J. Sánchez, and R. A. Feijóo, “An RVE-based multiscale theory of solids with micro-scale inertia and body force effects,” *Mech. Mater.*, vol. 80, no. Part A, pp. 136–144, Jan. 2015, doi: http://dx.doi.org/10.1016/j.mechmat.2014.10.007.

[36] P. J. Blanco, P. J. Sánchez, E. A. de Souza Neto, and R. A. Feijóo, “Variational Foundations and Generalized Unified Theory of RVE-Based Multiscale Models,” *Arch. Comput. Methods Eng.*, vol. 23, no. 2, pp. 191–253, Jun. 2016, doi: http://dx.doi.org/10.1007/s11831-014-9137-5.

[37] A. Chatterjee, “An introduction to the proper orthogonal decomposition,” *Curr. Sci.*, vol. 78, no. 7, pp. 808–817, 2000.

[38] P. Krysl, S. Lall, and J. E. Marsden, “Dimensional model reduction in non-linear finite element dynamics of solids and structures,” *Int. J. Numer. Methods Eng.*, vol. 51, no. 4, pp. 479–504, Jun. 2001, doi: http://dx.doi.org/10.1002/nme.167.

[39] T. W. McDevitt, G. M. Hulbert, and N. Kikuchi, “An assumed strain method for the dispersive global–local modeling of periodic structures,” *Comput. Methods Appl. Mech. Eng.*, vol. 190, no. 48, pp. 6425–6440, Sep. 2001, doi: http://dx.doi.org/10.1016/S0045-7825(00)00184-5.

[40] M. I. Hussein and G. M. Hulbert, “Mode-enriched dispersion models of periodic materials within a multiscale mixed finite element framework,” *Finite Elem. Anal. Des.*, vol. 42, no. 7, pp. 602–612, Apr. 2006, doi: http://dx.doi.org/10.1016/j.finel.2005.11.002.

[41] M. P. Bendsøe and N. Kikuchi, “Generating optimal topologies in structural design using a homogenization method,” *Comput. Methods Appl. Mech. Eng.*, vol. 71, no. 2, pp. 197–224, Nov. 1988, doi: http://dx.doi.org/10.1016/0045-7825(88)90086-2.

[42] M. P. Bendsøe, “Optimal shape design as a material distribution problem,” *Struct. Optim.*, vol. 1, no. 4, pp. 193–202, Dec. 1989, doi: http://dx.doi.org/10.1007/BF01650949.

[43] P. Duysinx and M. P. Bendsøe, “Topology optimization of continuum structures with local stress constraints,” *Int. J. Numer. Methods Eng.*, vol. 43, no. 8, pp. 1453–1478, Dec. 1998, doi: http://dx.doi.org/10.1002/(SICI)1097-0207(19981230)43:8<1453::AID-NME480>3.0.CO;2-2.

[44] M. P. Bendsøe and O. Sigmund, *Topology Optimization*. Berlin, Heidelberg: Springer Berlin Heidelberg, 2004.

[45] O. Sigmund, “On the Design of Compliant Mechanisms Using Topology Optimization*,” *Mech. Struct. Mach.*, vol. 25, no. 4, pp. 493–524, Jan. 1997, doi: http://dx.doi.org/10.1080/08905459708945415.

[46] T. Buhl, C. B. W. Pedersen, and O. Sigmund, “Stiffness design of geometrically nonlinear structures using topology optimization,” *Struct. Multidiscip. Optim.*, vol. 19, no. 2, pp. 93–104, Apr. 2000, doi: http://dx.doi.org/10.1007/s001580050089.

[47] O. Sigmund, “Design of multiphysics actuators using topology optimization – Part I: One-material structures,” *Comput. Methods Appl. Mech. Eng.*, vol. 190, no. 49–50, pp. 6577–6604, Oct. 2001, doi: http://dx.doi.org/10.1016/S0045-7825(01)00251-1.

[48] J. S. Jensen and O. Sigmund, “Systematic design of photonic crystal structures using topology optimization: Low-loss waveguide bends,” *Appl. Phys. Lett.*, vol. 84, no. 12, pp. 2022–2024, Mar. 2004, doi: http://dx.doi.org/10.1063/1.1688450.

[49] O. Sigmund and J. Søndergaard Jensen, “Systematic design of phononic band–gap materials and structures by topology optimization,” *Philos. Trans. R. Soc. London. Ser. A Math. Phys. Eng. Sci.*, vol. 361, no. 1806, pp. 1001–1019, May 2003, doi: http://dx.doi.org/10.1098/rsta.2003.1177.

[50] H. A. Eschenauer, V. V. Kobelev, and A. Schumacher, “Bubble method for topology and shape optimization of structures,” *Struct. Optim.*, vol. 8, no. 1, pp. 42–51, Aug. 1994, doi: http://dx.doi.org/10.1007/BF01742933.

[51] J. Sokolowski and A. Zochowski, “On the Topological Derivative in Shape Optimization,” *SIAM J. Control Optim.*, vol. 37, no. 4, pp. 1251–1272, Jan. 1999, doi: http://dx.doi.org/10.1137/S0363012997323230.

[52] S. J. Osher and F. Santosa, “Level Set Methods for Optimization Problems Involving Geometry and Constraints,” *J. Comput. Phys.*, vol. 171, no. 1, pp. 272–288, Jul. 2001, doi: http://dx.doi.org/10.1006/jcph.2001.6789.

[53] G. Allaire, F. Jouve, and A.-M. Toader, “Structural optimization using sensitivity analysis and a level-set method,” *J. Comput. Phys.*, vol. 194, no. 1, pp. 363–393, Feb. 2004, doi: http://dx.doi.org/10.1016/j.jcp.2003.09.032.

[54] S. Amstutz and H. Andrä, “A new algorithm for topology optimization using a level-set method,” *J. Comput. Phys.*, vol. 216, no. 2, pp. 573–588, Aug. 2006, doi: http://dx.doi.org/10.1016/j.jcp.2005.12.015.

[55] S. M. Giusti, A. A. Novotny, and C. Padra, “Topological sensitivity analysis of inclusion in two-dimensional linear elasticity,” *Eng. Anal. Bound. Elem.*, vol. 32, no. 11, pp. 926–935, Nov. 2008, doi: http://dx.doi.org/10.1016/j.enganabound.2007.12.007.

[56] J. Oliver, D. Yago, J. Cante, and O. Lloberas-Valls, “Variational approach to relaxed topological optimization: Closed form solutions for structural problems in a sequential pseudo-time framework,” *Comput. Methods Appl. Mech. Eng.*, vol. 355, pp. 779–819, Oct. 2019, doi: http://dx.doi.org/10.1016/j.cma.2019.06.038.

[57] D. Yago, J. Cante, O. Lloberas-Valls, and J. Oliver, “Topology optimization of thermal problems in a nonsmooth variational setting: closed-form optimality criteria,” *Comput. Mech.*, 2020, doi: http://dx.doi.org/10.1007/s00466-020-01850-0.

[58] Y. Xiao, B. R. Mace, J. Wen, and X. Wen, “Formation and coupling of band gaps in a locally resonant elastic system comprising a string with attached resonators,” *Phys. Lett. A*, vol. 375, no. 12, pp. 1485–1491, Mar. 2011, doi: http://dx.doi.org/10.1016/j.physleta.2011.02.044.

[59] L. Liu and M. I. Hussein, “Wave Motion in Periodic Flexural Beams and Characterization of the Transition Between Bragg Scattering and Local Resonance,” *J. Appl. Mech.*, vol. 79, no. 1, p. 11003, Jan. 2012, doi: http://dx.doi.org/10.1115/1.4004592.

[60] M. Moscatelli, R. Ardito, L. Driemeier, and C. Comi, “Band-gap structure in two- and three-dimensional cellular locally resonant materials,” *J. Sound Vib.*, vol. 454, pp. 73–84, Aug. 2019, doi: http://dx.doi.org/10.1016/j.jsv.2019.04.027.

[61] M. I. Hussein, “Reduced Bloch mode expansion for periodic media band structure calculations,” *Proc. R. Soc. A Math. Phys. Eng. Sci.*, vol. 465, no. 2109, pp. 2825–2848, Sep. 2009, doi: http://dx.doi.org/10.1098/rspa.2008.0471.

[62] V. Fokin, M. Ambati, C. Sun, and X. Zhang, “Method for retrieving effective properties of locally resonant acoustic metamaterials,” *Phys. Rev. B*, vol. 76, no. 14, p. 144302, Oct. 2007, doi: http://dx.doi.org/10.1103/PhysRevB.76.144302.

[63] S. Nemat-Nasser, J. R. Willis, A. Srivastava, and A. V Amirkhizi, “Homogenization of periodic elastic composites and locally resonant sonic materials,” *Phys. Rev. B*, vol. 83, no. 10, p. 104103, Mar. 2011, doi: http://dx.doi.org/10.1103/PhysRevB.83.104103.

[64] A. Sridhar, V. G. Kouznetsova, and M. G. D. D. Geers, “Homogenization of locally resonant acoustic metamaterials towards an emergent enriched continuum,” *Comput. Mech.*, vol. 57, no. 3, pp. 423–435, Mar. 2016, doi: http://dx.doi.org/10.1007/s00466-015-1254-y.

[65] A. Sridhar, V. G. Kouznetsova, and M. G. D. Geers, “A semi-analytical approach towards plane wave analysis of local resonance metamaterials using a multiscale enriched continuum description,” *Int. J. Mech. Sci.*, vol. 133, no. August, pp. 188–198, Nov. 2017, doi: http://dx.doi.org/10.1016/j.ijmecsci.2017.08.027.

[66] D. Roca, O. Lloberas-Valls, J. Cante, and J. Oliver, “A computational multiscale homogenization framework accounting for inertial effects: Application to acoustic metamaterials modelling,” *Comput. Methods Appl. Mech. Eng.*, vol. 330, pp. 415–446, Mar. 2018, doi: http://dx.doi.org/10.1016/j.cma.2017.10.025.

[67] D. Roca, D. Yago, J. Cante, O. Lloberas-Valls, and J. Oliver, “Computational design of locally resonant acoustic metamaterials,” *Comput. Methods Appl. Mech. Eng.*, vol. 345, pp. 161–182, Mar. 2019, doi: http://dx.doi.org/10.1016/j.cma.2018.10.037.

[68] A. O. Krushynska, V. G. Kouznetsova, and M. G. D. Geers, “Towards optimal design of locally resonant acoustic metamaterials,” *J. Mech. Phys. Solids*, vol. 71, no. 1, pp. 179–196, Nov. 2014, doi: http://dx.doi.org/10.1016/j.jmps.2014.07.004.

[69] T. Matsuki, T. Yamada, K. Izui, and S. Nishiwaki, “Topology optimization for locally resonant sonic materials,” *Appl. Phys. Lett.*, vol. 104, no. 19, p. 191905, May 2014, doi: http://dx.doi.org/10.1063/1.4878259.

[70] M. I. Hussein and M. J. Frazier, “Metadamping: An emergent phenomenon in dissipative metamaterials,” *J. Sound Vib.*, vol. 332, no. 20, pp. 4767–4774, Sep. 2013, doi: http://dx.doi.org/10.1016/j.jsv.2013.04.041.

[71] M. J. Frazier and M. I. Hussein, “Viscous-to-viscoelastic transition in phononic crystal and metamaterial band structures,” *J. Acoust. Soc. Am.*, vol. 138, no. 5, pp. 3169–3180, Nov. 2015, doi: http://dx.doi.org/10.1121/1.4934845.

[72] D. DePauw, H. Al Ba’ba’a, and M. Nouh, “Metadamping and energy dissipation enhancement via hybrid phononic resonators,” *Extrem. Mech. Lett.*, vol. 18, pp. 36–44, Jan. 2018, doi: http://dx.doi.org/10.1016/j.eml.2017.11.002.

[73] J. M. Manimala and C. T. Sun, “Microstructural design studies for locally dissipative acoustic metamaterials,” *J. Appl. Phys.*, vol. 115, no. 2, p. 023518, Jan. 2014, doi: http://dx.doi.org/10.1063/1.4861632.

[74] A. O. Krushynska, V. G. Kouznetsova, and M. G. D. Geers, “Visco-elastic effects on wave dispersion in three-phase acoustic metamaterials,” *J. Mech. Phys. Solids*, vol. 96, pp. 29–47, Nov. 2016, doi: http://dx.doi.org/10.1016/j.jmps.2016.07.001.

[75] M. A. Lewińska, V. G. Kouznetsova, J. A. W. van Dommelen, A. O. Krushynska, and M. G. D. Geers, “The attenuation performance of locally resonant acoustic metamaterials based on generalised viscoelastic modelling,” *Int. J. Solids Struct.*, vol. 126–127, pp. 163–174, Nov. 2017, doi: http://dx.doi.org/10.1016/j.ijsolstr.2017.08.003.

[76] O. R. Bilal and M. I. Hussein, “Trampoline metamaterial: Local resonance enhancement by springboards,” *Appl. Phys. Lett.*, vol. 103, no. 11, p. 111901, Sep. 2013, doi: http://dx.doi.org/10.1063/1.4820796.

[77] P. Sheng, X. X. Zhang, Z. Liu, and C. T. Chan, “Locally resonant sonic materials,” *Phys. B Condens. Matter*, vol. 338, no. 1–4, pp. 201–205, Oct. 2003, doi: http://dx.doi.org/10.1016/S0921-4526(03)00487-3.

[78] G. Wang, X. Wen, J. Wen, L. Shao, and Y. Liu, “Two-Dimensional Locally Resonant Phononic Crystals with Binary Structures,” *Phys. Rev. Lett.*, vol. 93, no. 15, p. 154302, Oct. 2004, doi: http://dx.doi.org/10.1103/PhysRevLett.93.154302.

[79] K. M. Ho, Z. Yang, X. X. Zhang, and P. Sheng, “Measurements of sound transmission through panels of locally resonant materials between impedance tubes,” *Appl. Acoust.*, vol. 66, no. 7, pp. 751–765, Jul. 2005, doi: http://dx.doi.org/10.1016/j.apacoust.2004.11.005.

[80] E. P. Calius, X. Bremaud, B. Smith, and A. Hall, “Negative mass sound shielding structures: Early results,” *Phys. status solidi*, vol. 246, no. 9, pp. 2089–2097, Sep. 2009, doi: http://dx.doi.org/10.1002/pssb.200982040.

[81] E. C. Wester, X. Brémaud, and B. Smith, “Meta-Material Sound Insulation,” *Build. Acoust.*, vol. 16, no. 1, pp. 21–30, Jan. 2009, doi: http://dx.doi.org/10.1260/135101009788066555.

[82] R. Sainidou, B. Djafari-Rouhani, Y. Pennec, and J. O. Vasseur, “Locally resonant phononic crystals made of hollow spheres or cylinders,” *Phys. Rev. B*, vol. 73, no. 2, p. 024302, Jan. 2006, doi: http://dx.doi.org/10.1103/PhysRevB.73.024302.

[83] C. Boutin and F. X. Becot, “Theory and experiments on poro-acoustics with inner resonators,” *Wave Motion*, vol. 54, pp. 76–99, Apr. 2015, doi: http://dx.doi.org/10.1016/j.wavemoti.2014.11.013.

[84] D. Yu, Y. Liu, H. Zhao, G. Wang, and J. Qiu, “Flexural vibration band gaps in Euler-Bernoulli beams with locally resonant structures with two degrees of freedom,” *Phys. Rev. B*, vol. 73, no. 6, p. 064301, Feb. 2006, doi: http://dx.doi.org/10.1103/PhysRevB.73.064301.

[85] Y. Pennec, B. Djafari-Rouhani, H. Larabi, J. O. Vasseur, and A. C. Hladky-Hennion, “Low-frequency gaps in a phononic crystal constituted of cylindrical dots deposited on a thin homogeneous plate,” *Phys. Rev. B*, vol. 78, no. 10, p. 104105, Sep. 2008, doi: http://dx.doi.org/10.1103/PhysRevB.78.104105.

[86] M. Badreddine Assouar, M. Senesi, M. Oudich, M. Ruzzene, and Z. Hou, “Broadband plate-type acoustic metamaterial for low-frequency sound attenuation,” *Appl. Phys. Lett.*, vol. 101, no. 17, p. 173505, Oct. 2012, doi: http://dx.doi.org/10.1063/1.4764072.

[87] M. Badreddine Assouar and M. Oudich, “Enlargement of a locally resonant sonic band gap by using double-sides stubbed phononic plates,” *Appl. Phys. Lett.*, vol. 100, no. 12, p. 123506, Mar. 2012, doi: http://dx.doi.org/10.1063/1.3696050.

[88] H.-J. Zhao, H.-W. Guo, M.-X. Gao, R.-Q. Liu, and Z.-Q. Deng, “Vibration band gaps in double-vibrator pillared phononic crystal plate,” *J. Appl. Phys.*, vol. 119, no. 1, p. 014903, Jan. 2016, doi: http://dx.doi.org/10.1063/1.4939484.

[89] O. R. Bilal, A. Foehr, and C. Daraio, “Observation of trampoline phenomena in 3D-printed metamaterial plates,” *Extrem. Mech. Lett.*, vol. 15, pp. 103–107, Sep. 2017, doi: http://dx.doi.org/10.1016/j.eml.2017.06.004.

[90] K. Wang, J. Zhou, C. Cai, D. Xu, and H. Ouyang, “Mathematical modeling and analysis of a meta-plate for very low-frequency band gap,” *Appl. Math. Model.*, vol. 73, pp. 581–597, Sep. 2019, doi: http://dx.doi.org/10.1016/j.apm.2019.04.033.

[91] Z. Yang, J. Mei, M. Yang, N. H. Chan, and P. Sheng, “Membrane-Type Acoustic Metamaterial with Negative Dynamic Mass,” *Phys. Rev. Lett.*, vol. 101, no. 20, p. 204301, Nov. 2008, doi: http://dx.doi.org/10.1103/PhysRevLett.101.204301.

[92] A. Khanolkar, S. Wallen, M. Abi Ghanem, J. Jenks, N. Vogel, and N. Boechler, “A self-assembled metamaterial for Lamb waves,” *Appl. Phys. Lett.*, vol. 107, no. 7, p. 071903, Aug. 2015, doi: http://dx.doi.org/10.1063/1.4928564.

[93] M. Hiraiwa, M. Abi Ghanem, S. P. Wallen, A. Khanolkar, A. A. Maznev, and N. Boechler, “Complex Contact-Based Dynamics of Microsphere Monolayers Revealed by Resonant Attenuation of Surface Acoustic Waves,” *Phys. Rev. Lett.*, vol. 116, no. 19, p. 198001, May 2016, doi: http://dx.doi.org/10.1103/PhysRevLett.116.198001.

[94] M. Rupin, F. Lemoult, G. Lerosey, and P. Roux, “Experimental Demonstration of Ordered and Disordered Multiresonant Metamaterials for Lamb Waves,” *Phys. Rev. Lett.*, vol. 112, no. 23, p. 234301, Jun. 2014, doi: http://dx.doi.org/10.1103/PhysRevLett.112.234301.

[95] A. Banerjee, R. Das, and E. P. Calius, “Frequency graded 1D metamaterials: A study on the attenuation bands,” *J. Appl. Phys.*, vol. 122, no. 7, p. 075101, Aug. 2017, doi: http://dx.doi.org/10.1063/1.4998446.

[96] C. Liu and C. Reina, “Broadband locally resonant metamaterials with graded hierarchical architecture,” *J. Appl. Phys.*, vol. 123, no. 9, p. 095108, Mar. 2018, doi: http://dx.doi.org/10.1063/1.5003264.

[97] P. Celli, B. Yousefzadeh, C. Daraio, and S. Gonella, “Bandgap widening by disorder in rainbow metamaterials,” *Appl. Phys. Lett.*, vol. 114, no. 9, p. 091903, Mar. 2019, doi: http://dx.doi.org/10.1063/1.5081916.

[98] C. Claeys, E. Deckers, B. Pluymers, and W. Desmet, “A lightweight vibro-acoustic metamaterial demonstrator: Numerical and experimental investigation,” *Mech. Syst. Signal Process.*, vol. 70–71, pp. 853–880, Mar. 2016, doi: http://dx.doi.org/10.1016/j.ymssp.2015.08.029.

[99] D. Roca, T. Pàmies, J. Cante, O. Lloberas-Valls, and J. Oliver, “Experimental and Numerical Assessment of Local Resonance Phenomena in 3D-Printed Acoustic Metamaterials,” *J. Vib. Acoust.*, vol. 142, no. 2, pp. 1–9, Apr. 2020, doi: http://dx.doi.org/10.1115/1.4045774.

[100] A. Leblanc and A. Lavie, “Three-dimensional-printed membrane-type acoustic metamaterial for low frequency sound attenuation,” *J. Acoust. Soc. Am.*, vol. 141, no. 6, pp. EL538–EL542, Jun. 2017, doi: http://dx.doi.org/10.1121/1.4984623.

[101] O. McGee *et al.*, “3D printed architected hollow sphere foams with low-frequency phononic band gaps,” *Addit. Manuf.*, vol. 30, p. 100842, Dec. 2019, doi: http://dx.doi.org/10.1016/j.addma.2019.100842.

ARTICLE I

- Online published title page -

Computer Methods in Applied Mechanics and Engineering
Volume 330, 1 March 2018, Pages 415-446

A computational multiscale homogenization framework accounting for inertial effects: Application to acoustic metamaterials modelling

D. Roca [a, b], O. Lloberas-Valls [a, c], J. Cante [a, b], J. Oliver [a, c]

[a] Centre Internacional de Mètodes Numèrics en Enginyeria (CIMNE), Campus Nord UPC, Mòdul C-1 101, c/ Jordi Girona 1-3, 08034 Barcelona, Spain
[b] Escola Superior d'Enginyeries Industrial, Aeroespacial i Audiovisual de Terrassa (ESEIAAT), Technical University of Catalonia (Barcelona Tech), Campus Terrassa UPC, c/ Colom 11, 08222 Terrassa, Spain
[c] E.T.S d'Enginyers de Camins, Canals i Ports de Barcelona (ETSECCPB), Technical University of Catalonia (Barcelona Tech), Campus Nord UPC, Mòdul C-1, c/ Jordi Girona 1-3, 08034 Barcelona, Spain

Received 4 May 2017, Revised 22 September 2017, Accepted 26 October 2017, Available online 14 November 2017.

Check for updates

Show less

https://doi.org/10.1016/j.cma.2017.10.025

Get rights and content

Under a Creative Commons license

open access

Article I

A computational multiscale homogenization framework accounting for inertial effects: Application to acoustic metamaterials modelling

D. Roca[a,b], O. Lloberas-Valls[a,c], J. Cante[a,b], J. Oliver[a,c,(*)]

[a] *Centre Internacional de Mètodes Numèrics en Enginyeria (CIMNE), Campus Nord UPC, Mòdul C-1 101, c/ Jordi Girona 1-3, 08034 Barcelona, Spain*

[b] *Escola Superior d'Enginyeries Industrial, Aeroespacial i Audiovisual de Terrassa (ESEIAAT), Technical University of Catalonia (Barcelona Tech), Campus Terrassa UPC, c/ Colom 11, 08222 Terrassa, Spain*

[c] *E.T.S. d'Enginyers de Camins, Canals i Ports de Barcelona (ETSECCPB), Technical University of Catalonia (Barcelona Tech), Campus Nord UPC, Mòdul C-1, c/ Jordi Girona 1-3, 080304 Barcelona, Spain*

Abstract

A framework, based on an extended Hill-Mandel principle accounting for inertial effects (Multiscale Virtual Work principle), is developed for application to acoustic problems in the context of metamaterials modelling. The classical restrictions in the mean values of the micro-displacement fluctuations and their gradients are then accounted for in a saddle-point formulation of that variational principle in terms of Lagrange functionals. A physical interpretation of the involved Lagrange multipliers can then be readily obtained.

The framework is specifically tailored for modelling the phenomena involved in Locally Resonant Acoustic Metamaterials (LRAM). In this view, several additional hypotheses based on scale separation are used to split the fully coupled micro-macro set of equations into a quasi-static and an inertial system. These are then solved by considering a projection of the microscale equations into their natural modes, which allows for a low-cost computational treatment of the multiscale problem. On this basis, the issue of numerically capturing the local resonance phenomena in a FE^2 context is addressed. Objectivity of the obtained results in terms of the macroscopic Finite Element (FE) discretization is checked as well as accuracy of the homogenization procedure by comparing with direct numerical simulations (DNS). The appearance of local resonance

bandgaps is then modelled for a homogeneous 2D problem and its extension to multi-layered macroscopic material is presented as an initial attempt towards acoustic metamaterial design for tailored band-gap attenuation.

Keywords: Multiscale modelling, Computational homogenization, Inertial problems, Acoustic metamaterials, Local resonance phenomena

I.1 Motivation

The field of computational multiscale modelling has experienced a significant development in the last decades and its progressively penetrating many different application fields within simulation-based techniques. Hierarchical multiscale techniques, based on homogenization theory, have specially captured the attention of the computational mechanics community given their ability to account for microstructural physical phenomena and their impact at a macroscopic scale. Moreover, homogenization-based multiscale simulations are regarded significantly inexpensive from a computational viewpoint compared to (single scale) direct numerical simulations (DNS) or concurrent multiscale techniques [1, 2] in which micro and macro levels are simultaneously processed in the computations. This feature is obviously more evident when the separation between lower and upper scales increases.

Our focus is centered in computational homogenization techniques in which the constitutive information driving the macroscopic analysis is computed from consecutive interactions between the macro and microscale. In other words, there is no explicit (or closed form) macroscopic constitutive behavior, but it is obtained through successive computations performed over a Representative Volume Element (RVE) of the microstructure. Such macro/micro interactions are generally referred to as downscaling and upscaling, indicating the sense of the information flow. Examples of these kind of techniques are found in Feyel and Chaboche [3], Kouznetsova *et al*. [4] in which homogenization of non-linear behavior of complex microstructures is considered. Different types of boundary conditions Miehe and Koch [5], Mesarovic and Padbidri [6] can be chosen for the downscaling, which impact the solution field at the boundary of the RVE. In the last years, a remarkable progress has been accomplished when applying these type of techniques to a wide range of quasi-static applications including complex

material behavior such as softening and localization phenomena Verhoosel *et al*. [7], Nguyen *et al*. [8], [9], Oliver *et al*. [10], multiphysics phenomena Özdemir *et al*. [11], large deformations [12] and specific structural elements such as beams and plates [13].

Computational homogenization techniques including inertial effects constitute the main subject of the current contribution. The objective is to present a physically sound formulation for the two-scale problem and highlight one of its main emerging applications, i.e. multiscale computational analysis and design of materials with unusual properties when submitted to dynamic excitations. Several homogenization approaches which include inertial effects have been proposed so far, e.g. [14–16], but their formulation in a rigorous variational form has only recently been stated in [17, 18], where a general multiscale framework is presented, which is grounded on kinematic admissibility, duality (relating force and stress-like quantities) and a generalized Hill-Mandel principle postulated in terms of a variational statement named the Multiscale Virtual Power Principle (MVPP).

In the present contribution, attention is focused on the application of the aforementioned MVPP in acoustics. This allowing some simplifications with respect to the general framework. In order to facilitate the corresponding simplifying hypotheses, it turns out to be convenient the modification of the MVPP as a saddle-point variational problem incorporating Lagrange multipliers associated to the kinematic restrictions. This enables deriving the corresponding Euler Lagrange equations as well as the identification of the Lagrange multipliers representing the macroscopic D'Alembert forces (body forces minus inertial forces) and the overall stresses. Such a formulation is particularly useful for the multiscale design approach, since the targeted macroscopic behavior can now be easily linked to the microstructural design variables. After defining this multiscale setting, the second part of this contribution is specifically tailored to modelling acoustic problems. More specifically, for the study of sound cancelling and attenuating acoustic metamaterials based on local resonance phenomena. For instance, the formulation as a saddle-point problem including Lagrange multipliers enables to identify the limits of the frequency bandgaps in terms of the resonant effects of a partially or fully restricted RVE and their impact at the macroscopic level. To the authors knowledge, a precedental dual formulation written in terms of Lagrange multipliers has appeared in [19], where macroscale forces and stresses are identified as the Lagrange multipliers linked to microscale fields but applied to the Navier-Stokes equations. The saddle-point problem

formulation employing Lagrange multipliers obtained in this contribution from fundamental micro-macro balance principles, allows for a clear interpretation of the connections between scales in a dynamic context.

In the current contribution, the microstructural augmented system of equations emanating from the Lagrange multipliers-based approach (including the microscopic displacements as well as the Lagrange multipliers as unknowns) is then extended, for acoustic problems, from minimal kinematic constraints to periodic boundary conditions. In contrast with other approaches [16, 20], the resolution of the microstructural system with micro-macro constraints is split here into the superposition of a quasi-static and an inertial solution (on the resulting Finite Elements RVE system of equations rather than on different material phases). This split is grounded on the superposition principle for linear systems and the following assumptions for the acoustic material: (i) macroscopic strains produce, by themselves, no inertial microscopic response (quasi-static system) and (ii) macroscopic displacements produce, by themselves (independently of the strains), negligible microscopic reactive stresses against the inertial response (inertial system). The aforementioned identification of the Lagrange multipliers plays a fundamental role in the justification of these assumptions. In addition, the quasi-static system provides directly the homogenized stresses as one of the Lagrange multipliers and the homogenized constitutive tensor appearing in classical quasi-static homogenization theory, whereas the inertial system, returns the macroscopic inertial forces as the other Lagrange multiplier (when body forces are neglected). In order to reduce the computational cost of the micro-macro coupled inertial system, a specific Reduced Order Modelling technique (ROM) is suggested, i.e. a modal analysis approach where microscopic displacements are projected onto the space spanned by the most dominant resonating modes. Both quasi-static and reduced inertial systems provide closed form expressions for the effective macroscopic stress and inertial forces that lead to the full homogenized problem when considered in the macroscale linear momentum balance equations.

Particularizing the micro and macroscale displacement fields for wave-like solution in infinite and homogeneous media, the macroscopic linear momentum balance equation, with effective properties, turns into a dispersion relation, i.e. for a given frequency and propagating wave direction, the wave numbers and associated propagation modes can be obtained at the macrostructure. The effect of locally resonating modes for given

frequencies is captured at the macroscopic dispersion curves in terms of a band gap region in which the wave is attenuated when the excitation frequency lies in the obtained bandgap.

A specific feature of the proposed framework is that a Craig-Bampton reduction technique is not required at the RVE level as in [16] and, therefore, assumptions on specific material phases are not necessary, conferring to the proposed approach a more general character. In fact, the Craig-Bampton technique used in [16] to obtain the relevant dynamics considers a fully fixed matrix at the boundary and the resonant modes account only for the dynamics of the dense inclusions. In the present approach, the split into quasi-static and dynamic solutions mentioned above is referred to the augmented system of equations and not to the particular material phases, allowing a more general description of the internal dynamics, since all present microstructural phases participate in the resonant behavior. This assumption is proven to capture sufficiently well the local resonance phenomena compared to Direct Numerical Simulations and objectivity of the homogenized response is found for different macroscopic meshes.

As for acoustic problems modelling, the microstructural topology is considered structured in regular cells in the present contribution, this strongly motivating the use of periodic boundary conditions, which allows working with generally simpler RVEs or unit cells. Up to date, most of contributions in computational homogenization of acoustic metamaterials focus on the design of microstructures periodically repeated at the macro level representing macroscopic homogeneous layers (cf. [16, 20–23]). From an industrial point of view, it is even more interesting to conceive the macrostructure as a heterogeneous body, e.g. composed by layers with different underlying resonant microstructures. This allows to program the metamaterial assembly to attenuate a wider spectrum of frequencies characterizing a certain noise or sound. To the authors knowledge, a computational framework for the multidimensional study of multi-layered acoustic metamaterials with underlying resonating microstructures has not yet been devised and opens the possibility of tackling an enormous range of applications in which a wider frequency band is obtained and, therefore, a more complex acoustic signal can be attenuated. The applications for the design of such metamaterials are countless, for instance, one could devise an acoustic metamaterial for a given target noise source or frequency spectra to be attenuated.

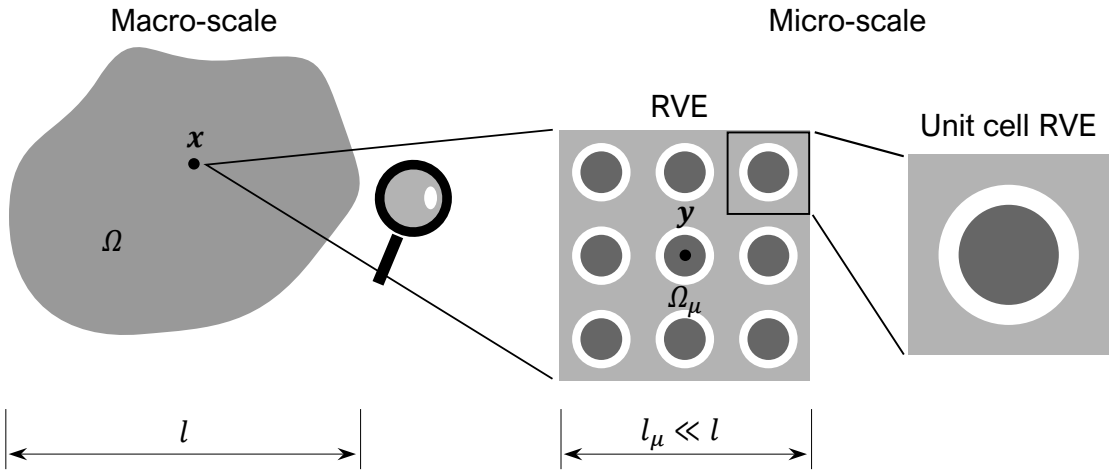

FIG. 1 Typical multiscale problem configuration. The characteristic size of the microscale, l_μ, must satisfy $l_\mu \ll l$ in order to preserve the separation of scales.

In order to demonstrate the capabilities of the proposed formulation in the computational modelling and design of LRAM, a number of 2D representative simulations (both at the micro and macro scales) have been carried out in this work: first, dispersion analyses have been performed in an ideal (infinite and homogeneous) medium; second, a more realistic FE analysis has been taken to the design of an acoustic panel consisting on a finite-size layer of LRAM where the attenuation properties are studied. Finally, the potential for material acoustic design aspects is displayed by modelling a two-layer macroscopic LRAM.

I.2 Generalized energetic equivalence-based homogenization framework

I.2.1 Multi-scale problem set-up

Let's consider a macroscopic solid body occupying a domain $\Omega \subset \mathbb{R}^m$ with smooth boundary $\partial\Omega$ (for the sake of simplicity, in the present work, we will assume $m = 2$, but the formulation is general and valid also for $m = 3$). Spatial coordinates in the macroscale will be referred by $\mathbf{x}$ and the set of generalized displacement fields will be defined as

$$\boldsymbol{u}(\boldsymbol{x},t):\Omega\times[0,T]\rightarrow\mathbb{R}^m \tag{1}$$

The displacement gradient tensor $\mathbf{J}$ is defined as

$$\mathbf{J}(\boldsymbol{x},t)=\boldsymbol{u}(\boldsymbol{x},t)\otimes\boldsymbol{\nabla}_x\equiv\boldsymbol{\nabla}_x\boldsymbol{u}(\boldsymbol{x},t) \tag{2}$$

$$\mathbf{J}(\boldsymbol{x},t)=\boldsymbol{\varepsilon}(\boldsymbol{x},t)+\widehat{\boldsymbol{\Omega}}(\boldsymbol{x},t) \tag{3}$$

where

$$\boldsymbol{\varepsilon}(\boldsymbol{x},t)=\boldsymbol{\nabla}_x^{\mathrm{S}}\boldsymbol{u}(\boldsymbol{x},t)=\frac{1}{2}\Big(\boldsymbol{u}(\boldsymbol{x},t)\otimes\boldsymbol{\nabla}_x+\boldsymbol{\nabla}_x\otimes\boldsymbol{u}(\boldsymbol{x},t)\Big). \tag{4}$$

$$\widehat{\boldsymbol{\Omega}}(\boldsymbol{x},t)=\boldsymbol{\nabla}_x^{\mathrm{skew}}\boldsymbol{u}(\boldsymbol{x},t)=\frac{1}{2}\Big(\boldsymbol{u}(\boldsymbol{x},t)\otimes\boldsymbol{\nabla}_x-\boldsymbol{\nabla}_x\otimes\boldsymbol{u}(\boldsymbol{x},t)\Big). \tag{5}$$

With $\boldsymbol{\varepsilon}$ and $\widehat{\boldsymbol{\Omega}}$ being, respectively, the (symmetric) infinitesimal strain tensor and the (skew-symmetric) infinitesimal rotation tensor [24].

At each point $\boldsymbol{x}$ one can associate a representative volume element (RVE) of the microscale and, sometimes, it is also possible to identify a periodically repetitive structure known as unit cell (cf. Fig. 1). In order to distinguish those variables associated to the microscale from their macroscopic counterparts, the subscript μ will be used when referring to the former. Following this rule, the RVE will be denoted by $\Omega_\mu\subset\mathbb{R}^m$, with a smooth boundary $\partial\Omega_\mu$ and its spatial coordinates referred by $\boldsymbol{y}$. Also, for the sake of readability, angle brackets $\langle\cdot\rangle_{\Omega_\mu}/\langle\cdot\rangle_{\Gamma_\mu}$ will be used throughout the paper as an operator for the RVE volume average integral of the field $(\cdot)$, so that

$$\langle\cdot\rangle_{\Omega_\mu}\equiv\frac{1}{|\Omega_\mu|}\int_{\Omega_\mu}(\cdot)d\Omega\,;\quad\langle\cdot\rangle_{\Gamma_\mu}\equiv\frac{1}{|\Omega_\mu|}\int_{\Gamma_\mu}(\cdot)d\Gamma \tag{6}$$

where $\Gamma_\mu\subset\partial\Omega_\mu$.

A kinematic connection between both scales will be established by considering the first order expansion of the kinematic variables associated to point $\boldsymbol{x}$ in the macroscale, so

$$\boldsymbol{u}_\mu(\boldsymbol{y},t)=\boldsymbol{u}(\boldsymbol{x},t)+\mathbf{J}(\boldsymbol{x},t)\cdot(\boldsymbol{y}-\boldsymbol{y}_0)+\tilde{\boldsymbol{u}}_\mu(\boldsymbol{y},t), \tag{7}$$

$$\boldsymbol{\nabla}_y\boldsymbol{u}_\mu(\boldsymbol{y},t)=\mathbf{J}(\boldsymbol{x},t)+\boldsymbol{\nabla}_y\tilde{\boldsymbol{u}}_\mu(\boldsymbol{y},t), \tag{8}$$

where $\boldsymbol{u}$ and $\mathbf{J}$ are the local values of the displacement field and their gradient at the macroscopic level, $\boldsymbol{y}_0$ are the coordinates of the centroid of the RVE and $\tilde{\boldsymbol{u}}_\mu$ is the micro-

fluctuation field. In this context, we impose the fluctuation field and its *symmetric gradient* to satisfy, for any time $t \in [0, T]$,

$$\langle \tilde{\boldsymbol{u}}_\mu(\boldsymbol{y}, t)\rangle_{\Omega_\mu} = \boldsymbol{0}, \qquad \text{or} \qquad \langle \boldsymbol{u}_\mu(\boldsymbol{y}, t)\rangle_{\Omega_\mu} = \boldsymbol{u}(\boldsymbol{x}, t); \tag{9}$$

$$\langle \nabla^{\mathrm{S}}_{\boldsymbol{y}} \tilde{\boldsymbol{u}}_\mu(\boldsymbol{y}, t)\rangle_{\Omega_\mu} = \boldsymbol{0} \qquad \text{or} \qquad \langle \nabla^{\mathrm{S}}_{\boldsymbol{y}} \boldsymbol{u}_\mu(\boldsymbol{y}, t)\rangle_{\Omega_\mu} = \boldsymbol{\varepsilon}(\boldsymbol{x}, t); \tag{10}$$

In Eqs. (9) and (10) the fact that $\boldsymbol{y}_0$ is the centroid of the RVE domain and, therefore, $\langle \boldsymbol{y} - \boldsymbol{y}_0 \rangle_{\Omega_\mu} = \boldsymbol{0}$, has been considered. Eqs. (9) and (10) are often referred to in the literature as *minimal kinematic restrictions* [18].

> REMARK 1 It is important to note that the time scale is the same for both the macro and the micro scales, so by fixing a kinematic connection in the displacement fields, we also establish a relation between rate (velocity) fields. In particular, this means that restrictions (9) and (10) are satisfied also for the rate fields and their corresponding symmetric gradients.

I.2.2 Fundamental hypothesis

The homogenization framework proposed here is a generalization to inertial cases of the classical Hill-Mandel principle for quasi-static problems. The model will be derived from the work of Blanco *et al*. [18], in which a general multiscale framework is presented based on three main hypotheses: (a) kinematic admissibility between scales, (b) mathematical duality of the macroscopic force/stress quantities with the corresponding kinematic variables, and (c) the so-called *Multiscale Virtual Power Principle*, which is used to derive the equilibrium equations from variational arguments. Also in [15], a generalization to inertial cases of the Hill-Mandel principle is proposed.

The model proposed here is grounded on the application at the macroscale of the classical postulates of continuum mechanics, i.e. linear and angular momentum balance laws:

$$\boldsymbol{\nabla}_x \cdot \boldsymbol{\sigma}(\boldsymbol{x}, t) + \boldsymbol{f}(\boldsymbol{x}, t) = \boldsymbol{0}, \tag{11}$$

$$\boldsymbol{\sigma}(\boldsymbol{x}, t) = \boldsymbol{\sigma}^{\mathrm{T}}(\boldsymbol{x}, t), \qquad \forall\, \boldsymbol{x} \in \Omega, \qquad \forall\, t \in [0, T]. \tag{12}$$

where $\boldsymbol{\sigma}$ is the macroscopic stress and $\boldsymbol{f}$ is the D'Alembert force density.

For the sake of simplicity, we will remain in the present work in the context of infinitesimal strains and elastic behavior (linear elasticity), and in the framework of Cauchy's continua, only accounting for body forces and surface tractions as external actions on the continuum medium [24].

Eqs. (11) and (12) are complemented by the D'Alembert force density definition and the Cauchy's stress theorem applied to the boundary of Ω:

$$f(x,t) = b(x,t) - \dot{p}(x,t), \tag{13}$$

$$\sigma(x,t) \cdot n(x) = t(x,t), \qquad \forall x \in \partial\Omega \tag{14}$$

where $\mathbf{b}$ and $\mathbf{p}$ are the body force and the linear momentum densities, respectively, while $\mathbf{n}$ and $\mathbf{t}$ are the outward unit normal and traction vectors at the corresponding boundary, respectively. Note that we use the dot accent $\dot{(\cdot)}$ to refer to time derivatives and the superscript $(\cdot)^{\mathrm{T}}$ stands for tensor transposition.

Now, in the context of linear elasticity, for the microscale, we assume

$$\sigma_\mu(y,t) = \mathbf{C}_\mu(y) : \nabla_y^{\mathrm{S}} u_\mu(y,t), \tag{15}$$

where $\mathbf{C}_\mu(y)$ is the constitutive elastic tensor associated to the microscale material phases. Furthermore, given the density field in the microscale $\rho_\mu(y)$, we will define the linear momentum density at the microscale as

$$p_\mu(y,t) = \rho_\mu(y)\dot{u}_\mu(y,t) \tag{16}$$

so the microscopic D'Alembert force density becomes

$$f_\mu(y,t) = b_\mu(y,t) - \dot{p}_\mu(y,t) = b_\mu(y,t) - \rho_\mu(y)\ddot{u}_\mu(y,t) \tag{17}$$

where $\rho_\mu \ddot{u}_\mu$ is the microscopic inertial force.

> REMARK 2 Notice that the macroscopic counterparts of equations (15) and (17) are not specifically postulated since they will be obtained as a result of the homogenization procedure.

I.2.3 Hill-Mandel principle

The *Multiscale Virtual Power Principle* in [18] postulates an energetic equivalence between scales and can be regarded as a generalization of the classical Hill-Mandel principle for quasi-static problems. It is formulated as

GIVEN

$$f(u(x,t)), \quad \sigma(u(x,t)), \quad x \in \Omega, t \in [0,T] \tag{18}$$

and

$$f_\mu(u_\mu(y,t)), \quad \sigma_\mu(u_\mu(y,t)), \quad y \in \Omega_\mu, t \in [0,T] \tag{19}$$

THEN

$$\sigma : \nabla_x^S \dot{u} - f \cdot \dot{u} = \langle \sigma_\mu : \nabla_y^S \dot{u}_\mu - f_\mu \cdot \dot{u}_\mu \rangle_{\Omega_\mu}, \tag{20}$$

$\forall\, \dot{u}$ and $\forall\, \dot{u}_\mu \in \mathscr{U}_\mu$, where $\mathscr{U}_\mu$ is the space of *kinematically admissible displacement-rate fields*, $\dot{u}_\mu$ in the microscale

$$\mathscr{U}_\mu := \left\{ \dot{u}_\mu = \dot{u} + \nabla_x \dot{u} \cdot (y - y_0) + \tilde{\dot{u}}_\mu \mid \tilde{\dot{u}}_\mu \in \mathscr{U}_\mu^0 \right\}, \tag{21}$$

which, in turn, is defined in terms of the space $\mathscr{U}_\mu^0$ of *admissible micro-fluctuation displacement-rate fields*, $\tilde{\dot{u}}_\mu$, as

$$\mathscr{U}_\mu^0 := \left\{ \tilde{\dot{u}}_\mu : \Omega_\mu \times [0,T] \to \mathbb{R}^m \mid \langle \tilde{\dot{u}}_\mu \rangle_{\Omega_\mu} = \mathbf{0};\ \langle \nabla_y^S \tilde{\dot{u}}_\mu \rangle_{\Omega_\mu} = \mathbf{0} \right\}. \tag{22}$$

REMARK 3 Notice that, in Eqs. (20) to (22), perturbations $\dot{u}$ are not subjected to any restriction, so this allows us to choose, for a given spatial point x^*, independent *local* values of $\dot{u}(x,t)|_{x=x^*}$ and $\nabla_x^S \dot{u}(x,t)|_{x=x^*}$. Then, following the procedure in [18], one can obtain expressions for the homogenized values for the local macroscopic D'Alembert force density and stress:

$$f = \langle f_\mu \rangle_{\Omega_\mu}; \tag{23}$$

$$\sigma = \langle \sigma_\mu - f_\mu \otimes^S (y - y_0) \rangle_{\Omega_\mu}. \tag{24}$$

From now on, the symbol $\otimes^S$ will be used to express

$$a \otimes^S b = \frac{1}{2}(a \otimes b + b \otimes a) \tag{25}$$

Insertion of results (23) and (24) into Eq. (20), returns the variational problem to be solved in the RVE. Denoting $\hat{\boldsymbol{u}}_\mu$ as $\delta\boldsymbol{u}_\mu$, it reads

FIND

$$\boldsymbol{u}_\mu(\boldsymbol{y},t) : \Omega_\mu \times [0,T] \to \mathbb{R}^m, \qquad \boldsymbol{u}_\mu \in \mathscr{U}_\mu$$

FULFILLING

$$\langle \dot{\boldsymbol{p}}_\mu \cdot \delta\boldsymbol{u}_\mu + \boldsymbol{\sigma}_\mu : \nabla_{\boldsymbol{y}}^{\mathrm{S}} \delta\boldsymbol{u}_\mu - \boldsymbol{b}_\mu \cdot \delta\boldsymbol{u}_\mu \rangle_{\Omega_\mu} = 0, \qquad \forall\, \delta\boldsymbol{u}_\mu \in \mathscr{U}_\mu^0 \tag{26}$$

where the microscopic counterpart of Eq. (13) has been considered.

REMARK 4 Eq. (26) is a constrained variational principle that is restricted to solutions in $\mathscr{U}_\mu$ (cf. Eq. (21)), i.e. fulfilling

$$\begin{cases} \langle \boldsymbol{u}_\mu(\boldsymbol{y},t) - \boldsymbol{u}(\boldsymbol{x},t) \rangle_{\Omega_\mu} = \boldsymbol{0}, \\ \langle \nabla_{\boldsymbol{y}}^{\mathrm{S}} \boldsymbol{u}_\mu(\boldsymbol{y},t) - \boldsymbol{\varepsilon}(\boldsymbol{x},t) \rangle_{\Omega_\mu} = \boldsymbol{0}. \end{cases} \tag{27}$$

I.2.4 Lagrange functional-based homogenization

While the variational problem in Eq. (26) can be solved, given the geometrical and material distribution of the RVE along with values for the macroscopic displacement and strain [18], it will prove more convenient to reformulate it as a saddle-point problem using Lagrange multipliers. In this way, one can work with unconstrained perturbation fields and obtain the reactions to the constraints (27) directly through the Lagrange multipliers identification. A similar approach has already been adopted, for instance, in the work of Blanco *et al*. [19], in the context of the so-called *Multiscale Virtual Power Principle* for homogenization of the Navier-Stokes equations.

To do so, let's first consider the variational statement (26) as the optimality condition for a *constrained* minimization problem in the RVE, that is

$$\delta\Pi_\mu(\boldsymbol{u}_\mu; \delta\boldsymbol{u}_\mu) = \langle \dot{\boldsymbol{p}}_\mu \cdot \delta\boldsymbol{u}_\mu + \boldsymbol{\sigma}_\mu : \nabla_{\boldsymbol{y}}^{\mathrm{S}} \delta\boldsymbol{u}_\mu - \boldsymbol{b}_\mu \cdot \delta\boldsymbol{u}_\mu \rangle_{\Omega_\mu} = 0, \tag{28}$$

with restrictions $\boldsymbol{u}_\mu \in \mathscr{U}_\mu$ and $\delta\boldsymbol{u}_\mu \in \mathscr{U}_\mu^0$.

Disregard the explicit expression of functional $\Pi_\mu(\boldsymbol{u}_\mu)$, we can obtain the extended Lagrangian functional by adding constraints (9) and (10) through their corresponding

Lagrange multipliers, $\boldsymbol{\beta}$ and $\boldsymbol{\lambda}$, respectively. This yields the following saddle-point problem in terms of *unconstrained* displacement fields as

FIND

$$\boldsymbol{u}_\mu(\boldsymbol{y},t) : \Omega_\mu \times [0\times T] \to \mathbb{R}^m,$$

$$\boldsymbol{\beta}(t) : [0,T] \to \mathbb{R}^m,$$

$$\boldsymbol{\lambda}(t) : [0,T] \to \mathrm{Sym}^2(\mathbb{R}^m),$$

FULFILLING

$$\left\{\boldsymbol{u}_\mu,\boldsymbol{\beta},\boldsymbol{\lambda}\right\} = \arg\min_{\boldsymbol{u}_\mu}\max_{\boldsymbol{\beta},\boldsymbol{\lambda}}\left\{\Pi_\mu(\boldsymbol{u}_\mu) - \boldsymbol{\beta}\cdot\langle\boldsymbol{u}_\mu - \boldsymbol{u}\rangle_{\Omega_\mu} - \boldsymbol{\lambda} : \langle\boldsymbol{\nabla}^{\mathrm{S}}_{\boldsymbol{y}}\boldsymbol{u}_\mu - \boldsymbol{\varepsilon}\rangle_{\Omega_\mu}\right\}. \tag{29}$$

The optimality conditions for the saddle-point problem (29) result in the following variational system of equations:

$$\langle(\dot{\boldsymbol{p}}_\mu - \boldsymbol{b}_\mu - \boldsymbol{\beta})\cdot\delta\boldsymbol{u}_\mu + (\boldsymbol{\sigma}_\mu - \boldsymbol{\lambda}) : \boldsymbol{\nabla}^{\mathrm{S}}_{\boldsymbol{y}}\delta\boldsymbol{u}_\mu\rangle_{\Omega_\mu} = 0, \quad \forall\,\delta\boldsymbol{u}_\mu; \tag{30}$$

$$\langle\boldsymbol{u}_\mu - \boldsymbol{u}\rangle_{\Omega_\mu}\cdot\delta\boldsymbol{\beta} = 0, \qquad \forall\,\delta\boldsymbol{\beta}; \tag{31}$$

$$\langle\boldsymbol{\nabla}^{\mathrm{S}}_{\boldsymbol{y}}\boldsymbol{u}_\mu - \boldsymbol{\varepsilon}\rangle_{\Omega_\mu} : \delta\boldsymbol{\lambda} = 0, \qquad \forall\,\delta\boldsymbol{\lambda}. \tag{32}$$

Note that, in contrast to the restricted variational equation (26), in expressions (30) to (32), the variables (including the perturbation fields $\delta\boldsymbol{u}_\mu$, $\delta\boldsymbol{\beta}$ and $\delta\boldsymbol{\lambda}$) are totally unconstrained. In this regard, one can take advantage of this situation, appropriately choosing $\delta\boldsymbol{u}_\mu$ so that, in particular,

(a) for $\delta\boldsymbol{u}_\mu = \boldsymbol{a}$, $\forall\,\boldsymbol{a}$ spatially constant vector, one gets, from Eq. (30),

$$\boldsymbol{\beta} = \langle\dot{\boldsymbol{p}}_\mu - \boldsymbol{b}_\mu\rangle_{\Omega_\mu} = -\langle\boldsymbol{f}_\mu\rangle_{\Omega_\mu}; \tag{33}$$

(b) for $\delta\boldsymbol{u}_\mu = \mathbf{A}\cdot(\boldsymbol{y} - \boldsymbol{y}_0)$, $\forall\,\mathbf{A}$ spatially constant symmetric second-order tensor, then

$$\boldsymbol{\lambda} = \langle\boldsymbol{\sigma}_\mu + (\dot{\boldsymbol{p}}_\mu - \boldsymbol{b}_\mu)\otimes^{\mathrm{S}}(\boldsymbol{y} - \boldsymbol{y}_0)\rangle_{\Omega_\mu} = \langle\boldsymbol{\sigma}_\mu - \boldsymbol{f}_\mu\otimes^{\mathrm{S}}(\boldsymbol{y} - \boldsymbol{y}_0)\rangle_{\Omega_\mu}. \tag{34}$$

Comparing the results with expressions (23) and (24), prior to fully solving the system of Eqs. (30) to (32), one can identify the Lagrange multipliers $\boldsymbol{\beta}$ and $\boldsymbol{\lambda}$ as the local macroscopic homogenized D'Alembert force density and stress, respectively, thus

$$\boldsymbol{\beta}(\boldsymbol{x},t) = -\boldsymbol{f}(\boldsymbol{x},t) = -\langle\boldsymbol{f}_\mu\rangle_{\Omega_\mu} \tag{35}$$

$$\boldsymbol{\lambda}(\boldsymbol{x},t) = \boldsymbol{\sigma}(\boldsymbol{x},t) = \langle\boldsymbol{\sigma}_\mu - \boldsymbol{f}_\mu\otimes^{\mathrm{S}}(\boldsymbol{y} - \boldsymbol{y}_0)\rangle_{\Omega_\mu} \tag{36}$$

In Fig. 2 a sketch of the key ideas involving the proposed homogenization procedure is presented. In addition, Fig. 3 shows a graphical representation of the actions and reactions involved in the RVE problem.

Hill-Mandel principle

$$\boldsymbol{\sigma} : \dot{\boldsymbol{\varepsilon}} - \boldsymbol{f} \cdot \dot{\boldsymbol{u}} = \langle \boldsymbol{\sigma}_\mu : \boldsymbol{\nabla}_{\boldsymbol{y}}^{\mathrm{S}} \dot{\boldsymbol{u}}_\mu - \boldsymbol{f}_\mu \cdot \dot{\boldsymbol{u}}_\mu \rangle_{\Omega_\mu}$$

Classical variational problem formulation	**Saddle-point problem formulation**
Unknown field: $\boldsymbol{u}_\mu$	Unknown fields: $\boldsymbol{u}_\mu, \boldsymbol{\beta}, \boldsymbol{\lambda}$
Perturbation restrictions: $\delta \boldsymbol{u}_\mu \in \mathcal{U}_\mu^0$	Perturbation restrictions: None
Variational statement (constrained): $\langle \boldsymbol{\sigma}_\mu : \boldsymbol{\nabla}_{\boldsymbol{y}}^{\mathrm{S}} \delta \boldsymbol{u}_\mu - \boldsymbol{f}_\mu \cdot \delta \boldsymbol{u}_\mu \rangle_{\Omega_\mu} = 0, \quad \forall \delta \boldsymbol{u}_\mu \in \mathcal{U}_\mu^0$	Variational statement (unconstrained): $\langle (\boldsymbol{\sigma}_\mu - \boldsymbol{\lambda}) : \boldsymbol{\nabla}_{\boldsymbol{y}}^{\mathrm{S}} \delta \boldsymbol{u}_\mu - (\boldsymbol{f}_\mu + \boldsymbol{\beta}) \cdot \delta \boldsymbol{u}_\mu \rangle_{\Omega_\mu} = 0, \forall \delta \boldsymbol{u}_\mu$ $\langle \boldsymbol{u}_\mu \rangle_{\Omega_\mu} = \boldsymbol{u}$ $\langle \boldsymbol{\nabla}_{\boldsymbol{y}}^{\mathrm{S}} \boldsymbol{u}_\mu \rangle_{\Omega_\mu} = \boldsymbol{\varepsilon}$
Results: $\boldsymbol{f} = \langle \boldsymbol{f}_\mu \rangle_{\Omega_\mu}$ $\boldsymbol{\sigma} = \langle \boldsymbol{\sigma}_\mu - \boldsymbol{f}_\mu \otimes^{\mathrm{S}} (\boldsymbol{y} - \boldsymbol{y}_0) \rangle_{\Omega_\mu}$	Results: $\boldsymbol{\beta} = -\langle \boldsymbol{f}_\mu \rangle_{\Omega_\mu}$ $\boldsymbol{\lambda} = \langle \boldsymbol{\sigma}_\mu - \boldsymbol{f}_\mu \otimes^{\mathrm{S}} (\boldsymbol{y} - \boldsymbol{y}_0) \rangle_{\Omega_\mu}$

FIG. 2 Summary and key concepts of the two equivalent homogenization procedures based on the Hill-Mandel principle of energetic equivalence between scales: using the classical variational formulation and the saddle-point problem formulation.

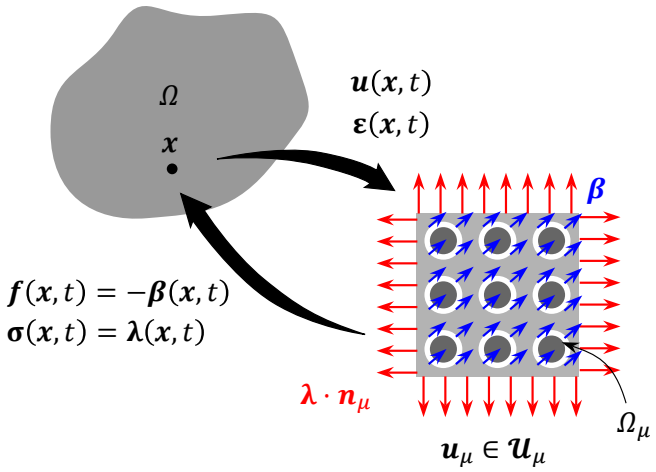

FIG. 3 Schematic representation of the RVE problem. The macroscopic displacement and strain at a given point are inputs in the associated RVE system. The macroscopic stress and D'Alembert force density are related to microscopic traction forces $\boldsymbol{\sigma} \cdot \boldsymbol{n}_\mu$ and constant body force $\boldsymbol{f}$ reactions, respectively.

I.3 Application to acoustic problems

The formulation presented so far, takes into account the minimal kinematic restrictions for the micro-displacement and strain fields (see expressions (9) and (10)) and is general for all kind of inertial problems as far as the energetic equivalence principle (and thus the separation of scales) holds. From now on, we will focus on problems in the field of acoustics, for which some additional hypotheses may be suitably employed in order to simplify both the analysis and the interpretation of the results. It should be noted that, in the context of acoustic problems, one may already find other homogenization schemes available in the literature. For instance, in the work of Sridhar *et al*. [16], an extension of the Hill-Mandel principle to inertial cases is used along with substructuring techniques (namely the Craig-Bampton Mode Synthesis) to derive a multiscale model for locally resonant acoustic metamaterials. The proposed homogenization framework, although eventually leading to similar results, offers a clear approach that allows us to simplify the model in the context of acoustic problems by simply employing physical hypotheses that do not require us to rely on substructuring techniques. In addition, from now on, body forces in equations in Section I.2 will be neglected, which is considered a reasonable assumption for the tackled acoustic problems. That is

$$\boldsymbol{f} = \boldsymbol{b} - \dot{\boldsymbol{p}} \approx -\dot{\boldsymbol{p}} \tag{37}$$

$$\boldsymbol{f}_\mu = \boldsymbol{b}_\mu - \dot{\boldsymbol{p}}_\mu \approx -\dot{\boldsymbol{p}}_\mu \tag{38}$$

I.3.1 Introduction of periodic boundary conditions

When dealing with periodic materials or structures (such as, for instance, in several problems involving acoustic metamaterials), it is sometimes convenient to impose additional sets of conditions which may offer a more accurate representation of the kinematic coupling between scales.

In this particular framework, it proves suitable to consider periodic boundary conditions for the micro-fluctuation field $\tilde{\boldsymbol{u}}_\mu$ on the RVE boundary.

For the sake of simplicity, let's consider the common case of a squared (or rectangular) RVE[1] (see Fig. 4). In order to introduce periodic boundary conditions, one can consider

[1] More general RVE shapes can be considered by a generalization of the proposed scheme.

the boundary lines $\Gamma^{(-)} = \Gamma_1^{(-)} \cup \Gamma_2^{(-)}$ and $\Gamma^{(+)} = \Gamma_1^{(+)} \cup \Gamma_2^{(+)}$, such that $\partial\Omega_\mu = \Gamma^{(-)} \cup \Gamma^{(+)}$. Let's define the jump function of $(\cdot)$ as

$$[\![\cdot]\!](\boldsymbol{y}, t) = (\cdot)(\boldsymbol{y} + \ell(\boldsymbol{y}), t) - (\cdot)(\boldsymbol{y}, t), \qquad \forall\, \boldsymbol{y} \in \Gamma^{(-)} \tag{39}$$

where

$$\ell(\boldsymbol{y}) = \begin{cases} \ell_1, & \text{for } \boldsymbol{y} \in \Gamma_1^{(-)} \\ \ell_2, & \text{for } \boldsymbol{y} \in \Gamma_2^{(-)} \end{cases} \tag{40}$$

with ℓ_{i} being the periodicity vector associated to each boundary region $\Gamma_i^{(-)}$ (cf. Fig. 4). It should be noted, from the definition of ℓ, that $[\![\boldsymbol{y}]\!] = \ell(\boldsymbol{y})$, $\forall\, \boldsymbol{y} \in \Gamma^{(-)}$. In this framework, periodic boundary conditions can be formulated (see Eq. (7)) as

$$[\![\tilde{\boldsymbol{u}}_\mu]\!] = 0, \quad \text{or} \quad [\![\boldsymbol{u}_\mu]\!] = \mathbf{J} \cdot [\![\tilde{\boldsymbol{u}}_\mu]\!] = \mathbf{J} \cdot \ell, \qquad \forall\, \boldsymbol{y} \in \Gamma^{(-)} \tag{41}$$

It is worth noting that, by construction, the periodic boundary conditions in Eq. (41) fulfil the following equation:

$$\langle \tilde{\boldsymbol{u}}_\mu \otimes^{\mathrm{S}} \boldsymbol{n}_\mu \rangle_{\partial\Omega_\mu} = \mathbf{0} \rightarrow \langle \boldsymbol{u}_\mu \otimes^{\mathrm{S}} \boldsymbol{n}_\mu \rangle_{\partial\Omega_\mu} = \boldsymbol{\nabla}_{\boldsymbol{x}}^{\mathrm{S}} \boldsymbol{u} \equiv \boldsymbol{\varepsilon} \rightarrow \langle \boldsymbol{\nabla}_{\boldsymbol{y}}^{\mathrm{S}} \boldsymbol{u}_\mu \rangle_{\Omega_\mu} = \boldsymbol{\nabla}_{\boldsymbol{x}}^{\mathrm{S}} \boldsymbol{u} \equiv \boldsymbol{\varepsilon}. \tag{42}$$

where the divergence theorem has been applied in Eq. (42). Therefore, periodic boundary conditions, automatically impose the requested minimal kinematic restriction (10), and the later does not need to be imposed any more.

Then, periodic conditions modify the space of admissible micro-fluctuation fields $\mathscr{U}_\mu^0$ to $\mathscr{U}_\mu^{0*}$, where

$$\mathscr{U}_\mu^{0*} := \left\{ \tilde{\boldsymbol{u}}_\mu : \Omega_\mu \times [0, T] \rightarrow \mathbb{R}^m \mid \langle \tilde{\boldsymbol{u}}_\mu \rangle_{\Omega_\mu} = \mathbf{0};\ [\![\tilde{\boldsymbol{u}}_\mu]\!] = \mathbf{0} \right\} \subset \mathscr{U}_\mu^0. \tag{43}$$

Note that expressions (23) and (24), derived as consequences from the generalized Hill-Mandel principle, are still valid in this context, as the micro-fluctuation fields chosen to obtain them, $\dot{\tilde{\boldsymbol{u}}}_\mu = \mathbf{0}$, still satisfy $\dot{\tilde{\boldsymbol{u}}}_\mu \in \mathscr{U}_\mu^{0*}$. In addition, the periodic boundary conditions in the saddle-point problem (29) can then be accounted simply by removing $\boldsymbol{\lambda}$ in those equations and considering a new field of Lagrange multipliers $\boldsymbol{\gamma}(\boldsymbol{y})$ enforcing restriction (41) point-wise at the boundary $\Gamma^{(-)}$. The saddle-point problem (29) can then be rephrased as

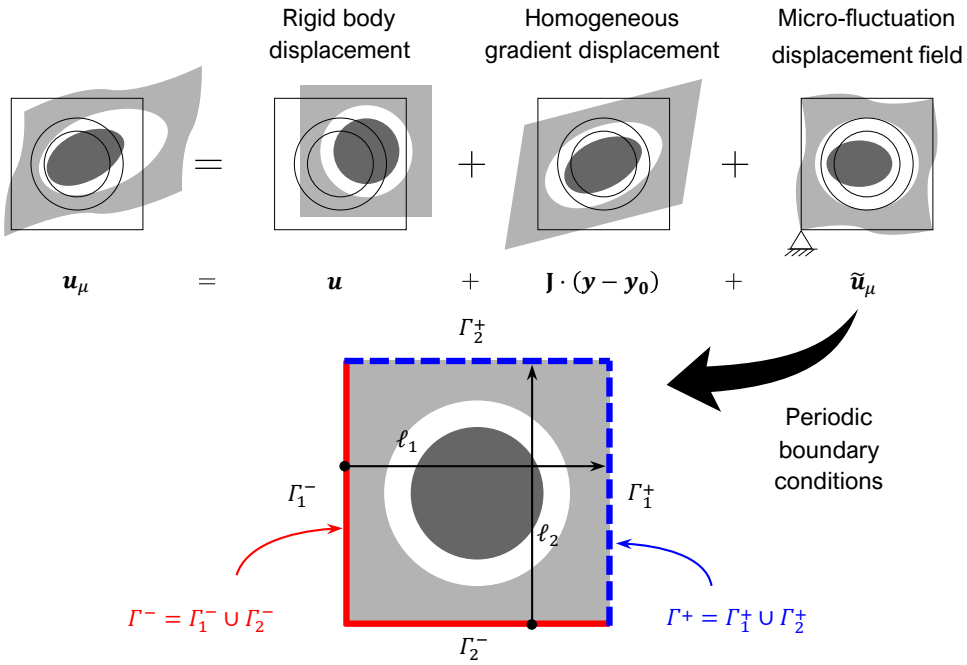

FIG. 4 Micro-displacement field components and representation of the periodic boundaries in a typical 2D square unit cell. Periodic boundary conditions can be applied in the micro-fluctuation field in order to better represent the kinematic connection in some specific problems.

FIND

$$\boldsymbol{u}_\mu(\boldsymbol{y},t) : \Omega_\mu \times [0\times T] \rightarrow \mathbb{R}^m,$$

$$\boldsymbol{\beta}(t) : [0,T] \rightarrow \mathbb{R}^m,$$

$$\boldsymbol{\gamma}(\boldsymbol{y},t) : \Gamma^{(-)} \times [0,T] \rightarrow \mathbb{R}^m$$

FULFILLING

$$\{\boldsymbol{u}_\mu,\boldsymbol{\beta},\boldsymbol{\gamma}\} = \arg\min_{\boldsymbol{u}_\mu}\max_{\boldsymbol{\beta},\boldsymbol{\gamma}}\{\Pi_\mu(\boldsymbol{u}_\mu) - \boldsymbol{\beta}\cdot\langle\boldsymbol{u}_\mu-\boldsymbol{u}\rangle_{\Omega_\mu} - \langle\boldsymbol{\gamma}\cdot([\![\boldsymbol{u}_\mu]\!]-\mathbf{J}\cdot\ell)\rangle_{\Gamma^{(-)}}\}, \tag{44}$$

where the constraint in Eq. (41) has been considered, with the optimality conditions yielding

$$\langle(\dot{\boldsymbol{p}}_\mu-\boldsymbol{\beta})\cdot\delta\boldsymbol{u}_\mu + \boldsymbol{\sigma}_\mu : \nabla_{\boldsymbol{y}}^{\mathrm{S}}\delta\boldsymbol{u}_\mu\rangle_{\Omega_\mu} - \langle\boldsymbol{\gamma}\cdot\ [\![\delta\boldsymbol{u}_\mu]\!]\rangle_{\Gamma^{(-)}} = 0, \quad \forall\,\delta\boldsymbol{u}_\mu; \tag{45}$$

$$\langle\boldsymbol{u}_\mu-\boldsymbol{u}\rangle_{\Omega_\mu}\cdot\delta\boldsymbol{\beta} = 0, \qquad \forall\,\delta\boldsymbol{\beta}; \tag{46}$$

$$\langle([\![\boldsymbol{u}_\mu]\!]-\mathbf{J}\cdot\ell)\cdot\boldsymbol{\gamma}\rangle_{\Gamma^{(-)}} = 0, \qquad \forall\,\delta\boldsymbol{\gamma}. \tag{47}$$

REMARK 5 Interestingly, one should note that the identification of $\boldsymbol{\beta}$ as the effective macro-inertia still holds in this case, as one can take $\delta\boldsymbol{u}_\mu = \boldsymbol{a}$ constant, so that $[\![\delta\boldsymbol{u}_\mu]\!] = \mathbf{0}$ and $\boldsymbol{\nabla}^{\mathrm{S}}_{\boldsymbol{y}}\delta\boldsymbol{u}_\mu = \mathbf{0}$ in Eq. (45), and still get the expression (33). As for the macro-stress, it can be related with $\boldsymbol{\gamma}$ by considering, again, $\delta\boldsymbol{u}_\mu = \mathbf{A}\cdot(\boldsymbol{y}-\boldsymbol{y}_0)$ (with $\mathbf{A}$ being a constant symmetric second-order tensor) in (45) so it finally yields

$$\langle\boldsymbol{\gamma}\otimes^{\mathrm{S}}\boldsymbol{\ell}\rangle_{\Gamma^{(-)}} = \langle\boldsymbol{\sigma}_\mu + \dot{\boldsymbol{p}}_\mu\otimes^{\mathrm{S}}(\boldsymbol{y}-\boldsymbol{y}_0)\rangle_{\Omega_\mu} = \boldsymbol{\sigma} \tag{48}$$

where $[\![\delta\boldsymbol{u}_\mu]\!] = \mathbf{A}\cdot[\![\boldsymbol{y}]\!] = \mathbf{A}\cdot\boldsymbol{\ell}$ (see Eq. (41)) has been considered.

REMARK 6 Note that, in contrast to $\boldsymbol{\lambda}$, which turned out to be constant over the RVE, thus only incorporating 3 new degrees of freedom in the extended Lagrange multipliers system, $\boldsymbol{\gamma}(\boldsymbol{y})$ has a point-wise variation in the boundary $\Gamma^{(-)}$, which translates into a large set of degrees of freedom when the system is spatially discretized. Hence, it is better, in practice, the strong-form imposition of periodic boundary conditions on $\boldsymbol{u}_\mu$ in the system of equations (45) to (47), so the *semi-restricted* saddle-point problem reads

FIND

$$\boldsymbol{u}_\mu(\boldsymbol{y},t) : \Omega_\mu\times[0,T]\to\mathbb{R}^m, \quad \text{with } \boldsymbol{u}_\mu \mid [\![\boldsymbol{u}_\mu]\!] = \mathbf{J}\cdot\boldsymbol{\ell},$$

$$\boldsymbol{\beta}(t) : [0,T]\to\mathbb{R}^m,$$

FULFILLING

$$\{\boldsymbol{u}_\mu,\boldsymbol{\beta}\} = arg\min_{\boldsymbol{u}_\mu}\max_{\boldsymbol{\beta}}\{\Pi_\mu(\boldsymbol{u}_\mu) - \boldsymbol{\beta}\cdot\langle\boldsymbol{u}_\mu-\boldsymbol{u}\rangle_{\Omega_\mu}\}. \tag{49}$$

I.3.2 Multi-scale problem resolution

In what follows, the analysis will be focused on problems that, at a macroscopic level, have the following setup:

$$\begin{aligned}
&\boldsymbol{\nabla}_x\cdot\boldsymbol{\sigma} = \dot{\boldsymbol{p}},\\
&\text{s.t.}\quad \boldsymbol{u}(\boldsymbol{x},0) = \boldsymbol{u}_0(\boldsymbol{x}), \qquad \dot{\boldsymbol{u}}(\boldsymbol{x},0) = \boldsymbol{v}_0(\boldsymbol{x}),\\
&\qquad\ \boldsymbol{u}(\boldsymbol{x},t) = \overline{\boldsymbol{u}}(\boldsymbol{x},t), \qquad \forall\,\boldsymbol{x}\in\Gamma_u,\\
&\qquad\ \boldsymbol{\sigma}(\boldsymbol{x},t)\cdot\boldsymbol{n}(\boldsymbol{x}) = \overline{\boldsymbol{t}}(\boldsymbol{x},t), \quad \forall\,\boldsymbol{x}\in\Gamma_\sigma.
\end{aligned} \tag{50}$$

where the macroscopic body forces have been neglected, $\boldsymbol{b}\approx\mathbf{0}$, and Γ_u and Γ_σ denote the boundary regions of Ω (such that $\Gamma_u\cup\Gamma_\sigma = \partial\Omega$) where displacements and tractions are prescribed, respectively.

The resolution scheme starts with the analysis of the RVE, where a Galerkin-based spatial finite element discretization has been considered, with the resulting discretized augmented system in matrix form given by

$$\begin{bmatrix} \mathbb{M}_\mu & \mathbf{0} & \mathbf{0} \\ \mathbf{0} & \mathbf{0} & \mathbf{0} \\ \mathbf{0} & \mathbf{0} & \mathbf{0} \end{bmatrix} \begin{bmatrix} \ddot{\widehat{\boldsymbol{u}}}_\mu \\ \ddot{\boldsymbol{\beta}} \\ \ddot{\boldsymbol{\lambda}} \end{bmatrix} + \begin{bmatrix} \mathbb{K}_\mu & -\mathbb{N}_\mu^{\mathrm{T}} & -\mathbb{B}_\mu^{\mathrm{T}} \\ -\mathbb{N}_\mu & \mathbf{0} & \mathbf{0} \\ -\mathbb{B}_\mu & \mathbf{0} & \mathbf{0} \end{bmatrix} \begin{bmatrix} \widehat{\boldsymbol{u}}_\mu \\ \boldsymbol{\beta} \\ \boldsymbol{\lambda} \end{bmatrix} = - \begin{bmatrix} \mathbf{0} \\ \boldsymbol{u} \\ \boldsymbol{\varepsilon} \end{bmatrix}, \tag{51}$$

where $\widehat{\boldsymbol{u}}_\mu$ stands for the vector of the micro-displacement field nodal values, $\mathbb{M}_\mu$ and $\mathbb{K}_\mu$ are the standard mass and stiffness matrices, respectively, while $\mathbb{N}_\mu$ and $\mathbb{B}_\mu$ are additional matrices, the derivation and definitions of which are detailed in Appendix I.A.

I.3.2.1 Right-hand side decomposition

To proceed with the derivation, given that the RVE system is linear, we will split it into two subsystems, each of them accounting for some part of the right-hand side of Eq. (51):

$$\begin{bmatrix} \mathbb{M}_\mu & \mathbf{0} & \mathbf{0} \\ \mathbf{0} & \mathbf{0} & \mathbf{0} \\ \mathbf{0} & \mathbf{0} & \mathbf{0} \end{bmatrix} \begin{bmatrix} \ddot{\widehat{\boldsymbol{u}}}_\mu^{(1)} \\ \ddot{\boldsymbol{\beta}}^{(1)} \\ \ddot{\boldsymbol{\lambda}}^{(1)} \end{bmatrix} + \begin{bmatrix} \mathbb{K}_\mu & -\mathbb{N}_\mu^{\mathrm{T}} & -\mathbb{B}_\mu^{\mathrm{T}} \\ -\mathbb{N}_\mu & \mathbf{0} & \mathbf{0} \\ -\mathbb{B}_\mu & \mathbf{0} & \mathbf{0} \end{bmatrix} \begin{bmatrix} \widehat{\boldsymbol{u}}_\mu^{(1)} \\ \boldsymbol{\beta}^{(1)} \\ \boldsymbol{\lambda}^{(1)} \end{bmatrix} = - \begin{bmatrix} \mathbf{0} \\ \mathbf{0} \\ \boldsymbol{\varepsilon} \end{bmatrix}, \tag{52}$$

and

$$\begin{bmatrix} \mathbb{M}_\mu & \mathbf{0} & \mathbf{0} \\ \mathbf{0} & \mathbf{0} & \mathbf{0} \\ \mathbf{0} & \mathbf{0} & \mathbf{0} \end{bmatrix} \begin{bmatrix} \ddot{\widehat{\boldsymbol{u}}}_\mu^{(2)} \\ \ddot{\boldsymbol{\beta}}^{(2)} \\ \ddot{\boldsymbol{\lambda}}^{(2)} \end{bmatrix} + \begin{bmatrix} \mathbb{K}_\mu & -\mathbb{N}_\mu^{\mathrm{T}} & -\mathbb{B}_\mu^{\mathrm{T}} \\ -\mathbb{N}_\mu & \mathbf{0} & \mathbf{0} \\ -\mathbb{B}_\mu & \mathbf{0} & \mathbf{0} \end{bmatrix} \begin{bmatrix} \widehat{\boldsymbol{u}}_\mu^{(2)} \\ \boldsymbol{\beta}^{(2)} \\ \boldsymbol{\lambda}^{(2)} \end{bmatrix} = - \begin{bmatrix} \mathbf{0} \\ \boldsymbol{u} \\ \mathbf{0} \end{bmatrix}, \tag{53}$$

so that the sum of the systems (52) and (53) returns the original system (51).

REMARK 7 The hypotheses that will be assumed here, while acceptable in a wide range of acoustic problems, will simplify the resolution approach at the cost of establishing a certain limiting frequency up to which the model is valid. It should be noted, however, that for most acoustic applications, the frequency region of interest raises up to 20 kHz, which is the typical upper bound of the human hearing range, so that higher frequencies may be considered not relevant in those contexts. This includes also, for instance, the low-frequency range at which locally resonant acoustic metamaterials typically operate, which is given by the separation of scales condition that, in this context, translates into

that macroscopic wavelengths λ must satisfy $\lambda \gg l_\mu$ [16]. This makes the proposed approach well-suited for the study and characterization of local resonance phenomena[2].

I.3.2.2 Quasi-static solution

Focusing on the subsystem (52), the hypothesis that will be assumed here is that the macroscopic strain accelerations for the tackled acoustic (elastic wave propagation) problems is small enough to consider that the RVE system behaves quasi-statically [24], that is, its inertial response is negligible ($\ddot{\boldsymbol{u}}_\mu^{(1)} \approx \mathbf{0}$). This hypothesis is supported by the separation of scales assumption, according to which $\lambda \gg \mathrm{l}_\mu$ and, therefore, macroscopic strains time evolution $\boldsymbol{\varepsilon}(\boldsymbol{x}, t)$ can be considered slow enough to not induce, by themselves, relevant microscopic acceleration $\ddot{\boldsymbol{u}}_\mu^{(1)}(\boldsymbol{y}, t)$. This, according to Eq. (33), allows us to anticipate

$$\ddot{\boldsymbol{u}}_\mu^{(1)} \approx \mathbf{0} \;\rightarrow\; \boldsymbol{\beta}^{(1)} = \langle \rho_\mu \ddot{\boldsymbol{u}}_\mu^{(1)} \rangle_{\Omega_\mu} \approx \mathbf{0}, \tag{54}$$

making us able to take out the second row and column from the system (52), yielding the classical *quasi-static system* of equations[3]

$$\begin{bmatrix} \mathbb{K}_\mu & -\mathbb{B}_\mu^{\mathrm{T}} \\ -\mathbb{B}_\mu & \mathbf{0} \end{bmatrix} \begin{bmatrix} \widehat{\boldsymbol{u}}_\mu^{(1)} \\ \boldsymbol{\lambda}^{(1)} \end{bmatrix} = - \begin{bmatrix} \mathbf{0} \\ \boldsymbol{\varepsilon} \end{bmatrix}, \tag{55}$$

which can be solved for $\boldsymbol{\lambda}^{(1)}$ giving

$$\boldsymbol{\lambda}^{(1)} = \boldsymbol{\sigma}^{(1)} = \mathbf{C}_{\min}^{\mathrm{eff}} : \boldsymbol{\varepsilon} \tag{56}$$

where $\mathbf{C}_{\min}^{\mathrm{eff}}$ is the classical elastic effective (homogenized) and quasi-static constitutive tensor.

---

[2] In addition, in the considered acoustic homogenization settings, the microscopic cells will exhibit at least two symmetry axes and the inertial component of the macroscopic stresses, $\langle \rho_\mu \ddot{\boldsymbol{u}}_\mu(\boldsymbol{y}, t) \otimes^{\mathrm{S}} (\boldsymbol{y} - \boldsymbol{y}_0) \rangle_{\Omega_\mu}$, is exactly equal to zero. Therefore, this term will be neglected in what follows.

[3] Where, under the hypothesis of infinitesimal microfluctuation field, $\tilde{\boldsymbol{u}}_\mu^{(1)} \approx \mathbf{0}$, and for the considered case $\mathbf{u} = \mathbf{0}$, the remaining condition, in Eq. (52), $\mathbb{N}_\mu \widehat{\boldsymbol{u}}_\mu^{(1)} = \langle \boldsymbol{u}_\mu^{(1)} \rangle_{\Omega_\mu} = \langle \boldsymbol{u} + \boldsymbol{\varepsilon} \cdot (\boldsymbol{y} - \boldsymbol{y}_0) + \tilde{\boldsymbol{u}}_\mu^{(1)} \rangle_{\Omega_\mu} = \langle \tilde{\boldsymbol{u}}_\mu^{(1)} \rangle_{\Omega_\mu} \approx \mathbf{0}$ is automatically fulfilled.

REMARK 8 For the case of applying periodic boundary conditions, as mentioned in Section I.3.1, the variable $\boldsymbol{\lambda}^{(1)}$ is withdrawn from equation (55) and periodic boundary conditions are directly applied on $\widehat{\boldsymbol{u}}_{\mu}^{(1)}$, leading to

$$\mathbb{K}_{\mu}^{*}\widehat{\boldsymbol{u}}_{\mu}^{*(1)} = -\mathbb{S}^{\mathrm{T}}\boldsymbol{\varepsilon}. \tag{57}$$

$$\boldsymbol{\sigma}^{(1)} = \mathbf{C}_{\mathrm{per}}^{\mathrm{eff}} : \boldsymbol{\varepsilon}. \tag{58}$$

Details on the resolution of the systems (55) and (57) and the computation of $\mathbf{C}_{\mathrm{min}}^{\mathrm{eff}}$ and $\mathbf{C}_{\mathrm{per}}^{\mathrm{eff}}$ can be found in Appendix I.B.2.

I.3.2.3 Inertial solution

As for the subsystem (53), since only small displacements $\boldsymbol{u}$ appear on the right-hand side as driving actions, the following assumption is made[4]

$$\boldsymbol{\lambda}^{(2)} \approx \mathbf{0}. \tag{59}$$

Similarly to the previous case, this hypothesis allows us to remove the third row and column from the system (53), which results in what is called here the *inertial system* of equations[5]

$$\begin{bmatrix} \mathbb{M}_{\mu} & \mathbf{0} \\ \mathbf{0} & \mathbf{0} \end{bmatrix}\begin{bmatrix} \ddot{\widehat{\boldsymbol{u}}}_{\mu}^{(2)} \\ \ddot{\boldsymbol{\beta}}^{(2)} \end{bmatrix} + \begin{bmatrix} \mathbb{K}_{\mu} & -\mathbb{N}_{\mu}^{\mathrm{T}} \\ -\mathbb{N}_{\mu} & \mathbf{0} \end{bmatrix}\begin{bmatrix} \widehat{\boldsymbol{u}}_{\mu}^{(2)} \\ \boldsymbol{\beta}^{(2)} \end{bmatrix} = -\begin{bmatrix} \mathbf{0} \\ \boldsymbol{u} \end{bmatrix} \tag{60}$$

The variable $\boldsymbol{\beta}^{(2)}$ can be condensed out in Eq. (60) giving rise to the system

$$\mathbb{M}_{\mu}^{*}\ddot{\widehat{\boldsymbol{u}}}_{\mu}^{*} + \mathbb{K}_{\mu}^{*}\widehat{\boldsymbol{u}}_{\mu}^{*} = -\mathbb{D}^{\mathrm{T}}\ddot{\boldsymbol{u}}, \tag{61}$$

where $\widehat{\boldsymbol{u}}_{\mu}^{*}$ stands for the vector of nodal values of a fluctuation-like field, $\mathbb{D}$ can be regarded as a *density-like* matrix coupling the micro and macro accelerations, while $\mathbb{M}_{\mu}^{*}$ and $\mathbb{K}_{\mu}^{*}$ are, respectively, the mass and stiffness matrices that one obtains after condensing the restrictions in system (60). Details on the derivations of these terms are given in Appendix I.B.3. From now on, we will refer to system (61) as the *restricted inertial*

---

[4] Since, under the assumption that the microfluctuation gradient is infinitesimal, $\boldsymbol{\nabla}_{\boldsymbol{y}}^{\mathrm{S}}\tilde{\boldsymbol{u}}_{\mu}^{(2)} \approx \mathbf{0}$, then, for $\boldsymbol{\varepsilon} = \mathbf{0}$, $\boldsymbol{\varepsilon}_{\mu}^{(2)} = \boldsymbol{\varepsilon} + \boldsymbol{\nabla}_{\boldsymbol{y}}^{\mathrm{S}}\tilde{\boldsymbol{u}}_{\mu}^{(2)} \approx \mathbf{0}$, and $\boldsymbol{\sigma}_{\mu}^{(2)} = \mathbf{C}_{\mu} : \boldsymbol{\varepsilon}_{\mu}^{(2)} \approx \mathbf{0}$. Thus $\boldsymbol{\lambda}^{(2)} \approx \langle \boldsymbol{\sigma}_{\mu}^{(2)} \rangle_{\Omega_{\mu}} \approx \mathbf{0}$.

[5] Where, the additional condition, in Eq. (53), $\mathbb{B}_{\mu}\widehat{\boldsymbol{u}}_{\mu}^{(2)} = \langle \boldsymbol{\varepsilon}_{\mu}^{(2)} \rangle_{\Omega_{\mu}} \approx \mathbf{0}$, is automatically fulfilled from the assumption of infinitesimal microfluctuation gradient.

system. It should be noted that expressions obtained in this case apply disregard periodic boundary conditions are considered or not (the only difference is in how the matrices involved are defined, which is explained in more detail in Appendix I.B.3.

As for the resulting macroscopic inertial force, it reads

$$\boldsymbol{\beta}^{(2)} = \overline{\mathbf{R}} \cdot \ddot{\boldsymbol{u}} + \mathbb{D}\ddot{\hat{\boldsymbol{u}}}^{*}_{\mu}, \tag{62}$$

where $\overline{\mathbf{R}}$ is the effective average density tensor that, as explained in Appendix I.B.3, for some specific cases, $\overline{\mathbf{R}} = \bar{\rho}\mathbf{I}$, and $\overline{\mathbf{R}} \cdot \ddot{\boldsymbol{u}} = \bar{\rho}\ddot{\boldsymbol{u}}$ with $\bar{\rho}$ being the RVE average density,

$$\bar{\rho} = \langle \rho_{\mu} \rangle_{\Omega_{\mu}}. \tag{63}$$

REMARK 9 Note that, according to Eq. (62), we can identify a component in the homogenized inertial force that accounts for its own macroscopic acceleration, $\overline{\mathbf{R}} \cdot \ddot{\boldsymbol{u}}$, and an additional inertial term, $\mathbb{D}\ddot{\hat{\boldsymbol{u}}}^{*}_{\mu}$ (coupled micro-macro inertial forces), that arises from the density-like matrix, $\mathbb{D}$, and the micro-fluctuation acceleration field, $\ddot{\hat{\boldsymbol{u}}}^{*}_{\mu}$, stemming from the solution to the RVE Eq. (61). We anticipate that local resonance phenomena result from the mutual cancellation of both these terms, giving rise to unusual dynamic properties, such as the *frequency bandgaps*, that will be tackled in Section I.4.

I.3.3 Modal analysis

I.3.3.1 Micro-inertial problem projection onto the restricted system modes

The hypotheses made in the resolution of the global RVE system have allowed us to isolate the inertial contribution of the micro-fluctuation field that is transferred to the macroscale in Eq. (61). Now, in order to allow for a better interpretation of the dynamic role that $\ddot{\hat{\boldsymbol{u}}}^{*}_{\mu}$ plays in the macroscale, it will be useful to consider the generalized eigenvalue problem of the restricted system $\mathbb{K}^{*}_{\mu} - \mathbb{M}^{*}_{\mu}$ defined as

FIND

$$\boldsymbol{\Phi}^{*}_{\mu} = [\widehat{\boldsymbol{\phi}}^{*(1)}_{\mu} \quad \dots \quad \widehat{\boldsymbol{\phi}}^{*(N)}_{\mu}] \tag{64}$$

$$\boldsymbol{\Lambda}^{*} = [\lambda^{*(1)} \quad \dots \quad \lambda^{*(N)}]^{\mathrm{T}} \tag{65}$$

FULFILLING

$$\left(\mathbb{K}_{\mu}^{*} - \lambda^{*(k)}\mathbb{M}_{\mu}^{*}\right)\widehat{\boldsymbol{\phi}}^{*(k)} = \mathbf{0}, \qquad \widehat{\boldsymbol{\phi}}_{\mu}^{*(k)\mathrm{T}}\mathbb{M}_{\mu}^{*}\widehat{\boldsymbol{\phi}}_{\mu}^{*(k)} = 1 \tag{66}$$

where the second equation (66) simply indicates that the eigenmodes are mass-normalized.

For the specific case of a dynamic system, each eigenvalue $\lambda^{*(k)}$ can be identified as the squared natural frequency $\omega_{\mu}^{*(k)2}$ ($\lambda^{*(k)} = \omega_{\mu}^{*(k)2}$), with $\widehat{\boldsymbol{\phi}}_{\mu}^{*(k)}$ being the k-th natural vibration mode, fulfilling

$$\boldsymbol{\Phi}_{\mu}^{*\mathrm{T}}\mathbb{M}_{\mu}^{*}\boldsymbol{\Phi}_{\mu}^{*} = \mathbf{I} \quad \text{and} \quad \boldsymbol{\Phi}_{\mu}^{*\mathrm{T}}\,\mathbb{K}_{\mu}^{*}\boldsymbol{\Phi}_{\mu}^{*} = \boldsymbol{\Omega}_{\mu}^{*2}, \tag{67}$$

$$\boldsymbol{\Omega}_{\mu}^{*} = \mathrm{diag}[\omega_{\mu}^{*(1)} \quad \ldots \quad \omega_{\mu}^{*(N)}], \tag{68}$$

where $\boldsymbol{\Omega}_{\mu}^{*}$ is a diagonal matrix containing the natural frequencies, $\omega_{\mu}^{*(k)}$, of the restricted system.

Now, the solution $\widehat{\boldsymbol{u}}_{\mu}^{*}$ can be projected onto the space spanned by the eigenmodes $\boldsymbol{\Phi}_{\mu}^{*}$ as

$$\widehat{\boldsymbol{u}}_{\mu}^{*} = \sum_{k} \widehat{\boldsymbol{\phi}}_{\mu}^{*(k)} q_{\mu}^{*(k)} = \boldsymbol{\Phi}_{\mu}^{*}\boldsymbol{q}_{\mu}^{*}, \tag{69}$$

where $\boldsymbol{q}_{\mu}^{*}$ is the column vector of modal amplitudes, $q_{\mu}^{*(k)}$, for the restricted system. Note that this decomposition does not imply any additional simplifications as long as we consider k ranging from 1 to the total number of degrees of freedom of the system (61).

Additionally, Eq. (61) can be also projected onto the whole set of its mass-normalized natural vibration modes, yielding

$$\boldsymbol{\Phi}_{\mu}^{*\mathrm{T}}\mathbb{M}_{\mu}^{*}\boldsymbol{\Phi}_{\mu}^{*}\ddot{\boldsymbol{q}}_{\mu}^{*} + \boldsymbol{\Phi}_{\mu}^{*\mathrm{T}}\mathbb{K}_{\mu}^{*}\boldsymbol{\Phi}_{\mu}^{*}\boldsymbol{q}_{\mu}^{*} = -\boldsymbol{\Phi}_{\mu}^{*\mathrm{T}}\mathbb{D}^{\mathrm{T}}\ddot{\boldsymbol{u}}, \tag{70}$$

which, taking into account Eq. (67), results

$$\boldsymbol{\Omega}_{\mu}^{*2}\boldsymbol{q}_{\mu}^{*} + \ddot{\boldsymbol{q}}_{\mu}^{*} = -\mathbb{Q}^{\mathrm{T}}\ddot{\boldsymbol{u}}, \tag{71}$$

with $\mathbb{Q}$ being the from now on called *coupling matrix*

$$\mathbb{Q} = \mathbb{D}\boldsymbol{\Phi}_{\mu}^{*}. \tag{72}$$

Note also that, by introducing expression (69) into Eq. (62), we obtain

$$\boldsymbol{\beta}^{(2)} = \overline{\mathbf{R}} \cdot \ddot{\boldsymbol{u}} + \mathbb{Q}\ddot{\boldsymbol{q}}_{\mu}^{*}. \tag{73}$$

The system of equations (71) turns out to be uncoupled for every degree of freedom $q_{\mu}^{(k)}$, which facilitates the physical and mathematical interpretation of the solution.

Precedent settings in which the RVE problem is projected onto the natural modes of the RVE can be found, in the context of Bloch-Floquet theory, in [25]. However, the specific issue in the present approach is that it allows discrimination of the projection relevant modes on the basis of the information provided by the coupling matrix in Eq. (72), similarly to what is done in [16].

I.3.3.2 Micro-inertial problem projection onto the unrestricted system modes

By considering the generalized eigenvalue problem, but now in terms of the *unrestricted* system $\mathbb{K}_{\mu} - \mathbb{M}_{\mu}$ in the first equation (60), i.e.

$$\mathbb{M}_{\mu}\ddot{\widehat{\boldsymbol{u}}}_{\mu} + \mathbb{K}_{\mu}\widehat{\boldsymbol{u}}_{\mu} = \mathbf{0}, \tag{74}$$

one may find also the natural frequencies and the mass-normalized vibration modes matrices, in this case reading $\boldsymbol{\Omega}_{\mu}$ and $\boldsymbol{\Phi}_{\mu}$, respectively.

Again, the solution field $\widehat{\boldsymbol{u}}_{\mu}^{(2)}$ to problem (60) can be alternatively projected onto the space spanned by the unrestricted system eigenmodes, $\boldsymbol{\Phi}_{\mu}$, as

$$\widehat{\boldsymbol{u}}_{\mu}^{(2)} = \boldsymbol{\Phi}_{\mu}\boldsymbol{q}_{\mu}, \tag{75}$$

so

$$\begin{bmatrix} \mathbf{I} & \mathbf{0} \\ \mathbf{0} & \mathbf{0} \end{bmatrix} \begin{bmatrix} \ddot{\boldsymbol{q}}_{\mu} \\ \ddot{\boldsymbol{\beta}}^{(2)} \end{bmatrix} + \begin{bmatrix} \boldsymbol{\Omega}_{\mu}^{2} & -\boldsymbol{\Phi}_{\mu}^{\mathrm{T}}\mathbb{N}_{\mu}^{\mathrm{T}} \\ -\mathbb{N}_{\mu}\boldsymbol{\Phi}_{\mu} & \mathbf{0} \end{bmatrix} \begin{bmatrix} \boldsymbol{q}_{\mu} \\ \boldsymbol{\beta}^{(2)} \end{bmatrix} = - \begin{bmatrix} \mathbf{0} \\ \boldsymbol{u} \end{bmatrix}. \tag{76}$$

This alternative system projection will be useful to tackle the dynamic effects of the RVE system.

I.3.3.3 Micro-inertial system reduction

Let's now focus on the optimization of the computational cost of the problem. For these purposes, we will use a procedure that could be inserted into the so-called Reduced

Order Model (ROM) techniques. The goal is to solve the problem in an optimal low-dimension sub-space spanned by the most relevant modes [26].

> REMARK 10 Note that the system (71) has, in principle, as much degrees of freedom as $\widehat{\boldsymbol{u}}_{\mu}^{(2)}$ in the original system. However, as the coupling matrix $\mathbb{Q}$ in Eq. (73) reveals, not all the natural vibration modes will have the same effect on the macroscale. In particular, the relative importance of each mode k can be assessed by its corresponding column, $\boldsymbol{Q}^{(k)}$, in the coupling matrix $\mathbb{Q}$, allowing us to determine the set of relevant modes as those whose associated column, $\boldsymbol{Q}^{(k)}$, is not negligible. The setting proposed here automatically yields a reduced order model of the microscale RVE problem, i.e. based on the projection of the FE problem in Eq. (60) on the space spanned by the relevant resonant RVE modes. As it will be seen in Section I.4, the number of required modes (RVE degrees of freedom) is enormously reduced in comparison to the original FE element problem, this leading to a substantial reduction of the multiscale analysis computational cost.

Since the modal amplitudes $\boldsymbol{q}_{\mu}^{*}$ in the system (71) are uncoupled, a first reduction can be performed retaining only the relevant modes and amplitudes ($\widehat{\boldsymbol{\phi}}_{\mu}^{*(k)}$, $q_{\mu}^{*(k)}$) in both the system (71) and their corresponding columns in $\mathbb{Q}$.

Additionally, as pointed out in Remark 7, in the particular context of acoustic problems, one could perform this reduction considering also that the macroscopic frequency range of interest is restricted to a certain set below a limiting frequency ω_{lim}. This makes all the relevant modes associated to higher natural frequencies not interesting in this framework allowing us to remove also their corresponding degrees of freedom from the system. In this regard, this approach is, for instance, especially well-suited for the analysis of locally resonant acoustic metamaterials, as it will be seen in the examples in Section I.4, where this *computational cost reduction strategy* will be applied.

I.3.4 Homogenized macroscale problem

I.3.4.1 General model

With the hypotheses considered for the RVE system resolution (see Sections I.3.2.2 and I.3.2.3), including the micro-inertial system modal projection, we obtain, as effective macroscopic inertial force and stress,

$$\dot{\boldsymbol{p}}(\boldsymbol{x},t) = \boldsymbol{\beta}^{(1)}(\boldsymbol{x},t) + \boldsymbol{\beta}^{(2)}(\boldsymbol{x},t) \approx \boldsymbol{\beta}^{(2)}(\boldsymbol{x},t) = \overline{\mathbf{R}} \cdot \ddot{\boldsymbol{u}}(\boldsymbol{x},t) + \mathbb{Q}\ddot{\boldsymbol{q}}_{\mu}^{*}(\boldsymbol{x},t), \tag{77}$$

$$\boldsymbol{\sigma}(\boldsymbol{x},t) = \boldsymbol{\lambda}^{(1)}(\boldsymbol{x},t) + \boldsymbol{\lambda}^{(2)}(\boldsymbol{x},t) \approx \boldsymbol{\lambda}^{(1)}(\boldsymbol{x},t) = \mathbf{C}^{\text{eff}} : \boldsymbol{\nabla}_{\boldsymbol{x}}^{\text{S}}\boldsymbol{u}(\boldsymbol{x},t), \tag{78}$$

where Eqs. (54) and (59) have been considered.

Introducing the previous expressions into the macroscale equation (50) yields the general homogenized equivalent problem

Macroscopic problem:

$$\boldsymbol{\nabla}_{\boldsymbol{x}} \cdot (\mathbf{C}^{\text{eff}} : \boldsymbol{\nabla}_{\boldsymbol{x}}^{\text{S}}\boldsymbol{u}) = (\dot{\boldsymbol{p}} \approx \boldsymbol{\beta}^{(2)}) = \overline{\mathbf{R}} \cdot \ddot{\boldsymbol{u}} + \mathbb{Q}\ddot{\boldsymbol{q}}_{\mu}^{*}, \tag{79}$$

Microscopic problem:

$$\ddot{\boldsymbol{q}}_{\mu}^{*} + \boldsymbol{\Omega}_{\mu}^{*2}\boldsymbol{q}_{\mu}^{*} = -\mathbb{Q}^{\text{T}}\ddot{\boldsymbol{u}}. \tag{80}$$

Eqs. (79) and (80) constitute a coupled system of equations which allows for solving the macroscopic and microscopic unknowns $\boldsymbol{u}$ and $\boldsymbol{q}_{\mu}^{*}$, respectively.

BOX 1 Algorithm for the resolution of the multiscale homogenized acoustic problem

Data:

- Frequency range of interest: $[\omega_0, \omega_{\text{lim}}]$
- Unit cell finite element discretization results:

Mass matrix:	$\mathbb{M}_{\mu}$	→ Eq. (A.20)
Stiffness matrix:	$\mathbb{K}_{\mu}$	→ Eq. (A.21)
Restrictions matrices:	$\mathbb{N}_{\mu}$	→ Eq. (A.22)
	$\mathbb{B}_{\mu}$	→ Eq. (A.23)
Additional matrices:	$\mathbb{I}$	→ Eq. (B.25)
	$\mathbb{Y}$	→ Eq. (B.26)

Determine the homogenized mechanical and inertial properties (homogenization):

- Apply periodic boundary conditions?

→ No

- Compute matrix: $\mathbb{T} = \mathbf{I}$
- Compute effective constitutive tensor: $\mathbf{C}_{\text{min}}^{\text{eff}}$ → Eq. (B.12)

→ Yes

- Compute matrix: $\mathbb{P}$ → Eq. (B.3)
  $\mathbb{L}_{\varepsilon}$ → Eq. (B.4)
  $\mathbb{L}_{\theta}$ → Eq. (B.5)
  $\mathbb{T} = \mathbb{P}$
- Compute effective constitutive tensor: $\mathbf{C}_{per}^{\text{eff}}$ → Eq. (B.22)

BOX 1 Algorithm for the resolution of the multiscale homogenized acoustic problem

- Compute matrices for the inertia problem:
  Restricted mass matrix: $\mathbb{M}_\mu^*$ → Eq. (B.38)
  Restricted stiffness matrix: $\mathbb{K}_\mu^*$ → Eq. (B.37)
  Average density tensor: $\overline{\boldsymbol{R}}$ → Eq. (B.34)
  Density-like matrix: $\mathbb{D}$ → Eq. (B.35)
- Modal analysis of the restricted RVE system:

$$(\mathbb{K}_\mu^* - \omega_\mu^{*2}\mathbb{M}_\mu^*)\widehat{\boldsymbol{\phi}}_\mu^* = \mathbf{0} \quad \rightarrow \quad \boldsymbol{\Omega}_\mu^{*2}, \boldsymbol{\Phi}_\mu^*$$

- Retain only relevant modes and frequencies:

$$\omega_\mu^{*(k)}, \widehat{\boldsymbol{\phi}}_\mu^{*(k)} \mid \left\| \mathbb{D}\widehat{\boldsymbol{\phi}}_\mu^{*(k)} \right\| > \delta_{\text{tol}} \quad \text{and} \quad \omega_\mu^{*(k)} < \omega_{\text{lim}} \tag{81}$$

- Compute coupling matrix: $\mathbb{Q} = \mathbb{D}\boldsymbol{\Phi}_\mu^*$

Solve the coupled macro-micro acoustic problem (FE discretization of Eqs. (79) and (80)):

$$\begin{bmatrix} \mathbb{M}_{\text{uu}} & \mathbb{M}_{\text{uq}} \\ \mathbb{M}_{\text{qu}} & \mathbb{M}_{\text{qq}} \end{bmatrix} \begin{bmatrix} \ddot{\widehat{\boldsymbol{u}}} \\ \ddot{\widehat{\boldsymbol{q}}} \end{bmatrix} + \begin{bmatrix} \mathbb{K}_{\text{uu}} & \mathbf{0} \\ \mathbf{0} & \mathbb{K}_{\text{qq}} \end{bmatrix} \begin{bmatrix} \widehat{\boldsymbol{u}} \\ \widehat{\boldsymbol{q}} \end{bmatrix} = \begin{bmatrix} \hat{\boldsymbol{f}} \\ \mathbf{0} \end{bmatrix}$$

I.3.4.2 A model for the ideal wave propagation problem

Note that the formulation presented so far is general within the hypotheses assumed for the RVE system resolution. In the particular framework of acoustic problems, we will consider wave-like solutions of the kind

$$\boldsymbol{u}(\boldsymbol{x}, t) = \boldsymbol{U}(\boldsymbol{\kappa} \cdot \boldsymbol{x} - \omega t), \tag{82}$$

where $\mathbf{U}$ is the amplitude function, ω is the angular frequency (time frequency). In Eq. (82), $\boldsymbol{\kappa} = \kappa \boldsymbol{n}_\kappa$ is the wavevector, where $\boldsymbol{n}_\kappa$ gives the propagation direction and κ the corresponding wavenumber (spatial frequency), which is in turn related with the wavelength according to $\kappa = 2\pi/\lambda$. The simplest representation of a plane wave of constant frequency ω and propagation direction $\boldsymbol{n}_\kappa$ travelling along a macroscopic infinite structure comes from expressing $\boldsymbol{u}$ as a harmonic function, typically formulated in the complex numbers space as

$$\boldsymbol{u}(\boldsymbol{x}, t) = \boldsymbol{U} e^{i(\kappa \boldsymbol{n}_\kappa \cdot \boldsymbol{x} - \omega t)}, \tag{83}$$

with

$$\ddot{\boldsymbol{u}}(\boldsymbol{x}, t) = -\omega^2 \boldsymbol{U} e^{i(\kappa \boldsymbol{n}_\kappa \cdot \boldsymbol{x} - \omega t)}, \tag{84}$$

$$\nabla_x^{\mathrm{S}} \boldsymbol{u}(x,t) = i\kappa \boldsymbol{n}_\kappa \otimes^{\mathrm{S}} \boldsymbol{U} e^{i(\kappa \boldsymbol{n}_\kappa \cdot \boldsymbol{x} - \omega t)}, \tag{85}$$

where, for the sake of simplicity, the amplitude vector $\boldsymbol{U} \in \mathbb{R}^m$ has been assumed constant.

REMARK 11 It has to be emphasized that the type of waves in Eqs. (83) to (85) can only be the solution of *ideal* wave propagation problems, typically: waves propagating in an *infinite* and *homogeneous* medium with the propagating wave not being affected by boundary conditions (reflected waves, etc.). This is what we term here as *ideal* wave propagation problem.

In this context, we look for solutions of the microscale problem with modal amplitudes vectors $\boldsymbol{q}_\mu^*$ behaving as harmonic oscillators with the excitation macroscopic frequency ω, thus satisfying

$$\ddot{\boldsymbol{q}}_\mu^*(t,\omega) = -\omega^2 \boldsymbol{q}_\mu^*(t,\omega), \tag{86}$$

whose general solution is $\boldsymbol{q}_\mu^* = \boldsymbol{Q}_\mu^* e^{-i\omega t}$.

By replacing expression (86) into Eq. (80), allows us to solve the unknowns $\boldsymbol{q}_\mu^*$ in the RVE as

$$\boldsymbol{q}_\mu^*(t,\omega) = (\omega^2 \mathbf{I} - \boldsymbol{\Omega}_\mu^{*2})^{-1} \mathbb{Q}^{\mathrm{T}} \ddot{\boldsymbol{u}}(\boldsymbol{x},t), \tag{87}$$

which can be transferred to the macroscale (by replacing Eq. (87) in Eq. (79)), yielding

$$\nabla_x \cdot (\mathbf{C}^{\mathrm{eff}} : \nabla_x^{\mathrm{S}} \boldsymbol{u}) = (\dot{\boldsymbol{p}} \approx \boldsymbol{\beta}^{(2)}) = \mathbf{R}^{\mathrm{eff}}(\omega) \cdot \ddot{\boldsymbol{u}}, \tag{88}$$

$$\mathbf{R}^{\mathrm{eff}}(\omega) = \overline{\mathbf{R}} + \tilde{\mathbf{R}}(\omega); \;\; \tilde{\mathbf{R}}(\omega) = \mathbb{Q}\left(\boldsymbol{\Omega}_\mu^{*2}/\omega^2 - \mathbf{I}\right)^{-1} \mathbb{Q}^{\mathrm{T}}, \tag{89}$$

where $\overline{\mathbf{R}}$ is the effective average density tensor defined in Appendix I.B.3 and $\mathbf{R}^{\mathrm{eff}}$ assumes the role of an effective, frequency dependent pseudo-density tensor.

Note also that expression (88) has the format of a wave equation for which Eq. (83) is expected to be a solution. In fact, replacing solutions of such kind into Eq. (88), one obtains the so-called dispersion relation:

$$\mathbf{D}(\omega,\kappa)\widehat{\boldsymbol{U}} = \left[\boldsymbol{n}_\kappa^{\mathrm{T}} \mathbf{C}^{\mathrm{eff}} \boldsymbol{n}_\kappa - \left(\frac{\omega}{\kappa}\right)^2 \mathbf{R}^{\mathrm{eff}}(\omega)\right] \widehat{\boldsymbol{U}} = \mathbf{0}. \tag{90}$$

Eq. (90) provides, for a given pair $(\omega,\ \boldsymbol{n}_\kappa)$, the corresponding wavenumber κ and amplitude unit vector $\widehat{\boldsymbol{U}}$, as a result of a standard eigenvalues and eigenvectors problem. It is worth noting that precedent and somehow alternative settings can be found for fast computation of dispersion properties of materials, in the context of Bloch-Floquet theory, in [27–29]. However, in this work, the goal is not a detailed comparison of different methods but to establish and assess a variational based hierarchical homogenization procedure suitable for computational modelling of real 2D and 3D acoustic problems.

Note that, in general, we cannot guarantee that $\mathbf{R}^{\text{eff}}(\omega)$ is positive definite for any frequency ω. In particular:

(a) For excitation frequencies ω equal to a natural frequency of the *unrestricted* system (74), $\omega = \omega_\mu^{(n)}$, one may consider $\ddot{\boldsymbol{q}}_\mu = -\omega^2 \boldsymbol{q}_\mu$ in Eq. (76) and solve for $\boldsymbol{\beta}^{(2)}$ yielding

$$\sum_k \frac{\left(\mathbb{N}_\mu \widehat{\boldsymbol{\phi}}_\mu^{(k)}\right)\left(\mathbb{N}_\mu \widehat{\boldsymbol{\phi}}_\mu^{(k)}\right)^{\mathrm{T}}}{\omega_\mu^{(k)2} - \omega}\boldsymbol{\beta}^{(2)} = \boldsymbol{U} e^{i(\kappa \boldsymbol{n}_\kappa \cdot \boldsymbol{x} - \omega t)}. \tag{91}$$

Now, multiplying both sides of Eq. (91) by $\omega_\mu^{(n)2} - \omega^2$ and taking the limit for $\omega \to \omega_\mu^{(n)}$ it yields

$$\left(\mathbb{N}_\mu \widehat{\boldsymbol{\phi}}_\mu^{(n)}\right)\left(\mathbb{N}_\mu \widehat{\boldsymbol{\phi}}_\mu^{(n)}\right)^{\mathrm{T}}\boldsymbol{\beta}^{(2)} = \mathbf{0}. \tag{92}$$

As long as $\widehat{\boldsymbol{\phi}}_\mu^{(n)} \notin \ker \mathbb{N}_\mu$, Eq. (92) yields $\boldsymbol{\beta}^{(2)} = \mathbf{0}$ disregard the value of $\boldsymbol{U}$. Recalling that, in this considered *ideal* case, the macroscopic inertial force is given by (see Eq. (88))

$$\boldsymbol{\beta}^{(2)} = \mathbf{R}^{\text{eff}} \cdot \ddot{\boldsymbol{u}} = -\omega^2 \mathbf{R}^{\text{eff}}(\omega) \cdot \boldsymbol{U} e^{i(\kappa \boldsymbol{n}_\kappa \cdot \boldsymbol{x} - \omega t)} = \mathbf{0}, \tag{93}$$

$\forall\, \boldsymbol{U}$, it yields

$$\mathbf{R}^{\text{eff}} = \mathbf{0}. \tag{94}$$

This means that, at excitation frequencies, ω, equal to some *natural frequencies of the unrestricted* system, $\omega_\mu^{(n)}$, the matrix $\mathbf{R}^{\text{eff}}$ becomes null and, therefore, the macroscopic problem (79) becomes quasi-static. In addition, by replacing this condition into Eq. (90), it yields $\kappa = 0$ and then $\lambda = 2\pi/\kappa \to \infty$.

(b) For excitation frequencies ω approaching to a natural frequency of the *restricted* system (61), $\omega \to \omega_\mu^{*(n)}$, Eq. (89) expressed in index notation reveals

$$R_{ij}^{\text{eff}}(\omega) = \bar{R}_{ij} + \sum_k \frac{Q_{ik}Q_{jk}}{\left(\omega_\mu^{*(k)}/\omega\right)^2 - 1}, \tag{95}$$

Now, with regard to matrix $\mathbf{D}$ in Eq. (90), we consider the following possible situations:

(b1) $\omega \to \omega_\mu^{*(n)}$ *from the left* ($\omega \lesssim \omega_\mu^{*(n)}$),

$$\begin{aligned} R_{ij}^{\text{eff}} \to +\infty \to &\text{ matrix } \mathbf{D} \text{ is positive-definite,} \\ \to &\ \kappa \in \mathbb{R} \text{ with } \kappa \to \infty. \end{aligned} \tag{96}$$

(b2) $\omega \to \omega_\mu^{*(n)}$ *from the right* ($\omega \gtrsim \omega_\mu^{*(n)}$),

$$\begin{aligned} R_{ij}^{\text{eff}} \to -\infty \to &\text{ matrix } \mathbf{D} \text{ is negative-definite,} \\ \to &\ \kappa \in \mathbb{C} \text{ with } \begin{matrix} \text{Im}(\kappa) \to \infty \\ \text{Re}(\kappa) = 0 \end{matrix}. \end{aligned} \tag{97}$$

This means that, at excitation frequencies, ω, equal to some *natural frequencies of the restricted* system, $\omega_\mu^{*(n)}$, some components of the pseudo-density tensor, $\mathbf{R}^{\text{eff}}$, pass from $-\infty$ to $+\infty$ and the wavenumber κ passes from real-valued to imaginary-valued.

REMARK 12 It should be noted that in case (b2) (or, in general, for any purely imaginary κ), the complex character of the wavenumber κ makes Eq. (83) to become

$$\boldsymbol{u}(\boldsymbol{x}, t) = \boldsymbol{A}(\boldsymbol{x})e^{-i\omega t};\ \boldsymbol{A}(\boldsymbol{x}) = \boldsymbol{U}e^{-|\kappa|\boldsymbol{n}_\kappa \cdot \boldsymbol{x}} \tag{98}$$

where $\boldsymbol{A}(\boldsymbol{x})$ implies an amplitude decay in the propagation direction (the wave amplitude decreases as the wave advances).

As a consequence of the previous considerations, one could identify frequency intervals bounded by natural frequencies of the restricted and unrestricted problems, $[\omega_\mu^*,\ \omega_\mu]$, where the effective pseudo-density matrix, $\mathbf{R}^{\text{eff}}$, becomes unbounded and negative-definite (at the beginning of the interval) and it subsequently evolves to $\mathbf{R}^{\text{eff}} = \mathbf{0}$ (at the end of the interval), while the wavenumber κ remains imaginary-valued.

In addition, $[\omega_\mu^*,\ \omega_\mu]$ defines a band of incidental frequencies where the macroscopic wave gets progressively attenuated, due to local resonance phenomena, as it advances in the infinite medium according to Eq. (98). This corresponds to the so-called frequency bandgaps [30].

The specific determination of the band-gap positions in the frequency domain can only be *analytically* obtained for the considered ideal problem (infinite and homogeneous media). Otherwise, one should resort to numerical solutions (see Section I.4 for examples illustrating such behavior).

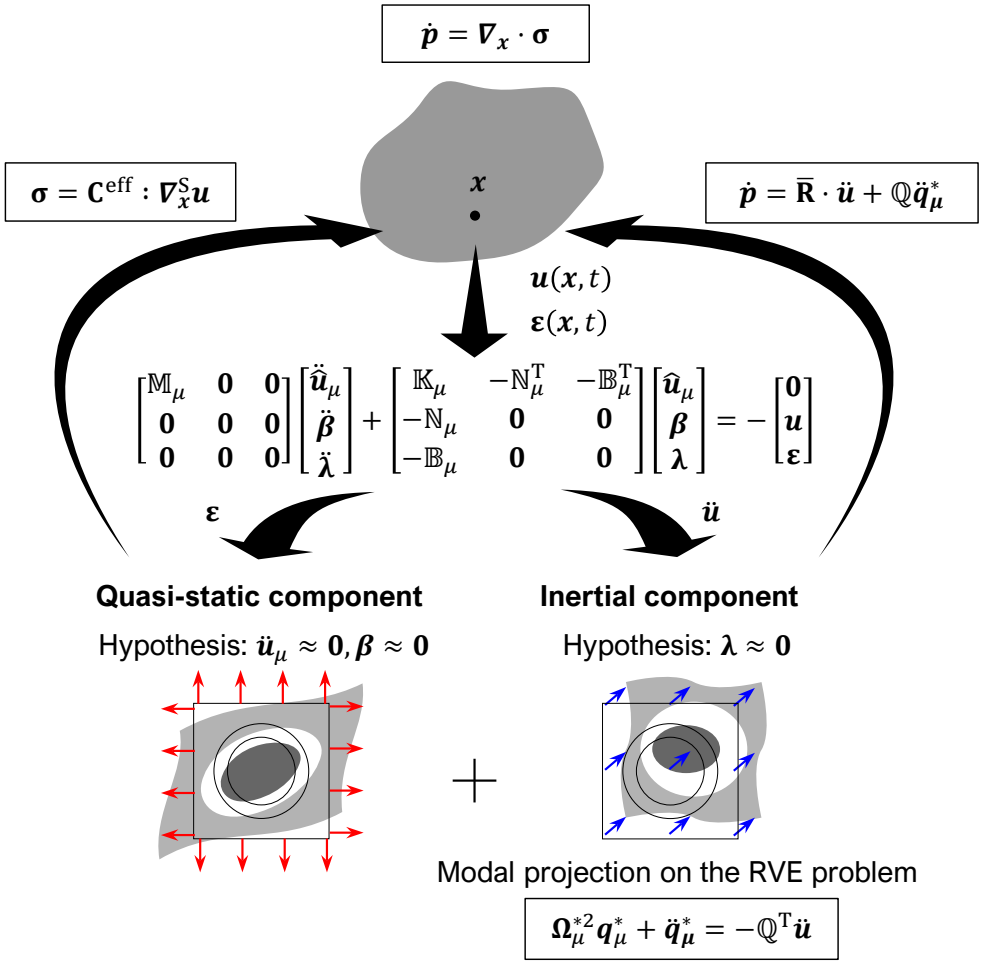

FIG. 5 Global homogenization scheme applied to acoustic problems. Macroscopic displacement and strain are actions in the RVE system. The macro-stress is obtained as a reaction of the quasi-static component of the RVE system, while the macro-inertial force, which accounts for local micro-resonating modes, comes from the inertial component of the RVE system.

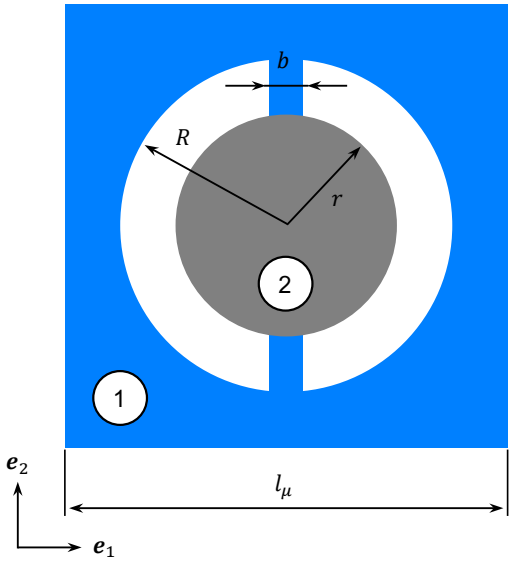

FIG. 6 Unit cell configuration parameters. The numbers correspond to each material ID in Tab. 1.

I.4 Examples

In the following, the algorithm sketch in Box 1 is applied to the resolution of a number of 2D multiscale homogenized acoustic problems.

I.4.1 Unit cell effects for the ideal problem

We will consider here an infinite and homogeneous domain in the macroscale so that the assumptions considered for the developments in Section I.3.4.2 can be applied. The goal would be to compare the effects of the cell design into the acoustic macroscopic properties. The macroscopic problem Eq. (79) can be solved analytically, in this case, while the microscopic equation (80) will be solved numerically with FE discretization.

Even though the results that will be obtained in this example may not represent the actual material behavior, it is interesting for academic purposes as it provides a controlled environment for easily understand the phenomena involved in the unusual properties of acoustic metamaterials.

In order to achieve the typical properties of acoustic metamaterials, the unit cell design must be such that it guarantees the existence of relevant resonating modes in the frequency range of interest (up to 20 kHz). This is accomplished, for instance, with the so called locally resonant acoustic metamaterials (LRAM), as local resonance phenomena occur in conditions that meet the considered assumptions.

TAB. 1 Material and geometrical properties for the LRAM unit cell designs.

Parameter		Units	Nylon	Steel
Material ID		–	1	2
Density		kg m^{-3}	1100	7800
Young's modulus		GPa	2	180
Poisson's ratio		–	0.40	0.33
Dim.	Units	Config. A	Config. B	Config. C
l_μ	mm	5.000	5.000	5.000
r	mm	1.250	0.500	1.250
R	mm	1.875	1.000	1.750
b	mm	0.100	0.100	0.100

For a practical LRAM design, one needs, at least, the following elements as parts of the unit cell:

(a) A rigid component that supports the structure. This element assumes the role of a matrix in this configuration, supporting the resonating elements and attaching them together. The relative stiffness of these elements is what guarantees the separation of scales $\lambda \gg l_\mu$.

(b) A dense component that acts as resonating element. The key aspect for a practical LRAM design is to allow these elements to have natural vibration frequencies in the desired frequency range. They typically are surrounded by highly flexible materials (or void regions) in order to promote the appearance of low natural frequencies. Frequency bandgap sizes and locations are related to the shape and density of these elements.

In order to display these facts, three different geometric configurations have been considered. Fig. 6 depicts the geometrical parameters and material distribution for the considered reference unit cell. The values for the geometrical and material properties considered in the examples are listed in Tab. 1.

The meshes used consist of 2D linear triangular elements} with around 2000 degrees of freedom in each case. The global homogenization scheme of Section I.3 has been applied considering periodic boundary conditions and prescribing the micro-fluctuation field at some point in the RVE boundary in order to prevent rigid body motions. Therefore,

in one corner of the unit cell, the micro-fluctuation displacement has been prescribed[6] (this has already been done in other similar works such as [16])[7]. The mass and stiffness matrices have been computed considering, respectively, 3 and 1 Gaussian quadrature points for their integration over the element. A modal analysis has been performed with Matlab considering both the fully unrestricted $\mathbb{K}_\mu$-$\mathbb{M}_\mu$ and the restricted system $\mathbb{K}^*_\mu$-$\mathbb{M}^*_\mu$.

For the unit cell configuration A, Fig. 7 shows the first 5 vibration modes and the associated natural frequencies for both the unrestricted and restricted systems. The results show that the first and third vibration modes, which are the only ones (in the frequency range of interest) that exhibit some non-negligible[8] components in their corresponding columns of the coupling matrix $\mathbb{Q}$ (see Remark 10), appear to be good candidates as resonating modes. Focusing on longitudinal waves (with wave amplitudes in the propagation direction), which are the interesting ones in the context of acoustic problems, only the first mode becomes relevant. Therefore, one would expect the model to capture its effects on the macroscale. Tab. 2 gives the specific effective properties (for the horizontal component) that have been obtained from the analysis of each unit cell configuration.

A frequency analysis of the macroscopic problem has then been performed over a frequency range from 0 to 25 kHz (a total number of 500 evenly spaced frequency test points have been considered) aiming at studying the propagation characteristics in the horizontal direction ($\boldsymbol{n}_\kappa = \boldsymbol{e}_1$). Note that with the hypotheses assumed, the effective constitutive tensor, $\mathbf{C}^{\text{eff}}$ in Eq. (88), is considered constant in this frequency range.

In Fig. 8, the resulting macroscopic acoustic properties, namely the first component of the density tensors, R^{eff}_{11}, $\bar{R}_{11}$, and $\tilde{R}_{11}$ (see Eq. (89)), and the normalized wavenumber $\kappa l_\mu/2\pi$ obtained from the dispersion relation (90), are shown. It can be checked that the phenomena anticipated in Eqs. (96) and (97) at the frequency band interval (bandgap) $[\omega^{*(1)}_\mu, \omega^{(1)}_\mu]$ show up there.

---

[6] Periodic boundary conditions extend this restriction to the other three corners.

[7] Numerical experimentation shows that adding this type of restriction slightly improves the homogenized results (specific reasons for this are currently investigated). However, it can be proven that these restrictions add symmetric corresponding reactions at the squared RVE that cancel with each other in the summation and, therefore, do not change the physical interpretation of the Lagrange multiplier $\boldsymbol{\beta}$.

[8] The considered value of δ_{tol} in Eq. (81) has been $\delta_{\text{tol}} = 10^{-8}$.

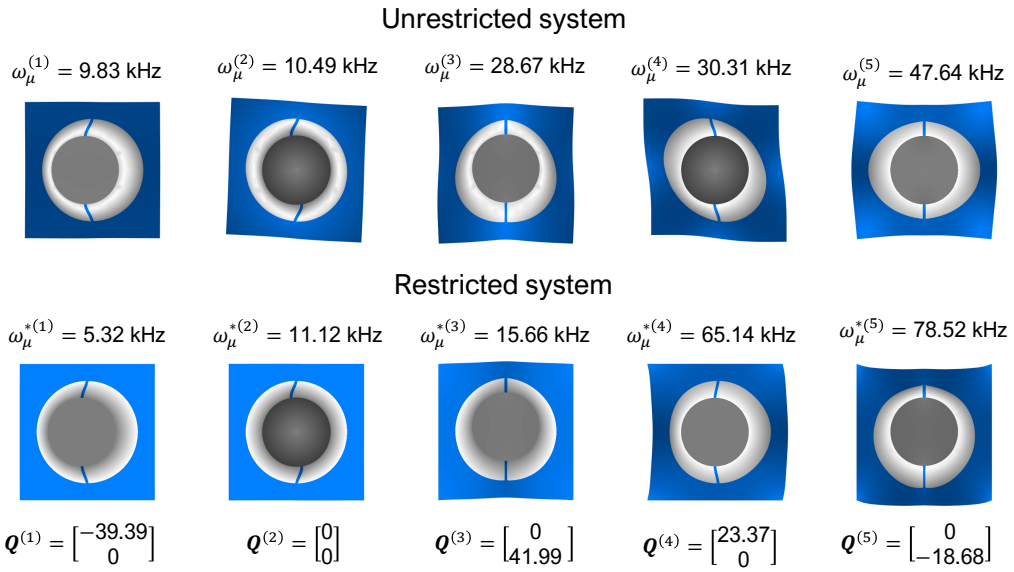

FIG. 7 First 5 vibration modes and the associated natural frequencies of the unit cell configuration A for the unrestricted system (top) and the restricted system (bottom). The corresponding columns $\boldsymbol{Q}^{(k)}$ of the coupling matrix $\mathbb{Q}$ are also shown (units of $kg^{1/2}\ m^{-3/2}$).

TAB. 2 Effective properties for the LRAM unit cell designs.

Param.	Units	Config. A	Config. B	Config. C
C_{11}^{eff}	GPa	0.948	2.532	1.125
$\bar{R}_{11}$	$kg\ m^{-3}$	2149	1208	2211
$Q_1^{(1)}$	$kg^{1/2}\ m^{-3/2}$	–39.39	17.42	–39.58
$\omega_\mu^{*(1)}$	kHz	5.32	17.48	6.89
$\omega_\mu^{(1)}$	kHz	9.83	19.82	12.39

I.4.2 Validation of the proposed homogenization model

In order to validate the homogenization model for acoustic problems proposed in Section I.3 (see also Fig. 5), let's now consider a more realistic macroscopic problem, similar[9] to the one proposed in [16], consisting of a small-width homogeneous macroscopic layer. Fig. 9 schematically represents the macroscopic problem setup. In the thickness

[9] It differs from the one in the referenced work in the 2D character of the homogenized macroscopic model considered here in contrast of the 1D model considered there.

(horizontal) direction, 10 stacked type A unit cells are considered to define the macro-structure. In the vertical direction, the layer is considered infinite-sized and the corresponding boundary conditions will be applied. For the sake of simplicity, and to properly capturing the local resonance phenomenon, we will focus the study on simulating a horizontal plane wave propagating through the finite macroscopic domain of analysis Ω in the thickness direction (see Fig. 9).

An harmonic wave at a given frequency ω on the horizontal direction is prescribed at the macroscopic left boundary of the layer as $\bar{\boldsymbol{u}} = \boldsymbol{U}_0 \sin \omega t \, \boldsymbol{e}_1$ (see Fig. 9). In order to represent the vertical infinite dimension of Ω, periodic macroscopic displacement conditions are imposed at the upper and lower boundaries of Ω, $\Gamma^{(+)}$ and $\Gamma^{(-)}$, respectively. As for the unit cell, the boundary conditions are the same than in the previous example.

The right macroscopic boundary of Ω will be left free, aiming at analysing how the displacement amplitude is affected by the presence of frequency bandgaps. The validation of the proposed homogenization scheme will be done by comparing the results of a Direct Numerical Simulation (DNS) analysis, using a mono-scale FEM mesh consisting of linear triangular elements (the same as considered for the RVE calculations), with the ones obtained with the homogenization model with different macroscopic FEM meshes consisting of linear quadrilateral elements with 4 Gaussian integration points.

A frequency analysis has been performed over a range of evenly spaced 500 excitation frequencies ω from 0 to 25 kHz, from which the amplitudes ratio between the horizontal displacements of the upper-right corner (point B in Fig. 9) and the input harmonic excitation has been obtained (point A in Fig. 9). The results are shown in Fig. 10. It is interesting to see that the obtained frequency bandgap is very similar to the one predicted in the ideal problem in the previous example. In addition, the other peaks shown up in the curve correspond to resonating frequencies of the homogenized macroscopic medium.

In Fig. 11, the profiles of the horizontal displacements amplitudes for the steady state response along the upper boundary $\Gamma^{(+)}$ are shown, for some selected frequencies, and compared for both the DNS and the multiscale model. We clearly observe the attenuating

effect on the wave amplitude only for frequencies inside the bandgap (see, for instance, the profile for $\omega = 7.21$ kHz in Fig. 11).

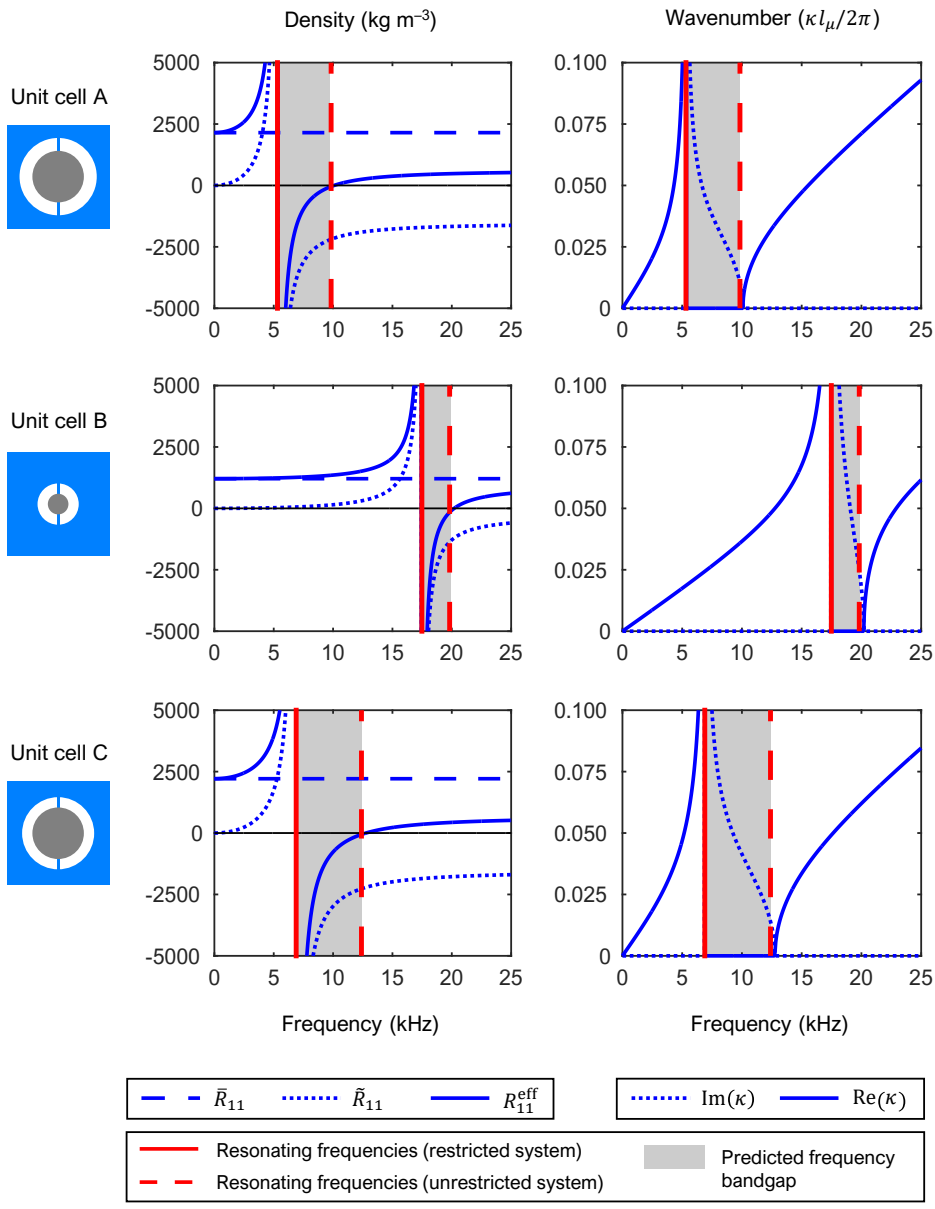

FIG. 8 First component of the effective pseudo-density tensor (left column) and corresponding normalized wavenumber (right column) for each unit cell configuration. The frequency bandgap is defined by the resonating frequencies for the restricted and unrestricted RVE systems in every configuration. See, for instance, for unit cell A, $\omega_\mu^{*(1)} = 5.32$ kHz and $\omega_\mu^{(1)} = 9.32$ kHz in Fig. 7. Notice the sign change of R_{11}^{eff} (from $+\infty$ to $-\infty$) at the beginning of the bands and $R_{11}^{\text{eff}} = 0$ at their end, as well as the imaginary character of the wavenumber (responsible for the attenuation of the macroscopic amplitude) at the bands for all cases. Since the number of tested frequencies is 500, the lines in the plots actually represent all the frequency test points studied.

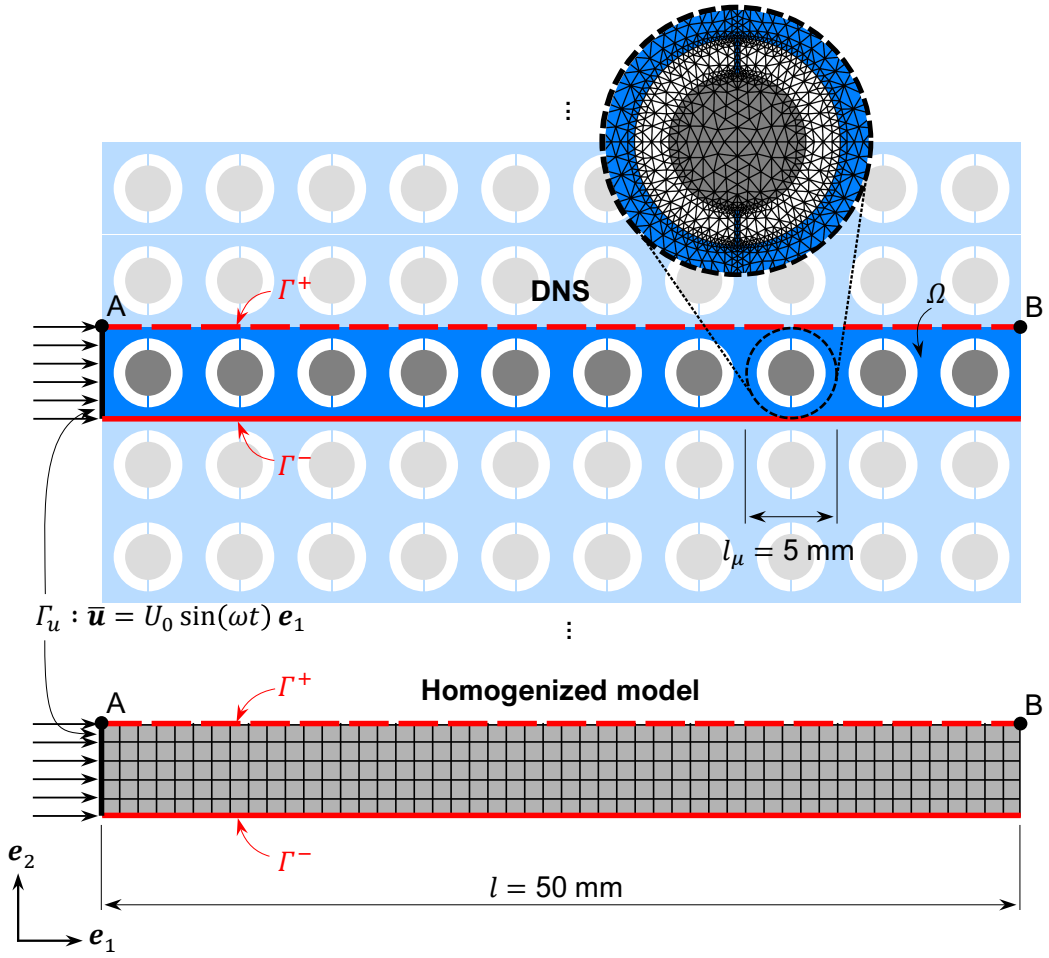

FIG. 9 Macro-scale problem setup. A harmonic horizontal displacement is prescribed on the left boundary of both the DNS (up) and the homogenized model (down). Periodic boundary conditions are applied on the upper and lower boundaries to simulate infinite material extension in the vertical direction. The mesh used for the DNS model is composed of 18400 triangular elements while for the homogenized model, meshes with 10, 40 and 250 (as in the figure) quadrilateral elements have been used.

It should be noted that the results from the homogenization differ from those of the DNS upon increasing the frequency of the analysis (see Fig. 10). This is expected since the simplifying hypotheses assumed hold more strongly the closer one gets to the quasi-static case ($\omega = 0$) and the effects of higher-frequency resonating modes (which are neglected here) become more relevant. In addition, upon increasing the macroscopic frequency we approach the separation of scales limit, causing the whole multiscale theory to fail. However, the results show excellent agreement in the frequency range of interest, where the hypotheses assumed hold more strongly. This proves the correctness of the proposed homogenization scheme for this case.

I.4.3 First approach to LRAM design

In Section I.4.1 we have been able to see that minor changes in the RVE topology can lead to different results and, in this particular case, different bandgap location and sizes. This fact alone opens a wide range of possibilities towards topology optimization designs aiming, for instance, to control the size and location of the frequency bandgaps (here alternatively termed acoustic attenuation bands). Let's consider that we aim at designing an artificial material (metamaterial) with optimal attenuation properties, for instance, in the human hearing range. Materials with homogeneous macro-structures (see Section I.4.2) show a limited number of band-gaps not covering the full interval of interest, so the following question arises: by stacking homogeneous layers (every one attenuating a certain range of frequencies), can one design a multi-layered material whose attenuation band spans the full range of interest?

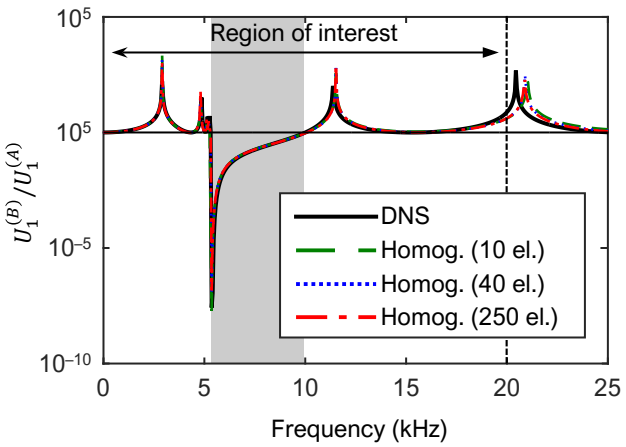

FIG. 10 Amplitudes ratio of the horizontal component of the displacement at point B. Comparison of the DNS and the homogenized model results for different number of elements. Amplitude ratios smaller than 1 imply effective wave attenuation whereas those larger than 1 imply effective wave amplification. Since 500 test points have been considered in the range [0, 25] kHz, the lines in the plot represent the actual frequencies tested.

FIG. 11 Amplitudes ratio of the horizontal component of the displacement of the top boundary points along the horizontal direction. Comparison of the DNS and the homogenized model results for different input frequencies.

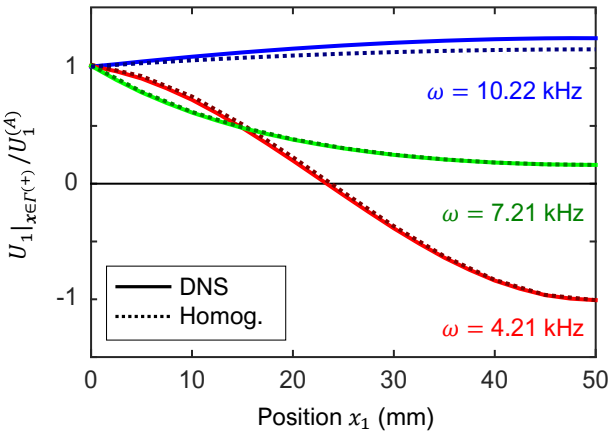

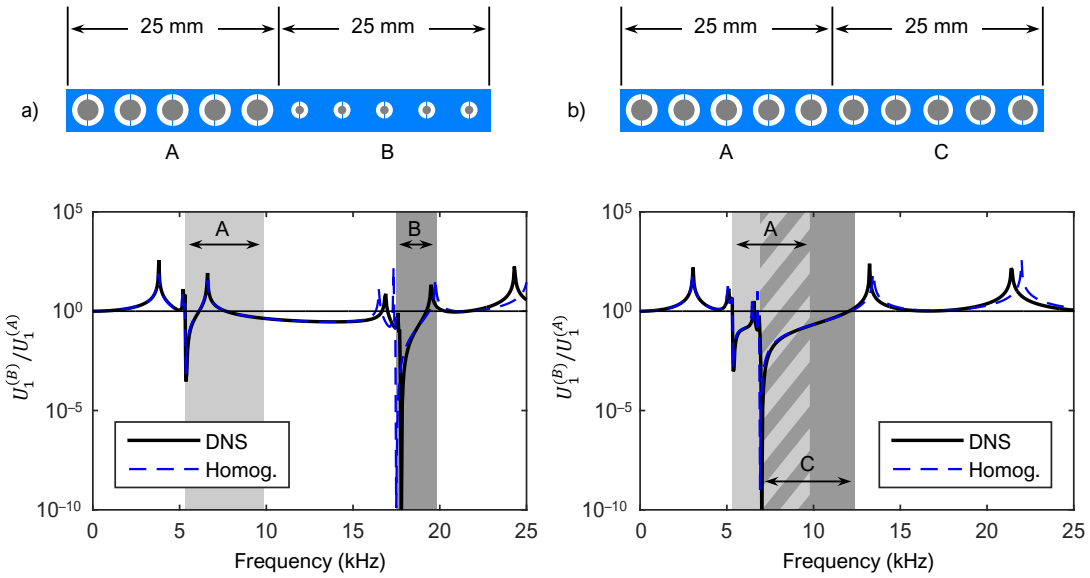

FIG. 12 Amplitudes ratio of the horizontal component of the displacement at point B for two multi-layer configurations: (a) two layers of 25 mm each with unit cell configurations A and B with their predicted band-gap regions (shaded areas) separated; and (b) two layers of 2.5 cm each with unit cell configurations A and C with their predicted bandgap regions (shaded areas) overlapped. The DNS results are compared with those obtained from the homogenized model. Amplitude ratios smaller than 1 imply effective wave attenuation whereas those larger than 1 imply effective wave amplification.

Fig. 12 shows the attenuation curves corresponding to two different bi-layered materials, obtained both from a DNS and homogenization analysis equal to those performed for the example in Section I.4.2. Also, the predicted bandgaps corresponding to every unit cell are depicted in the same figure. Once again, when comparing with the DNS solution, we realize the good performance of the proposed multiscale homogenization scheme also for non-homogeneous problems.

In the first case (a), the predicted bandgaps for each unit cell lie in two separated regions of the frequency domain, and in the macroscale, we observe an additional low-level attenuation that lies in between the two band-gap regions. In the second case (b), where the ideally predicted bandgaps overlap, the non-homogeneous solution shows an attenuation band that spans the two ideal bandgap regions with relevant attenuation levels. In this sense one could say that design (b) improves design (a) for the purposes of getting a continuous wider attenuation band for the multi-layer material.

This is a mere exemplification that there is room for the computational design of acoustic metamaterials, in this case with multi-layered configurations, when a reliable

homogenization scheme, as the one proposed in this work, is available. Additional research on this subject is currently ongoing.

I.5 Conclusions

Along this work, a hierarchical multiscale homogenization approach accounting for inertial effects in acoustic problems has been presented with the following features:

(a) Consideration of the standard Cauchy's continua at the macroscale assuming classical conservation of linear and angular momentum and the Multiscale Virtual Power Principle in [18].
(b) The resulting mechanical problem is then mathematically stated as an unrestricted *saddle-point* problem by incorporating Lagrange multipliers as new dual unknowns. Then, they can be analytically identified by an appropriate choice of the perturbation fields and explained in a physical manner in terms of macroscopic stresses and D'Alembert force density terms.
(c) The resulting formulation is finally specified for acoustic problems, and some assumptions (decomposition into the sum of a quasi-static and inertial systems) allow identifying the simple coupling terms between the micro and macroscale equations. In addition, a computational cost reduction strategy, based on projection onto the restricted and unrestricted natural modes of the microstructure, is used.
(d) In this context, a simple, physically meaningful and efficient homogenization scheme accounting for inertial effects is proposed. This scheme can then be applied to computational homogenization of acoustic metamaterials.

The multiscale formulation presented in this contribution is illustrated with a number of representative simulations for both a homogeneous macrostructure and an heterogeneous macroscopic body with a layered structure. In both cases a microstructure with a particular natural frequency is associated to each homogeneous portion of the macrostructure. The framework represents a starting point for the coupling of topology optimization tools in order to design specific microstructures rendering the desired macroscopic frequency cancelling and attenuating properties. The latter part is left for a future contribution in which a complete computational material design tool is outlined based on the proposed homogenization procedure and goal oriented macroscopic cost functions.

As shown in the presented results, our framework has proven to successfully capture the unusual macroscopic behavior of acoustic metamaterials caused by local resonance phenomena at a significantly low computational cost. A first academic example has validated the expected frequency band gap which is theoretically bounded (in terms of the wave number) between the microscopic eigenfrequencies obtained for the constrained and unconstrained cases. The expected behavior of the effective pseudo-density, i.e. nullifying at resonating frequencies of the unrestricted system and tending to infinite for the restricted system, is also observed in the reported validation test.

The multilayer metamaterial study reported in the second example suggests that there is room for the design of complex acoustic metamaterials capable of attenuating a specific target frequency spectrum, e.g. human voice, environmental noise or engine vibration. In this view, the combination of sufficient layers with different microscopic topologies are envisaged to cover the desired spectrum of frequencies to be attenuated. Further research is, however, required to complement these preliminary results and open the possibility to study more complex constitutive behaviors at the microscale, e.g. viscoelastic effects and other dissipative phenomena, in order to provide a wider attenuating frequency range and more effective attenuation mechanisms.

Acknowledgements

The research leading to these results has received funding from the European Research Council under the European Union's Seventh Framework Programme (FP/2007-2013) / ERC Grant Agreement n. 320815 (ERC Advanced Grant Project "Advanced tools for computational design of engineering materials" COMP-DES-MAT).

Oriol Lloberas-Valls gratefully acknowledges the funding received from the Spanish Ministry of Economy and Competitiveness through the National Research Plan 2014: MAT2014-60919-R.

Appendix I.A Finite element discretization

In order to solve the RVE problem, a Galerkin-based discretization is considered in the spatial domain, so that the microscale domain Ω_μ is split in N_e elements, $\Omega_\mu^{(e)} \subset \Omega_\mu$, for $e = 1, 2 \dots N_e$. In each $\Omega_\mu^{(e)}$, the solution fields and their variations are interpolated by

$$\boldsymbol{u}_\mu(\boldsymbol{y},t) = \boldsymbol{N}_\mu^{(e)}(\boldsymbol{y})\widehat{\boldsymbol{u}}_\mu^{(e)}(t) \quad \text{or} \quad \boldsymbol{u}_\mu(\boldsymbol{y},t) = \sum_a N_\mu^a(\boldsymbol{y})\widehat{\boldsymbol{u}}_\mu^a(t), \tag{A.1}$$

$$\ddot{\boldsymbol{u}}_\mu(\boldsymbol{y},t) = \boldsymbol{N}_\mu^{(e)}(\boldsymbol{y})\ddot{\widehat{\boldsymbol{u}}}_\mu^{(e)}(t) \quad \text{or} \quad \ddot{\boldsymbol{u}}_\mu(\boldsymbol{y},t) = \sum_a N_\mu^a(\boldsymbol{y})\ddot{\widehat{\boldsymbol{u}}}_\mu^a(t), \tag{A.2}$$

$$\delta\boldsymbol{u}_\mu(\boldsymbol{y}) = \boldsymbol{N}_\mu^{(e)}(\boldsymbol{y})\delta\widehat{\boldsymbol{u}}_\mu^{(e)} \quad \text{or} \quad \delta\boldsymbol{u}_\mu(\boldsymbol{y}) = \sum_a N_\mu^a(\boldsymbol{y})\delta\widehat{\boldsymbol{u}}_\mu^a, \tag{A.3}$$

where the superscript a denotes the discrete nodes where the solution fields are interpolated, with the interpolation values being $\boldsymbol{u}_\mu^a$ and $\delta\boldsymbol{u}_\mu^a$, and $N_\mu^a(\boldsymbol{y})$ are the associated shape functions. In compact form, $\widehat{\boldsymbol{u}}_\mu^{(e)}$ and $\delta\widehat{\boldsymbol{u}}_\mu^{(e)}$ dispose $\boldsymbol{u}_\mu^a$ and $\delta\boldsymbol{u}_\mu^a$, respectively, in column vector fashion, while $\boldsymbol{N}_\mu^{(e)}$ dispose $N_\mu^a(\boldsymbol{y})$ in row vector fashion. According to these definitions, the symmetric gradient of the displacement fields is obtained by

$$\nabla_{\boldsymbol{y}}^{\mathrm{S}}\boldsymbol{u}_\mu(\boldsymbol{y},t) = \mathbf{B}_\mu^{(e)}(\boldsymbol{y})\widehat{\boldsymbol{u}}_\mu^{(e)}(t) \quad \text{or} \quad \nabla_{\boldsymbol{y}}^{S}\boldsymbol{u}_\mu(\boldsymbol{y},t) = \sum_a \mathbf{B}_\mu^a(\boldsymbol{y})\widehat{\boldsymbol{u}}_\mu^a(t), \tag{A.4}$$

$$\nabla_{\boldsymbol{y}}^{\mathrm{S}}\delta\boldsymbol{u}_\mu(\boldsymbol{y}) = \mathbf{B}_\mu^{(e)}(\boldsymbol{y})\delta\widehat{\boldsymbol{u}}_\mu^{(e)} \quad \text{or} \quad \nabla_{\boldsymbol{y}}^{S}\delta\boldsymbol{u}_\mu(\boldsymbol{y}) = \sum_a \mathbf{B}_\mu^a(\boldsymbol{y})\delta\widehat{\boldsymbol{u}}_\mu^a, \tag{A.5}$$

where $\mathbf{B}_\mu^a(\boldsymbol{y})$ are defined, according to Voigt's notation, as

$$\mathbf{B}_\mu^a(\boldsymbol{y}) = \begin{bmatrix} \partial N_\mu^a/\partial y_1 & 0 \\ 0 & \partial N_\mu^a/\partial y_2 \\ \partial N_\mu^a/\partial y_2 & \partial N_\mu^a/\partial y_1 \end{bmatrix}, \tag{A.6}$$

and $\mathbf{B}_\mu^{(e)}$ corresponds to the arrangement of these terms in matrix form. The discretized form of the variational statements (30) to (32), can be written, for each element, as

$$\sum_a\sum_b \langle \delta\widehat{\boldsymbol{u}}_\mu^b \cdot (\rho_\mu^{(e)} N_\mu^b N_\mu^a \ddot{\widehat{\boldsymbol{u}}}_\mu^a + \mathbf{B}_\mu^{b\mathrm{T}}\mathbf{C}_\mu^{(e)}\mathbf{B}_\mu^a\widehat{\boldsymbol{u}}_\mu^a - N_\mu^b\boldsymbol{\beta} - B_\mu^{b\mathrm{T}}\boldsymbol{\lambda})\rangle_{\Omega_\mu^{(e)}} = 0, \qquad \forall\, \delta\widehat{\boldsymbol{u}}_\mu^b, \tag{A.7}$$

$$\sum_a \langle N_\mu^a\widehat{\boldsymbol{u}}_\mu^a\rangle_{\Omega_\mu^{(e)}} = \langle \boldsymbol{u}\rangle_{\Omega_\mu^{(e)}}, \tag{A.8}$$

$$\sum_a \langle \mathbf{B}_\mu^a\widehat{\boldsymbol{u}}_\mu^a\rangle_{\Omega_\mu^{(e)}} = \langle \boldsymbol{\varepsilon}\rangle_{\Omega_\mu^{(e)}}, \tag{A.9}$$

or, in matrix form,

$$\langle \rho_\mu^{(e)}\boldsymbol{N}_\mu^{(e)\mathrm{T}}\boldsymbol{N}_\mu^{(e)}\rangle_{\Omega_\mu^{(e)}}\ddot{\widehat{\boldsymbol{u}}}_\mu^{(e)} + \langle \mathbf{B}_\mu^{(e)\mathrm{T}}\mathbf{C}_\mu^{(e)}\mathbf{B}_\mu^{(e)}\rangle_{\Omega_\mu^{(e)}}\widehat{\boldsymbol{u}}_\mu^{(e)} - \langle \boldsymbol{N}_\mu^{(e)\mathrm{T}}\rangle_{\Omega_\mu^{(e)}}\boldsymbol{\beta} - \langle \mathbf{B}_\mu^{(e)\mathrm{T}}\rangle_{\Omega_\mu^{(e)}}\boldsymbol{\lambda} = \mathbf{0}, \tag{A.10}$$

$$\langle \boldsymbol{N}_{\mu}^{(e)} \rangle_{\Omega_{\mu}^{(e)}} \widehat{\boldsymbol{u}}_{\mu}^{(e)} = \langle \boldsymbol{u} \rangle_{\Omega_{\mu}^{(e)}}, \tag{A.11}$$

$$\langle \mathbf{B}_{\mu}^{(e)} \rangle_{\Omega_{\mu}^{(e)}} \widehat{\boldsymbol{u}}_{\mu}^{(e)} = \langle \boldsymbol{\varepsilon} \rangle_{\Omega_{\mu}^{(e)}}, \tag{A.12}$$

where, assuming each element is composed of a single material phase, then $\rho_{\mu}^{(e)}$ is the corresponding density and $\mathbf{C}_{\mu}^{(e)}$ the constitutive tensor. Considering plane strain behavior, $\mathbf{C}_{\mu}^{(e)}$ can be expressed, using Voigt's notation, as

$$\mathbf{C}_{\mu}^{(e)} = \frac{E^{(e)}}{(1+\nu^{(e)})(1-2\nu^{(e)})} \begin{bmatrix} 1-\nu^{(e)} & \nu^{(e)} & 0 \\ \nu^{(e)} & 1-\nu^{(e)} & 0 \\ 0 & 0 & 1-2\nu^{(e)}/2 \end{bmatrix}, \tag{A.13}$$

with $E^{(e)}$ being the element's associated material Young's modulus and $\nu^{(e)}$ its Poisson's ratio.

The system of equations (A.10) to (A.12) can be compactly written as

$$\begin{bmatrix} \mathbb{M}_{\mu}^{(e)} & \mathbf{0} & \mathbf{0} \\ \mathbf{0} & \mathbf{0} & \mathbf{0} \\ \mathbf{0} & \mathbf{0} & \mathbf{0} \end{bmatrix} \begin{bmatrix} \ddot{\widehat{\boldsymbol{u}}}_{\mu}^{(e)} \\ \ddot{\boldsymbol{\beta}} \\ \ddot{\boldsymbol{\lambda}} \end{bmatrix} + \begin{bmatrix} \mathbb{K}_{\mu}^{(e)} & -\mathbb{N}_{\mu}^{(e)\mathrm{T}} & -\mathbb{B}_{\mu}^{(e)\mathrm{T}} \\ -\mathbb{N}_{\mu}^{(e)} & \mathbf{0} & \mathbf{0} \\ -\mathbb{B}_{\mu}^{(e)} & \mathbf{0} & \mathbf{0} \end{bmatrix} \begin{bmatrix} \widehat{\boldsymbol{u}}_{\mu}^{(e)} \\ \boldsymbol{\beta} \\ \boldsymbol{\lambda} \end{bmatrix} = - \begin{bmatrix} \mathbf{0} \\ \langle \boldsymbol{u} \rangle_{\Omega_{\mu}^{(e)}} \\ \langle \boldsymbol{\varepsilon} \rangle_{\Omega_{\mu}^{(e)}} \end{bmatrix}, \tag{A.14}$$

with $$\mathbb{M}_{\mu}^{(e)} = \langle \rho_{\mu}^{(e)} \boldsymbol{N}_{\mu}^{(e)\mathrm{T}} \boldsymbol{N}_{\mu}^{(e)} \rangle_{\Omega_{\mu}^{(e)}}, \tag{A.15}$$

$$\mathbb{K}_{\mu}^{(e)} = \langle \mathbf{B}_{\mu}^{(e)\mathrm{T}} \mathbf{C}_{\mu}^{(e)} \mathbf{B}_{\mu}^{(e)} \rangle_{\Omega_{\mu}^{(e)}}, \tag{A.16}$$

$$\mathbb{N}_{\mu}^{(e)} = \langle \boldsymbol{N}_{\mu}^{(e)} \rangle_{\Omega_{\mu}^{(e)}}, \tag{A.17}$$

$$\mathbb{B}_{\mu}^{(e)} = \langle \mathbf{B}_{\mu}^{(e)} \rangle_{\Omega_{\mu}^{(e)}}. \tag{A.18}$$

After a standard matrix assembly process, the global system results

$$\begin{bmatrix} \mathbb{M}_{\mu} & \mathbf{0} & \mathbf{0} \\ \mathbf{0} & \mathbf{0} & \mathbf{0} \\ \mathbf{0} & \mathbf{0} & \mathbf{0} \end{bmatrix} \begin{bmatrix} \ddot{\widehat{\boldsymbol{u}}}_{\mu} \\ \ddot{\boldsymbol{\beta}} \\ \ddot{\boldsymbol{\lambda}} \end{bmatrix} + \begin{bmatrix} \mathbb{K}_{\mu} & -\mathbb{N}_{\mu}^{\mathrm{T}} & -\mathbb{B}_{\mu}^{\mathrm{T}} \\ -\mathbb{N}_{\mu} & \mathbf{0} & \mathbf{0} \\ -\mathbb{B}_{\mu} & \mathbf{0} & \mathbf{0} \end{bmatrix} \begin{bmatrix} \widehat{\boldsymbol{u}}_{\mu} \\ \boldsymbol{\beta} \\ \boldsymbol{\lambda} \end{bmatrix} = - \begin{bmatrix} \mathbf{0} \\ \boldsymbol{u} \\ \boldsymbol{\varepsilon} \end{bmatrix}, \tag{A.19}$$

with $$\mathbb{M}_{\mu} = \mathop{\mathbf{A}}_{e} \mathbb{M}_{\mu}^{(e)}, \tag{A.20}$$

$$\mathbb{K}_{\mu} = \mathop{\mathbf{A}}_{e} \mathbb{K}_{\mu}^{(e)}, \tag{A.21}$$

$$\mathbb{N}_{\mu} = \mathop{\mathbf{A}}_{e} \mathbb{N}_{\mu}^{(e)}, \tag{A.22}$$

$$\mathbb{B}_{\mu} = \mathop{\mathbf{A}}_{e} \mathbb{B}_{\mu}^{(e)}, \tag{A.23}$$

where the big A symbol has been used to denote the matrix assembly operation.

Appendix I.B RVE system resolution

I.B.1 Application of periodic boundary conditions

For 2D cases $\mathbf{J}$ in Eq. (41) can be written as

$$\mathbf{J} = \boldsymbol{\varepsilon} + \widehat{\boldsymbol{\Omega}}; \quad \boldsymbol{\varepsilon} = \begin{bmatrix} \varepsilon_{11} & \varepsilon_{12} \\ \varepsilon_{12} & \varepsilon_{22} \end{bmatrix}; \quad \widehat{\boldsymbol{\Omega}} = \begin{bmatrix} 0 & \theta \\ -\theta & 0 \end{bmatrix} \tag{B.1}$$

where $\theta(\boldsymbol{x}, t)$ is the infinitesimal in-plane rotation angle.

In order to apply the periodic boundary conditions, the second equation in expression (41) will be discretized, yielding

$$\widehat{\boldsymbol{u}}_{\mu} = [\mathbb{P} \quad \mathbb{L}_{\varepsilon} \quad \mathbb{L}_{\theta}] \begin{bmatrix} \widehat{\boldsymbol{u}}_{\mu}^{*} \\ \boldsymbol{\varepsilon} \\ \theta \end{bmatrix}, \quad \text{or} \quad \begin{bmatrix} \widehat{\boldsymbol{u}}_{\mu}^{(i)} \\ \widehat{\boldsymbol{u}}_{\mu}^{(-)} \\ \widehat{\boldsymbol{u}}_{\mu}^{(+)} \end{bmatrix} = \begin{bmatrix} \mathbf{I} & \mathbf{0} & \mathbf{0} & \mathbf{0} \\ \mathbf{0} & \mathbf{I} & \mathbf{0} & \mathbf{0} \\ \mathbf{0} & \mathbf{I} & \mathbf{L}_{\varepsilon} & \mathbf{L}_{\theta} \end{bmatrix} \begin{bmatrix} \widehat{\boldsymbol{u}}_{\mu}^{(i)} \\ \widehat{\boldsymbol{u}}_{\mu}^{(-)} \\ \boldsymbol{\varepsilon} \\ \theta \end{bmatrix}, \tag{B.2}$$

where, using 2D Voigt's notation,

$$\mathbb{P} = \begin{bmatrix} \mathbf{I} & \mathbf{0} \\ \mathbf{0} & \mathbf{I} \\ \mathbf{0} & \mathbf{I} \end{bmatrix} \tag{B.3}$$

$$\mathbf{L}_{\varepsilon} = \begin{bmatrix} \vdots & & \\ \ell_1(\widehat{\boldsymbol{y}}^{(j)}) & 0 & \ell_2(\widehat{\boldsymbol{y}}^{(j)})/2 \\ 0 & \ell_2(\widehat{\boldsymbol{y}}^{(j)}) & \ell_1(\widehat{\boldsymbol{y}}^{(j)})/2 \\ & \vdots & \end{bmatrix}, \forall\, \widehat{\boldsymbol{y}}^{(j)} \in \Gamma^{(-)}, \tag{B.4}$$

$$\mathbf{L}_{\theta} = \begin{bmatrix} \vdots \\ -\ell_2(\widehat{\boldsymbol{y}}^{(j)}) \\ \ell_1(\widehat{\boldsymbol{y}}^{(j)}) \\ \vdots \end{bmatrix}, \forall\, \widehat{\boldsymbol{y}}^{(j)} \in \Gamma^{(-)}, \tag{B.5}$$

where the superscripts (i), $(-)$ and $(+)$ refer to internal nodes and nodes lying on the boundary regions $\Gamma^{(-)}$ and $\Gamma^{(+)}$, respectively.

I.B.2 Resolution of the quasi-static system

I.B.2.1 Quasi-static system with minimal kinematic conditions

According to expression (55), the quasi-static system considering the minimal kinematic restrictions reads

$$\begin{bmatrix} \mathbb{K}_\mu & -\mathbb{B}_\mu^{\mathrm{T}} \\ -\mathbb{B}_\mu & \mathbf{0} \end{bmatrix} \begin{bmatrix} \widehat{\boldsymbol{u}}_\mu^{(1)} \\ \boldsymbol{\lambda}^{(1)} \end{bmatrix} = - \begin{bmatrix} \mathbf{0} \\ \boldsymbol{\varepsilon} \end{bmatrix}. \tag{B.6}$$

It should be noted that the system (B.6) is defined except for a rigid body motion, $\boldsymbol{u}^{\mathrm{RB}}$, which belongs to both the kernels of $\mathbb{K}_\mu$ and $\mathbb{B}_\mu$, that is

$$\mathbb{K}_\mu \boldsymbol{u}^{\mathrm{RB}} = \mathbf{0}, \tag{B.7}$$

$$\mathbb{B}_\mu \boldsymbol{u}^{\mathrm{RB}} = \mathbf{0}. \tag{B.8}$$

This means that, while no closed solution exists for $\widehat{\boldsymbol{u}}_\mu^{(1)}$, the solution for $\boldsymbol{\lambda}^{(1)}$ is defined disregard the value of $\boldsymbol{u}^{\mathrm{RB}}$. Then, by prescribing arbitrarily 3 DOFs in $\widehat{\boldsymbol{u}}_\mu^{(1)}$, the system (B.6) becomes

$$\begin{bmatrix} \mathbb{K}_\mu^{ff} & -\mathbb{B}_\mu^{f\mathrm{T}} \\ -\mathbb{B}_\mu^{f} & \mathbf{0} \end{bmatrix} \begin{bmatrix} \widehat{\boldsymbol{u}}_\mu^{f(1)} \\ \boldsymbol{\lambda}^{(1)} \end{bmatrix} = - \begin{bmatrix} \mathbf{0} \\ \boldsymbol{\varepsilon} \end{bmatrix} \tag{B.9}$$

which is now non-singular. Using the Schur complement of $\mathbb{K}_\mu^{ff}$ the system can be condensed so

$$\mathbb{B}_\mu^{f} (\mathbb{K}_\mu^{ff})^{-1} \mathbb{B}_\mu^{f\mathrm{T}} \boldsymbol{\lambda}^{(1)} = \boldsymbol{\varepsilon}, \tag{B.10}$$

and, eventually, $\boldsymbol{\lambda}^{(1)}$ becomes

$$\boldsymbol{\lambda}^{(1)} = \left(\mathbb{B}_\mu^{f} (\mathbb{K}_\mu^{ff})^{-1} \mathbb{B}_\mu^{f\mathrm{T}} \right)^{-1} \boldsymbol{\varepsilon}. \tag{B.11}$$

From expression (B.11), one can identify the quasi-static effective constitutive tensor as

$$\mathbf{C}_{\min}^{\mathrm{eff}} = \left(\mathbb{B}_\mu^{f} (\mathbb{K}_\mu^{ff})^{-1} \mathbb{B}_\mu^{f\mathrm{T}} \right)^{-1}. \tag{B.12}$$

I.B.2.2 Quasi-static system with periodic boundary conditions

Discretization of the optimality conditions of the problem (49), constrained by the periodic boundary conditions, yields

$$\mathbb{K}_\mu \widehat{\boldsymbol{u}}_\mu^{(1)} = \hat{\boldsymbol{r}}^{(1)}, \quad \text{or} \quad \begin{bmatrix} \mathbb{K}_\mu^{ii} & \mathbb{K}_\mu^{i-} & \mathbb{K}_\mu^{i+} \\ \mathbb{K}_\mu^{-i} & \mathbb{K}_\mu^{--} & \mathbb{K}_\mu^{-+} \\ \mathbb{K}_\mu^{+i} & \mathbb{K}_\mu^{+-} & \mathbb{K}_\mu^{++} \end{bmatrix} \begin{bmatrix} \widehat{\boldsymbol{u}}_\mu^{(i)} \\ \widehat{\boldsymbol{u}}_\mu^{(-)} \\ \widehat{\boldsymbol{u}}_\mu^{(+)} \end{bmatrix} = \begin{bmatrix} \mathbf{0} \\ -\widehat{\boldsymbol{\gamma}}^{(1)} \\ \widehat{\boldsymbol{\gamma}}^{(1)} \end{bmatrix} \tag{B.13}$$

where the superscripts (i), $(-)$ and $(+)$ refer, again, to internal nodes and nodes lying on the boundary regions $\Gamma^{(-)}$ and $\Gamma^{(+)}$, respectively. In Eq. (B.13), $\widehat{\boldsymbol{\gamma}}^{(1)}$ is the vector of the nodal Lagrange multipliers acting as boundary reactions to imposing the periodic boundary conditions.

Notice that $\widehat{\boldsymbol{u}}_\mu^{(1)}$ in Eq. (B.13) is defined except for a rigid body motion (involving an in-plane translation and rotation). Now, applying the periodic boundary conditions (see Eq. (B.2)) into the system (B.13), yields

$$\begin{bmatrix} \mathbb{P}^{\mathrm{T}} \\ \mathbb{L}_\varepsilon^{\mathrm{T}} \\ \mathbb{L}_\theta^{\mathrm{T}} \end{bmatrix} \mathbb{K}_\mu [\mathbb{P} \quad \mathbb{L}_\varepsilon \quad \mathbb{L}_\theta] \begin{bmatrix} \widehat{\boldsymbol{u}}_\mu^{*} \\ \boldsymbol{\varepsilon} \\ \theta \end{bmatrix} = \begin{bmatrix} \mathbb{P}^{\mathrm{T}} \\ \mathbb{L}_\varepsilon^{\mathrm{T}} \\ \mathbb{L}_\theta^{\mathrm{T}} \end{bmatrix} \begin{bmatrix} \mathbf{0} \\ -\widehat{\boldsymbol{\gamma}}^{(1)} \\ \widehat{\boldsymbol{\gamma}}^{(1)} \end{bmatrix} = \begin{bmatrix} \mathbf{0} \\ -\mathbf{L}_\varepsilon^{\mathrm{T}} \widehat{\boldsymbol{\gamma}}^{(1)} \\ \mathbf{L}_\theta^{\mathrm{T}} \widehat{\boldsymbol{\gamma}}^{(1)} \end{bmatrix}. \tag{B.14}$$

Now, since $\mathbb{L}_\theta \theta$ is a rigid body rotation field, thus belonging to the kernel of $\mathbb{K}_\mu$, then $\mathbb{K}_\mu \mathbb{L}_\theta = \mathbf{0}$, $\mathbb{L}_\theta^T \mathbb{K}_\mu = \mathbf{0}$ and Eq. (B.14) can be rewritten as

$$\begin{bmatrix} \mathbb{P}^{\mathrm{T}} \\ \mathbb{L}_\varepsilon^{\mathrm{T}} \end{bmatrix} \mathbb{K}_\mu [\mathbb{P} \quad \mathbb{L}_\varepsilon] \begin{bmatrix} \widehat{\boldsymbol{u}}_\mu^{*} \\ \boldsymbol{\varepsilon} \end{bmatrix} = \begin{bmatrix} \mathbf{0} \\ \mathbf{L}_\varepsilon^{\mathrm{T}} \widehat{\boldsymbol{\gamma}}^{(1)} \end{bmatrix}, \tag{B.15}$$

$$\mathbf{L}_\theta^{\mathrm{T}} \widehat{\boldsymbol{\gamma}}^{(1)} = \mathbf{0}, \tag{B.16}$$

Eq. (B.16) simply states the equilibrium of moments associated to the reactions $\widehat{\boldsymbol{\gamma}}^{(1)}$.

Additionally, since $\mathbf{L}_\varepsilon^{\mathrm{T}} \widehat{\boldsymbol{\gamma}}^{(1)} = \boldsymbol{\sigma}^{(1)}$ is the discrete counterpart of Eq. (48), we find

$$\begin{bmatrix} \mathbb{K}_\mu^{*} & \mathbb{S}^{\mathrm{T}} \\ \mathbb{S} & \overline{\mathbf{C}} \end{bmatrix} \begin{bmatrix} \widehat{\boldsymbol{u}}_\mu^{*(1)} \\ \boldsymbol{\varepsilon} \end{bmatrix} = \begin{bmatrix} \mathbf{0} \\ \boldsymbol{\sigma}^{(1)} \end{bmatrix} \tag{B.17}$$

with $$\mathbb{K}_\mu^{*} = \mathbb{P}^{\mathrm{T}} \mathbb{K}_\mu \mathbb{P}, \tag{B.18}$$

$$\overline{\mathbf{C}} = \mathbb{L}_\varepsilon^{\mathrm{T}} \mathbb{K}_\mu \mathbb{L}_\varepsilon, \tag{B.19}$$

$$\mathbb{S} = \mathbb{L}_\varepsilon^{\mathrm{T}} \mathbb{K}_\mu \mathbb{P}, \tag{B.20}$$

Note that, in systems (B.15) and (B.17), the homogenized stress, $\boldsymbol{\sigma}^{(1)}$, appears as a reaction to the action $\boldsymbol{\varepsilon}$. In Eq. (B.17), the solution field $\widehat{\boldsymbol{u}}_\mu^{*(1)}$ is now defined except for a rigid body translation (recall that the rotation, θ, has been removed from the original system (B.14) and does not appear in the equation). Hence, now only 2 DOFs in $\widehat{\boldsymbol{u}}_\mu^{*(1)}$

need to be arbitrarily prescribed in order to avoid the singularity of the system matrix. Under these conditions, for a given $\boldsymbol{\varepsilon}$, the system (B.17) can be solved for $\boldsymbol{\sigma}^{(1)}$, yielding

$$\boldsymbol{\sigma}^{(1)} = (\overline{\mathbf{C}} - \mathbb{S}^f(\mathbb{K}_\mu^{*ff})^{-1}\mathbb{S}^{f\mathrm{T}}) : \boldsymbol{\varepsilon} = \mathbf{C}_{\mathrm{per}}^{\mathrm{eff}} : \boldsymbol{\varepsilon}, \tag{B.21}$$

where $\mathbf{C}_{\mathrm{per}}^{\mathrm{eff}}$ is the quasi-static effective constitutive tensor accounting periodic boundary conditions, reading

$$\mathbf{C}_{\mathrm{per}}^{\mathrm{eff}} = \overline{\mathbf{C}} - \mathbb{S}^f(\mathbb{K}_\mu^{*ff})^{-1}\mathbb{S}^{f\mathrm{T}}. \tag{B.22}$$

I.B.3 Resolution of the inertial system

Recalling Eq. (60), the inertial RVE system reads

$$\begin{bmatrix} \mathbb{M}_\mu & \mathbf{0} \\ \mathbf{0} & \mathbf{0} \end{bmatrix} \begin{bmatrix} \ddot{\widehat{\boldsymbol{u}}}_\mu^{(2)} \\ \ddot{\boldsymbol{\beta}}^{(2)} \end{bmatrix} + \begin{bmatrix} \mathbb{K}_\mu & -\mathbb{N}_\mu^{\mathrm{T}} \\ -\mathbb{N}_\mu & \mathbf{0} \end{bmatrix} \begin{bmatrix} \widehat{\boldsymbol{u}}_\mu^{(2)} \\ \boldsymbol{\beta}^{(2)} \end{bmatrix} = - \begin{bmatrix} \mathbf{0} \\ \boldsymbol{u} \end{bmatrix} \tag{B.23}$$

In order to deal with the system(B.23), it will be useful to explicitly consider the rigid body motion of the micro-displacement field, $\widehat{\boldsymbol{u}}_\mu^{(2)}$, so

$$\widehat{\boldsymbol{u}}_\mu = [\mathbb{I} \quad \mathbb{Y} \quad \mathbb{T}] \begin{bmatrix} \boldsymbol{c} \\ \theta \\ \widehat{\boldsymbol{u}}_\mu^{*(2)} \end{bmatrix} \tag{B.24}$$

with

$$\mathbb{I} = \begin{bmatrix} \vdots & \\ 1 & 0 \\ 0 & 1 \\ \vdots & \end{bmatrix}, \tag{B.25}$$

$$\mathbb{Y} = \begin{bmatrix} \vdots \\ -(\widehat{y}_2^{(j)} - y_2^{(0)}) \\ \widehat{y}_1^{(j)} - y_1^{(0)} \\ \vdots \end{bmatrix}, \tag{B.26}$$

$$\mathbb{T} = \begin{cases} \mathbf{I}, & \text{for minimal kinematic conditions} \\ \mathbb{P}, & \text{for periodic boundary conditions} \end{cases} \tag{B.27}$$

where $\boldsymbol{c}$ is a rigid body translation, θ is an infinitesimal in-plane rotation angle and $\widehat{\boldsymbol{u}}_\mu^{*(2)}$ is the remaining component of the solution field that in this case assumes the role of a micro-fluctuation like field. Note that, since the driving action in this case is such that $\boldsymbol{\varepsilon} = \mathbf{0}$, periodic boundary conditions can be accounted in this resolution scheme simply by

setting $\mathbb{T} = \mathbb{P}$ instead of $\mathbb{T} = \mathbf{I}$, which would be the case when accounting for minimal kinematic restrictions.

Now, introducing expression (B.24) into the system (B.23) and pre-multiplying the first equation by $[\mathbb{I} \quad \mathbb{Y} \quad \mathbb{T}]^{\mathrm{T}}$, one finds

$$\begin{bmatrix} \mathbb{I}^{\mathrm{T}}\mathbb{M}_\mu\mathbb{I} & \mathbb{I}^{\mathrm{T}}\mathbb{M}_\mu\mathbb{Y} & \mathbb{I}^{\mathrm{T}}\mathbb{M}_\mu\mathbb{T} & \mathbf{0} \\ \mathbb{Y}^{\mathrm{T}}\mathbb{M}_\mu\mathbb{I} & \mathbb{Y}^{\mathrm{T}}\mathbb{M}_\mu\mathbb{Y} & \mathbb{Y}^{\mathrm{T}}\mathbb{M}_\mu\mathbb{T} & \mathbf{0} \\ \mathbb{T}^{\mathrm{T}}\mathbb{M}_\mu\mathbb{I} & \mathbb{T}^{\mathrm{T}}\mathbb{M}_\mu\mathbb{Y} & \mathbb{T}^{\mathrm{T}}\mathbb{M}_\mu\mathbb{T} & \mathbf{0} \\ \mathbf{0} & \mathbf{0} & \mathbf{0} & \mathbf{0} \end{bmatrix} \begin{bmatrix} \ddot{\boldsymbol{c}} \\ \ddot{\theta} \\ \ddot{\boldsymbol{u}}_\mu^{*(2)} \\ \ddot{\boldsymbol{\beta}}^{(2)} \end{bmatrix} + \begin{bmatrix} \mathbf{0} & \mathbf{0} & \mathbf{0} & -\mathbf{I} \\ \mathbf{0} & 0 & \mathbf{0} & \mathbf{0} \\ \mathbf{0} & \mathbf{0} & \mathbb{T}^{\mathrm{T}}\mathbb{K}_\mu\mathbb{T} & -\mathbb{T}^{\mathrm{T}}\mathbb{N}_\mu^{\mathrm{T}} \\ -\mathbf{I} & \mathbf{0} & -\mathbb{N}_\mu\mathbb{T} & \mathbf{0} \end{bmatrix} \begin{bmatrix} \boldsymbol{c} \\ \theta \\ \widehat{\boldsymbol{u}}_\mu^{*(2)} \\ \boldsymbol{\beta}^{(2)} \end{bmatrix} = -\begin{bmatrix} \mathbf{0} \\ \mathbf{0} \\ \mathbf{0} \\ \boldsymbol{u} \end{bmatrix}. \tag{B.28}$$

Note that since both $\mathbb{I}$ and $\mathbb{Y}$ are rigid body modes, then $\mathbb{K}_\mu[\mathbb{I} \quad \mathbb{Y}] = \mathbf{0}$, which has already been considered in Eq. (B.28). Furthermore, from the construction of the matrix $\mathbb{N}_\mu$, it should also be easy to verify that $\mathbb{N}_\mu\mathbb{I} = \mathbf{I}$ and, since $\boldsymbol{y}_0$ is the centroid of the RVE, $\mathbb{N}_\mu\mathbb{Y} = \mathbf{0}$.

From the second equation in system (B.28), we obtain

$$\ddot{\theta} = -(\mathbb{Y}^T\mathbb{M}_\mu\mathbb{Y})^{-1}\mathbb{Y}^T\mathbb{M}_\mu(\ddot{\boldsymbol{c}} - \ddot{\widehat{\boldsymbol{u}}}_\mu^{*(2)}), \tag{B.29}$$

which can be substituted into the system yielding

$$\begin{bmatrix} \mathbb{I}^{\mathrm{T}}\widehat{\mathbb{M}}_\mu\mathbb{I} & \mathbb{I}^{\mathrm{T}}\widehat{\mathbb{M}}_\mu\mathbb{T} & \mathbf{0} \\ \mathbb{T}^{\mathrm{T}}\widehat{\mathbb{M}}_\mu\mathbb{I} & \mathbb{T}^{\mathrm{T}}\widehat{\mathbb{M}}_\mu\mathbb{T} & \mathbf{0} \\ \mathbf{0} & \mathbf{0} & \mathbf{0} \end{bmatrix} \begin{bmatrix} \ddot{\boldsymbol{c}} \\ \ddot{\boldsymbol{u}}_\mu^{*(2)} \\ \ddot{\boldsymbol{\beta}}^{(2)} \end{bmatrix} + \begin{bmatrix} \mathbf{0} & \mathbf{0} & -\mathbf{I} \\ \mathbf{0} & \mathbb{T}^{\mathrm{T}}\mathbb{K}_\mu\mathbb{T} & -\mathbb{T}^{\mathrm{T}}\mathbb{N}_\mu^{\mathrm{T}} \\ -\mathbf{I} & -\mathbb{N}_\mu\mathbb{T} & \mathbf{0} \end{bmatrix} \begin{bmatrix} \boldsymbol{c} \\ \widehat{\boldsymbol{u}}_\mu^{*(2)} \\ \boldsymbol{\beta}^{(2)} \end{bmatrix} = -\begin{bmatrix} \mathbf{0} \\ \mathbf{0} \\ \boldsymbol{u} \end{bmatrix}. \tag{B.30}$$

where

$$\widehat{\mathbb{M}}_\mu = \mathbb{M}_\mu(I - \mathbb{Y}(\mathbb{Y}^{\mathrm{T}}\mathbb{M}_\mu\mathbb{Y})^{-1}\mathbb{Y}^{\mathrm{T}}\mathbb{M}_\mu), \tag{B.31}$$

Now, from the last equation in system (B.30), we obtain

$$\boldsymbol{c} = \boldsymbol{u} - \mathbb{N}_\mu\mathbb{T}\widehat{\boldsymbol{u}}_\mu^{*(2)}. \tag{B.32}$$

Introducing expression (B.32) into the second equation in system (B.30) yields

$$\boldsymbol{\beta}^{(2)} = \overline{\mathbf{R}} \cdot \ddot{\boldsymbol{u}} + \mathbb{D}\ddot{\widehat{\boldsymbol{u}}}_\mu^{*(2)}, \tag{B.33}$$

where

$$\overline{\mathbf{R}} = \mathbb{I}^{\mathrm{T}}\widehat{\mathbb{M}}_\mu\mathbb{I}, \tag{B.34}$$

$$\mathbb{D} = \mathbb{I}^{\mathrm{T}}\widehat{\mathbb{M}}_\mu(\mathbf{I} - \mathbb{I}\mathbb{N}_\mu)\mathbb{T}. \tag{B.35}$$

Finally, by introducing expressions (B.32) and (B.33) into the second equation in system (B.28), one finds

$$\mathbb{M}_{\mu}^{*}\ddot{\widehat{\boldsymbol{u}}}_{\mu}^{*(2)} + \mathbb{K}_{\mu}^{*}\widehat{\boldsymbol{u}}_{\mu}^{*(2)} = -\mathbb{D}^{\mathrm{T}}\ddot{\boldsymbol{u}}, \tag{B.36}$$

where

$$\mathbb{K}_{\mu}^{*} = \mathbb{T}^{\mathrm{T}}\mathbb{K}_{\mu}\mathbb{T}, \tag{B.37}$$

$$\mathbb{M}_{\mu}^{*} = \mathbb{T}^{\mathrm{T}}(\mathbf{I} - \mathbb{I}\mathbb{N}_{\mu})^{\mathrm{T}}\widehat{\mathbb{M}}_{\mu}(\mathbf{I} - \mathbb{I}\mathbb{N}_{\mu})\mathbb{T} \tag{B.38}$$

REMARK 13 It should be pointed out here, from the construction of the matrices $\mathbb{M}_{\mu}$, $\mathbb{I}$ and Υ, that

$$\mathbb{I}^{\mathrm{T}}\mathbb{M}_{\mu}\mathbb{I} = \begin{bmatrix} \langle\rho_{\mu}\rangle_{\Omega_{\mu}} & 0 \\ 0 & \langle\rho_{\mu}\rangle_{\Omega_{\mu}} \end{bmatrix}, \tag{B.39}$$

$$\mathbb{I}^{\mathrm{T}}\mathbb{M}_{\mu}\Upsilon = \begin{bmatrix} -\langle\rho_{\mu}(y_2 - y_2^{(0)})\rangle_{\Omega_{\mu}} \\ \langle\rho_{\mu}(y_1 - y_1^{(0)})\rangle_{\Omega_{\mu}} \end{bmatrix} = \begin{bmatrix} \langle\rho_{\mu}\rangle_{\Omega_{\mu}} y_2^{(0)} - \langle\rho_{\mu}y_2\rangle_{\Omega_{\mu}} \\ \langle\rho_{\mu}y_1\rangle_{\Omega_{\mu}} - \langle\rho_{\mu}\rangle_{\Omega_{\mu}} y_1^{(0)} \end{bmatrix} \tag{B.40}$$

From Eq. (B.40), we see that in cases where the geometric center of the RVE, $\boldsymbol{y}_0$, coincides with its center of mass $\boldsymbol{y}_G$, i.e.

$$\boldsymbol{y}_0 = \boldsymbol{y}_G = \frac{\langle\rho_{\mu}\boldsymbol{y}\rangle_{\Omega_{\mu}}}{\langle\rho_{\mu}\rangle_{\Omega_{\mu}}} \tag{B.41}$$

the matrix $\mathbb{I}^{T}\mathbb{M}_{\mu}\Upsilon$ automatically vanishes, yielding

$$\overline{\mathbf{R}} = \mathbb{I}^{\mathrm{T}}\mathbb{M}_{\mu}\mathbb{I} = \langle\rho_{\mu}\rangle_{\Omega_{\mu}}\mathbf{I}, \tag{B.42}$$

$$\mathbb{D} = \mathbb{I}^{\mathrm{T}}\mathbb{M}_{\mu}(\mathbf{I} - \mathbb{I}\mathbb{N}_{\mu})\mathbb{T}. \tag{B.43}$$

References

[1] O. Lloberas-Valls, D. J. Rixen, A. Simone, and L. J. Sluys, "Multiscale domain decomposition analysis of quasi-brittle heterogeneous materials," *Int. J. Numer. Methods Eng.*, vol. 89, no. 11, pp. 1337–1366, Mar. 2012, doi: http://dx.doi.org/10.1002/nme.3286.

[2] T. Belytschko, S. Loehnert, and J.-H. Song, "Multiscale aggregating discontinuities: A method for circumventing loss of material stability," *Int. J. Numer. Methods Eng.*, vol. 73, no. 6, pp. 869–894, Feb. 2008, doi: http://dx.doi.org/10.1002/nme.2156.

[3] F. Feyel and J.-L. Chaboche, "FE2 multiscale approach for modelling the elastoviscoplastic behaviour of long fibre SiC/Ti composite materials," *Comput. Methods Appl. Mech. Eng.*, vol. 183, no. 3–4, pp. 309–330, Mar. 2000, doi: http://dx.doi.org/10.1016/S0045-7825(99)00224-8.

[4] V. Kouznetsova, W. A. M. Brekelmans, and F. P. T. Baaijens, "An approach to micro-macro modeling of heterogeneous materials," *Comput. Mech.*, vol. 27, no. 1, pp. 37–48, Jan. 2001, doi: http://dx.doi.org/10.1007/s004660000212.

[5] C. Miehe and A. Koch, "Computational micro-to-macro transitions of discretized microstructures undergoing small strains," *Arch. Appl. Mech.*, vol. 72, no. 4–5, pp. 300–317, 2002, doi: http://dx.doi.org/10.1007/s00419-002-0212-2.

[6] S. D. Mesarovic and J. Padbidri, "Minimal kinematic boundary conditions for simulations of disordered microstructures," *Philos. Mag.*, vol. 85, no. 1, pp. 65–78, 2005, doi: http://dx.doi.org/10.1080/14786430412331313321.

[7] C. V. Verhoosel, J. J. C. Remmers, and M. A. Gutiérrez, "A partition of unity-based multiscale approach for modelling fracture in piezoelectric ceramics," *Int. J. Numer. Methods Eng.*, vol. 82, no. 8, pp. 966–994, Dec. 2009, doi: http://dx.doi.org/10.1002/nme.2792.

[8] V. Phu Nguyen, O. Lloberas-Valls, M. Stroeven, and L. Johannes Sluys, "On the existence of representative volumes for softening quasi-brittle materials – A failure zone averaging scheme," *Comput. Methods Appl. Mech. Eng.*, vol. 199, no. 45–48, pp. 3028–3038, Nov. 2010, doi: http://dx.doi.org/10.1016/j.cma.2010.06.018.

[9] V. P. Nguyen, O. Lloberas-Valls, M. Stroeven, and L. J. Sluys, "Homogenization-based multiscale crack modelling: From micro-diffusive damage to macro-cracks," *Comput. Methods Appl. Mech. Eng.*, vol. 200, no. 9–12, pp. 1220–1236, 2011, doi: http://dx.doi.org/10.1016/j.cma.2010.10.013.

[10] J. Oliver, M. Caicedo, E. Roubin, A. E. Huespe, and J. A. Hernández, "Continuum approach to computational multiscale modeling of propagating fracture," *Comput. Methods Appl. Mech. Eng.*, vol. 294, pp. 384–427, Sep. 2015, doi: http://dx.doi.org/10.1016/j.cma.2015.05.012.

[11] I. Özdemir, W. A. M. Brekelmans, and M. G. D. Geers, "Computational homogenization for heat conduction in heterogeneous solids," *Int. J. Numer. Methods Eng.*, vol. 73, no. 2, pp. 185–204, Jan. 2008, doi: http://dx.doi.org/10.1002/nme.2068.

[12] V. Kouznetsova, M. G. D. Geers, and W. A. M. Brekelmans, "Multi-scale constitutive modelling of heterogeneous materials with a gradient-enhanced computational homogenization scheme," *Int. J. Numer. Methods Eng.*, vol. 54, no. 8, pp. 1235–1260, Jul. 2002, doi: http://dx.doi.org/10.1002/nme.541.

[13] P. Cartraud and T. Messager, "Computational homogenization of periodic beam-like structures," *Int. J. Solids Struct.*, vol. 43, no. 3–4, pp. 686–696, Feb. 2006, doi: http://dx.doi.org/10.1016/j.ijsolstr.2005.03.063.

[14] A. Karamnejad, V. P. Nguyen, and L. J. Sluys, "A multi-scale rate dependent crack model for quasi-brittle heterogeneous materials," *Eng. Fract. Mech.*, vol. 104, pp. 96–113, May 2013, doi: http://dx.doi.org/10.1016/j.engfracmech.2013.03.009.

[15] K. Pham, V. G. Kouznetsova, and M. G. D. Geers, "Transient computational homogenization for heterogeneous materials under dynamic excitation," *J. Mech. Phys. Solids*, vol. 61, no. 11, pp. 2125–2146, Nov. 2013, doi: http://dx.doi.org/10.1016/j.jmps.2013.07.005.

[16] A. Sridhar, V. G. Kouznetsova, and M. G. D. D. Geers, "Homogenization of locally resonant acoustic metamaterials towards an emergent enriched continuum," *Comput. Mech.*, vol. 57, no. 3, pp. 423–435, Mar. 2016, doi: http://dx.doi.org/10.1007/s00466-015-1254-y.

[17] E. A. de Souza Neto, P. J. Blanco, P. J. Sánchez, and R. A. Feijóo, "An RVE-based multiscale theory of solids with micro-scale inertia and body force effects," *Mech. Mater.*, vol. 80, no. Part A, pp. 136–144, Jan. 2015, doi: http://dx.doi.org/10.1016/j.mechmat.2014.10.007.

[18] P. J. Blanco, P. J. Sánchez, E. A. de Souza Neto, and R. A. Feijóo, "Variational Foundations and Generalized Unified Theory of RVE-Based Multiscale Models," *Arch. Comput. Methods Eng.*, vol. 23, no. 2, pp. 191–253, Jun. 2016, doi: http://dx.doi.org/10.1007/s11831-014-9137-5.

[19] P. J. Blanco, A. Clausse, and R. A. Feijóo, "Homogenization of the Navier-Stokes equations by means of the Multi-scale Virtual Power Principle," *Comput. Methods Appl. Mech. Eng.*, vol. 315, pp. 760–779, Mar. 2017, doi: http://dx.doi.org/10.1016/j.cma.2016.11.022.

[20] A. O. Krushynska, M. Miniaci, V. G. Kouznetsova, and M. G. D. Geers, "Multilayered Inclusions in Locally Resonant Metamaterials: Two-Dimensional Versus Three-Dimensional Modeling," *J. Vib. Acoust.*, vol. 139, no. 2, pp. 3–6, Apr. 2017, doi: http://dx.doi.org/10.1115/1.4035307.

[21] M. I. Hussein, G. M. Hulbert, and R. A. Scott, "Dispersive elastodynamics of 1D banded materials and structures: analysis," *J. Sound Vib.*, vol. 289, no. 4–5, pp. 779–806, Feb. 2006, doi: http://dx.doi.org/10.1016/j.jsv.2005.02.030.

[22] M. I. Hussein, G. M. Hulbert, and R. A. Scott, "Dispersive elastodynamics of 1D banded materials and structures: Design," *J. Sound Vib.*, vol. 307, no. 3–5, pp. 865–893, Nov. 2007, doi: http://dx.doi.org/10.1016/j.jsv.2007.07.021.

[23] J. S. Jensen and O. Sigmund, "Systematic design of photonic crystal structures using topology optimization: Low-loss waveguide bends," *Appl. Phys. Lett.*, vol. 84, no. 12, pp. 2022–2024, Mar. 2004, doi: http://dx.doi.org/10.1063/1.1688450.

[24] X. Oliver and C. A. de Saracibar, *Continuum Mechanics for Engineers: Theory and Problems*. 2017.

[25] M. I. Hussein and G. M. Hulbert, "Mode-enriched dispersion models of periodic materials within a multiscale mixed finite element framework," *Finite Elem. Anal. Des.*, vol. 42, no. 7, pp. 602–612, Apr. 2006, doi: http://dx.doi.org/10.1016/j.finel.2005.11.002.

[26] J. A. Hernández, J. Oliver, A. E. Huespe, M. A. Caicedo, and J. C. Cante, "High-performance model reduction techniques in computational multiscale homogenization," *Comput. Methods Appl. Mech. Eng.*, vol. 276, pp. 149–189, Jul. 2014, doi: http://dx.doi.org/10.1016/j.cma.2014.03.011.

[27] D. C. Dobson, J. Gopalakrishnan, and J. E. Pasciak, "An Efficient Method for Band Structure Calculations in 3D Photonic Crystals," *J. Comput. Phys.*, vol. 161, no. 2, pp. 668–679, Jul. 2000, doi: http://dx.doi.org/10.1006/jcph.2000.6521.

[28] M. I. Hussein, "Reduced Bloch mode expansion for periodic media band structure calculations," *Proc. R. Soc. A Math. Phys. Eng. Sci.*, vol. 465, no. 2109, pp. 2825–2848, Sep. 2009, doi: http://dx.doi.org/10.1098/rspa.2008.0471.

[29] D. Krattiger and M. I. Hussein, "Bloch mode synthesis: Ultrafast methodology for elastic band-structure calculations," *Phys. Rev. E*, vol. 90, no. 6, p. 063306, Dec. 2014, doi: http://dx.doi.org/10.1103/PhysRevE.90.063306.

[30] M. I. Hussein, M. J. Leamy, and M. Ruzzene, "Dynamics of Phononic Materials and Structures: Historical Origins, Recent Progress, and Future Outlook," *Appl. Mech. Rev.*, vol. 66, no. 4, p. 040802, Jul. 2014, doi: http://dx.doi.org/10.1115/1.4026911.

ARTICLE II

- Online published title page -

Computer Methods in Applied Mechanics and Engineering
Volume 345, 1 March 2019, Pages 161-182

Computational design of locally resonant acoustic metamaterials

D. Roca [a, b], D. Yago [a, b], J. Cante [a, b], O. Lloberas-Valls [a, c], J. Oliver [a, c]

[a] Centre Internacional de Mètodes Numèrics en Enginyeria (CIMNE), Campus Nord UPC, Mòdul C-1 101, c/ Jordi Girona 1-3, 08034 Barcelona, Spain
[b] Escola Superior d'Enginyeries Industrial, Aeroespacial i Audiovisual de Terrassa (ESEIAAT), Technical University of Catalonia (Barcelona Tech), Campus Terrassa UPC, c/ Colom 11, 08222 Terrassa, Spain
[c] E.T.S d'Enginyers de Camins, Canals i Ports de Barcelona (ETSECCPB), Technical University of Catalonia (Barcelona Tech), Campus Nord UPC, Mòdul C-1, c/ Jordi Girona 1-3, 08034 Barcelona, Spain

Received 30 July 2018, Revised 19 October 2018, Accepted 23 October 2018, Available online 3 November 2018.

Check for updates

Show less

https://doi.org/10.1016/j.cma.2018.10.037

Get rights and content

Article II

Computational design of locally resonant acoustic metamaterials

D. Roca[a,b], D. Yago[a,b], J. Cante[a,b], O. Lloberas-Valls[a,c], J. Oliver[a,c,(*)]

[a] *Centre Internacional de Mètodes Numèrics en Enginyeria (CIMNE), Campus Nord UPC, Mòdul C-1 101, c/ Jordi Girona 1-3, 08034 Barcelona, Spain*

[b] *Escola Superior d'Enginyeries Industrial, Aeroespacial i Audiovisual de Terrassa (ESEIAAT), Technical University of Catalonia (Barcelona Tech), Campus Terrassa UPC, c/ Colom 11, 08222 Terrassa, Spain*

[c] *E.T.S. d'Enginyers de Camins, Canals i Ports de Barcelona (ETSECCPB), Technical University of Catalonia (Barcelona Tech), Campus Nord UPC, Mòdul C-1, c/ Jordi Girona 1-3, 080304 Barcelona, Spain*

Abstract

The so-called Locally Resonant Acoustic Metamaterials (LRAM) are considered for the design of specifically engineered devices capable of stopping waves from propagating in certain frequency regions (bandgaps), this making them applicable for acoustic insulation purposes. This fact has inspired the design of a new kind of lightweight acoustic insulation panels with the ability to attenuate noise sources in the low frequency range (below 5000 Hz) without requiring thick pieces of very dense materials. A design procedure based on different computational mechanics tools, namely, (1) a multiscale homogenization framework, (2) model order reduction strategies and (3) topological optimization procedures, is proposed. It aims at attenuating sound waves through the panel for a target set of resonance frequencies as well as maximizing the associated bandgaps. The resulting design's performance is later studied by introducing viscoelastic properties in the coating phase, in order to both analyse their effects on the overall design and account for more realistic behaviour. The study displays the emerging field of Computational Material Design (CMD) as a computational mechanics area with enormous potential for the design of metamaterial-based industrial acoustic parts.

Keywords: Multiscale modelling, Computational design, Topology optimization, Acoustic metamaterials

II.1 Motivation

The concept of Locally Resonant Acoustic Metamaterials (LRAM) has been object of growing interest among the scientific and technological communities in recent years. The notion of *metamaterials* emerged in the late 1990s as a new kind of engineered materials, by optimizing their morphology or arrangement at lower scales, capable of exhibiting properties "on demand" that are not found in naturally occurring materials. In the specific case of acoustic metamaterials, these properties involve exotic or counter-intuitive behavior caused by the interaction of the material with acoustic or elastic waves' propagation features. These types of materials could be used, for instance, to design acoustic insulation panels that target specific frequency bands (especially in the low-frequency range, i.e. below 5000 Hz, where most sources of environmental noise are produced). In contrast to conventional acoustic panels, which require either a large thickness or high mass density in order to provide effective sound attenuation at lower frequencies, LRAM-based panels can achieve good levels of transmission loss in the whole frequency range of interest with relatively thin, lightweight designs.

Scientific research in the field of metamaterials started in the late 19th century with the works of Floquet and Rayleigh among others, who studied phenomena related to the propagation of waves in periodic systems. However, it was not until the beginning of this century when the first implementation of an acoustic metamaterial capable of stopping waves from transmitting in a certain frequency band was reported by Liu *et al*. [1]. Later on, Ho *et al*. [2] and Calius *et al*. [3] performed other experimental demonstrations with silicone rubber-coated metal spheres embedded in polymer matrices, while more recently, Claeys *et al*. [4] have carried out tests with a fully 3D-printed design with internal resonators capable of achieving also good attenuation properties in the low-frequency range. The idea of LRAM-based insulation panels has already been explored, both theoretically and experimentally, for membrane-type [5, 6] and plate-type [7] acoustic metamaterials.

On the other hand, computational models for the study and characterization of LRAMs have been traditionally focused on periodically repeated microstructures where Bloch-Floquet boundary conditions can be applied [8, 9]. More recent developments include the works of Sridhar *et al*. [10, 11] and Roca *et al*. [12], in which computational

homogenization frameworks accounting for inertial effects have been proposed, capable of capturing the local resonance phenomena that characterizes such kind of materials.

Aiming at trying to enlarge the effective attenuation band achieved by the local resonance phenomenon in metamaterials is a challenging task, since the so-called frequency bandgaps produced by typical LRAM designs, which are the source of their attenuation capabilities, tend to be too narrow in the frequency spectrum. In this regard, several proposals have been made recently in the literature in order to find a solution for this problem. For instance, Matsuki *et al*. [13] proposed a topology optimization-based method to obtain optimal LRAM configurations with multiple attenuation peaks, which can be considered one of the first attempts to apply optimization procedures to LRAM materials. Other approaches are focused on taking advantage of the viscoelastic nature of the coating materials in typical LRAM configurations. The first notions on the beneficial effects of viscous damping in acoustic metamaterials were reported by Hussein and Frazier [14], who introduced the concept of *metadamping* to refer to the damping emergence phenomenon produced as a result of combining the effects of local resonance with viscous dissipation. The concept of metadamping has also been explored in more detail in subsequent works [15] and the idea of acoustic metamaterial configurations based on this (phononic resonators) has been proposed by DePauw *et al*. [16]. This phenomenon has also been studied more recently in the context of acoustic metamaterials in the work of Manimala and Sun [17], where they show, by means of an analytical approach, the dispersion properties of LRAMs with different models of viscoelastic (dissipative) behavior for the coating material, and the works of Krushynska *et al*. [18] and Lewinska *et al*. [19], in which generalized viscoelastic modelling is introduced in the study of the attenuation performance of LRAMs.

In this paper, the authors attempt at setting a computational based methodology for the modelling, analysis and design of metamaterial parts exhibiting local resonance phenomena by combining three well-established complementary computational tools: (1) a multiscale hierarchical homogenization procedure specifically devised for acoustic problems, described in [12], (2) the exploitation of Reduced Order Modelling (ROM) techniques, to minimize the resulting computational cost, based on selective projections of the RVE behaviour onto the space spanned by its natural modes and (3) topology optimization techniques.

A design strategy is proposed to optimize the attenuation performance of an insulation panel made of LRAMs for a target band of frequencies, by optimizing the topology of the material at the mesoscale. This allows considering its industrial manufacture by means of emergent 3D-printing or similar techniques. The proposed design strategy is based on (a) fitting the lower bound of the target band with some natural resonance frequency of the material at the design scale, and (b) maximizing the target band's bandwidth. The resulting design exhibits acoustic insulation properties much improved, in comparison to those that could have been obtained by simple trial-and-error procedures, which proves the benefits of the considered CMD methodology.

II.2 Multiscale modelling of LRAMs

The computational homogenization framework introduced in [12] has been used here as the base model upon which the methodology for the design of LRAMs will be built. The framework can be applied to problems where a separation of scales is present, for instance, allowing us to identify a representative volume element (RVE), typically a unit cell, in a macroscopic structure. This separation of scales is established in terms of the macroscopic characteristic wavelength, λ, which has to be larger than the characteristic size of the lower scale, ℓ_μ, otherwise the validity of the homogenization model cannot be guaranteed. This is not an impediment to deal with LRAMs considering they are designed to operate in the low-frequency regime where the condition

$$\lambda \gg \ell_\mu \tag{1}$$

is easily satisfied. In fact, expression (1) is also a condition required for local resonance phenomena to arise [9].

For clarity purposes, from now on magnitudes referring to the microscale will be subscripted by μ, in order to distinguish them from their macroscopic counterparts. Additionally, space coordinates for the macroscale will be referred by x, while those for the microscale will be referred by y, when necessary.

The framework is grounded on a generalization accounting for inertial effects of the classical Hill-Mandel principle [20], in which the macroscale is assumed to behave as a Cauchy's continua, thus satisfying the classical postulates of linear and angular momentum:

$$\nabla_x \cdot \sigma(x,t) = \dot{p}(x,t), \tag{2}$$

$$\sigma(x,t) = \sigma^{\mathrm{T}}(x,t), \qquad \forall\, x \in \Omega, \qquad \forall\, t \in [0,T], \tag{3}$$

where σ is the macroscopic stress, $\dot{p}$ is the macroscopic inertial force, t refers to the time variable, $\dot{(\cdot)}$ stands for the time derivative of $(\cdot)$, and Ω refers to the spatial macroscopic domain. Note that body forces have not been considered, for the sake of simplicity, since they are not relevant in the context of acoustic problems that are tackled here.

By applying an energetic equivalence between scales, which is given by a variational statement of the generalized Hill-Mandel principle, i.e.

$$\dot{p} \cdot \dot{u} + \sigma : \dot{\varepsilon} = \langle \dot{p}_\mu \cdot \dot{u}_\mu + \sigma_\mu : \nabla_y^{\mathrm{S}} \dot{u}_\mu \rangle_{\Omega_\mu}, \qquad \forall\, \dot{u}, \dot{\varepsilon} \quad \textit{and} \quad \forall\, \dot{u}_\mu \in \mathscr{U}_\mu; \tag{4}$$

along with kinematic restrictions that link the macroscopic displacements, u, and strains, $\varepsilon = \nabla_x^{\mathrm{S}} u$, with their microscale counterparts, u_μ and $\varepsilon_\mu = \nabla_y^{\mathrm{S}} u_\mu$, namely

$$\mathscr{U}_\mu := \left\{ u_\mu : \Omega \times [0,T] \to \mathbb{R}^m \;\middle|\; \langle u_\mu \rangle_{\Omega_\mu} = u;\ \langle \nabla_y^{\mathrm{S}} u_\mu \rangle_{\Omega_\mu} = \varepsilon \right\}, \tag{5}$$

one can obtain a Lagrange-extended dynamic system of equations for the RVE in which the Lagrange multipliers, β and λ respectively, corresponding to the reactions to the minimal kinematic restrictions given by Eq. (5) can be identified as

$$\beta = \langle \dot{p}_\mu \rangle_{\Omega_\mu} = \dot{p} \tag{6}$$

$$\lambda = \langle \sigma_\mu + \dot{p}_\mu \otimes^{\mathrm{S}} (y - y^{(0)}) \rangle_{\Omega_\mu}. \tag{7}$$

An in-depth explanation of the theory and further details on the derivation of these terms can be found in Roca *et al*. [12]. Note that the angle brackets symbol is used to refer to the average volume integral over the RVE, i.e. $\langle (\cdot) \rangle_{\Omega_\mu} = \int_{\Omega_\mu} (\cdot) d\Omega$.

After a Galerkin-based finite elements discretization, this so-called extended RVE system has the form:

$$\begin{bmatrix} \mathbb{M}_\mu & 0 & 0 \\ 0 & 0 & 0 \\ 0 & 0 & 0 \end{bmatrix} \begin{bmatrix} \ddot{\hat{u}}_\mu \\ \ddot{\beta} \\ \ddot{\lambda} \end{bmatrix} + \begin{bmatrix} \mathbb{K}_\mu & -\mathbb{N}_\mu^{\mathrm{T}} & -\mathbb{B}_\mu^{\mathrm{T}} \\ -\mathbb{N}_\mu & 0 & 0 \\ -\mathbb{B}_\mu & 0 & 0 \end{bmatrix} \begin{bmatrix} \hat{u}_\mu \\ \beta \\ \lambda \end{bmatrix} = \begin{bmatrix} 0 \\ -u \\ -\varepsilon \end{bmatrix}, \tag{8}$$

where $\mathbb{M}_\mu$ and $\mathbb{K}_\mu$ are the standard mass and stiffness matrices of the RVE system, $\hat{u}_\mu$ is the column vector with the nodal values for microscale displacement field, $u_\mu(y,t)$, while β and λ are, respectively, the Lagrange multipliers associated to the kinematic

restrictions over displacements and their gradient, which are imposed by the matrices $\mathbb{N}_\mu$ and $\mathbb{B}_\mu$, respectively.

Note that, in the system (8), the displacement and strain of the associated point, $\boldsymbol{u}(x,t)$, $\boldsymbol{\varepsilon}(x,t)$, become *actions* and, as indicated by Eqs. (6) and (7), one can relate the *resulting* Lagrange multipliers, $\boldsymbol{\beta}(x,t)$ and $\boldsymbol{\lambda}(x,t)$, with the macroscopic inertial force and stress at that point, $\dot{\boldsymbol{p}}(x,t)$ and $\boldsymbol{\sigma}(x,t)$, respectively. As it is shown in [12], the system (8) can be split into:

(1) *Quasi-static system* ($\boldsymbol{u} = \boldsymbol{0}$)

$$\begin{bmatrix} \mathbb{K}_\mu & -\mathbb{B}_\mu^{\mathrm{T}} \\ -\mathbb{B}_\mu & \boldsymbol{0} \end{bmatrix} \begin{bmatrix} \widehat{\boldsymbol{u}}_\mu^{(1)} \\ \boldsymbol{\lambda}^{(1)} \end{bmatrix} = \begin{bmatrix} \boldsymbol{0} \\ -\boldsymbol{\varepsilon} \end{bmatrix} \tag{9}$$

(2) *Inertial system* ($\boldsymbol{\varepsilon} = \boldsymbol{0}$)

$$\begin{bmatrix} \mathbb{M}_\mu & \boldsymbol{0} \\ \boldsymbol{0} & \boldsymbol{0} \end{bmatrix} \begin{bmatrix} \ddot{\widehat{\boldsymbol{u}}}_\mu^{(2)} \\ \ddot{\boldsymbol{\beta}}^{(2)} \end{bmatrix} + \begin{bmatrix} \mathbb{K}_\mu & -\mathbb{N}_\mu^{\mathrm{T}} \\ -\mathbb{N}_\mu & \boldsymbol{0} \end{bmatrix} \begin{bmatrix} \widehat{\boldsymbol{u}}_\mu^{(2)} \\ \boldsymbol{\beta}^{(2)} \end{bmatrix} = \begin{bmatrix} \boldsymbol{0} \\ -\boldsymbol{u} \end{bmatrix} \tag{10}$$

The split is based on considering each action separately in each subsystem along with certain hypotheses, which are suitable for the study of local resonance phenomena in acoustic problems. In particular:

(a) The macroscopic strain accelerations are negligible, i.e. $\ddot{\boldsymbol{\varepsilon}} \approx \boldsymbol{0}$, allowing for the system (9) to actually behave quasi-statically, thus $\boldsymbol{\beta}^{(1)} = \dot{\boldsymbol{p}}^{(1)} \approx \boldsymbol{0}$.

(b) The RVE's topology exhibits symmetry with respect to its geometric center, which allows us to assume, for the subsystem (10), $\boldsymbol{\lambda}^{(2)} = \boldsymbol{\sigma}^{(2)} \approx \boldsymbol{0}$.

From the quasi-static part of the system, one can derive an expression for the macroscopic stress that reads

$$\boldsymbol{\sigma}(x,t) \approx \mathbf{C}^{\mathrm{eff}}(x) : \boldsymbol{\varepsilon}(x,t), \tag{11}$$

where $\mathbf{C}^{\mathrm{eff}}$ is an effective constitutive tensor.

On the other hand, from the inertial subsystem, it is possible to obtain the macroscopic inertial force as

$$\dot{\boldsymbol{p}}(x,t) \approx \bar{\rho}(x)\ddot{\boldsymbol{u}}(x,t) + \mathbb{Q}(x) \cdot \ddot{\boldsymbol{q}}_\mu(x,t), \tag{12}$$

where $\bar{\rho}$ is the RVE average mass density and the second term in Eq. (12) represents the contribution of coupled micro-inertial effects (through the matrix $\mathbb{Q}$) whose behavior is dictated by the reduced set of uncoupled equations resulting from the modal projection of the inertial subsystem (10)

$$\ddot{\boldsymbol{q}}_{\mu}(\boldsymbol{x},t) + \boldsymbol{\Omega}_{\mu}^{2}(\boldsymbol{x})\boldsymbol{q}_{\mu}(\boldsymbol{x},t) = -\mathbb{Q}^{\mathrm{T}}(\boldsymbol{x}) \cdot \ddot{\boldsymbol{u}}(\boldsymbol{x},t), \tag{13}$$

where $\boldsymbol{\Omega}_{\mu}$ is a diagonal matrix containing the relevant natural frequencies of the inertial subsystem. More details on the derivation of these terms can be found in [12].

II.3 Modelling the viscoelastic behavior in LRAMs

The consideration of viscoelastic phenomena affects the model for the stress-strain relation. While in [12], materials in the microscale where assumed to behave as linear elastic solids, here, in order to account for rate-dependent effects, a more enriched Kelvin-Voigt model will be introduced [18, 19], so that the stress-strain relation becomes

$$\boldsymbol{\sigma}_{\mu}(\boldsymbol{y},t) = \mathbf{C}_{\mu}(\boldsymbol{y}) : \boldsymbol{\nabla}_{\boldsymbol{y}}^{\mathrm{S}}\boldsymbol{u}_{\mu}(\boldsymbol{y},t) + \boldsymbol{\eta}_{\mu}(\boldsymbol{y}) : \boldsymbol{\nabla}_{\boldsymbol{y}}^{\mathrm{S}}\dot{\boldsymbol{u}}_{\mu}(\boldsymbol{y},t), \tag{14}$$

where $\mathbf{C}_{\mu}$ remains as the fourth-order constitutive tensor for an isotropic, linear elastic material and $\boldsymbol{\eta}_{\mu}$ assumes the role of an analogous fourth-order viscous tensor. Since for most polymer-type materials (potential candidates as dissipative coating materials), rate-dependency affects mainly the deviatoric component of the strain velocity, typically the viscosity tensor will be considered as

$$\boldsymbol{\eta}(\boldsymbol{y}) = 2\mu_{\mu}(\boldsymbol{y})\mathbf{I}^{\mathrm{dev}}, \tag{15}$$

where μ_{μ} is the materials' viscosity distribution and $\mathbf{I}^{\mathrm{dev}}$ is the deviatoric fourth-order tensor, defined in index notation as

$$I_{ijkl}^{\mathrm{dev}} = \frac{1}{2}(\delta_{ik}\delta_{jl} + \delta_{il}\delta_{jk}) - \frac{1}{3}\delta_{ij}\delta_{kl}, \tag{16}$$

with δ_{ij} being Kronecker deltas (1 for $i = j$ and 0 otherwise).

Since the hypotheses for homogenization can be compatible with the introduction of this additional effect, the model still holds and the formulation naturally adapts to accommodate this new term. A detailed development of the model's equations with this additional term is provided in Appendix II.A, so in this section, only the changes in the results will be discussed, i.e.:

(a) The first relevant difference is in the expression for the macroscopic stress, which now reads

$$\sigma(x,t) \approx \mathbb{C}^{\text{eff}}(x) : \varepsilon(x,t) + \eta^{\text{eff}}(x) : \dot{\varepsilon}(x,t). \tag{17}$$

Notice the appearance of an effective viscous tensor η^{eff}. This is not surprising considering the viscoelastic model assumed for the microscale in Eq. (14), which has an analogous form.

(b) The second difference appears in the projected inertial system of reduced degrees of freedom. While formally the expression for the macroscopic inertia is the same than in Eq. (12), an additional damping term appears in former equation (13), which now reads

$$\ddot{q}_\mu(x,t) + \Omega_\mu^{\text{D}}(x)\dot{q}_\mu(x,t) + \Omega_\mu^2(x)q_\mu(x,t) = -\mathbb{Q}^{\text{T}}(x) \cdot \ddot{u}(x,t), \tag{18}$$

The new matrix Ω_μ^{D} is responsible for *damping* the vibration near the resonance frequencies of the RVE. While this counteracts the effects of local resonance phenomena in the macroscale (especially the higher the frequency becomes), in a relatively low-frequency regime (where LRAMs operate), and for certain levels of viscosity, it can provide the beneficial effect of extending the effective attenuation band. This phenomenon will be observed and further described in Section II.5.

REMARK 1 It is important to notice that, while the system of equations (13) is fully uncoupled, which allows us to perform an effective reduction of the number of degrees of freedom that need to be considered in the analysis, the same cannot be guaranteed for the system (18), due to the presence of the matrix Ω_μ^{D}, which is non-diagonal, in general, and can make the homogenization model more computationally expensive than in the case where no viscoelastic effects are considered. This increase in computational cost is related to the degree of coupling existing in the matrix Ω_μ^{D}, which ultimately depends on the RVE topology, material properties and modelling of viscoelastic effects in the microscale. For instance, the system (18) would remain fully uncoupled only in cases where the damping matrix is already diagonal or either it is proportional to the stiffness and/or the mass matrices (typically known as proportional Rayleigh damping model), which cause the matrix Ω_μ^{D} to be diagonal. In the specific cases accounting for viscous effects considered in this work, strain rate dependence is only considered in

one of the material components, i.e. the coating, thus, in general, the matrix $\boldsymbol{\Omega}_{\mu}^{\mathrm{D}}$ is non-diagonal. However, the degree of coupling with non-relevant modes will be small enough to be negligible in practice.

II.4 Topological design of LRAMs

Aiming at obtaining LRAMs with topologies designed to achieve better attenuation properties, i.e. increasing the levels and range of transmission loss (in the specific case of acoustic insulation panels), a level-set based topology optimization strategy is proposed here with two main objectives:

(a) Fit the relevant resonance frequencies of the resulting topology into a targeted band. This is done by matching the lower-bound of the target band with a relevant resonance frequency of the RVE (see **FIG. 1**).
(b) Maximize the bandwidth of the target band in terms of the topology of the RVE materials.

In such methodologies, a suitable cost function is minimized, in a variational way, with respect to a characteristic function

$$\chi(\boldsymbol{y}) : \Omega_{\mu} \rightarrow \{0,1\}, \tag{19}$$

that defines the material distribution in the design domain Ω_{μ}, taking values of 1 for *dense material* regions (inclusions): $\boldsymbol{y} \in \Omega_{\mu}^{+}$ and 0 for *soft material* regions (coating/void): $\boldsymbol{y} \in \Omega_{\mu}^{-}$ ($\Omega_{\mu}^{+} \cup \Omega_{\mu}^{-} = \Omega_{\mu}$). These regions are typically determined by a *smooth* level-set function $\phi(\boldsymbol{y})$ such that

$$\chi(\boldsymbol{y}) := \mathscr{H}(\phi(\boldsymbol{y})) \equiv \begin{cases} 0 & \forall\, \boldsymbol{y} \text{ such that } \phi(\boldsymbol{y}) < 0 \\ 1 & \forall\, \boldsymbol{y} \text{ such that } \phi(\boldsymbol{y}) \geq 0 \end{cases}' \tag{20}$$

so that the function $\phi(\boldsymbol{y})$ becomes the unknown of the problem in a variational context.

Prior to presenting the optimization problem itself, let us first review the RVE equations that will be required to solve this problem. First, in order to obtain the RVE's relevant resonance frequencies, the modal problem of the *restricted* system must be solved

$$\left(\mathbb{K}_{\mu}^{*} - \lambda_{\mu}^{*(k)} \mathbb{M}_{\mu}^{*}\right) \widehat{\boldsymbol{\phi}}_{\mu}^{*(k)} = \mathbf{0}, \qquad \widehat{\boldsymbol{\phi}}_{\mu}^{*(k)\mathrm{T}} \mathbb{M}_{\mu}^{*} \widehat{\boldsymbol{\phi}}_{\mu}^{*(k)} = 1, \tag{21}$$

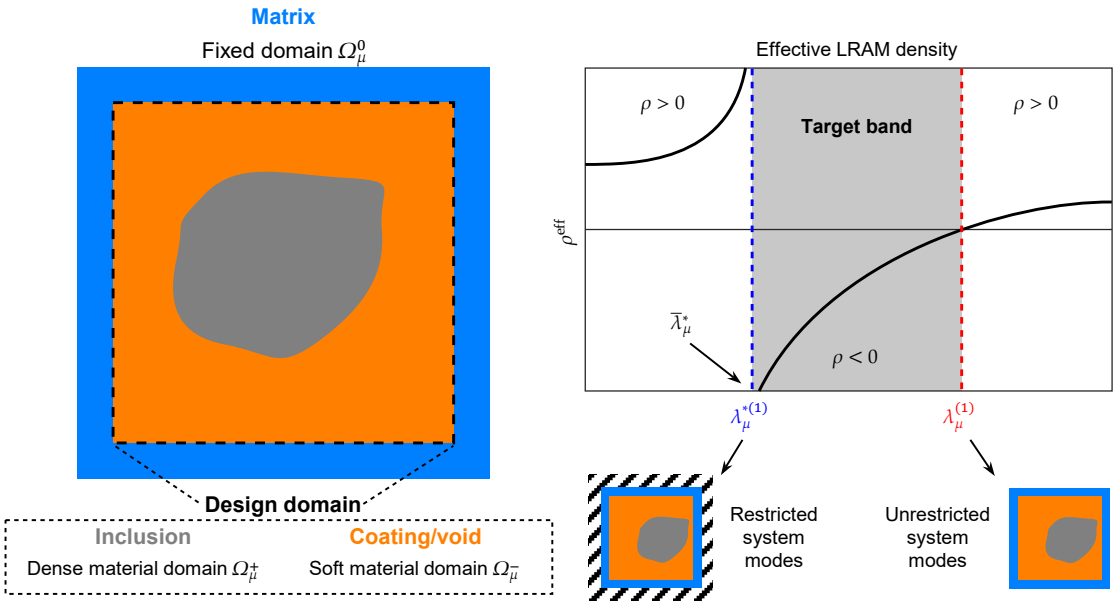

FIG. 1 RVE configuration for the LRAM topology optimization (left) and typical effective LRAM density diagram depicting the frequency bandgap corresponding to negative densities (right). In order to ensure LRAM-like behavior, a fixed matrix of material is considered, Ω_μ^0, with constant material properties and $\chi(y) = 1, \forall\, y \in \Omega_\mu^0$. Only in the inside region the characteristic function χ is allowed to change giving rise to dense material volumes corresponding to inclusions, Ω_μ^+, and soft material volumes corresponding to void/coating material, Ω_μ^-. The resulting resonance frequencies $\omega_\mu^{*(1)} = \sqrt{\lambda_\mu^{*(1)}}$ and $\omega_\mu^{(1)} = \sqrt{\lambda_\mu^{(1)}}$ associated to the restricted and unrestricted system modes, respectively, determine the lower and upper bounds of the target band, whose lower bound is matched to $\overline{\lambda}_\mu^*$.

where $\mathbb{K}_\mu^*$ and $\mathbb{M}_\mu^*$ are the resulting stiffness and mass matrices once the kinematic restrictions on the microfluctuation field have been applied. In this specific case, since the local resonance phenomenon occurs at frequencies corresponding to *internal* vibration modes, a good approximation to meet our goals consists of prescribing all RVE boundaries. The terms $\lambda_\mu^{*(k)}$ and $\widehat{\boldsymbol{\phi}}_\mu^{*(k)}$ correspond to the squared natural frequencies and mass-normalized vibration modes of the system. According to Eq. (12), only those modes $\widehat{\boldsymbol{\phi}}_\mu^{*(k)}$ such that their corresponding columns in the generalized coupling matrix $\mathbb{Q}$ are larger than a certain tolerance δ_{tol}, should be considered as relevant. Thus, the set of *relevant* resonance frequencies is given by

$$\omega_\mu^{*(k)} = \sqrt{\lambda_\mu^{*(k)}} \quad \text{such that} \quad \|\mathbb{Q}^{(k)}\| \equiv \|\langle \rho_\mu \boldsymbol{\phi}_\mu^{*(k)} \rangle_{\Omega_\mu}\| > \delta_{\text{tol}}. \tag{22}$$

Furthermore, since transmission loss peaks in LRAM panels are closely related to frequency bandgaps, whose lower and upper limits can be identified, respectively, with the relevant resonance frequencies of the *restricted* and *unrestricted* RVE system, $\omega_\mu^{*(k)}$ and $\omega_\mu^{(k)}$, as reported in [12] (see Fig. 1 for a schematic representation), one can maximize their bandwidth, for instance, by minimizing the ratio $\lambda_\mu^{*(k)}/\lambda_\mu^{(k)}$, where $\lambda_\mu^{(k)}$ comes from the modal problem considering the mass and stiffness matrices of the RVE system prior to applying the kinematic restrictions, i.e.

$$\left(\mathbb{K}_\mu - \lambda_\mu^{(k)}\mathbb{M}_\mu\right)\widehat{\boldsymbol{\phi}}_\mu^{(k)} = \mathbf{0}, \qquad \widehat{\boldsymbol{\phi}}_\mu^{(k)\mathrm{T}}\mathbb{M}_\mu\widehat{\boldsymbol{\phi}}_\mu^{(k)} = 1, \tag{23}$$

where in this case, the only relevant $\lambda_\mu^{(k)}$ that correspond to upper bounds of the frequency bandgaps can be identified by

$$\omega_\mu^{(k)} = \sqrt{\lambda_\mu^{(k)}} \quad \text{such that} \quad \lambda_\mu^{(k)} > 0 \quad \text{and} \quad \|\langle\boldsymbol{\phi}_\mu^{(k)}\rangle_{\Omega_\mu}\| > \delta_{\mathrm{tol}}. \tag{24}$$

Note that, in this case, the additional condition $\lambda_\mu^{(k)} > 0$ needs to be applied in order to avoid rigid body translation modes, which are relevant according to condition $\|\langle\boldsymbol{\phi}_\mu^{(k)}\rangle_{\Omega_\mu}\| > \delta_{\mathrm{tol}}$, but do not define the upper bounds of any bandgap.

In this regard, the objective function proposed to minimize is given by

$$\Pi(\chi(\phi)) = \alpha f^2 + (1-\alpha)g^2, \tag{25}$$

with

$$f = \frac{\ln\lambda_\mu^{*(1)}(\chi(\phi)) - \ln\bar{\lambda}_\mu^*}{\ln\lambda_\mu^{*(1)}(\chi(\phi)) + \ln\bar{\lambda}_\mu^*} \tag{26}$$

$$g = \frac{\ln\lambda_\mu^{*(1)}(\chi(\phi))}{\ln\lambda_\mu^{(1)}(\chi(\phi))} \tag{27}$$

subject to the state-equations (21) and (23). In Eqs. (25) to (27), α is a weighting parameter to establish the relative importance of each term in the global objective function, $\bar{\lambda}_\mu^*$ is the imposed targeted squared frequency to fit with the first relevant squared resonance frequency for the *restricted* RVE system $\lambda_\mu^{*(1)}$, while $\lambda_\mu^{(1)}$ refers to the first relevant squared resonance frequency for the *unrestricted* RVE system. Note that, as long as $0 \leq \alpha \leq 1$, the objective function will be bounded $\Pi \in [0,1]$, so that it reaches

its minimum value when all the desired objectives are fulfilled. For the sake of simplicity, only the first frequency band is targeted to fit in this framework, but Eq. (25) can be easily extended to target multiple frequency bands simply by adding the corresponding terms in the cost function.

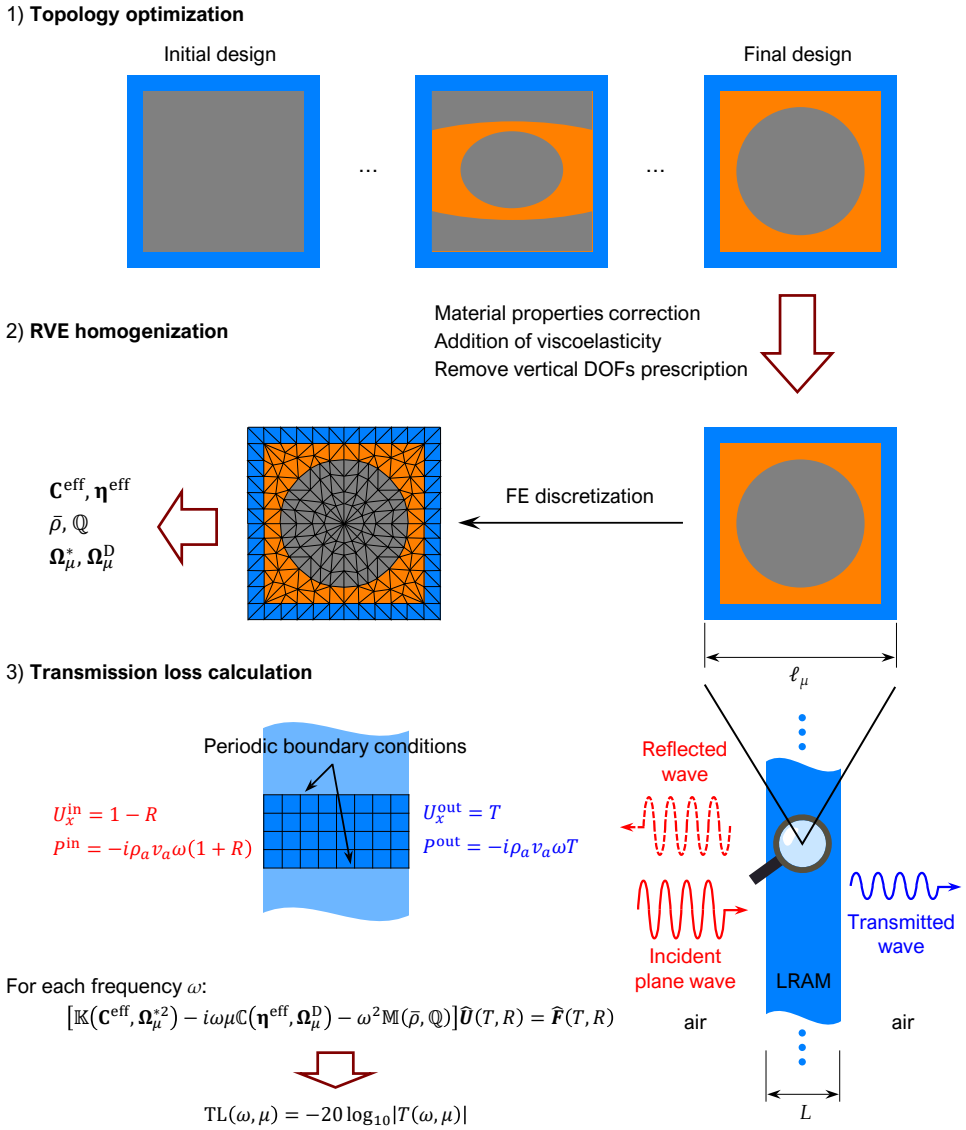

FIG. 2 Global procedure to evaluate the transmission loss of a LRAM panel with a topology optimized design. The material distribution is obtained from the topology optimization algorithm. This result is used to build an RVE with the actual material properties from which the effective properties are computed by employing the multiscale homogenization framework. Finally, a macroscale analysis is performed over a slice of the panel, imposing displacement and traction compatibility conditions with the incoming and outgoing waves and periodic boundary conditions at the material boundaries (in order to simulate the infinite extension of the panel in the vertical direction). This analysis is performed in the frequency domain for several test frequencies allowing us to obtain the transmission and reflection coefficients of the panel, T and R, respectively.

The optimization problem then reads

FIND

$$\chi(\boldsymbol{y}) = \mathscr{H}(\phi(\boldsymbol{y})) : \Omega_\mu \rightarrow \{0,1\};$$

FULFILLING

$$\begin{aligned} &\chi = \arg\min_{\chi} \Pi(\lambda_\mu^{*(1)}(\chi), \lambda_\mu^{(1)}(\chi)), \\ &\text{s.t.} \quad \left(\mathbb{K}_\mu^* - \lambda_\mu^{*(k)}\mathbb{M}_\mu^*\right)\widehat{\boldsymbol{\phi}}_\mu^{*(k)} = \mathbf{0}, \\ &\qquad \left(\mathbb{K}_\mu - \lambda_\mu^{(k)}\mathbb{M}_\mu\right)\widehat{\boldsymbol{\phi}}_\mu^{(k)} = \mathbf{0}. \end{aligned} \tag{28}$$

A time-marching technique is used to update the problem with a pseudo-time variable, from an initial state (typically all the design area full with dense material) towards a problem's solution. In this case, a Hamilton-Jacobi approach has been considered in which the problem's evolution has been defined in a rate form as

$$\dot{\phi}(\boldsymbol{y}, t) \equiv \frac{\partial \phi(\boldsymbol{y}, t)}{\partial t} = -C_1 \frac{\delta \Pi_t}{\delta \chi}(\boldsymbol{y}), \tag{29}$$

allowing us to obtain the updated value of function ϕ from the previous iteration step through a straightforward time discretization of Eq. (29)

$$\phi^{n+1}(\boldsymbol{y}) = \phi^n(\boldsymbol{y}) - \Delta t C_1 \frac{\delta \Pi_t}{\delta \chi}(\boldsymbol{y}), \qquad \forall\, \boldsymbol{y} \in \Omega_\mu \tag{30}$$

where Δt is a pseudo-time step, $C_1 > 0$ is a parameter and $\delta\Pi_t/\delta\chi$ is the topological sensitivity, evaluated at point $\boldsymbol{y}$, of the cost function (25), here named as the Variational Topological Derivative (VTD) of the functional Π. In Appendix II.B it is proven that the iterative scheme in Eq. (30) yields an iterative descend of the cost function Π, i.e. $\dot{\Pi}_t(\chi) \leq 0\ \forall\, t$, a crucial aspect for the convergence of the Hamilton-Jacobi algorithm.

To ensure that local resonance phenomena arise in the computed designs throughout the optimization process, the frequency fitting will always be required, and typically aimed at the smallest relevant resonance frequency achievable (i.e. $\alpha > 0$) which, for a given set of material properties, will be constrained by the dimensions of the design domain (in this case the RVE). Furthermore, the RVE will consist of a fixed matrix material frame (non-design domain) so that the actual design domain is the inclusion/coating distribution on the inside (see Fig. 1).

Some additional hypotheses have been made in order to avoid spurious modes resulting from the modal analysis, which helps the optimization algorithm to become more stable and converge to the desired solutions. These hypotheses are listed and explained below:

(a) The matrix fixed frame is considered infinitely stiff so that no deformation modes, which are non-relevant in this context, appear in the modal analysis. This is done to prevent modes in which the matrix interacts with the other materials, especially in early steps of the algorithm, when the whole domain is filled with material.

(b) The void/coating material is considered massless. Since the modes causing the local resonance phenomena to arise are those in which the inclusions vibrate inside the coating phase, the relevant properties that are to be considered will be the density of the inclusion phase and the stiffness of the coating material. Forcing the density of the coating material to zero (or a very small tolerance value), avoids the appearance of spurious modes in the modal analysis which greatly helps the identification of the relevant resonance modes.

(c) Since the focus in this context is in horizontally oriented modes (the panel will be subjected to plane waves propagating on the horizontal direction), all vertical degrees of freedom are prescribed in both the restricted and unrestricted systems. By restricting the analysis to a single dimension, both the identification of the relevant modes and the pairing of each bandgap limiting frequencies become much easier.

II.5 Application to the design of an acoustic insulation panel

Let us consider an infinitely large flat panel with a given thickness L built with stacked LRAM unit cells (of size ℓ_μ) consisting of 3 material phases: an epoxy matrix frame at the boundaries along with a certain distribution of steel inclusions embedded in a silicone rubber coating (see Fig. 1 for a graphical depiction of a typical RVE configuration). The material properties used in the examples that follow are listed in Tab. 1. The coating material will be considered viscoelastic, with the viscosity μ left out as a parameter in order to enable the possibility of evaluating the LRAM behaviour for various degrees of dissipation. Since the aim of this analysis is to assess the attenuation of acoustic waves through a slab of a designed LRAM panel, the transmission loss in the specific frequency range of interest (in this case below 3000 Hz) will be computed. To do so, a 3-step

analysis is performed. First, the topology optimization procedure explained in Section II.4 is used to obtain a material distribution for the LRAM design that meets the desired properties. Then, a RVE is built upon the results obtained from the previous step with the actual material properties, so the homogenization procedure detailed in Sections II.2 and II.3 can be applied to compute the effective material properties associated to that LRAM design. Finally, an analysis on the macroscale is performed by computing the transmission loss in the desired frequency range for a flat panel composed of the homogenized LRAM subjected to acoustic plane waves. Details on each of these procedures is given in the following sections, while a summary of the global scheme is depicted in Fig. 2. A plane-strain 2D approach is considered in all the examples instead of a 3D setting simply to avoid the unnecessary complexity associated with them which, at least regarding the effects and conclusions that are expected to point out in this work, do not give any relevant additional insights. Therefore, for the sake of clarity in terms of interpretation of the results, the examples shown here are all 2D, even though both the formulation and the conclusions that can be extracted can be extended to 3D.

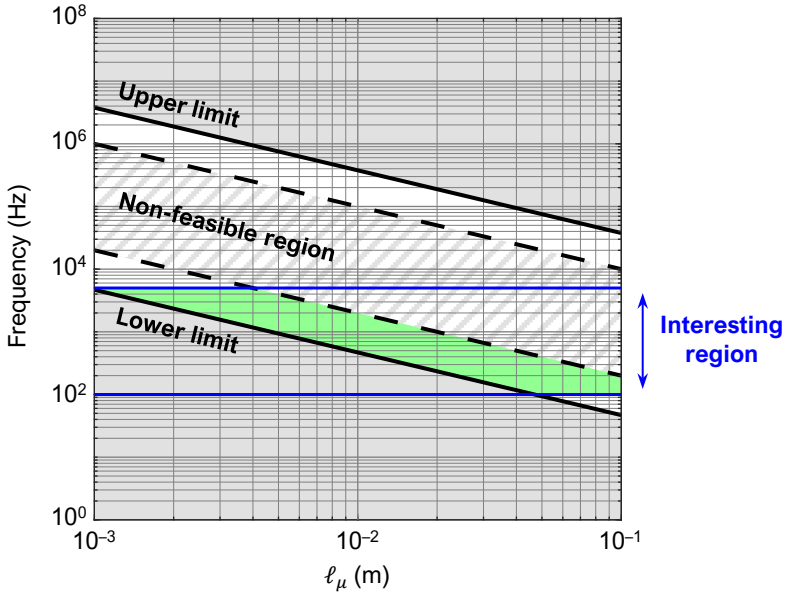

FIG. 3 Representation of the valid regions for achievable first target resonating frequencies in terms of the RVE size. Upper and lower limits and the so-called non-feasible region have been obtained with the material and numerical properties for this example, which are listed in Tab. 1. The green shaded area corresponds to the region of achievable first target resonating frequencies within the range of interest.

TAB. 1 Material properties [3].

Material	Density ρ_μ (kg/m^3)	Bulk mod. K_μ (MPa)	Shear mod. G_μ (MPa)
Epoxy	1180	5.49×10^3	1.59×10^3
Steel	7780	1.72×10^5	7.96×10^4
Silicone rubber	1300	0.63	0.04

II.5.1 Topology optimization of the LRAM

A 2D structured mesh of 100 $\times$ 100 quadrilateral elements with 4 Gaussian integration points has been used for the computations in this stage. The elastic properties of the matrix phase have been scaled by a factor 10^{10} to guarantee its behavior as a rigid component, while the density of the coating has been scaled by 10^{-10} to avoid spurious, non-relevant modes resulting from the modal analysis. A value of $\Delta t = 10^{-3}$ has been considered as a pseudo-timestep for the time-marching algorithm, along with an initial $\phi^0 > 0$ that makes all the design domain to be full of inclusion dense material (see Eq. (20)). The size of the RVE has been chosen to be 1 $\times$ 1 cm to ensure that the resulting resonating frequencies lie on the desired range. This is important since for a given set of material properties and a domain size, there are limitations in the achievable resonant frequencies. An obvious first upper limit can be found in the first resonant frequency obtained by the initial full-material configuration, which depends on the properties of the inclusion phase as well as the RVE size and is typically well above (by several orders of magnitude) the desired frequency range. On the other hand, a theoretical lower limit can also be estimated as

$$\omega_\mu^{*(1)} > \frac{1}{\ell_\mu}\sqrt{\frac{\min\limits_i \left\{K_\mu^{(i)} + \frac{4}{3}G_\mu^{(i)}\right\}}{\max\limits_i \rho_\mu^{(i)}}} \tag{31}$$

where the index i here refers to each material. Furthermore, given the high contrast between the properties of the inclusion and coating components, there is a range of frequencies between these lower and upper limits for which the algorithm finds it more difficult to converge to a solution. This is because solutions in this range typically contain physically unstable solutions characterized by large changes in the resonance frequencies for small perturbations in the topology (in this case, caused by the appearance of unrealistically thin strings of material). Therefore, designs inside this zone

should be avoided to preclude such unstable behavior. Note also that these solutions can be easily avoided for a given target frequency by reducing the size of the design domain (see Fig. 3 as an example).

For this example, a target frequency of $\overline{\omega}_{\mu}^{*(1)} = 1000$ Hz is selected and two different weighting parameters have been tested: one that causes only the frequency fitting to be considered in the objective function ($\alpha = 1$), and another one where the weight is distributed equally among the fitting and the bandgap maximization parts ($\alpha = 0.5$). Fig. 4 shows the evolution of the objective function and the volume fraction of material, respectively. The first relevant resonating frequencies for the restricted and unrestricted problems can be seen in Fig. 5.

These results show how the algorithm removes inclusion material in the topology, reducing the value returned by the objective function, as seen Fig. 4-(a), and thus approaching the desired targets with each iteration step. It is worth noting the sudden jump produced around the 100^{th} iteration in both cases. It is caused by the disengagement of the inclusion material from itself, which makes the coating phase to fully envelop it. Since the stiffness of the coating material is several orders of magnitude lower, the resulting configuration makes it easier for the enclosed inclusion to vibrate, which translates into a much lower resonance frequency.

Interestingly, while the volume fraction of material ends up being very similar in both cases, as seen in Fig. 4-(b), the resulting topologies are quite different. Note also that the resonance frequency for the restricted problem follows a similar evolution in both cases (eventually meeting the target frequency of 1000 Hz), but the differences between their associated topologies make their respective unrestricted system's resonance frequency to evolve differently (see Fig. 5). In particular, when the bandgap maximization is also part of the objective function the algorithm tends to remove material from the matrix internal borders, concentrating the maximum amount of mass onto the central inclusion. This translates into a significant increase of the bandgap size, for a similar volume fraction of material distribution, by almost 6 times (around 600 Hz in the first case and up to 3500 Hz in the second).

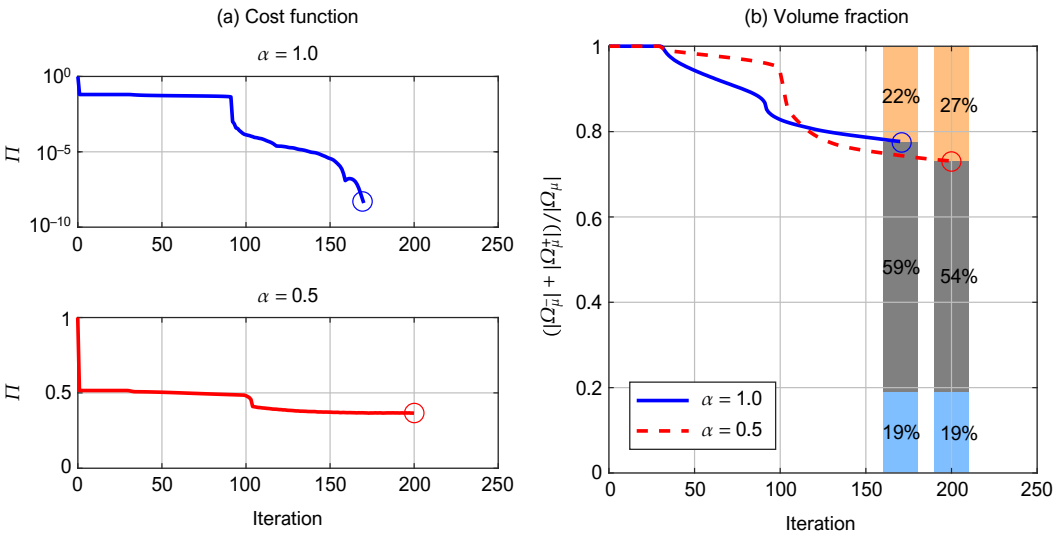

FIG. 4 (a) Evolution of the objective function upon each iteration for the frequency fitting case (top) and the frequency fitting along with bandgap maximization (bottom). For $\alpha = 0.5$, a trade-off must be met between the frequency fitting part and the bandgap maximization component, which makes it more difficult for the algorithm to converge. (b) Evolution of the volume fraction upon each iteration. Note that the colorbar represents the volume fraction distribution of each material in the domain. The fixed matrix (blue) represents 19% of the volume in both cases, and the remaining 81% is distributed between inclusion (grey) and coating phases (orange).

REMARK 2 It must be considered that the frequencies obtained from the optimization process will not be equal to those computed when actual material properties (without scaling factors) are considered, as it will be seen in the results of the next section. However, this is not a major issue for our purposes, since with the actual material properties, the system tends to be less restricted and so the resulting frequencies are smaller, which is often desirable. In any case, the size of the RVE can be adjusted accordingly to match the target frequencies, if desired.

II.5.2 Homogenization of the optimized LRAM

With the material distributions obtained in the previous step, RVEs are built, maintaining their size but with the actual material properties. The homogenization framework detailed in Sections II.2 and II.3 is applied to compute the effective material parameters associated to each LRAM design. These include the effective constitutive tensor, $\mathbf{C}^{\text{eff}}$, the average

density $\bar{\rho}$, the coupling matrices related to micro-inertial phenomena, $\mathbb{Q}$, $\boldsymbol{\Omega}_{\mu}$, and the additional terms $\boldsymbol{\eta}^{\mathrm{eff}}$, $\boldsymbol{\Omega}_{\mu}^{\mathrm{D}}$, accounting for viscous effects. For these computations, 2D meshes of triangle elements with an average relative size of 0.02 and 3 Gaussian integration points have been used, which provide around 7000 degrees of freedom. Fig. 6 shows the resulting first resonance modes and frequencies which, as previously anticipated in Remark 2, are smaller than the computed as part of the optimization process in the previous section. Note, however, that the predicted bandgap in the case with $\alpha = 0.5$ is much larger than in the other case (around 1500 to 450 Hz, which is between 3 and 4 times bigger). This can also be seen in the dispersion diagrams of Fig. 7, which are calculated assuming a plane wave travelling in the x-direction in an infinite extension of the homogenized material domain (see [12] for details on this computation). For the case without viscosity ($\mu = 0$), a non-null imaginary component of the wavenumber indicates the presence of a frequency bandgap. In Fig. 7, the results of applying Bloch-Floquet boundary conditions on the same RVEs [9] are also shown to validate the proposed model. Note that there is good agreement between both computations, even for the cases where viscosity is present.

II.5.3 Transmission loss computation

Finally, a macroscale analysis is performed over a homogenized panel from which the transmission coefficient is obtained. For the sake of simplicity, the panel is assumed to be surrounded by air (with density $\rho_a = 1.2$ kg/m^3 and sound propagation speed $v_a = 344$ m/s) where a plane wave travels perpendicular to the panel's surface. In order to find the transmission coefficient in this case, compatibility conditions for the normal component of the displacement and traction forces are imposed at the panel's interfaces with the air media. In this context, one can assume the air at the left-hand side to propagate as a wave at a certain frequency ω:

$$u_x^{(l)}(\boldsymbol{x}, t) = (e^{i\kappa_a x} - Re^{-i\kappa_a x})e^{-i\omega t} \tag{32}$$

$$p^{(l)}(\boldsymbol{x}, t) = -i\rho_a v_a \omega (e^{i\kappa_a x} + Re^{-i\kappa_a x})e^{-i\omega t} \tag{33}$$

where $u_x^{(l)}$ and $p^{(l)}$ are the horizontal displacement and pressure fields, respectively, $\kappa_a = \omega / v_a$ is the wavenumber and R is the reflection coefficient, i.e. the fraction of the incident wave's amplitude that is reflected at the panel's interface. At the right-hand side, only part of the wave is transmitted, so

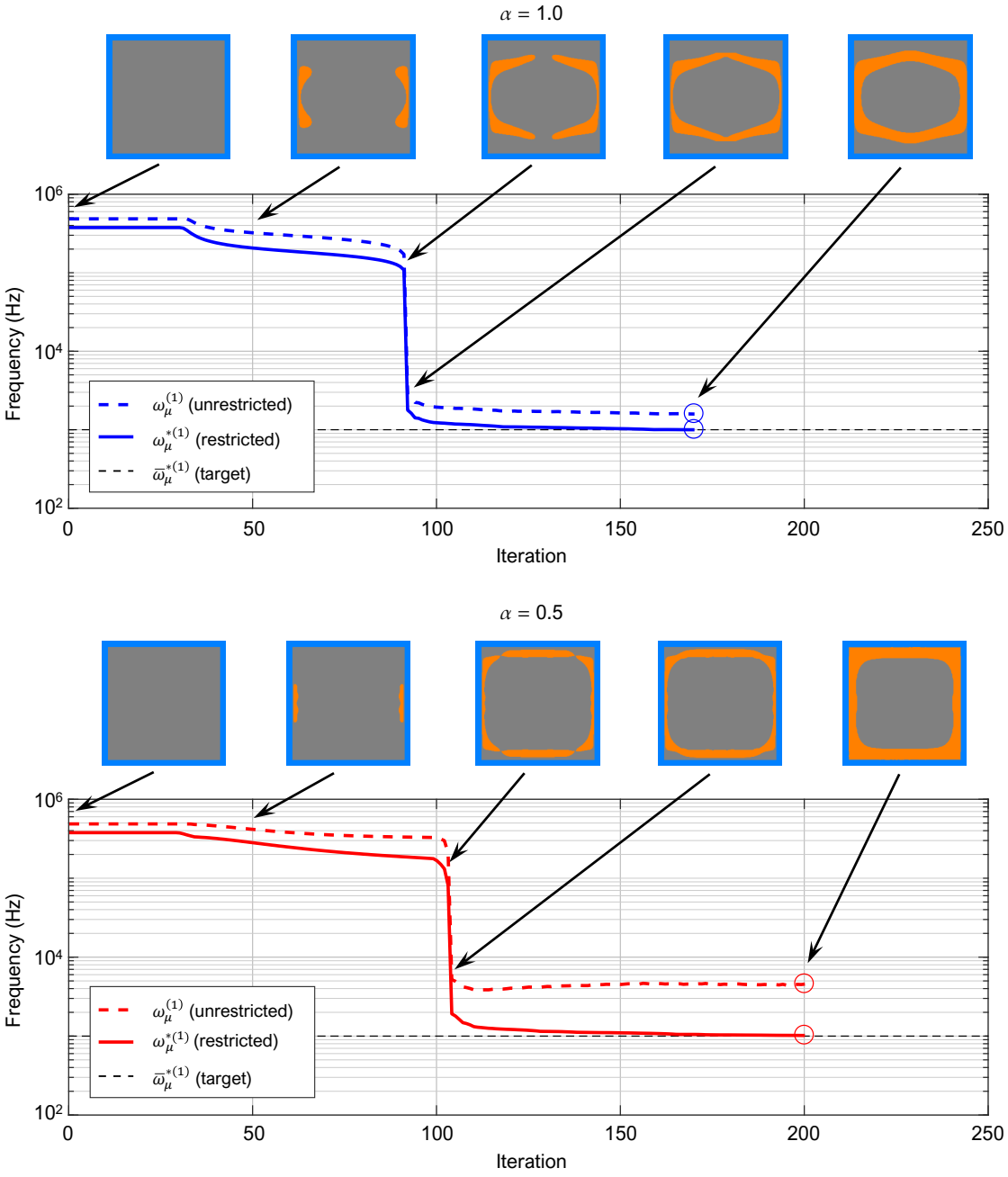

FIG. 5 Evolution of the first relevant resonance frequencies for the restricted and unrestricted systems upon each iteration for the frequency fitting case (top) and frequency fitting along with bandgap maximization case (bottom). The topology determined by the level-set function ϕ at several iteration steps is also shown. Note the sudden jump in frequencies coincides with the iteration when the inclusion is disengaged. This gap gives an idea of the region of unattainable frequencies due to numerical issues.

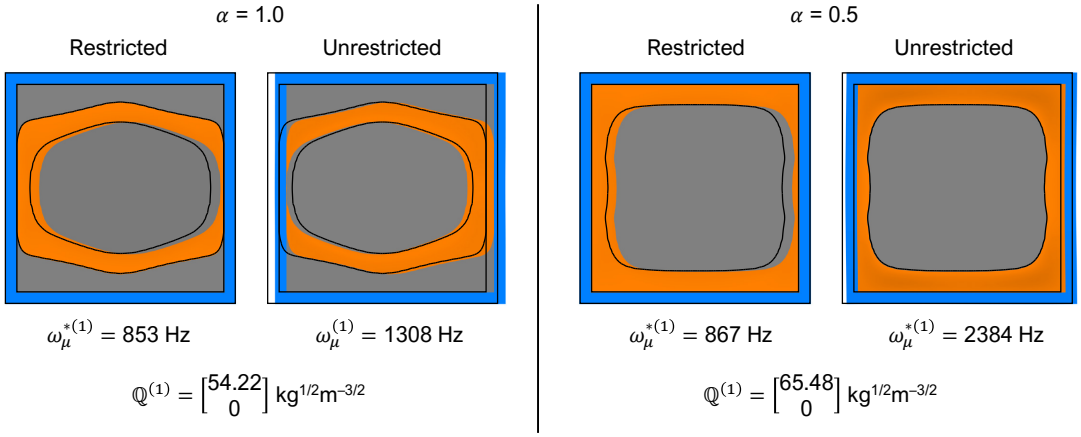

FIG. 6 First relevant resonance modes and frequencies for the restricted and unrestricted systems for the topologies resulting from the frequency fitting optimization (left) and the frequency fitting coupled with the bandgap maximization (right). The solid black lines represent the material interfaces of the non-deformed state.

$$u_x^{(r)}(\boldsymbol{x},t) = Te^{i(\kappa_a x-\omega t)} \tag{34}$$

$$p^{(r)}(\boldsymbol{x},t) = -i\rho_a v_a \omega T e^{i(\kappa_a x-\omega t)} \tag{35}$$

where T is the transmission coefficient, i.e. the fraction of the incident wave's amplitude that is transmitted through the panel. To find R and T, a simple 2D FE discretization of 4 $\times$ 4 quadrilateral elements with 4 gaussian integration points over a portion of the panel is performed. The resulting system is solved in the frequency domain for each frequency in the desired range, in this case from 0 to 3000 Hz. Periodic boundary conditions are applied on the top and bottom boundary nodes (to simulate the infinite extension of the panel in the vertical direction) and the compatibility conditions given by Eqs. (32) to (35) are applied on the left and right boundary nodes. The resulting system can be expressed in matrix form as

$$\left(\mathbb{K} - i\omega\mu\mathbb{C} - \omega^2\mathbb{M}\right)\widehat{\mathbf{U}}(R,T) = \widehat{\mathbf{F}}(R,T). \tag{36}$$

Since both $\widehat{\mathbf{U}}$ and $\widehat{\mathbf{F}}$ are functions of the reflection and transmission coefficients (as a result of applying the compatibility conditions), Eq. (36) can be reduced to a system with only R and T as unknowns (details on the derivation of this system are given in Appendix II.C). Thus, for a given frequency ω and viscosity μ, once the transmission coefficient T is solved, the transmission loss is computed using the expression

$$\mathrm{TL}(\omega,\mu) = -20\log_{10}\left|T(\omega,\mu)\right| \text{ [dB]}. \tag{37}$$

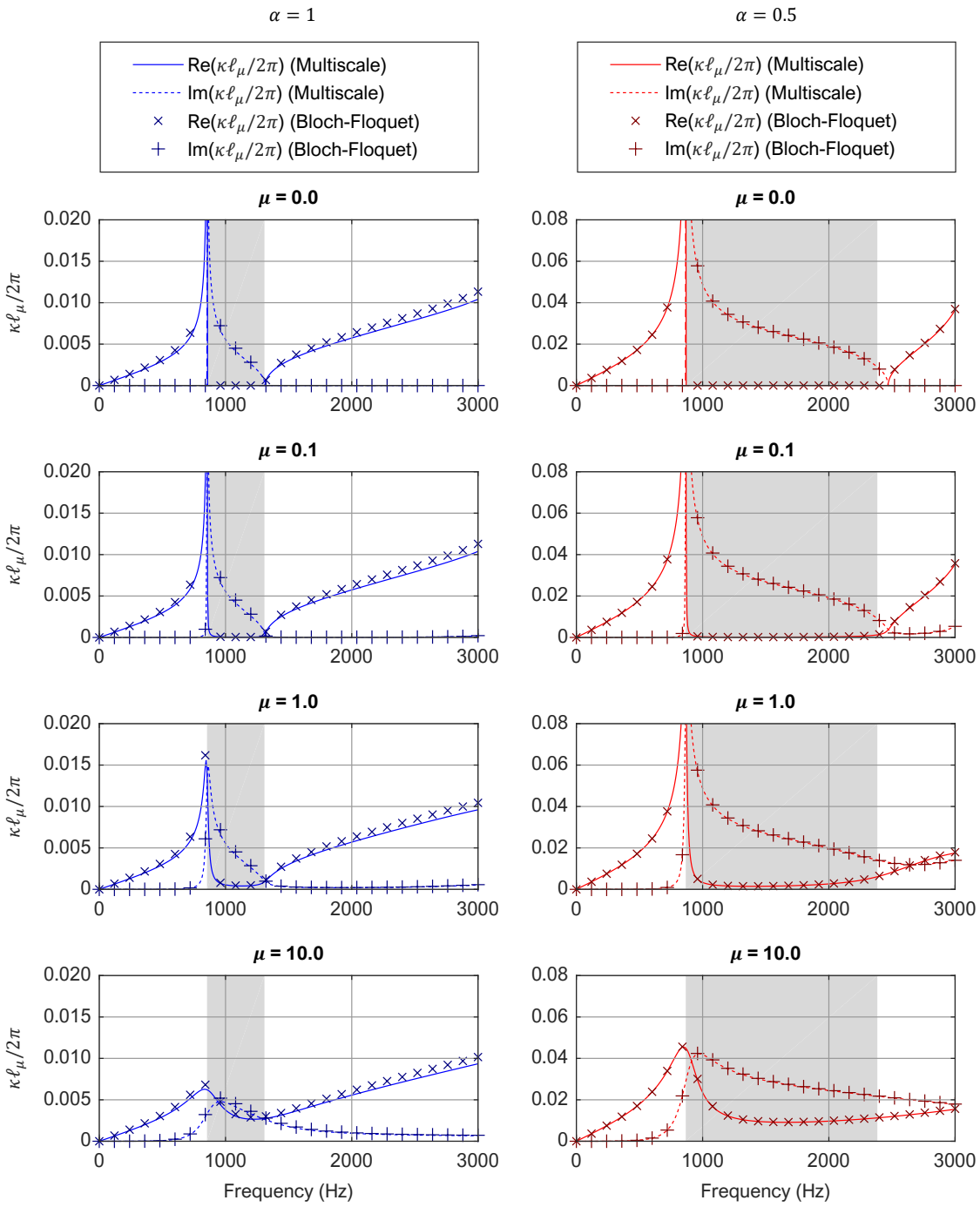

FIG. 7 Dispersion diagram for the topologies resulting from the frequency fitting optimization (left) and the frequency fitting coupled with the bandgap maximization (right). The shaded areas correspond to the bandgap regions corresponding to purely imaginary wavenumbers in the case without viscosity ($\mu = 0$). The units for the viscosity parameter μ are Pa·s. Note that the real part of the normalized wavenumber corresponds to the solid lines and 'x' markers, while its imaginary component is represented through dashed lines and '+' markers in the same axes. The results obtained with the multiscale homogenization procedure are compared with those obtained applying Bloch-Floquet boundary conditions on the same RVEs, for validation purposes.

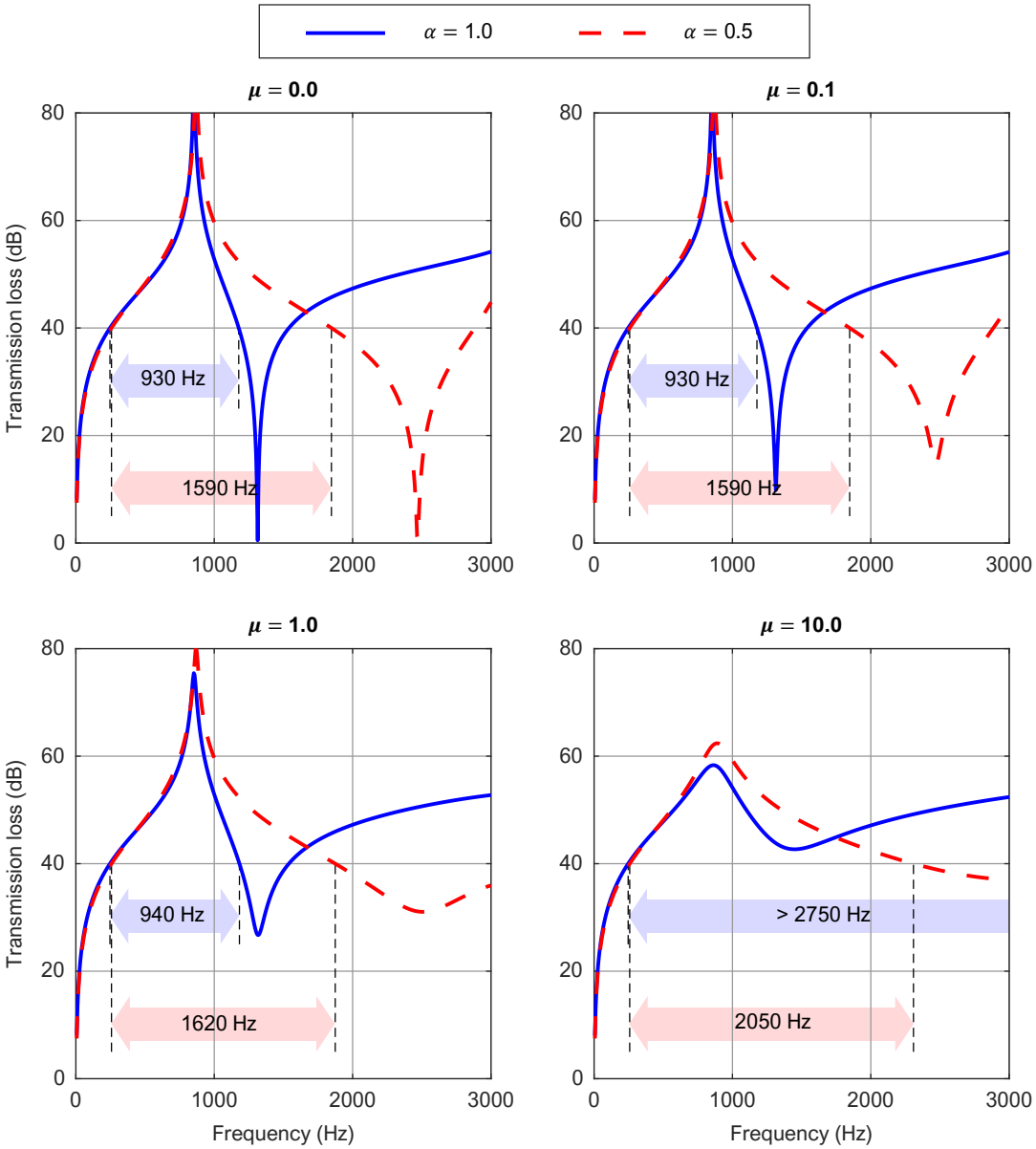

FIG. 8 Transmission loss (TL) for the topologies resulting from the frequency fitting optimization (solid blue line) and the frequency fitting coupled with the bandgap maximization (red dashed line). The light-shaded arrows indicate the bandwidth of the effective attenuation bands corresponding to the first uninterrupted attenuations > 40 dB. The units for the viscosity parameter μ are Pa·s.

The results are shown in Fig. 8 where the transmission loss has been computed for a panel with thickness of 1 cm (equivalent to a single RVE) and for both the topologies without and with the bandgap maximized. One can observe that the effect of the bandgap maximization ($\alpha = 0.5$) translates also into a larger frequency range of effective attenuation. For instance, for attenuation levels above 40 dB, the effective bands in both

cases start around 250 Hz, but they extend to 1180 Hz in the first case and to 1840 in the second (660 Hz increase).

It can also be observed that the viscosity has the beneficial effect of smoothing the undesired inverted resonance peaks but at the same time it also dampens the attenuation peaks caused by the local resonance phenomena occurring at the microscale. Depending on the desired attenuation performance, one can take advantage of the viscoelastic properties of the coating component to slightly increase the effective attenuation band or even bypass the undesired inverted resonance peak while keeping a continuous effective attenuation band with a good level of attenuation in the low frequency range of interest (as it can be seen for the case of $\mu = 10$ Pa · s, where viscous effects are more relevant).

II.6 Concluding remarks

While the methodology presented has been used in the study of flat panels under plane acoustic pressure waves, it can be suitably adapted to more complex cases still satisfying the low-frequency range restriction. On the one hand, the objective function of the topology optimization algorithm can be adapted to tackle one or multiple frequencies depending on the user interest. On the other hand, the ability of the homogenization procedure to provide a set of effective *constitutive* properties makes it possible to easily study the behavior of complex geometries in the macroscale under several sets of boundary conditions and external actions, including, for instance, the characterization of transient states or multiple layer configurations, so long as they satisfy the hypotheses considered. This is in contrast to other homogenization approaches, such as those based on the Bloch-Floquet theory, which have the ability to study the effective behavior of RVEs without restrictions in terms of frequencies, but that are limited to predetermined macroscopic configurations, namely, infinitely periodic structures, in the case of the Bloch-Floquet theory, that cannot account for the introduction of other more realistic sets of boundary conditions.

In this regard, the design procedure presented in this work offers a powerful tool for the design of LRAM acoustic insulation devices tackling the low frequency range. By combining the optimization algorithm for designing the RVE topology with the homogenization method for characterizing the material's performance, one can easily assess the transmission loss of a panel for a broad range of frequencies. The studies

carried out show the influence of the RVE topology in achieving certain properties in the final design such as, for instance, an increased bandgap size for a given frequency range with the same amount of material, and thus the same mass. It is worth noting that while the target frequencies and choice of materials greatly determine the size of the RVE, its topology optimization can be used to reduce the effective density making the resulting panel suitable for lightweight applications. On the other hand, it has been observed that the presence of highly viscoelastic materials in the design generally affects negatively the local resonance performance of the RVE. However, in certain viscosity ranges, one can take advantage of the resulting damping effects to smooth undesired resonance peaks in the macroscale and even join attenuation bands, especially in higher frequency ranges, while still maintaining good attenuation levels in the low-frequency range of interest where the local resonance of the RVE takes place.

Acknowledgements

This research has received funding from the European Research Council (ERC) under the European Union's Horizon 2020 research and innovation programme (Proof of Concept Grant agreement nº 779611) through the project "Computational catalog of multiscale materials: a plugin library for industrial finite element codes" (CATALOG). The authors also acknowledge the funding received from the Spanish Ministry of Economy and Competitiveness through the research grant DPI2017-85521-P for the project "Computational design of Acoustic and Mechanical Metamaterials" (METAMAT).

Appendix II.A Introduction of viscoelastic effects in the homogenization framework

Considering Eq. (14) for the stress definition in the microscale, causes a damping matrix, $\mathbb{C}_\mu$, to arise from the Finite Element discretization of the RVE system, in addition to the standard mass and stiffness matrices, $\mathbb{M}_\mu$ and $\mathbb{K}_\mu$. This damping matrix appears only in the elements where viscoelastic effects are considered, in which it is defined as

$$\mathbb{C}_\mu^{(e)} = \langle \mathbf{B}_\mu^{(e)T} : \boldsymbol{\eta}_\mu^{(e)} : \mathbf{B}_\mu^{(e)} \rangle_{\Omega_\mu^{(e)}} \tag{A.1}$$

where $\mathbf{B}_\mu^{(e)}$ gives the derivatives of the shape functions for the type of elements considered, and $\boldsymbol{\eta}_\mu^{(e)}$ is the element's viscous tensor, which can be expressed, following Voigt's notation, in terms of the associated material's viscosity, $\mu^{(e)}$, as

$$\boldsymbol{\eta}_{\mu}^{(e)} = \mu^{(e)} \begin{bmatrix} 4/3 & -2/3 & -2/3 & 0 & 0 & 0 \\ -2/3 & 4/3 & -2/3 & 0 & 0 & 0 \\ -2/3 & -2/3 & 4/3 & 0 & 0 & 0 \\ 0 & 0 & 0 & 1 & 0 & 0 \\ 0 & 0 & 0 & 0 & 1 & 0 \\ 0 & 0 & 0 & 0 & 0 & 1 \end{bmatrix}. \tag{A.2}$$

After a standard assembly process, denoted here with the big A symbol, one can obtain the global damping matrix

$$\mathbb{C}_{\mu} = \mathop{\mathbf{A}}_{e} \mathbb{C}_{\mu}^{(e)}, \tag{A.3}$$

and the extended RVE dynamic system results

$$\begin{bmatrix} \mathbb{M}_{\mu} & \mathbf{0} & \mathbf{0} \\ \mathbf{0} & \mathbf{0} & \mathbf{0} \\ \mathbf{0} & \mathbf{0} & \mathbf{0} \end{bmatrix} \begin{bmatrix} \ddot{\widehat{\boldsymbol{u}}}_{\mu} \\ \ddot{\boldsymbol{\beta}} \\ \ddot{\boldsymbol{\lambda}} \end{bmatrix} + \begin{bmatrix} \mathbb{C}_{\mu} & \mathbf{0} & \mathbf{0} \\ \mathbf{0} & \mathbf{0} & \mathbf{0} \\ \mathbf{0} & \mathbf{0} & \mathbf{0} \end{bmatrix} \begin{bmatrix} \dot{\widehat{\boldsymbol{u}}}_{\mu} \\ \dot{\boldsymbol{\beta}} \\ \dot{\boldsymbol{\lambda}} \end{bmatrix} + \begin{bmatrix} \mathbb{K}_{\mu} & -\mathbb{N}_{\mu}^{\mathrm{T}} & -\mathbb{B}_{\mu}^{\mathrm{T}} \\ -\mathbb{N}_{\mu} & \mathbf{0} & \mathbf{0} \\ -\mathbb{B}_{\mu} & \mathbf{0} & \mathbf{0} \end{bmatrix} \begin{bmatrix} \widehat{\boldsymbol{u}}_{\mu} \\ \boldsymbol{\beta} \\ \boldsymbol{\lambda} \end{bmatrix} = \begin{bmatrix} \mathbf{0} \\ -\boldsymbol{u} \\ -\boldsymbol{\varepsilon} \end{bmatrix}. \tag{A.4}$$

Note also that matrices denoted by $\mathbb{N}_{\mu}$ and $\mathbb{B}_{\mu}$ appear in system (A.4). These come from the discretization of the minimal kinematic restrictions, as explained in detail in Roca *et al*. [12]. As a reminder,

$$\mathbb{N}_{\mu} = \mathop{\mathbf{A}}_{e} \langle \boldsymbol{N}_{\mu}^{(e)} \rangle_{\Omega_{\mu}^{(e)}}, \quad \text{so} \quad \mathbb{N}_{\mu} \widehat{\boldsymbol{u}}_{\mu} \equiv \langle \boldsymbol{u}_{\mu} \rangle_{\Omega_{\mu}} = \boldsymbol{u}, \tag{A.5}$$

$$\mathbb{B}_{\mu} = \mathop{\mathbf{A}}_{e} \langle \mathbf{B}_{\mu}^{(e)} \rangle_{\Omega_{\mu}^{(e)}}, \quad \text{so} \quad \mathbb{B}_{\mu} \widehat{\boldsymbol{u}}_{\mu} \equiv \langle \boldsymbol{\nabla}_{\boldsymbol{y}}^{\mathrm{S}} \boldsymbol{u}_{\mu} \rangle_{\Omega_{\mu}} = \boldsymbol{\varepsilon}, \tag{A.6}$$

where $\boldsymbol{N}_{\mu}^{(e)}$ corresponds to the shape functions for the type of elements considered.

Since the hypotheses for the split of the system (A.4) into its quasi-static and inertial components still hold, despite the introduction of viscoelastic effects in the framework, one obtains:

(a) *Quasi-static system*

$$\begin{bmatrix} \mathbb{C}_{\mu} & \mathbf{0} \\ \mathbf{0} & \mathbf{0} \end{bmatrix} \begin{bmatrix} \dot{\widehat{\boldsymbol{u}}}_{\mu}^{(1)} \\ \dot{\boldsymbol{\lambda}}^{(1)} \end{bmatrix} + \begin{bmatrix} \mathbb{K}_{\mu} & -\mathbb{B}_{\mu}^{\mathrm{T}} \\ -\mathbb{B}_{\mu} & \mathbf{0} \end{bmatrix} \begin{bmatrix} \widehat{\boldsymbol{u}}_{\mu}^{(1)} \\ \boldsymbol{\lambda}^{(1)} \end{bmatrix} = \begin{bmatrix} \mathbf{0} \\ -\boldsymbol{\varepsilon} \end{bmatrix}. \tag{A.7}$$

For the sake of generality, let us assume that kinematic conditions are imposed directly on the system through

$$\boldsymbol{u}_{\mu}^{(1)} = \boldsymbol{\varepsilon} \cdot \Delta \boldsymbol{y} + \tilde{\boldsymbol{u}}_{\mu}^{(1)} \tag{A.8}$$

where $\Delta \boldsymbol{y} = \boldsymbol{y} - \boldsymbol{y}^{(0)}$, and $\boldsymbol{y}^{(0)}$ is the centroid of the RVE ($\boldsymbol{y}^{(0)} = \langle \boldsymbol{y} \rangle_{\Omega_\mu}$). In discretized form, this is

$$\boldsymbol{u}_\mu^{(1)} = \begin{bmatrix} \Upsilon & \mathbb{P}_\mu \end{bmatrix} \begin{bmatrix} \boldsymbol{\varepsilon} \\ \widehat{\boldsymbol{u}}_\mu^{*(1)} \end{bmatrix} \tag{A.9}$$

with

$$\Upsilon = \begin{bmatrix} & & & \vdots & & \\ \Delta \widehat{y}_1^{(j)} & 0 & 0 & 0 & \Delta \widehat{y}_3^{(j)}/2 & \Delta \widehat{y}_2^{(j)}/2 \\ 0 & \Delta \widehat{y}_2^{(j)} & 0 & \Delta \widehat{y}_3^{(j)}/2 & 0 & \Delta \widehat{y}_1^{(j)}/2 \\ 0 & 0 & \Delta \widehat{y}_3^{(j)} & \Delta \widehat{y}_2^{(j)}/2 & \Delta \widehat{y}_1^{(j)}/2 & 0 \\ & & & \vdots & & \end{bmatrix}. \tag{A.10}$$

and $\mathbb{P}_\mu$ being a matrix that imposes the desired boundary conditions on the discretized microfluctuation field, $\widehat{\boldsymbol{u}}_\mu^{(1)}$. Typically, for the kind of problems tackled, periodic boundary conditions along with prescription of certain degrees of freedom to prevent rigid body motions offer good results. In such cases,

$$\begin{bmatrix} \widehat{\boldsymbol{u}}_\mu^{(1)0} \\ \widehat{\boldsymbol{u}}_\mu^{(1)i} \\ \widehat{\boldsymbol{u}}_\mu^{(1)+} \\ \widehat{\boldsymbol{u}}_\mu^{(1)-} \end{bmatrix} = \begin{bmatrix} \mathbf{0} & \mathbf{0} \\ \mathbf{I} & \mathbf{0} \\ \mathbf{0} & \mathbf{I} \\ \mathbf{0} & \mathbf{I} \end{bmatrix} \begin{bmatrix} \widehat{\boldsymbol{u}}_\mu^{*(1)i} \\ \widehat{\boldsymbol{u}}_\mu^{*(1)+} \end{bmatrix}, \tag{A.11}$$

where superscripts 0, i, $+$ and $-$ are used to refer to prescribed, internal, and periodic boundaries degrees of freedom, respectively.

Note that, from the definition of matrix $\mathbb{B}_\mu$ (see Eq. (A.6)), it can be seen that $\mathbb{B}_\mu \Upsilon \equiv \langle \boldsymbol{\nabla}_{\boldsymbol{y}}^{\mathrm{S}} \Delta \boldsymbol{y} \rangle_{\Omega_\mu} = \mathbf{I}$. Thus, by premultiplying the first equation in system (A.7) by Υ^{T} and introducing expression (A.9) allows us to find, after some algebraic manipulation,

$$\boldsymbol{\lambda}^{(1)} = \Upsilon^{\mathrm{T}} \mathbb{C}_\mu (\Upsilon \dot{\boldsymbol{\varepsilon}} + \mathbb{P}_\mu \dot{\widehat{\boldsymbol{u}}}_\mu^{*(1)}) + \Upsilon^{\mathrm{T}} \mathbb{K}_\mu (\Upsilon \boldsymbol{\varepsilon} + \mathbb{P}_\mu \widehat{\boldsymbol{u}}_\mu^{*(1)}). \tag{A.12}$$

Assuming the kinematic restriction imposed is compatible with that associated to the Lagrange multiplier, projecting the system into a set satisfying the micro-fluctuation field boundary conditions, i.e. pre-multiplying the first equation in system (A.7) by $\mathbb{P}_\mu^{\mathrm{T}}$, results in

$$\mathbb{P}_\mu^{\mathrm{T}} \mathbb{C}_\mu \mathbb{P}_\mu \dot{\widehat{\boldsymbol{u}}}_\mu^{*(1)} + \mathbb{P}_\mu^{\mathrm{T}} \mathbb{K}_\mu \mathbb{P}_\mu \widehat{\boldsymbol{u}}_\mu^{*(1)} = -\mathbb{P}_\mu^{\mathrm{T}} \mathbb{C}_\mu \Upsilon \dot{\boldsymbol{\varepsilon}} - \mathbb{P}_\mu^{\mathrm{T}} \mathbb{K}_\mu \Upsilon \boldsymbol{\varepsilon}. \tag{A.13}$$

Taking the time derivative of Eq. (A.13) gives

$$\mathbb{P}_\mu^{\mathrm{T}}\mathbb{K}_\mu\mathbb{P}_\mu\dot{\widehat{\boldsymbol{u}}}_\mu^{*(1)} = -\mathbb{P}_\mu^{\mathrm{T}}\mathbb{K}_\mu\Upsilon\dot{\boldsymbol{\varepsilon}}, \tag{A.14}$$

where the hypothesis for the quasi-static system, $\ddot{\boldsymbol{\varepsilon}} \approx \mathbf{0}$ (which makes $\ddot{\widehat{\boldsymbol{u}}}_\mu^{*(1)} \approx \mathbf{0}$), has been considered. The solution for $\dot{\widehat{\boldsymbol{u}}}_\mu^{*(1)}$ obtained from Eq. (A.14) in terms of the macroscopic strain rate, $\dot{\boldsymbol{\varepsilon}}$, can be introduced into Eq. (A.13) to compute the solution field

$$\widehat{\boldsymbol{u}}_\mu^{*(1)} = -(\mathbb{P}_\mu^{\mathrm{T}}\mathbb{K}_\mu\mathbb{P}_\mu)^{-1}\mathbb{P}_\mu^{\mathrm{T}}(\mathbb{K}_\mu\Upsilon\boldsymbol{\varepsilon} + \mathbb{C}_\mu\tilde{\Upsilon}\dot{\boldsymbol{\varepsilon}}), \tag{A.15}$$

with

$$\tilde{\Upsilon} = (\mathbf{I} - \mathbb{P}_\mu(\mathbb{P}_\mu^{\mathrm{T}}\mathbb{K}_\mu\mathbb{P}_\mu)^{-1}\mathbb{P}_\mu^{\mathrm{T}}\mathbb{K}_\mu)\Upsilon. \tag{A.16}$$

Finally, substituting expression (A.15) into Eq. (A.12), yields

$$\boldsymbol{\lambda}^{(1)} = \underbrace{\Upsilon^{\mathrm{T}}\mathbb{K}_\mu\tilde{\Upsilon}}_{\mathbf{C}^{\mathrm{eff}}} : \boldsymbol{\varepsilon} + \underbrace{\tilde{\Upsilon}^{\mathrm{T}}\mathbb{C}_\mu\tilde{\Upsilon}}_{\boldsymbol{\eta}^{\mathrm{eff}}} : \dot{\boldsymbol{\varepsilon}}. \tag{A.17}$$

Note that $\mathbf{C}^{\mathrm{eff}}$ in Eq. (A.17) assumes the role of an effective constitutive tensor and it is the same than the one obtained in Roca *et al*. [12], without considering viscoelastic effects. In fact, the quasi-static influence of viscoelasticity in the model is accounted by the new term $\boldsymbol{\eta}^{\mathrm{eff}}$, which acts as a sort of effective viscous tensor relating the macroscopic stress with strain rates.

(b) *Inertial system*

$$\begin{bmatrix}\mathbb{M}_\mu & \mathbf{0}\\ \mathbf{0} & \mathbf{0}\end{bmatrix}\begin{bmatrix}\ddot{\widehat{\boldsymbol{u}}}_\mu^{(2)}\\ \ddot{\boldsymbol{\beta}}^{(2)}\end{bmatrix} + \begin{bmatrix}\mathbb{C}_\mu & \mathbf{0}\\ \mathbf{0} & \mathbf{0}\end{bmatrix}\begin{bmatrix}\dot{\widehat{\boldsymbol{u}}}_\mu^{(2)}\\ \dot{\boldsymbol{\beta}}^{(2)}\end{bmatrix} + \begin{bmatrix}\mathbb{K}_\mu & -\mathbb{N}_\mu^{\mathrm{T}}\\ -\mathbb{N}_\mu & \mathbf{0}\end{bmatrix}\begin{bmatrix}\widehat{\boldsymbol{u}}_\mu^{(2)}\\ \boldsymbol{\beta}^{(2)}\end{bmatrix} = \begin{bmatrix}\mathbf{0}\\ -\boldsymbol{u}\end{bmatrix}. \tag{A.18}$$

Following a similar procedure than in the quasi-static case, in order to maintain the generality of the formulation, the specific kinematic conditions considered here will also be introduced directly in the system (A.18) by taking

$$\boldsymbol{u}_\mu^{(2)} = \boldsymbol{u} + \tilde{\boldsymbol{u}}_\mu^{(2)}, \tag{A.19}$$

which can be expressed in discretized form as

$$\widehat{\boldsymbol{u}}_\mu^{(2)} = [\mathbb{I} \quad \mathbb{P}_\mu]\begin{bmatrix}\boldsymbol{u}\\ \widehat{\boldsymbol{u}}_\mu^{*(2)}\end{bmatrix}, \tag{A.20}$$

with

$$\mathbb{I} = \begin{bmatrix} \vdots & & \\ 1 & 0 & 0 \\ 0 & 1 & 0 \\ 0 & 0 & 1 \\ \vdots & & \end{bmatrix}, \tag{A.21}$$

and $\mathbb{P}_\mu$ being, again, a matrix imposing the desired boundary conditions over the micro-fluctuation field (see, for instance, Eq. (A.11)). In this case, it is easy to verify, from the matrix $\mathbb{N}_\mu$ definition in Eq. (A.5), that $\mathbb{N}_\mu\mathbb{I} = \mathbf{I}$. Also note that, since $\mathbb{I}$ is a rigid body translation mode, it belongs to both the kernels of $\mathbb{K}_\mu$ and $\mathbb{C}_\mu$ (i.e. $\mathbb{K}_\mu\mathbb{I} = \mathbf{0}$ and $\mathbb{C}_\mu\mathbb{I} = \mathbf{0}$). These properties allow us to obtain, after pre-multiplying the first equation in system (A.18) by $\mathbb{I}^{\mathrm{T}}$ and some algebraic manipulation,

$$\boldsymbol{\beta}^{(2)} = \underbrace{\mathbb{I}^T\mathbb{M}_\mu\mathbb{I}}_{\bar{\rho}\mathbf{I} = \langle\rho_\mu\rangle_{\Omega_\mu}\mathbf{I}}\ddot{\boldsymbol{u}} + \underbrace{\mathbb{I}^T\mathbb{M}_\mu\mathbb{P}_\mu}_{\mathbb{D}}\ddot{\tilde{\boldsymbol{u}}}_\mu^{*(2)}. \tag{A.22}$$

Again, projecting the system (A.18) into a set satisfying the imposed kinematic restrictions on the micro-fluctuation field through $\mathbb{P}_\mu$ (nullifying the effect of the Lagrange multiplier), allows us to obtain

$$\underbrace{\mathbb{P}_\mu^{\mathrm{T}}\mathbb{M}_\mu\mathbb{P}_\mu}_{\mathbb{M}_\mu^*}\ddot{\tilde{\boldsymbol{u}}}_\mu^{*(2)} + \underbrace{\mathbb{P}_\mu^{\mathrm{T}}\mathbb{C}_\mu\mathbb{P}_\mu}_{\mathbb{C}_\mu^*}\dot{\tilde{\boldsymbol{u}}}_\mu^{*(2)} + \underbrace{\mathbb{P}_\mu^{\mathrm{T}}\mathbb{K}_\mu\mathbb{P}_\mu}_{\mathbb{K}_\mu^*}\tilde{\boldsymbol{u}}_\mu^{*(2)} = -\underbrace{\mathbb{P}_\mu^{\mathrm{T}}\mathbb{M}_\mu\mathbb{I}}_{\mathbb{D}^{\mathrm{T}}}\ddot{\boldsymbol{u}}. \tag{A.23}$$

In order to make the model computationally efficient, a model order reduction is performed by projecting the solution field $\tilde{\boldsymbol{u}}_\mu^{*(2)}$ onto the space spanned by the eigenmodes of the *undamped* system (A.23)

$$(\mathbb{K}_\mu^* - \lambda_\mu^{*(k)}\mathbb{M}_\mu^*)\hat{\boldsymbol{\phi}}_\mu^{*(k)} = \mathbf{0}, \tag{A.24}$$

where $\lambda_\mu^{*(k)} = (\omega_\mu^{*(k)})^2$ here refer to the squared natural frequencies and $\hat{\boldsymbol{\phi}}_\mu^{*(k)}$ are the associated mass-normalized vibration modes (i.e. $\hat{\boldsymbol{\phi}}_\mu^{*(k)\mathrm{T}}\mathbb{M}_\mu^*\hat{\boldsymbol{\phi}}_\mu^{*(k)} = 1$ and $\hat{\boldsymbol{\phi}}_\mu^{*(k)\mathrm{T}}\mathbb{K}_\mu^*\hat{\boldsymbol{\phi}}_\mu^{*(k)} = (\omega_\mu^{*(k)})^2$)[1]. Now, defining $\boldsymbol{\Omega}_\mu^*$ as the diagonal matrix with only the

[1] Code functionalities allowing the computation of only the smallest eigenvalues in magnitude and their associated eigenvectors (which are potential candidates to become relevant modes in the frequency range of interest) have been used, this translating into a reduction of the computational cost of the modal problem evaluation.

natural frequencies in the range of interest, $\boldsymbol{\Phi}_{\mu}^{*}$ as a matrix that contains their associated mass-normalized eigenmodes, and $\boldsymbol{q}_{\mu}^{*}$ as the column vector with their corresponding modal amplitudes, one can express

$$\widehat{\boldsymbol{u}}_{\mu}^{*(2)} = \boldsymbol{\Phi}_{\mu}^{*}\boldsymbol{q}_{\mu}^{*}, \tag{A.25}$$

and Eqs. (A.22) and (A.23) become

$$\boldsymbol{\beta}^{(2)} = \bar{\rho}\ddot{\boldsymbol{u}} + \underbrace{\mathbb{D}\boldsymbol{\Phi}_{\mu}^{*}}_{\mathbb{Q}}\ \ddot{\boldsymbol{q}}_{\mu}^{*}, \tag{A.26}$$

$$\ddot{\boldsymbol{q}}_{\mu}^{*} + \underbrace{\boldsymbol{\Phi}_{\mu}^{*T}\mathbb{C}_{\mu}\boldsymbol{\Phi}_{\mu}^{*}}_{\boldsymbol{\Omega}_{\mu}^{\mathrm{D}}}\dot{\boldsymbol{q}}_{\mu}^{*} + \boldsymbol{\Omega}_{\mu}^{*2}\boldsymbol{q}_{\mu}^{*} = \underbrace{\boldsymbol{\Phi}_{\mu}^{*T}\mathbb{D}^{T}}_{\mathbb{Q}^{\mathrm{T}}}\ddot{\boldsymbol{u}}. \tag{A.27}$$

Appendix II.B Sensitivity of the LRAM topology optimization cost function

For any functional of the form

$$\Pi_{t}\big(\chi(\phi)\big) = \int_{\Omega_{\mu}} \pi(\chi(\phi(\boldsymbol{y},t)))d\Omega \tag{B.1}$$

the VTD at any point $\widehat{\boldsymbol{y}}$ in the domain is given by

$$\frac{\delta\Pi}{\delta\chi}(\widehat{\boldsymbol{y}}) = \int_{\Omega_{\mu}} \frac{\partial\pi(\chi(\phi(\boldsymbol{y},t)))}{\partial\chi}\delta_{\widehat{\boldsymbol{y}}}d\Omega = \left.\frac{\partial\pi(y,t)}{\partial\chi}\right|_{y=\widehat{\boldsymbol{y}}} \tag{B.2}$$

where $\delta_{\widehat{\boldsymbol{y}}}$ is the point-Dirac's delta shifted to point $\widehat{\boldsymbol{y}}$ fulfilling

$$\int_{\Omega_{\mu}} f(\boldsymbol{y})\delta_{\widehat{\boldsymbol{y}}}d\Omega = f(\widehat{\boldsymbol{y}}). \tag{B.3}$$

On the other hand, the evolution of the cost function can be computed, accounting for Eq. (29), as

$$\dot{\Pi} = \int_{\Omega_{\mu}} \frac{\partial\pi}{\partial\chi}\frac{\partial\chi}{\partial\phi}\dot{\phi}d\Omega = -C_{1}\int_{\Omega_{\mu}} \frac{\partial\pi}{\partial\chi}\frac{\partial\chi}{\partial\phi}\underbrace{\frac{\delta\Pi}{\delta\chi}(\boldsymbol{y})}_{\frac{\partial\pi}{\partial\chi}(\boldsymbol{y},t)}\ d\Omega = -C_{1}\int_{\Omega_{\mu}} \frac{\partial\chi}{\partial\phi}\left(\frac{\partial\pi}{\partial\chi}\right)^{2}d\Omega, \tag{B.4}$$

where Eq. (B.2) has been considered. From Eq. (20), it can be proven that

$$\frac{\partial\chi}{\partial\phi} = \|\nabla\phi\|^{-1}\delta_{\Gamma_{\phi}} \tag{B.5}$$

where δ_{Γ_ϕ} stands for the line/surface-Dirac's delta shifted to the zero level-set of ϕ in Ω_μ, i.e. $\Gamma_\phi := \{\boldsymbol{y} \in \Omega_\mu \mid \phi(\boldsymbol{y}) = 0\}$, thus fulfilling

$$\int_{\Omega_\mu} f(\boldsymbol{y})\delta_{\Gamma_\phi} d\Omega = \int_{\Gamma_\phi} f(\boldsymbol{y}) d\Gamma. \tag{B.6}$$

Replacing Eqs. (B.5) and (B.6) into Eq. (B.4) yields

$$\dot{\Pi} = -C_1 \int_{\Gamma_\phi} \|\boldsymbol{\nabla}\phi\|^{-1} \left(\frac{\partial \pi}{\partial \chi}\right)^2 d\Gamma \leq 0. \tag{B.7}$$

Eq. (B.7) proofs the descending character of the cost function Π along time/iteration evolution.

The sensitivity of the cost function (25) will be evaluated using the variational topological derivative (VTD). To do so, first the chain rule will be applied to Eq. (25) to obtain

$$\frac{\delta \Pi}{\delta \chi} = \frac{4\alpha f}{\lambda_\mu^{*(1)} \ln \overline{\lambda}_\mu^*} \left(\frac{\ln \overline{\lambda}_\mu^*}{\ln \lambda_\mu^{*(1)} + \ln \overline{\lambda}_\mu^*}\right)^2 \frac{\delta \lambda_\mu^{*(1)}}{\delta \chi} + \frac{2(1-\alpha)g}{\lambda_\mu^{*(1)} \ln \lambda_\mu^{(1)}} \left(\frac{\delta \lambda_\mu^{*(1)}}{\delta \chi} - g \frac{\lambda_\mu^{*(1)}}{\lambda_\mu^{(1)}} \frac{\delta \lambda_\mu^{(1)}}{\delta \chi}\right). \tag{B.8}$$

Now, in order to compute $\delta\lambda_\mu^{*(1)}/\delta\chi$ and $\delta\lambda_\mu^{(1)}/\delta\chi$ let us take the derivative of the state-equations (21) and (23), which gives

$$\mathbb{M}_\mu^* \widehat{\boldsymbol{\phi}}_\mu^{*(1)} \frac{\delta \lambda_\mu^{*(1)}}{\delta \chi} = \left(\frac{\delta \mathbb{K}_\mu^*}{\delta \chi} - \lambda_\mu^{*(1)} \frac{\delta \mathbb{M}_\mu^*}{\delta \chi}\right) \widehat{\boldsymbol{\phi}}_\mu^{*(1)} + \left(\mathbb{K}_\mu^* - \lambda_\mu^{*(1)} \mathbb{M}_\mu^*\right) \frac{\delta \widehat{\boldsymbol{\phi}}_\mu^{*(1)}}{\delta \chi}, \tag{B.9}$$

$$\mathbb{M}_\mu \widehat{\boldsymbol{\phi}}_\mu^{(1)} \frac{\delta \lambda_\mu^{(1)}}{\delta \chi} = \left(\frac{\delta \mathbb{K}_\mu}{\delta \chi} - \lambda_\mu^{(1)} \frac{\delta \mathbb{M}_\mu}{\delta \chi}\right) \widehat{\boldsymbol{\phi}}_\mu^{(1)} + \left(\mathbb{K}_\mu - \lambda_\mu^{(1)} \mathbb{M}_\mu\right) \frac{\delta \widehat{\boldsymbol{\phi}}_\mu^{(1)}}{\delta \chi}. \tag{B.10}$$

Pre-multiplying Eqs. (B.9) and (B.10) by $\widehat{\boldsymbol{\phi}}_\mu^{*(1)\mathrm{T}}$ and $\widehat{\boldsymbol{\phi}}_\mu^{(1)\mathrm{T}}$, respectively, allows us to obtain

$$\frac{\delta \lambda_\mu^{*(1)}}{\delta \chi} = \widehat{\boldsymbol{\phi}}_\mu^{*(1)\mathrm{T}} \left(\frac{\delta \mathbb{K}_\mu^*}{\delta \chi} - \lambda_\mu^{*(1)} \frac{\delta \mathbb{M}_\mu^*}{\delta \chi}\right) \widehat{\boldsymbol{\phi}}_\mu^{*(1)}, \tag{B.11}$$

$$\frac{\delta \lambda_\mu^{(1)}}{\delta \chi} = \widehat{\boldsymbol{\phi}}_\mu^{(1)\mathrm{T}} \left(\frac{\delta \mathbb{K}_\mu}{\delta \chi} - \lambda_\mu^{(1)} \frac{\delta \mathbb{M}_\mu}{\delta \chi}\right) \widehat{\boldsymbol{\phi}}_\mu^{(1)}. \tag{B.12}$$

Notice that the fact the vibration modes in each system are mass-normalized has been used. See also how the term multiplying the derivatives of the vibration modes in each system vanishes due to Eqs. (21) and (23). According to the VTD definition, one finds

$$\widehat{\boldsymbol{\phi}}_{\mu}^{(1)\mathrm{T}} \frac{\delta \mathbb{K}_{\mu}}{\delta \chi}(\widehat{\boldsymbol{y}}) \widehat{\boldsymbol{\phi}}_{\mu}^{(1)} \equiv \boldsymbol{\nabla}_{\boldsymbol{y}}^{\mathrm{S}} \boldsymbol{\phi}_{\mu}^{(1)}(\widehat{\boldsymbol{y}}) : \frac{\partial \mathbf{C}_{\mu}(\chi(\widehat{\boldsymbol{y}}))}{\partial \chi} : \boldsymbol{\nabla}_{\boldsymbol{y}}^{\mathrm{S}} \boldsymbol{\phi}_{\mu}^{(1)}(\widehat{\boldsymbol{y}}), \tag{B.13}$$

$$\widehat{\boldsymbol{\phi}}_{\mu}^{(1)\mathrm{T}} \frac{\delta \mathbb{M}_{\mu}}{\delta \chi}(\widehat{\boldsymbol{y}}) \widehat{\boldsymbol{\phi}}_{\mu}^{(1)} \equiv \frac{\partial \rho_{\mu}(\chi(\widehat{\boldsymbol{y}}))}{\partial \chi} \|\boldsymbol{\phi}_{\mu}^{(1)}(\widehat{\boldsymbol{y}})\|^2, \tag{B.14}$$

where $\partial \mathbf{C}_{\mu}(\chi(\widehat{\boldsymbol{y}}))/\partial \chi$ and $\partial \rho_{\mu}(\chi(\widehat{\boldsymbol{y}}))/\partial \chi$ are regular function derivatives of the constitutive tensor and density distribution on the design domain evaluated at point $\widehat{\boldsymbol{y}}$. In the context of linear elastic isotropic behavior of the material phases, let us now consider K_{μ}^{+}, G_{μ}^{+} and ρ_{μ}^{+} the bulk modulus, shear modulus and density of the *dense material* region Ω_{μ}^{+} (inclusions) and K_{μ}^{-}, G_{μ}^{-} and ρ_{μ}^{-} the bulk modulus, shear modulus and density of the *soft material* region Ω_{μ}^{-} (void/coating), such that

$$\mathbf{C}_{\mu}(\chi) = \widehat{K}_{\mu}(\chi) \mathbf{I} \otimes \mathbf{I} + 2\widehat{G}_{\mu}(\chi) \mathbf{I}^{\mathrm{dev}}, \tag{B.15}$$

$$\rho_{\mu}(\chi) = \hat{\rho}_{\mu}(\chi), \tag{B.16}$$

where $\widehat{K}_{\mu}$, $\widehat{G}_{\mu}$, $\hat{\rho}_{\mu}$ are interpolation functions of the form

$$\widehat{h}(\chi) = \left[\chi (h^{+})^{\frac{1}{n}} + (1-\chi)(h^{-})^{\frac{1}{n}}\right]^{n}. \tag{B.17}$$

Note that for $n > 0$ (typically a value of 2 is chosen), Eq. (B.17) returns h^{+} for dense material regions ($\chi = 1$) and h^{-} for soft material regions ($\chi = 0$). Eventually, one can compute

$$\frac{\partial \mathbf{C}_{\mu}(\chi)}{\partial \chi} = n(\widehat{K}_{\mu}(\chi))^{\frac{n-1}{n}} \left((K_{\mu}^{+})^{\frac{1}{n}} - (K_{\mu}^{-})^{\frac{1}{n}}\right) \mathbf{I} \otimes \mathbf{I} + 2n(\widehat{G}_{\mu}(\chi))^{\frac{n-1}{n}} \left((G_{\mu}^{+})^{\frac{1}{n}} - (G_{\mu}^{-})^{\frac{1}{n}}\right) \mathbf{I}^{\mathrm{dev}}, \tag{B.18}$$

$$\frac{\partial \rho_{\mu}(\chi)}{\partial \chi} = n(\hat{\rho}_{\mu}(\chi))^{\frac{n-1}{n}} \left((\rho_{\mu}^{+})^{\frac{1}{n}} - (\rho_{\mu}^{-})^{\frac{1}{n}}\right) \tag{B.19}$$

Appendix II.C Transmission loss computation for a dynamic system

Let us consider a 2D section of a flat panel with a certain material distribution inside such that a FE discretization of the dynamic system yields

$$\mathbb{M}\ddot{\widehat{\boldsymbol{u}}} + \mathbb{C}\dot{\widehat{\boldsymbol{u}}} + \mathbb{K}\widehat{\boldsymbol{u}} = \hat{\boldsymbol{f}}. \tag{C.1}$$

The domain is assumed infinite in the vertical direction and in contact with air at both sides in the horizontal direction. A plane wave travels at a certain frequency in the air domain in contact with the left side of the panel and it continues to propagate at the same

frequency once it reaches the right side of the panel. Note that, since the analysis is performed for a given frequency, the system (C.1) may be expressed in the frequency domain as

$$\mathbb{D}(\omega)\widehat{\boldsymbol{U}} = \hat{\boldsymbol{F}}, \quad \mathbb{D}(\omega) = \mathbb{K} - i\omega\mathbb{C} - \omega^2\mathbb{M}. \tag{C.2}$$

Since the air domain is assumed to spread infinitely at both sides, there will be two waves on the left side propagating in opposite directions perpendicular to the panel's surface as a result of the incident wave reflection, while only one wave will be transmitted to the air in the right side. The analytical solutions for the displacement and pressure fields of these waves are given by Eqs. (32) and (33) for the air on the left side and by Eqs. (34) and (35) for the air on the right side. Note that the reflection and transmission coefficients, R and T respectively, are the unknowns to be solved in this problem.

In order to express the system (C.2) in terms of R and T compatibility conditions for the horizontal component of the displacements and pressure will be applied, which yields:

$$\widehat{\boldsymbol{U}} = \begin{bmatrix} \widehat{\boldsymbol{U}}^{(i)} \\ \widehat{\boldsymbol{U}}^{(b)} \\ \widehat{\boldsymbol{U}}^{(t)} \\ \widehat{\boldsymbol{U}}^{(l)} \\ \widehat{\boldsymbol{U}}^{(r)} \end{bmatrix} = \underbrace{\begin{bmatrix} \mathbf{I} & \mathbf{0} & \mathbf{0} & \mathbf{0} \\ \mathbf{0} & \mathbf{I} & \mathbf{0} & \mathbf{0} \\ \mathbf{0} & \mathbf{I} & \mathbf{0} & \mathbf{0} \\ \mathbf{0} & \mathbf{0} & -\mathbf{1} & \mathbf{0} \\ \mathbf{0} & \mathbf{0} & \mathbf{0} & \mathbf{1} \end{bmatrix}}_{\mathbb{P}_u} \underbrace{\begin{bmatrix} \widehat{\boldsymbol{U}}^{(i)} \\ \widehat{\boldsymbol{U}}^{(b)} \\ R \\ T \end{bmatrix}}_{\widehat{\boldsymbol{U}}_1} + \underbrace{\begin{bmatrix} \mathbf{0} \\ \mathbf{0} \\ \mathbf{0} \\ \mathbf{1} \\ \mathbf{0} \end{bmatrix}}_{\widehat{\boldsymbol{U}}_0} \tag{C.3}$$

$$\hat{\boldsymbol{F}} = \begin{bmatrix} \hat{\boldsymbol{F}}^{(i)} \\ \hat{\boldsymbol{F}}^{(b)} \\ \hat{\boldsymbol{F}}^{(t)} \\ \hat{\boldsymbol{F}}^{(l)} \\ \hat{\boldsymbol{F}}^{(r)} \end{bmatrix} = -iK_a \left(\underbrace{\begin{bmatrix} \mathbf{0} & \mathbf{0} & \mathbf{0} & \mathbf{0} \\ \mathbf{0} & \mathbf{0} & \mathbf{0} & \mathbf{0} \\ \mathbf{0} & \mathbf{0} & \mathbf{0} & \mathbf{0} \\ \mathbf{0} & \mathbf{0} & \mathbf{1} & \mathbf{0} \\ \mathbf{0} & \mathbf{0} & \mathbf{0} & \mathbf{1} \end{bmatrix}}_{\mathbb{P}_f} \underbrace{\begin{bmatrix} \widehat{\boldsymbol{U}}^{(i)} \\ \widehat{\boldsymbol{U}}^{(b)} \\ R \\ T \end{bmatrix}}_{\widehat{\boldsymbol{U}}_1} + \underbrace{\begin{bmatrix} \mathbf{0} \\ \mathbf{0} \\ \mathbf{0} \\ \mathbf{1} \\ \mathbf{0} \end{bmatrix}}_{\widehat{\boldsymbol{U}}_0} \right), \tag{C.4}$$

where $\mathbf{I}$ are identity matrices, $\mathbf{0}$ refer to matrices/vectors of zeros, $\mathbf{1}$ are column vectors of ones, $K_a = \rho_a v_a \omega S$ (with S being the panel's surface area in contact with the air at each side) and the superscripts (l) and (r) refer to the left and right side horizontal degrees of freedom, respectively, (b) and (t) refer to both horizontal and vertical degrees of freedom at the bottom and top sides of the domain, respectively, and (i) refers to the remaining degrees of freedom. Pre-multiplying the system (C.2) by $\mathbb{P}_u^{\mathrm{T}}$ yields

$$\underbrace{(\mathbb{P}_u^{\mathrm{T}}\mathbb{D}\mathbb{P}_u + iK_a\mathbb{P}_u^{\mathrm{T}}\mathbb{P}_f)}_{\mathbb{A}}\widehat{\boldsymbol{U}}_1 = \underbrace{-\mathbb{P}_u^{\mathrm{T}}(\mathbb{D} + iK_a\mathbf{I})\widehat{\boldsymbol{U}}_0}_{\widehat{\boldsymbol{B}}}. \tag{C.5}$$

Now, defining

$$\widehat{\boldsymbol{U}}^{(f)} = \begin{bmatrix} \widehat{\boldsymbol{U}}^{(i)} \\ \widehat{\boldsymbol{U}}^{(b)} \end{bmatrix} \tag{C.6}$$

allows one to express

$$\begin{bmatrix} \mathbb{A}^{(ff)} & \boldsymbol{A}^{(fL)} & \boldsymbol{A}^{(fR)} \\ \boldsymbol{A}^{(Lf)} & A^{(LL)} & A^{(LR)} \\ \boldsymbol{A}^{(Rf)} & A^{(RL)} & A^{(RR)} \end{bmatrix} \begin{bmatrix} \widehat{\boldsymbol{U}}^{(f)} \\ R \\ T \end{bmatrix} = \begin{bmatrix} \widehat{\boldsymbol{B}}^{(f)} \\ \widehat{B}^{(L)} \\ \widehat{B}^{(R)} \end{bmatrix}. \tag{C.7}$$

The system in Eq. (C.7) can be reduced by first expressing

$$\widehat{\boldsymbol{U}}^{(f)} = (\mathbb{A}^{(ff)})^{-1}(\widehat{\boldsymbol{B}}^{(f)} - \boldsymbol{A}^{(fL)}R - \boldsymbol{A}^{(fR)}T) \tag{C.8}$$

and then introducing expression (C.8) into the second and third equations of system (C.7), so that

$$\begin{bmatrix} \bar{A}^{(LL)} & \bar{A}^{(LR)} \\ \bar{A}^{(RL)} & \bar{A}^{(RR)} \end{bmatrix} \begin{bmatrix} R \\ T \end{bmatrix} = \begin{bmatrix} \bar{B}^{(L)} \\ \bar{B}^{(R)} \end{bmatrix} \tag{C.9}$$

where, for each row $a = \{L, R\}$ and column b $= \{L, R\}$,

$$\bar{A}^{(a,b)} = A^{(a,b)} - \boldsymbol{A}^{(af)}(\bar{A}^{(LL)})^{-1}\boldsymbol{A}^{(fb)}, \tag{C.10}$$

$$\bar{B}^{(a)} = B^{(a)} - \boldsymbol{A}^{(af)}(\bar{A}^{(LL)})^{-1}\widehat{\boldsymbol{B}}^{(f)}. \tag{C.11}$$

Note that the system in Eq. (C.9) is a complex 2×2 system, the solution of which gives the reflection and transmission coefficients:

$$R = \frac{\bar{A}^{(RR)}\bar{B}^{(L)} - \bar{A}^{(LR)}\bar{B}^{(R)}}{\bar{A}^{(LL)}\bar{A}^{(RR)} - \bar{A}^{(RL)}\bar{A}^{(LR)}}, \tag{C.12}$$

$$T = \frac{\bar{A}^{(LL)}\bar{B}^{(R)} - \bar{A}^{(RL)}\bar{B}^{(L)}}{\bar{A}^{(LL)}\bar{A}^{(RR)} - \bar{A}^{(RL)}\bar{A}^{(LR)}}. \tag{C.13}$$

The transmission loss is finally obtained by

$$\mathrm{TL} = -20\log_{10}|T| \tag{C.14}$$

where $|T|$ refers to the complex module of the transmission coefficient T.

References

[1] Z. Liu *et al*., "Locally Resonant Sonic Materials," *Science (80-.).*, vol. 289, no. 5485, pp. 1734–1736, Sep. 2000, doi: http://dx.doi.org/10.1126/science.289.5485.1734.

[2] K. M. Ho, Z. Yang, X. X. Zhang, and P. Sheng, "Measurements of sound transmission through panels of locally resonant materials between impedance tubes," *Appl. Acoust.*, vol. 66, no. 7, pp. 751–765, Jul. 2005, doi: http://dx.doi.org/10.1016/j.apacoust.2004.11.005.

[3] E. P. Calius, X. Bremaud, B. Smith, and A. Hall, "Negative mass sound shielding structures: Early results," *Phys. status solidi*, vol. 246, no. 9, pp. 2089–2097, Sep. 2009, doi: http://dx.doi.org/10.1002/pssb.200982040.

[4] C. Claeys, E. Deckers, B. Pluymers, and W. Desmet, "A lightweight vibro-acoustic metamaterial demonstrator: Numerical and experimental investigation," *Mech. Syst. Signal Process.*, vol. 70–71, pp. 853–880, Mar. 2016, doi: http://dx.doi.org/10.1016/j.ymssp.2015.08.029.

[5] Z. Yang, H. M. Dai, N. H. Chan, G. C. Ma, and P. Sheng, "Acoustic metamaterial panels for sound attenuation in the 50–1000 Hz regime," *Appl. Phys. Lett.*, vol. 96, no. 4, p. 041906, Jan. 2010, doi: http://dx.doi.org/10.1063/1.3299007.

[6] Y. Zhang, J. Wen, H. Zhao, D. Yu, L. Cai, and X. Wen, "Sound insulation property of membrane-type acoustic metamaterials carrying different masses at adjacent cells," *J. Appl. Phys.*, vol. 114, no. 6, p. 063515, Aug. 2013, doi: http://dx.doi.org/10.1063/1.4818435.

[7] M. Badreddine Assouar, M. Senesi, M. Oudich, M. Ruzzene, and Z. Hou, "Broadband plate-type acoustic metamaterial for low-frequency sound attenuation," *Appl. Phys. Lett.*, vol. 101, no. 17, p. 173505, Oct. 2012, doi: http://dx.doi.org/10.1063/1.4764072.

[8] M. I. Hussein, "Reduced Bloch mode expansion for periodic media band structure calculations," *Proc. R. Soc. A Math. Phys. Eng. Sci.*, vol. 465, no. 2109, pp. 2825–2848, Sep. 2009, doi: http://dx.doi.org/10.1098/rspa.2008.0471.

[9] M. I. Hussein, M. J. Leamy, and M. Ruzzene, "Dynamics of Phononic Materials and Structures: Historical Origins, Recent Progress, and Future Outlook," *Appl. Mech. Rev.*, vol. 66, no. 4, p. 040802, Jul. 2014, doi: http://dx.doi.org/10.1115/1.4026911.

[10] A. Sridhar, V. G. Kouznetsova, and M. G. D. D. Geers, "Homogenization of locally resonant acoustic metamaterials towards an emergent enriched continuum," *Comput. Mech.*, vol. 57, no. 3, pp. 423–435, Mar. 2016, doi: http://dx.doi.org/10.1007/s00466-015-1254-y.

[11] A. Sridhar, V. G. Kouznetsova, and M. G. D. Geers, "A semi-analytical approach towards plane wave analysis of local resonance metamaterials using a multiscale enriched continuum description," *Int. J. Mech. Sci.*, vol. 133, no. August, pp. 188–198, Nov. 2017, doi: http://dx.doi.org/10.1016/j.ijmecsci.2017.08.027.

[12] D. Roca, O. Lloberas-Valls, J. Cante, and J. Oliver, "A computational multiscale homogenization framework accounting for inertial effects: Application to acoustic metamaterials modelling," *Comput. Methods Appl. Mech. Eng.*, vol. 330, pp. 415–446, Mar. 2018, doi: http://dx.doi.org/10.1016/j.cma.2017.10.025.

[13] T. Matsuki, T. Yamada, K. Izui, and S. Nishiwaki, "Topology optimization for locally resonant sonic materials," *Appl. Phys. Lett.*, vol. 104, no. 19, p. 191905, May 2014, doi: http://dx.doi.org/10.1063/1.4878259.

[14] M. I. Hussein and M. J. Frazier, "Metadamping: An emergent phenomenon in dissipative metamaterials," *J. Sound Vib.*, vol. 332, no. 20, pp. 4767–4774, Sep. 2013, doi: http://dx.doi.org/10.1016/j.jsv.2013.04.041.

[15] M. J. Frazier and M. I. Hussein, "Viscous-to-viscoelastic transition in phononic crystal and metamaterial band structures," *J. Acoust. Soc. Am.*, vol. 138, no. 5, pp. 3169–3180, Nov. 2015, doi: http://dx.doi.org/10.1121/1.4934845.

[16] D. DePauw, H. Al Ba'ba'a, and M. Nouh, "Metadamping and energy dissipation enhancement via hybrid phononic resonators," *Extrem. Mech. Lett.*, vol. 18, pp. 36–44, Jan. 2018, doi: http://dx.doi.org/10.1016/j.eml.2017.11.002.

[17] J. M. Manimala and C. T. Sun, "Microstructural design studies for locally dissipative acoustic metamaterials," *J. Appl. Phys.*, vol. 115, no. 2, p. 023518, Jan. 2014, doi: http://dx.doi.org/10.1063/1.4861632.

[18] A. O. Krushynska, V. G. Kouznetsova, and M. G. D. Geers, "Visco-elastic effects on wave dispersion in three-phase acoustic metamaterials," *J. Mech. Phys. Solids*, vol. 96, pp. 29–47, Nov. 2016, doi: http://dx.doi.org/10.1016/j.jmps.2016.07.001.

[19] M. A. Lewińska, V. G. Kouznetsova, J. A. W. van Dommelen, A. O. Krushynska, and M. G. D. Geers, "The attenuation performance of locally resonant acoustic metamaterials based on generalised viscoelastic modelling," *Int. J. Solids Struct.*, vol. 126–127, pp. 163–174, Nov. 2017, doi: http://dx.doi.org/10.1016/j.ijsolstr.2017.08.003.

[20] P. J. Blanco, P. J. Sánchez, E. A. de Souza Neto, and R. A. Feijóo, "Variational Foundations and Generalized Unified Theory of RVE-Based Multiscale Models," *Arch. Comput. Methods Eng.*, vol. 23, no. 2, pp. 191–253, Jun. 2016, doi: http://dx.doi.org/10.1007/s11831-014-9137-5.

ARTICLE III

- Online published title page -

ASME DIGITAL COLLECTION
THE AMERICAN SOCIETY OF MECHANICAL ENGINEERS

Volume 142, Issue 2
April 2020

Journal of Vibration and Acoustics

RESEARCH PAPERS

Experimental and Numerical Assessment of Local Resonance Phenomena in 3D-Printed Acoustic Metamaterials

D. Roca , T. Pàmies , J. Cante , O. Lloberas-Valls , J. Oliver

Check for updates

— Author and Article Information

D. Roca
Centre Internacional de Mètodes, Numèrics en Enginyeria (CIMNE),
Universitat Politècnica de Catalunya (UPC/BarcelonaTech),
Campus Nord UPC, Mòdul C-1 101, c/ Jordi Girona 1-3, 08034 Barcelona, Spain

T. Pàmies
Laboratori d'Enginyeria, Acústica i Mecànica (LEAM), Universitat Politècnica de Catalunya (UPC/BarcelonaTech),
Campus Terrassa UPC, Edifici TR45, c/ Colom 11, 08222 Terrassa, Spain

J. Cante
Centre Internacional de Mètodes, Numèrics en Enginyeria (CIMNE),
Universitat Politècnica de Catalunya (UPC/BarcelonaTech),
Campus Terrassa UPC, Ed. GAIA, D-176, c/ Rambla de Sant Nebridi 22, 08222 Terrassa, Spain

O. Lloberas-Valls
Centre Internacional de Mètodes, Numèrics en Enginyeria (CIMNE),
Universitat Politècnica de Catalunya (UPC/BarcelonaTech),
Campus Nord UPC, Mòdul C-1 101, c/ Jordi Girona 1-3, 08034 Barcelona, Spain

J. Oliver
Centre Internacional de Mètodes, Numèrics en Enginyeria (CIMNE),
Universitat Politècnica de Catalunya (UPC/BarcelonaTech),
Campus Nord UPC, Mòdul C-1 101, c/ Jordi Girona 1-3, 08034 Barcelona, Spain

Contributed by the Technical Committee on Vibration and Sound of ASME for publication in the Journal of Vibration and Acoustics.

J. Vib. Acoust. Apr 2020, 142(2): 021017 (9 pages)
Paper No: VIB-19-1395 https://doi.org/10.1115/1.4045774
Published Online: January 25, 2020 Article history

Article III

Experimental and Numerical Assessment of Local Resonance Phenomena in 3D-Printed Acoustic Metamaterials

D. Roca[a,(*)], T. Pàmies[b], J. Cante[c], O. Lloberas-Valls[a], J. Oliver[a]

[a] *Centre Internacional de Mètodes Numèrics en Enginyeria (CIMNE), Universitat Politècnica de Catalunya (UPC/BarcelonaTech), Campus Nord UPC, Mòdul C-1 101, c/ Jordi Girona 1-3, 08034 Barcelona, Spain*

[b] *Laboratori d'Enginyeria Acústica i Mecànica (LEAM), Universitat Politècnica de Catalunya (UPC/BarcelonaTech), Campus Terrassa UPC, Edifici TR45, c/ Colom 11, 08222 Terrassa, Spain*

[c] *Centre Internacional de Mètodes Numèrics en Enginyeria (CIMNE), Universitat Politècnica de Catalunya (UPC/BarcelonaTech), Campus Terrassa UPC, Ed. GAIA, D-176, c/ Colom 11, 08222 Terrassa, Spain*

Abstract

The so-called Locally resonant acoustic metamaterials (LRAMs) are a new kind of artificially engineered materials capable of attenuating acoustic waves. As the name suggests, this phenomenon occurs in the vicinity of internal frequencies of the material structure and can give rise to acoustic bandgaps. One possible way to achieve this is by considering periodic arrangements of a certain topology (unit cell), smaller in size than the characteristic wavelength. In this context, a computational model based on a homogenization framework has been developed from which one can obtain the aforementioned resonance frequencies for a given LRAM unit cell design in the sub-wavelength regime, which is suitable for low-frequency applications. Aiming at validating both the proposed numerical model and the local resonance phenomena responsible for the attenuation capabilities of such materials, a 3D-printed prototype consisting of a plate with a well selected LRAM unit cell design has been built and its acoustic response to normal incident waves in the range between 500 and 2000 Hz has been tested in an impedance tube. The results demonstrate the attenuating capabilities of the proposed design in the targeted frequency range for normal incident sound pressure waves and also establish the proposed formulation as the fundamental base for the computational design of 3D-printed LRAM-based structures.

Keywords: materials in vibration and acoustics, modal analysis, noise control, smart materials and structures

III.1 Introduction

The notion of metamaterials as artificially engineered structures capable of exhibiting properties which cannot be found in ordinary materials has awoken the interest among both the scientific and industrial communities due to their potential applications [1]. Even though the concept was born in the context of electromagnetism, where materials behave as if they had negative refractive indices, the idea rapidly extended to other fields where wave propagation phenomena occur. Specifically for this matter, in the context of acoustics, metamaterials show the ability to effectively stop waves from propagating in certain frequency ranges, typically called frequency bandgaps, due to local resonance effects [2]. These kinds of phenomena are triggered when the material is excited by an acoustic wave at a frequency close to certain internal resonance frequencies, typically related to the metamaterial's topology in the lower scale, effectively causing significant levels of attenuation of the wave's amplitude from a macroscopic point of view [3, 4]. This is interesting in applications where significant levels of acoustic attenuation need to be achieved for specific frequency regions, especially in the low-frequency range (i.e. around 1000 Hz), where more conventional solutions would require impractical amounts of mass.

Among the first actual realizations of acoustic metamaterials, Liu *et al*. [2] built a composite structure that possessed negative elastic constants, exhibiting bandgaps in localized regions of the frequency spectrum. Research in this line was followed by several other experimental demonstrations [5–8], in which the acoustic metamaterial consisted of a polymer-based matrix structure with embedded silicone rubber-coated metal inclusions. In fact, this is the typical configuration that allows local resonance phenomena to arise, since the relative rigidity of the polymer matrix allows resonance modes to be localized in each cell and the combination of the low stiffness of the silicone rubber with the high density of the metal inclusions trigger these internal resonance modes in the low-frequency range. Other acoustic metamaterial configurations based on the concept of local resonance have also been explored, including the use of binary materials [9], materials with porous topologies or hollow cavities [10, 11] or contact-based

metamaterials consisting of microspheres attached to a membrane [12, 13], among others. Configurations based on resonating beams [14], plates [15, 16] or membranes [17] have also been explored. While most studies have been carried out on periodic arrangements, recent works show that irregularities and random structures also exhibit attenuation capabilities and can even improve them with proper selection of certain parameters [18–21].

In terms of numerical modelling of acoustic metamaterials and their related phenomena, several works can be found in the literature. For instance, in Xiao *et al*. [22] an analytical model for a simple 1D string with spring-mass resonators attached is developed in order to understand the bandgap formation mechanisms. A more sophisticated analysis based on the Bloch-Floquet theory has been performed by Liu and Hussein [23] to study wave propagation effects in periodic media, which has been used, for instance, to study the dispersion properties of 2D and 3D periodic unit cells [24]. Also in this line, Bloch-based models have been used to characterize resonance modes responsible for local resonance effects in periodic structures [25]. In the homogenization field, Fokin *et al*. [26] proposed a method to retrieve effective properties of LRAM from experimental measurements of the transmission and reflection coefficients, while in Nemat-Nasser *et al*. [27] a homogenization method based on the Floquet theory for elastic composites with periodic structures is presented. In more recent works, computational homogenization frameworks based on multiscale variational principles have also been proposed and proved to be capable of accounting for local resonance phenomena [28–32].

While the concepts and realizations discussed so far have provided a better understanding of the local resonance phenomenon, and served as a proof of the properties of acoustic metamaterials, they are still far from actual industrial application, mainly due to limitations in the construction process. In this regard, a new kind of acoustic metamaterial has been devised, which is meant to be built entirely through emerging additive manufacturing techniques (i.e. 3D-printing). Experiments have been performed focused on the vibration attenuation properties of 3D-printed structures such as in McGee *et al*. [33], where both experimental and numerical analysis of a 3D-printed foam based on resonating hollow-spheres and binders have been performed. Given the material properties of common 3D-printing materials available and current limitations of manufacturing techniques, proper experimental evaluation of acoustic attenuation capabilities of these kinds of devices have been more challenging, since either their

dimensions or the frequency ranges of operation are unsuitable for common measuring devices such as impedance tubes. However, some attempts have been made and can be found in the literature. As examples, Claeys *et al*. [34] have carried out experimental tests measuring the insertion loss of acoustic enclosures consisting of unit cells with internal resonators, built entirely through Selective Laser Sintering (SLS) methods. On the other hand, Leblanc and Lavie [35] have measured the transmission loss in a 3D-printed single cell of a membrane-type acoustic metamaterial built with Fused Deposition Modeling (FDM) technology. Following this line, the aim of this work is to present both a numerical and an experimental assessment of the acoustic attenuating capabilities, namely the normal-incidence transmission loss, to demonstrate the appearance of local resonance effects in a metamaterial entirely 3D-printed through Multi Jet Fusion (MJF) technique. To this end, a computational model has been used to obtain the relevant resonant modes and frequencies for a LRAM unit cell design, and the corresponding 3D-printed samples in the shape of panels have been built in order to test their transmission loss capabilities at normal incidence.

III.2 Experimental Setup

The impedance tube method has been typically used to evaluate the acoustic performance of materials. It consists of two impedance tubes of constant section, with a speaker on one end and an anechoic termination on the other. The material sample to be tested is placed between both tubes and the sound pressure level of the acoustic wave emitted by the speaker is measured at different locations along the tube with microphones. In particular, the reflection coefficient can be obtained through measurements from two or more microphones located at different distances from the sample's incident surface in the front tube section. For transmission loss determination, typically two additional microphones are placed on the rear tube section.

While in the standard method for measuring the normal incidence sound transmission loss, a sample of the material is put inside the tubes (and so it needs to be cut so that it fills the whole section of the enclosure), a slightly modified version was proposed by Ho *et al*. [6], which is suitable for locally resonant acoustic metamaterials testing. In this case, a sample panel is pressed and held firmly between both impedance tubes. This method allows more flexibility for the samples shape and configuration while also being able to capture the local resonance behavior expected, as reported in Ho *et al*. [6].

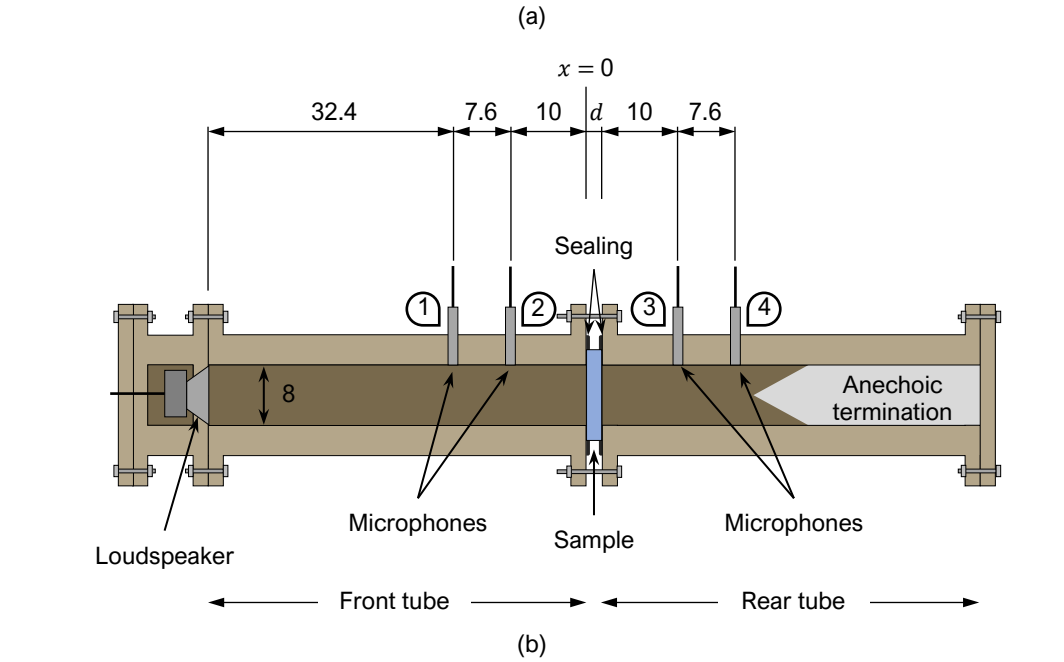

FIG. 1 Experiment setup representation of the impedance tubes used for measuring the normal incidence sound transmission loss of a sample LRAM panel. The tube cavity has a 8 cm × 8 cm squared section and each pair of microphones are separated 7.6 cm apart. The frequency range of operation goes from 500 to 2000 Hz. All measures in the figure represent cm. (a) Schematic representation and (b) actual experimental setup.

The apparatus employed for measuring the normal incidence sound transmission loss consists of two impedance tubes with an 8 cm × 8 cm section with 4 cm thick medium-density fiberboard (MDF) walls for isolating the acoustic wave inside from environmental sources. A 3.3 inch loudspeaker (4 Ohm, 30 Watts) connected to an amplifier is located on one end of the front tube, and the last 30 cm of the other tube are filled with a polyurethane foam, acting as absorbing material in order to guarantee an anechoic

termination. A total of 4 1/2" pre-polarized microphones with an ICP preamplifier are placed at different positions: two on the front tube positioned at 10 and 17.6 cm from the sample's front surface, and two on the rear tube positioned also at 10 and 17.6 cm from the sample's rear surface. According to ASTM E1050-98 [36], the section size and separation between each pair of microphones should guarantee valid results in the frequency range between 200 and 2000 Hz. A schematic representation of the experimental setup can be found in Fig. 1.

The transmission of each sample panel can be obtained from the measurements of the four microphones. Considering the acoustic wave inside the tube is plane, it can be expressed, in the frequency domain, as

$$P_f(x,\omega) = A(\omega)e^{i\kappa x} + B(\omega)e^{-i\kappa x} \tag{1}$$

in the front tube, and

$$P_r(x,\omega) = C(\omega)e^{i\kappa x} + D(\omega)e^{-i\kappa x} \tag{2}$$

in the rear tube.

In the above equations, x refers to the distance with respect to the front surface of the sample panel, ω is the wave's frequency, $\kappa = \omega/c$ is the wavenumber (with c being the speed of sound in air) and A, B, C and D are the complex amplitudes of (a) the wave emitted by the loudspeaker, (b) the wave reflected by the panel in the front tube, (c) the wave transmitted through the panel to the rear tube and (d) the wave reflected on the rear tube, respectively.

Under anechoic termination condition in the rear tube, i.e. $D = 0$, the transmission T of the sample panel can be obtained directly as

$$T(\omega) = \frac{C(\omega)}{A(\omega)} \tag{3}$$

The coefficients A and C appearing in Eq. (3) can be obtained from Eqs. (1) and (2) by replacing P_f and P_r with the corresponding sound pressure values measured at each frequency:

$$P_1(\omega) = A(\omega)e^{i\kappa x_1} + B(\omega)e^{-i\kappa x_1}, \quad \text{with } x_1 = -17.6 \text{ cm} \tag{4}$$

$$P_2(\omega) = A(\omega)e^{i\kappa x_2} + B(\omega)e^{-i\kappa x_2}, \quad \text{with } x_2 = -10 \text{ cm} \tag{5}$$

$$P_3(\omega) = C(\omega)e^{i\kappa x_3} + D(\omega)e^{-i\kappa x_3}, \quad \text{with } x_3 = d + 10 \text{ cm} \tag{6}$$

$$P_4(\omega) = C(\omega)e^{i\kappa x_4} + D(\omega)e^{-i\kappa x_4}, \quad \text{with } x_4 = d + 17.6 \text{ cm} \tag{7}$$

where d is the thickness of the sample panel. The values of each P_k (the subscript k here refers to each microphone, i.e. k = 1, 2, 3 or 4) have been obtained from the Fourier transform of the time samples of actual pressure measurements in the corresponding microphone positions. For this experiment, a pink noise (a noise source on the whole audible frequency range with equal amount of energy for each octave) has been emitted by the loudspeaker and pressure measurements at each position have been recorded for a total of 10 s, with a sample time of 2×10^{-4} s.

The procedure described in ASTM E1050-98 [36] has been considered for correcting the amplitude and phase of the measured pressure values. To do so, a calibration transfer function, H_k^c has been computed for each microphone:

$$H_k^c(\omega) = \sqrt{\frac{P_1^I(\omega)P_k^{II}(\omega)}{P_k^I(\omega)P_1^{II}(\omega)}} \tag{8}$$

where P_1^I and P_k^I are the complex Fourier transformed pressures measured by microphones 1 and k for the empty tube case (without a sample panel), and P_1^{II} and P_k^{II} are the corresponding values for the same case but in which the microphones 1 and k have switched positions. Note that the microphone position 1 is being used as a reference.

Now, from Eqs. (4) and (5) and by correcting the pressure values at each microphone position with their corresponding calibration transfer function, it can be obtained

$$A(\omega) = i\frac{P_1H_1^ce^{-i\kappa x_2} - P_2H_2^ce^{-i\kappa x_1}}{2\,sin(x_2 - x_1)} \tag{9}$$

while from Eqs. (6) and (7),

$$C(\omega) = i\frac{P_3H_3^ce^{-i\kappa x_4} - P_4H_4^ce^{-i\kappa x_3}}{2\,sin(x_4 - x_3)} \tag{10}$$

Finally, by inserting into Eq. (3) the values obtained for coefficients A and C from Eqs. (9) and (10), respectively, the transmission loss can be obtained as

$$\mathrm{TL}(\omega) = 10\log_{10}\left(\frac{1}{|T|^2}\right) \tag{11}$$

It should be noted that the anechoic termination condition has been validated in the employed apparatus by comparing the transmission loss for an empty tube case (no panel) obtained with Eq. (3) with that obtained considering all four coefficients,

$$T(\omega) = \frac{A(\omega) \cdot C(\omega) - B(\omega) \cdot D(\omega)}{A^2(\omega) - D^2(\omega)} \tag{12}$$

and verifying that they give almost the same result with differences of less than 0.2 dB.

III.3 Numerical Model

The computational homogenization framework introduced by Roca *et al*. [31] will be used in this work to characterize the modes and frequencies responsible for local resonance phenomena to arise and to identify the metamaterial unit cell homogenized properties to understand the response of the medium in the impedance tube. Even though a detailed description of the model can be found in Roca *et al*. [31, 32], a brief summary will also be presented here, for completeness.

The model is based on multiscale theory and can be applied as long as the unit cell size, ℓ_μ, is much smaller (at least an order of magnitude) than the macroscopic wavelength, λ, i.e.

$$\lambda \gg \ell_\mu \tag{13}$$

The whole formulation is grounded on the application of the linear and angular momentum balance postulates for continuum mechanics in the macroscale, which read, respectively,

$$\boldsymbol{\nabla}_x \cdot \boldsymbol{\sigma}(\boldsymbol{x}, t) = \dot{\boldsymbol{p}}(\boldsymbol{x}, t) \tag{14}$$

$$\boldsymbol{\sigma}(\boldsymbol{x}, t) = \boldsymbol{\sigma}^{\mathrm{T}}(\boldsymbol{x}, t) \tag{15}$$

where t refers to time, $\boldsymbol{x}$ are the spatial coordinates in the macroscale, $\boldsymbol{\sigma}$ is the macroscopic effective second-order stress tensor and $\dot{\boldsymbol{p}}$ is the macroscopic effective inertial force density. Note that the symbol $(\cdot)^{\mathrm{T}}$ is used to denote the transpose of $(\cdot)$. To each point $\boldsymbol{x}$ in the macroscale, a representative volume element (RVE) or, in this case, a unit cell, is assigned, and a kinematic relation for the displacement field is imposed, in particular,

$$\boldsymbol{u}_\mu(\boldsymbol{y}, t) = \boldsymbol{u}(\boldsymbol{x}, t) + (\boldsymbol{y} - \boldsymbol{y}^{(0)}) \cdot \boldsymbol{\nabla}_x \boldsymbol{u}(\boldsymbol{x}, t) + \tilde{\boldsymbol{u}}_\mu(\boldsymbol{y}, t) \tag{16}$$

where the subscript μ is used to distinguish microscale variables from their macroscopic counterparts, $\boldsymbol{y}$ are the spatial coordinates in the microscale context, $\boldsymbol{y}^{(0)}$ are the coordinates of the centroid of the RVE and $\tilde{\boldsymbol{u}}_\mu$ is a micro-fluctuation field, satisfying the minimal kinematic conditions

$$\langle \tilde{\boldsymbol{u}}_\mu \rangle_{\Omega_\mu} = \boldsymbol{0} \tag{17}$$

$$\langle \boldsymbol{\nabla}_{\boldsymbol{y}}^{\mathrm{S}} \tilde{\boldsymbol{u}}_\mu \rangle_{\Omega_\mu} = \boldsymbol{0} \tag{18}$$

Note that the notation $\langle \cdot \rangle_{\Omega_\mu}$ is used to refer to the mean value of $(\cdot)$ integrated over the RVE volume Ω_μ, i.e.

$$\langle \cdot \rangle_{\Omega_\mu} = \frac{1}{|\Omega_\mu|} \int_{\Omega_\mu} (\cdot) d\Omega \tag{19}$$

Finally, an energetic equivalence between both scales is established, by means of the generalized Hill-Mandel principle, which reads

$$\dot{\boldsymbol{p}} \cdot \dot{\boldsymbol{u}} + \boldsymbol{\sigma} : \boldsymbol{\nabla}_{\boldsymbol{x}}^{\mathrm{S}} \dot{\boldsymbol{u}} = \langle \dot{\boldsymbol{p}}_\mu \cdot \dot{\boldsymbol{u}}_\mu + \boldsymbol{\sigma}_\mu : \boldsymbol{\nabla}_{\boldsymbol{y}}^{\mathrm{S}} \dot{\boldsymbol{u}}_\mu \rangle_{\Omega_\mu}, \qquad \forall\, \dot{\boldsymbol{u}}, \boldsymbol{\nabla}_{\boldsymbol{x}}^{\mathrm{S}} \dot{\boldsymbol{u}}, \qquad \forall\, \dot{\boldsymbol{u}}_\mu \in \mathscr{U}_\mu \tag{20}$$

where $\mathscr{U}_\mu$ is the space of admissible microdisplacement fields, i.e. those satisfying Eq. (16) along with conditions (17) and (18), and the superscript $(\cdot)^{\mathrm{S}}$ is used to indicate the symmetric component of tensor $(\cdot)$. From the variational statement given by Eq. (20), and after considering the kinematic restrictions of Eqs. (16) to (18), one can obtain the following relations (again, the reader is referred to Roca *et al*. [31] for details):

$$\boldsymbol{\sigma} = \langle \boldsymbol{\sigma}_\mu + \left(\boldsymbol{y} - \boldsymbol{y}^{(0)} \right) \otimes^{\mathrm{S}} \dot{\boldsymbol{p}}_\mu \rangle_{\Omega_\mu} \tag{21}$$

$$\dot{\boldsymbol{p}} = \langle \dot{\boldsymbol{p}}_\mu \rangle_{\Omega_\mu} \tag{22}$$

where the symbol $\otimes^{\mathrm{S}}$ refers to the symmetric outer product, i.e. $\boldsymbol{a} \otimes^{S} \boldsymbol{b} = (\boldsymbol{a} \otimes \boldsymbol{b} + \boldsymbol{b} \otimes \boldsymbol{a})/2$. Then, the weak form of the RVE problem, upon the introduction of the test function $\delta \boldsymbol{u}_\mu \equiv \dot{\tilde{\boldsymbol{u}}}_\mu$, reads

$$\langle \dot{\boldsymbol{p}}_\mu \cdot \delta \boldsymbol{u}_\mu + \boldsymbol{\sigma}_\mu : \boldsymbol{\nabla}_{\boldsymbol{y}}^{\mathrm{S}} \delta \boldsymbol{u}_\mu \rangle_{\Omega_\mu} = 0, \qquad \forall\, \boldsymbol{u}_\mu \in \mathscr{U}_\mu, \qquad \forall\, \delta \boldsymbol{u}_\mu \in \mathscr{U}_\mu^0 \tag{23}$$

where $\mathscr{U}_\mu^0$ is the space of admissible micro-fluctuation fields (i.e. satisfying Eqs. (17) and (18)). Then, by considering

$$\boldsymbol{\sigma}_\mu = \mathbf{C}_\mu : \boldsymbol{\nabla}_{\boldsymbol{y}}^{\mathrm{S}} \boldsymbol{u}_\mu + \boldsymbol{\eta}_\mu : \boldsymbol{\nabla}_{\boldsymbol{y}}^{\mathrm{S}} \dot{\boldsymbol{u}}_\mu \tag{24}$$

$$\dot{\boldsymbol{p}}_\mu = \rho_\mu \ddot{\boldsymbol{u}}_\mu \tag{25}$$

where $\mathbf{C}_\mu$ is the fourth-order constitutive tensor, $\boldsymbol{\eta}_\mu$ is a viscosity fourth-order tensor accounting for viscoelastic effects and ρ_μ is the mass density distribution of the RVE, the variational statement given by Eq. (23) can be used to find the micro-fluctuation field solution, $\tilde{\boldsymbol{u}}_\mu$, in terms of the macroscopic displacement and displacement gradient, $\boldsymbol{u}$, $\boldsymbol{\nabla}_x \boldsymbol{u}$, which become *actions* in the resulting system.

The resolution scheme that follows is based on two main simplifying hypotheses:

(a) The separation of scales condition given by Eq. (13) is satisfied so that the natural frequencies triggering local resonance effects arising in the low-frequency region, far below the range where the first RVE deformation modes appear.
(b) The center of mass of the RVE is close enough to its centroid so that the inertial contributions on the effective macroscopic stress can be neglected.

The first hypothesis (a) allows us to neglect the inertial response due to macroscopic deformation actions, because they will not be relevant in the frequency range of interest. This makes it possible to split the system into a quasi-static component whose action is simply the macroscopic strain, $\boldsymbol{\nabla}_x^{\mathrm{S}} \boldsymbol{u}$, and an inertial component whose action becomes the macroscopic acceleration, $\ddot{\boldsymbol{u}}$. From the quasi-static subsystem, an expression for the macroscopic stress tensor can be obtained, relating it to the macroscopic strain through an effective constitutive tensor:

$$\boldsymbol{\sigma} = \mathbf{C}^{\mathrm{eff}} : \boldsymbol{\nabla}_x^{\mathrm{S}} \boldsymbol{u} + \boldsymbol{\eta}^{\mathrm{eff}} : \boldsymbol{\nabla}_x^{\mathrm{S}} \dot{\boldsymbol{u}} \tag{26}$$

The terms $\mathbf{C}^{\mathrm{eff}}$ and $\boldsymbol{\eta}^{\mathrm{eff}}$ in the previous equation are obtained applying the classical homogenization theory to the quasi-static system, i.e. by imposing periodic boundary conditions on the RVE system under the action of a macroscopic strain. By performing a Galerkin-based Finite Element (FE) discretization, the system can be solved yielding

$$\mathbf{C}^{\mathrm{eff}} = \tilde{\mathbb{Y}}^{\mathrm{T}} \mathbb{K}_\mu \tilde{\mathbb{Y}} \tag{27}$$

$$\boldsymbol{\eta}^{\mathrm{eff}} = \tilde{\mathbb{Y}}^{\mathrm{T}} \mathbb{C}_\mu \tilde{\mathbb{Y}} \tag{28}$$

with

$$\tilde{\mathbb{Y}} = \mathbb{Y} - \mathbb{P}(\mathbb{P}^{\mathrm{T}} \mathbb{K}_\mu \mathbb{P})^{-1} \mathbb{P}^{\mathrm{T}} \mathbb{K}_\mu \mathbb{Y} \tag{29}$$

where $\mathbb{K}_\mu$ is the RVE stiffness matrix, $\mathbb{C}_\mu$ is the RVE damping matrix, $\mathbb{P}$ is a boolean matrix imposing the periodic boundary conditions and Υ is a matrix containing the nodal coordinates, $\widehat{\boldsymbol{y}}^{(i)}$, arranged such that

$$\Upsilon = \begin{bmatrix} & & & \vdots & & \\ \widehat{y}_1^{(i)} & 0 & 0 & 0 & \widehat{y}_3^{(i)}/2 & \widehat{y}_2^{(i)}/2 \\ 0 & \widehat{y}_2^{(i)} & 0 & \widehat{y}_3^{(i)}/2 & 0 & \widehat{y}_1^{(i)}/2 \\ 0 & 0 & \widehat{y}_3^{(i)} & \widehat{y}_2^{(i)}/2 & \widehat{y}_1^{(i)}/2 & 0 \\ & & & \vdots & & \end{bmatrix} \tag{30}$$

The second hypothesis (b) allows us to condense all the inertial effects into a macroscopic inertial force density term, including all the local resonance phenomena that are the focus of this analysis. In particular, by combining Eqs. (22) and (16) (considering, by the definition of $\boldsymbol{y}^{(0)}$ as the centroid of the RVE, $\langle \boldsymbol{y} - \boldsymbol{y}^{(0)} \rangle_{\Omega_\mu} = \boldsymbol{0}$), one can obtain

$$\dot{\boldsymbol{p}} = \bar{\rho}\ddot{\boldsymbol{u}} + \langle \rho_\mu \ddot{\tilde{\boldsymbol{u}}}_\mu \rangle_{\Omega_\mu} \tag{31}$$

where $\bar{\rho} = \langle \rho_\mu \rangle_{\Omega_\mu}$ is the volume averaged RVE density and $\langle \rho_\mu \ddot{\tilde{\boldsymbol{u}}}_\mu \rangle_{\Omega_\mu}$ is the averaged micro-inertial fluctuation contribution and the term responsible for local resonance phenomena. It should be noted that, according to hypothesis (a), the micro-fluctuation field responsible for those effects is obtained from the inertial subsystem, i.e. the RVE system under the action of a uniform acceleration field and a set of boundary conditions capable of triggering internal resonance modes. This can be achieved, for instance, by prescribing all boundary degrees of freedom, and then solving the modal problem

$$(\mathbb{K}_\mu^* - \lambda_\mu^{*(k)} \mathbb{M}_\mu^*) \widehat{\boldsymbol{\phi}}_\mu^{*(k)} = \boldsymbol{0} \tag{32}$$

where $\mathbb{K}_\mu$ and $\mathbb{M}_\mu$ are the RVE stiffness and mass matrices, respectively (the superscript $(\cdot)^*$ indicates that the considered boundary conditions have already been applied), $\widehat{\boldsymbol{\phi}}_\mu^{*(k)}$ are the resulting mass-normalized eigenvectors and $\lambda_\mu^{*(k)} = (\omega_\mu^{*(k)})^2$ are the eigenvalues. The resulting microfluctuation field can be expressed in terms of internal variables, $q_\mu^{*(k)}$, associated to each of the resonance modes:

$$\tilde{\boldsymbol{u}}_\mu = \sum_k \mathbb{P}_0 \widehat{\boldsymbol{\phi}}_\mu^{*(k)} q_\mu^{*(k)} \tag{33}$$

where $\mathbb{P}_0$ is a boolean matrix imposing the required boundary conditions. This allows us to express the second term in Eq. (31) as

$$\langle \rho_\mu \ddot{\tilde{\boldsymbol{u}}}_\mu \rangle_{\Omega_\mu} = \sum_k \underbrace{\frac{1}{\sqrt{|\Omega_\mu|}} \mathbb{I}^T \mathbb{M}_\mu \mathbb{P}_0 \widehat{\boldsymbol{\phi}}_\mu^{*(k)}}_{\boldsymbol{r}_\mu^{(k)}} \ddot{q}_\mu^{*(k)} \tag{34}$$

where $\mathbb{I}$ is a column vector of identity second-order tensors. The internal variables are solved through the following microscale system:

$$\ddot{q}_\mu^{*(k)} + \sum_j \omega_\mu^{D(k,j)} \dot{q}_\mu^{*(j)} + (\omega_\mu^{*(k)})^2 q_\mu^{*(k)} = -\boldsymbol{r}_\mu^{(k)} \cdot \ddot{\boldsymbol{u}} \tag{35}$$

with

$$\omega_\mu^{D(k,j)} = \frac{1}{|\Omega_\mu|} \widehat{\boldsymbol{\phi}}_\mu^{*(k)\mathrm{T}} \mathbb{P}_0^{\mathrm{T}} \mathbb{C}_\mu \mathbb{P}_0 \widehat{\boldsymbol{\phi}}_\mu^{*(j)} \tag{36}$$

It is important to note that not all the internal modes obtained from Eq. (32) are responsible for triggering local resonance effects. In particular, only those with a relevant effect on the macroscale are capable of affecting the metamaterial behavior, giving rise to frequency bandgaps of acoustic wave attenuation. This discrimination can be easily performed in the present context by evaluating the norm of $\boldsymbol{r}_\mu^{(k)}$, so

$$\|\boldsymbol{r}_\mu^{(k)}\| \quad \begin{cases} > 0 & \rightarrow \text{ the } k\text{-th mode is relevant} \\ = 0 & \rightarrow \text{the } k\text{-the mode is non-relevant} \end{cases} \tag{37}$$

allowing us to identify the resonance modes and frequencies that trigger local resonance effects for a given RVE design.

III.4 Prototypes Design

The sample used for the experimental tests consists of a 120 mm $\times$ 120 mm panel 5 mm thick with a 6 $\times$ 6 grid of unit cells at the central part, occupying the whole 80 mm $\times$ 80 mm tube section. The overall size of each unit cell, 12 mm $\times$ 12 mm $\times$ 5 mm, is chosen so as to be thin enough for practical applications and to satisfy the separation of scales condition given in Eq. (13) (note that in the limit case, i.e. for a frequency of 2000 Hz, and considering air as acoustic propagation medium, $\lambda/\ell_\mu > 10$, which is acceptable for triggering local resonance effects and considering the homogenization framework valid). In Fig. 2 a schematic representation of the panel can be found. The metamaterial panel

has been monolithically 3D-printed and two 120 mm × 120 mm × 2 mm skin panels of the same material have been stuck to each side, in order to isolate and constrain the unit cells, enabling the appearance of internal resonance modes. The unit cells have been designed so that they can be easily 3D-printed from a single block or material, while still being composed of the required elements for local resonance phenomena to arise. Namely, (1) the support rods at the vertices, which become the union points of the cells with the skin panels, isolate each cell, enabling the appearance of internal modes, (2) the central inclusion acts as a mass, becoming the resonating component and (3) the thin attachments allow the unit cell to have relevant resonance modes in the desired frequency range. The panels have been manufactured using Polyamide 11 (PA 11) as 3D-printing material through MJF technology. MJF employs a process similar to SLS in which parts are built by fusing layers of powder polymer. Unlike with SLS, a fusing agent is previously dispensed in the powder in order to promote the absorption of infrared light in each cross section, which typically yields faster and slightly more accurate results, for smaller features, than those obtained with SLS [37].

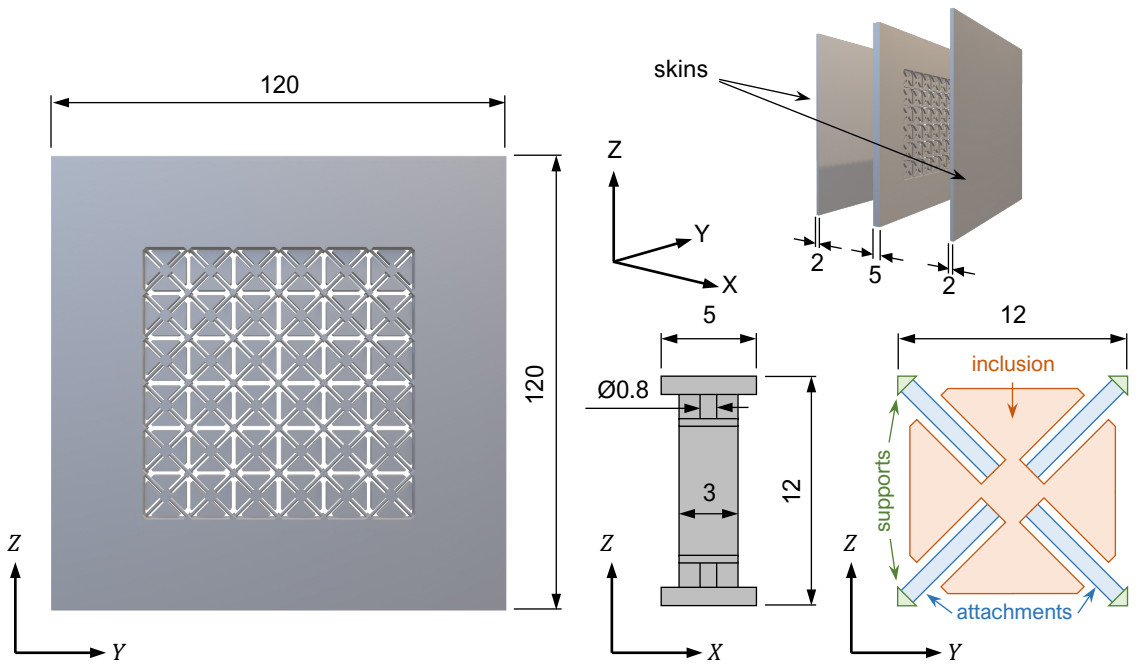

FIG. 2 Acoustic metamaterial panel design. The panel is stuck to two skins made with the same material, as in the top right corner of the figure, in order to hold and isolate the unit cells. A detailed unit cell design is depicted in the bottom right corner of the figure. Dimensions in millimeters.

The homogenization procedure described in Section III.3 has been applied to the metamaterial unit cell design with the material properties, provided by the manufacturer, given in Tab. 1. To do so, a FE mesh of tetrahedra has been used, consisting of around 137000 elements with 3 Gaussian integration points each. In the range between 500 and 2000 Hz, there is only one relevant internal resonance mode (see Fig. 3) at a frequency around 1050 Hz, which can trigger local resonance phenomena at the macroscale. It should be noted that the specific design of the unit cell results from the challenge of achieving the internal resonance in the desired frequency range, for the given material properties, while keeping the overall unit cell thin and small (within manufacturability limitations) for practical applications. To do so, (1) the bending stiffness for the thin attachments (which is responsible for the internal resonance mode depicted in Fig. 3) must be small and (2) the mass of the resonating inclusion must be large enough. Since the diameters of the attachments are close to the manufacturability limitations, the easiest way to minimize its stiffness to bending is by increasing its length. On the other hand, the mass of the resonating inclusion can be also increased if its volume occupies as much space available in the unit cell as possible. The combination of both yields the flower-like look of the design and enables the appearance of the internal resonance mode at a frequency around 1000 Hz.

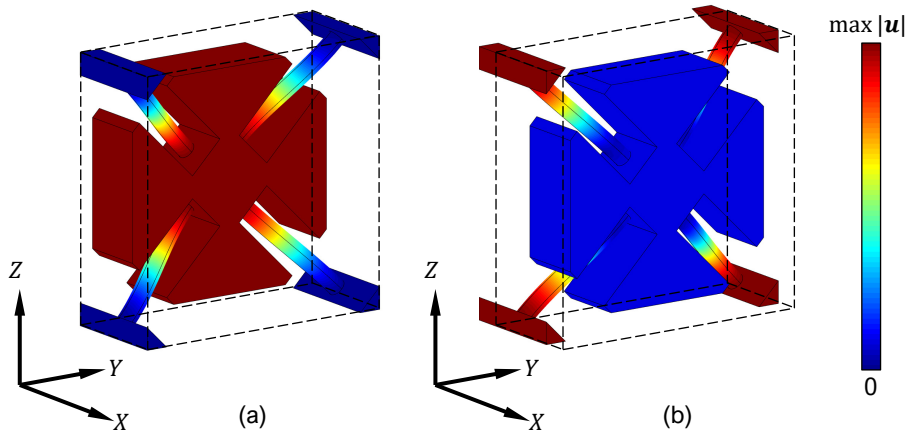

FIG. 3 (a) Displacement of the internal vibration mode responsible for the attenuation peak at 1050 Hz and (b) corresponding mode causing the transmission peak indicating the upper bandgap limit at 1380 Hz. The black dashed line indicates the undeformed unit cell contour. Note that in the attenuation peak, the inclusion vibrates keeping the supports fixed (causing the macroscopic wave to effectively stop propagating), while in the transmission peak, the inclusion remains nearly fixed and the supports vibrate (further increasing the wave transmission through the panel).

TAB. 1 3D-printing material properties.

Material	Density (kg/m^3)	Young's modulus (MPa)	Poisson's ratio
PA 11	1050	1800	0.405

III.5 Results

III.5.1 Experimental test

The sample metamaterial panel has been tested and the normal incidence sound transmission loss for a range of frequencies from 500 to 1500 Hz has been obtained as described in Section III.2. The results are given in Fig. 5 where a region of increased acoustic attenuation can be identified around the frequency of 1000 Hz, very close to the frequency of 1050 Hz, where local resonance phenomena were expected to arise according to the unit cell analysis. For comparison, the same test has been performed on two 120 mm $\times$ 120 mm homogeneous panels 3D-printed with the same material: one with the same equivalent mass as the metamaterial panel assembly, and another with the same thickness, which correspond to panel sizes of 6 and 9 mm, respectively. Fig. 5 shows the average results from three different measures for each sample panel. The standard deviation has been measured in each case with values ranging from 0.4 dB for the homogeneous panels to 2.9 dB for the metamaterial case, with this being higher due to very small variations in the peaks location (< 1 %) causing larger differences in their transmission loss levels. However, these values are acceptable for a proper qualitative assessment of the phenomenon.

It should be noted that, for the metamaterial panel, aside from the attenuation peak around the frequency of 1000 Hz, there are also two inverted peaks, i.e. transmission peaks, at frequencies of 550 Hz and 1250 Hz. The latter (transmission peak at 1250 Hz) corresponds to the unit cell resonance frequency that typically marks the end of the bandgap region, while the former (transmission peak at 550 Hz) is caused by the pressing of the panel against the sealing component (which allows certain elasticity) that holds it between the two parts of the impedance tube. This inverted peak also appears for the homogeneous panels at the approximate frequencies of 800 and 950 Hz. It should be noted that these results, and in particular the aforementioned transmission peaks, are not expected in standard impedance tube measurements where the sample is placed inside the tube. However, several tests have been performed with different samples

(varying materials and geometric properties) in order to verify the repeatability of the results is guaranteed even with the non-standard mounting procedure. It has been observed that even though those peaks are caused by the mounting of the sample, they are related to material and geometric properties of the samples (results are the same for different samples with equivalent material and geometric properties).

III.5.2 Numerical analysis

A macroscopic analysis of the panel response in the tube has been performed, with the simulation setup depicted in Fig. 4. The solid domain has been discretized with 18 × 18 × 9 hexahedral elements with 4 Gaussian quadrature points each and consists of two material phases. The skins and the metamaterial panel outer frame have both been modelled as standard solid isotropic materials, with the properties given in Tab. 1. The internal volume, corresponding to where the actual metamaterial unit cells can be found in the panel, has been modelled as a homogenized material with an effective constitutive tensor, $\mathbf{C}^{\text{eff}}$, an effective viscosity tensor $\boldsymbol{\eta}^{\text{eff}}$, an average density, $\bar{\rho}$, and the relevant internal resonance modes and frequencies, $\boldsymbol{r}_{\mu}^{(k)}$ and $\omega_{\mu}^{*(k)}$, along with $\omega_{\mu}^{\mathrm{D}(k,j)}$, obtained from the unit cell analysis. The procedure described in Roca *et al*. [32] has been considered in this case for computing the transmission coefficient, from which the transmission loss can be directly obtained. To do so, an appropriate set of displacements and traction forces have been imposed in the sections of the front and rear faces that are exposed to the plane waves travelling inside the tube: (a) an incident wave of arbitrary amplitude towards the panel's front face, (b) a reflected wave, with a reflection coefficient R, travelling in the opposite direction, also from the panel's front face, and (c) a transmitted wave, with a transmission coefficient T, travelling away from the panel's rear face. In particular, defining $\kappa = \omega/c$ as the wavenumber (with c being the speed of sound in air) and ρ_a as the density of air, the boundary conditions (on both displacements $\boldsymbol{u}$ and traction forces $\boldsymbol{f}$) to simulate the normal incident plane wave on the front and rear faces can be written as:

(a) In the front face

$$\boldsymbol{n} \cdot \boldsymbol{u} = (e^{i\kappa x} - Re^{-i\kappa x})e^{-i\omega t} \tag{38}$$

$$\boldsymbol{f} = -i\boldsymbol{n}\rho_a c\omega(e^{i\kappa x} + Re^{-i\kappa x})e^{-i\omega t} \tag{39}$$

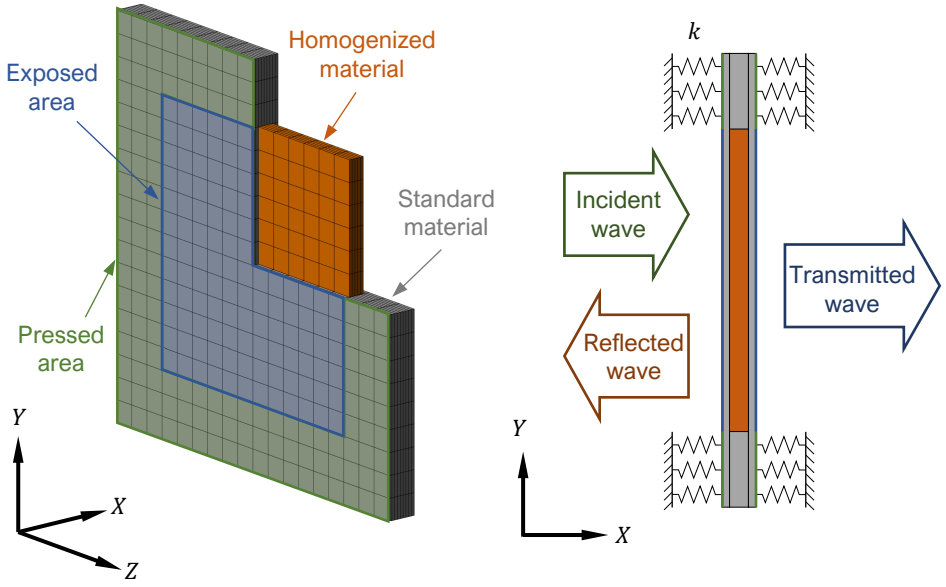

FIG. 4 Transmission loss simulation set-up. The solid domain consists of two material phases: the standard isotropic 3D-printing material and an internal region where the actual metamaterial cells can be found. The latter has been modelled as a homogenized material, with the properties obtained from the RVE analysis. Springs of a certain stiffness k have been introduced in the pressed area of both the front and rear faces of the panel, in order to simulate the elastic behavior of the sealing. In the remaining region, which is the area actually exposed to the acoustic waves inside the tube, an incident, a reflected and a transmitted plane wave have been imposed as depicted in the figure in order to obtain the transmission coefficient.

(b) In the rear face

$$\boldsymbol{n} \cdot \boldsymbol{u} = Te^{i(\kappa x - \omega t)} \tag{40}$$

$$\boldsymbol{f} = -i\boldsymbol{n}\rho_a c\omega Te^{i(\kappa x - \omega t)} \tag{41}$$

where R and T become the unknowns. The system from which both coefficients can be obtained has been solved in the frequency domain for a range of 500 frequencies between 500 and 1500 Hz. The results can be seen on Fig. 5, where the simulated curves can be compared to the ones obtained from the experimental test with the impedance tube. As for the accuracy of the numerical results, it should be noted that it depends mainly on (a) the number of internal modes considered and (b) the frequency range of study, so that the model is more accurate the smaller the frequency. In particular for this case (normal-incidence plane wave excitation), the next relevant modes frequencies are above 10 kHz, so the single mode considered is enough to guarantee accurate results. More specifically, from previous studies [31], it could be verified that the expected relative

error when comparing results to full direct numerical simulations is smaller than 0.1 % when the separation of scales is $\lambda/\ell_\mu > 10$ (as in this case), reaching localized peaks of errors around 1 % near the resonance frequencies, with these numbers not being largely affected by mesh size.

Note that in order to simulate the effect of the panel's holding against the sealing component (i.e. the transmission peak at 550 Hz), springs of a given stiffness $k = 4000$ N/m have been considered in the pressed area of both the front and rear faces of the panel (see **FIG. 4**). Furthermore, in order to smooth the simulated resonance peaks, an additional analysis has been performed where damping effects have been considered by introducing a certain degree of viscoelastic behavior to the material (with a viscosity of $\mu = 3000$ Pa·s, chosen in order to fit the experimental results).

III.6 Discussion

Results from Fig. 5 show that the metamaterial panel attenuation performance as a response to normal incident acoustic waves around the region where local resonance effects were expected is improved when compared to those of homogeneous panels with the same effective mass or thickness. Even without considering the transmission peaks in the homogeneous panels' cases, an increase of 15 to 25 dB from the baseline values can be observed in a frequency range of around 300 Hz. It is worth noting the normal incidence sound transmission loss decrease in the metamaterial panel for frequencies above the upper bandgap limit, which make it a suitable choice especially for low-frequency applications.

On the other hand, from the obtained results in Fig. 5, it can be seen that both the experimental and simulated curves' shapes are the same, capturing in each case the attenuation rise around the frequency responsible for the local resonance effects and then the transmission peak indicating the bandgap end. However, it should be noted that there are some differences in the frequencies where the peaks are produced, which are most likely caused by geometrical tolerances in the fabrication process of the samples. In particular, the internal resonance frequency is very sensitive to the thickness of the attachments, causing variations of the order of ± 200 Hz for diameter deviations of ± 0.1 mm. This is an indication that small variations in the geometry of the unit cells can give rise to several attenuation peaks, a fact that, if properly considered in the design process, may be of interest, for instance, when trying to enlarge the effective attenuation band.

This shows the importance of the design process of acoustic metamaterials and how there is room for improvement and optimization towards achieving the desired properties and behavior. In this regard, the need for very accurate fabrication methods is also of utmost importance in order to achieve the expected results and performance, as unplanned variations of just 12 % in the diameter at this scale, can cause a 20 % deviation in the expected frequencies. It is important to note that for the present study, measurements have been performed with only one sample panel. However, in order to evaluate the accuracy of the 3D-printed prototype, measurements of the thickness of the attachments have been made, yielding an average value of 0.79 ± 0.03 mm, with a standard deviation of 0.009 mm. This represents around 1.2 % variation from the design value (0.8 mm), and while the expected impact on the results should not be large (around 2 % deviation in frequency), it certainly is an issue that should be considered when designing unit cell models at this scale with the current state of 3D-printing technologies.

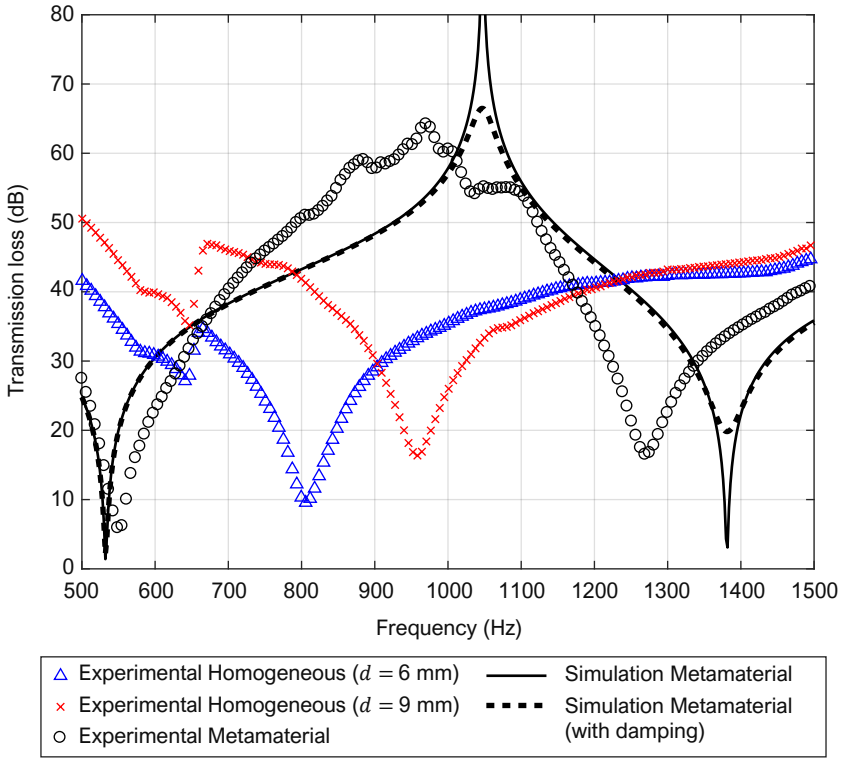

FIG. 5 Transmission loss results obtained experimentally for the homogeneous sample panels of equivalent mass (blue triangles) and thickness (red crosses) and the metamaterial sample panel (black circles). The results obtained numerically for the metamaterial panel are also given for comparison, both for the undamped case (solid black line) and the case accounting for viscoelastic effects on the material (dashed black line).

III.7 Conclusions

The results of this work can be used to both confirm the appearance of local resonance effects in 3D-printed acoustic metamaterials as a response to normal incident sound pressure waves, and to validate the proposed numerical scheme as a tool for characterizing such kinds of phenomena. This can be regarded as a first step towards an alternative approach to what has been the standard in acoustic metamaterial unit cell design so far, where instead of achieving the desired metamaterial behavior by combining two or more materials with different properties, the same effects are obtained with only one material and relying more on geometric and topological aspects of the design. On a next stage, more sophisticated computational techniques, such as topology optimization algorithms, can be involved in the design process in order to achieve optimized designs for targeted sets of properties. Additionally, this novel approach is naturally compatible with emerging manufacturing technologies, which can facilitate the fabrication process, making these materials more appealing and bringing them one step closer to practical applications.

Acknowledgements

This research has received funding from the European Research Council (ERC) under the European Union's Horizon 2020 research and innovation program (Proof of Concept Grant call reference ERC-2019-PoC-25-04-2019, proposal no. 874481) through the project "Computational design and prototyping of acoustic metamaterials for tailored insulation of noise" (METACOUSTIC). The authors also acknowledge the funding received by the Spanish Ministry of Economy and Competitiveness through the research grant DPI2017-85521-P for the project "Computational design of Acoustic and Mechanical Metamaterials" (METAMAT). D. Roca acknowledges the support received by the Spanish Ministry of Education through the FPU program for PhD grants.

The authors also gratefully acknowledge the collaboration of HP Printing and Computing Solutions S.L.U. in Sant Cugat (Spain), for the 3D-printing of the prototypes used in the experimental part of this work, as well as providing the datasheet specifications of the printing material, and Isidre Roca, for providing the impedance tubes used in the experiments.

References

[1] P. A. Deymier, “Introduction to Phononic Crystals and Acoustic Metamaterials,” in *Acoustic metamaterials and phononic crystals*, vol. 173, Springer Science & Business Media, 2013, pp. 1–12.

[2] Z. Liu *et al.*, “Locally Resonant Sonic Materials,” *Science (80-.).*, vol. 289, no. 5485, pp. 1734–1736, Sep. 2000, doi: http://dx.doi.org/10.1126/science.289.5485.1734.

[3] M. I. Hussein, M. J. Leamy, and M. Ruzzene, “Dynamics of Phononic Materials and Structures: Historical Origins, Recent Progress, and Future Outlook,” *Appl. Mech. Rev.*, vol. 66, no. 4, p. 040802, Jul. 2014, doi: http://dx.doi.org/10.1115/1.4026911.

[4] S. A. Cummer, J. Christensen, and A. Alù, “Controlling sound with acoustic metamaterials,” *Nat. Rev. Mater.*, vol. 1, no. 3, p. 16001, Mar. 2016, doi: http://dx.doi.org/10.1038/natrevmats.2016.1.

[5] P. Sheng, X. X. Zhang, Z. Liu, and C. T. Chan, “Locally resonant sonic materials,” *Phys. B Condens. Matter*, vol. 338, no. 1–4, pp. 201–205, Oct. 2003, doi: http://dx.doi.org/10.1016/S0921-4526(03)00487-3.

[6] K. M. Ho, Z. Yang, X. X. Zhang, and P. Sheng, “Measurements of sound transmission through panels of locally resonant materials between impedance tubes,” *Appl. Acoust.*, vol. 66, no. 7, pp. 751–765, Jul. 2005, doi: http://dx.doi.org/10.1016/j.apacoust.2004.11.005.

[7] E. P. Calius, X. Bremaud, B. Smith, and A. Hall, “Negative mass sound shielding structures: Early results,” *Phys. status solidi*, vol. 246, no. 9, pp. 2089–2097, Sep. 2009, doi: http://dx.doi.org/10.1002/pssb.200982040.

[8] E. C. Wester, X. Brémaud, and B. Smith, “Meta-Material Sound Insulation,” *Build. Acoust.*, vol. 16, no. 1, pp. 21–30, Jan. 2009, doi: http://dx.doi.org/10.1260/135101009788066555.

[9] G. Wang, X. Wen, J. Wen, L. Shao, and Y. Liu, “Two-Dimensional Locally Resonant Phononic Crystals with Binary Structures,” *Phys. Rev. Lett.*, vol. 93, no. 15, p. 154302, Oct. 2004, doi: http://dx.doi.org/10.1103/PhysRevLett.93.154302.

[10] C. Boutin and F. X. Becot, “Theory and experiments on poro-acoustics with inner resonators,” *Wave Motion*, vol. 54, pp. 76–99, Apr. 2015, doi: http://dx.doi.org/10.1016/j.wavemoti.2014.11.013.

[11] R. Sainidou, B. Djafari-Rouhani, Y. Pennec, and J. O. Vasseur, “Locally resonant phononic crystals made of hollow spheres or cylinders,” *Phys. Rev. B*, vol. 73, no. 2, p. 024302, Jan. 2006, doi: http://dx.doi.org/10.1103/PhysRevB.73.024302.

[12] A. Khanolkar, S. Wallen, M. Abi Ghanem, J. Jenks, N. Vogel, and N. Boechler, "A self-assembled metamaterial for Lamb waves," *Appl. Phys. Lett.*, vol. 107, no. 7, p. 071903, Aug. 2015, doi: http://dx.doi.org/10.1063/1.4928564.

[13] M. Hiraiwa, M. Abi Ghanem, S. P. Wallen, A. Khanolkar, A. A. Maznev, and N. Boechler, "Complex Contact-Based Dynamics of Microsphere Monolayers Revealed by Resonant Attenuation of Surface Acoustic Waves," *Phys. Rev. Lett.*, vol. 116, no. 19, p. 198001, May 2016, doi: http://dx.doi.org/10.1103/PhysRevLett.116.198001.

[14] D. Yu, Y. Liu, H. Zhao, G. Wang, and J. Qiu, "Flexural vibration band gaps in Euler-Bernoulli beams with locally resonant structures with two degrees of freedom," *Phys. Rev. B*, vol. 73, no. 6, p. 064301, Feb. 2006, doi: http://dx.doi.org/10.1103/PhysRevB.73.064301.

[15] T.-T. Wu, Z.-G. Huang, T.-C. Tsai, and T.-C. Wu, "Evidence of complete band gap and resonances in a plate with periodic stubbed surface," *Appl. Phys. Lett.*, vol. 93, no. 11, p. 111902, Sep. 2008, doi: http://dx.doi.org/10.1063/1.2970992.

[16] K. Wang, J. Zhou, C. Cai, D. Xu, and H. Ouyang, "Mathematical modeling and analysis of a meta-plate for very low-frequency band gap," *Appl. Math. Model.*, vol. 73, pp. 581–597, Sep. 2019, doi: http://dx.doi.org/10.1016/j.apm.2019.04.033.

[17] Z. Yang, J. Mei, M. Yang, N. H. Chan, and P. Sheng, "Membrane-Type Acoustic Metamaterial with Negative Dynamic Mass," *Phys. Rev. Lett.*, vol. 101, no. 20, p. 204301, Nov. 2008, doi: http://dx.doi.org/10.1103/PhysRevLett.101.204301.

[18] M. Rupin, F. Lemoult, G. Lerosey, and P. Roux, "Experimental Demonstration of Ordered and Disordered Multiresonant Metamaterials for Lamb Waves," *Phys. Rev. Lett.*, vol. 112, no. 23, p. 234301, Jun. 2014, doi: http://dx.doi.org/10.1103/PhysRevLett.112.234301.

[19] A. Banerjee, R. Das, and E. P. Calius, "Frequency graded 1D metamaterials: A study on the attenuation bands," *J. Appl. Phys.*, vol. 122, no. 7, p. 075101, Aug. 2017, doi: http://dx.doi.org/10.1063/1.4998446.

[20] C. Liu and C. Reina, "Broadband locally resonant metamaterials with graded hierarchical architecture," *J. Appl. Phys.*, vol. 123, no. 9, p. 095108, Mar. 2018, doi: http://dx.doi.org/10.1063/1.5003264.

[21] P. Celli, B. Yousefzadeh, C. Daraio, and S. Gonella, "Bandgap widening by disorder in rainbow metamaterials," *Appl. Phys. Lett.*, vol. 114, no. 9, p. 091903, Mar. 2019, doi: http://dx.doi.org/10.1063/1.5081916.

[22] Y. Xiao, B. R. Mace, J. Wen, and X. Wen, "Formation and coupling of band gaps in a locally resonant elastic system comprising a string with attached resonators," *Phys. Lett. A*, vol. 375, no. 12, pp. 1485–1491, Mar. 2011, doi: http://dx.doi.org/10.1016/j.physleta.2011.02.044.

[23] L. Liu and M. I. Hussein, “Wave Motion in Periodic Flexural Beams and Characterization of the Transition Between Bragg Scattering and Local Resonance,” *J. Appl. Mech.*, vol. 79, no. 1, p. 11003, Jan. 2012, doi: http://dx.doi.org/10.1115/1.4004592.

[24] M. Moscatelli, R. Ardito, L. Driemeier, and C. Comi, “Band-gap structure in two- and three-dimensional cellular locally resonant materials,” *J. Sound Vib.*, vol. 454, pp. 73–84, Aug. 2019, doi: http://dx.doi.org/10.1016/j.jsv.2019.04.027.

[25] M. I. Hussein, “Reduced Bloch mode expansion for periodic media band structure calculations,” *Proc. R. Soc. A Math. Phys. Eng. Sci.*, vol. 465, no. 2109, pp. 2825–2848, Sep. 2009, doi: http://dx.doi.org/10.1098/rspa.2008.0471.

[26] V. Fokin, M. Ambati, C. Sun, and X. Zhang, “Method for retrieving effective properties of locally resonant acoustic metamaterials,” *Phys. Rev. B*, vol. 76, no. 14, p. 144302, Oct. 2007, doi: http://dx.doi.org/10.1103/PhysRevB.76.144302.

[27] S. Nemat-Nasser, J. R. Willis, A. Srivastava, and A. V Amirkhizi, “Homogenization of periodic elastic composites and locally resonant sonic materials,” *Phys. Rev. B*, vol. 83, no. 10, p. 104103, Mar. 2011, doi: http://dx.doi.org/10.1103/PhysRevB.83.104103.

[28] A. O. Krushynska, V. G. Kouznetsova, and M. G. D. Geers, “Towards optimal design of locally resonant acoustic metamaterials,” *J. Mech. Phys. Solids*, vol. 71, no. 1, pp. 179–196, Nov. 2014, doi: http://dx.doi.org/10.1016/j.jmps.2014.07.004.

[29] A. Sridhar, V. G. Kouznetsova, and M. G. D. D. Geers, “Homogenization of locally resonant acoustic metamaterials towards an emergent enriched continuum,” *Comput. Mech.*, vol. 57, no. 3, pp. 423–435, Mar. 2016, doi: http://dx.doi.org/10.1007/s00466-015-1254-y.

[30] A. Sridhar, V. G. Kouznetsova, and M. G. D. Geers, “A semi-analytical approach towards plane wave analysis of local resonance metamaterials using a multiscale enriched continuum description,” *Int. J. Mech. Sci.*, vol. 133, no. August, pp. 188–198, Nov. 2017, doi: http://dx.doi.org/10.1016/j.ijmecsci.2017.08.027.

[31] D. Roca, O. Lloberas-Valls, J. Cante, and J. Oliver, “A computational multiscale homogenization framework accounting for inertial effects: Application to acoustic metamaterials modelling,” *Comput. Methods Appl. Mech. Eng.*, vol. 330, pp. 415–446, Mar. 2018, doi: http://dx.doi.org/10.1016/j.cma.2017.10.025.

[32] D. Roca, D. Yago, J. Cante, O. Lloberas-Valls, and J. Oliver, “Computational design of locally resonant acoustic metamaterials,” *Comput. Methods Appl. Mech. Eng.*, vol. 345, pp. 161–182, Mar. 2019, doi: http://dx.doi.org/10.1016/j.cma.2018.10.037.

[33] O. McGee *et al.*, "3D printed architected hollow sphere foams with low-frequency phononic band gaps," *Addit. Manuf.*, vol. 30, p. 100842, Dec. 2019, doi: http://dx.doi.org/10.1016/j.addma.2019.100842.

[34] C. Claeys, E. Deckers, B. Pluymers, and W. Desmet, "A lightweight vibro-acoustic metamaterial demonstrator: Numerical and experimental investigation," *Mech. Syst. Signal Process.*, vol. 70–71, pp. 853–880, Mar. 2016, doi: http://dx.doi.org/10.1016/j.ymssp.2015.08.029.

[35] A. Leblanc and A. Lavie, "Three-dimensional-printed membrane-type acoustic metamaterial for low frequency sound attenuation," *J. Acoust. Soc. Am.*, vol. 141, no. 6, pp. EL538–EL542, Jun. 2017, doi: http://dx.doi.org/10.1121/1.4984623.

[36] "Standard Test Method for Impedance and Absorption of Acoustical Materials Using a Tube, Two Microphones, and a Digital Frequency Analysis System," West Conshohocken, PA, 1998.

[37] Z. Xu, Y. Wang, D. Wu, K. P. Ananth, and J. Bai, "The process and performance comparison of polyamide 12 manufactured by multi jet fusion and selective laser sintering," *J. Manuf. Process.*, vol. 47, pp. 419–426, Nov. 2019, doi: http://dx.doi.org/10.1016/j.jmapro.2019.07.014.

Research dissemination

Publications

Title	A computational multiscale homogenization framework accounting for inertial effects: Application to acoustic metamaterials modelling
Authors	D. Roca, O. Lloberas-Valls, J. Cante, J. Oliver
Journal	Comp. Methods Appl. Eng.
Issue	330
Pages	415-446
Year	2018
DOI	10.1016/j.cma.2017.10.025
Impact factor	4.441 (Q1)
Citations	11

Title	Computational design of locally resonant acoustic metamaterials
Authors	D. Roca, D. Yago, J. Cante, O. Lloberas-Valls, J. Oliver
Journal	Comp. Methods Appl. Eng.
Issue	345
Pages	161-182
Year	2019
DOI	10.1016/j.cma.2018.10.037
Impact factor	4.441 (Q1)
Citations	5

Title	Experimental and numerical assessment of local resonance phenomena in 3D-printed acoustic metamaterials
Authors	D. Roca, T. Pàmies, J. Cante, O. Lloberas-Valls, J. Oliver
Journal	ASME. J. Vib. Acoust
Issue	142(2)
Pages	021017
Year	2020
DOI	10.1115/1.4045774
Impact factor	1.777 (Q2)
Citations	-

Conference presentations

Title	Computational homogenization procedure for acoustic problems
Authors	D. Roca, O. Lloberas Valls, J. Cante, J. Oliver
Congress name	Congreso de Métodos Numéricos en Ingeniería
Location	València (Spain)
Date	July 2017

Title	Multi-scale computational design of engineering metamaterials: application to acoustic insulation cases
Authors	J. Oliver, D. Roca, J. Cante, O. Lloberas-Valls
Congress name	World Congress in Computational Mechanics and Pan American Congress on Computational Mechanics
Location	New York (USA)
Date	June 2018

Title	Computational multiscale design of engineering metamaterials: application to acoustic insulation panels
Authors	D. Roca, D. Yago, J. Cante, O. Lloberas-Valls, J. Oliver
Congress name	European Conference on Computational Mechanics (Solids, Structures and Coupled Problems) / European Conference on Computational Fluid Dynamics
Location	Glasgow (UK)
Date	June 2018

Title	Computational procedure for optimal design of acoustic metamaterials
Authors	D. Roca, D. Yago, J. Cante, O. Lloberas-Valls, J. Oliver
Congress name	International Conference on Computational Plasticity
Location	Barcelona (Spain)
Date	September 2019

Participation in projects

Project title	Advanced Tools for Computational Design of Engineering Materials (COMP-DES-MAT). ERC-2010-AdG 320815
Funding	European Research Council
Dates	01/02/2013 – 31/01/2018
PI	Oliver Olivella, Javier
Role	PhD student

Foreign stays

Research group	Smead Department of Aerospace Engineering Sciences, University of Colorado Boulder
Host	Mahmoud I. Hussein
Location	Boulder, CO (USA)
Dates	01/09/2019 – 29/11/2019
Research topic	Study of the transmission loss properties of acoustic metamaterials based on pillared plates with holes to characterize the trampoline effect for enhancing the frequency bandgap.

Evolution of topology optimization

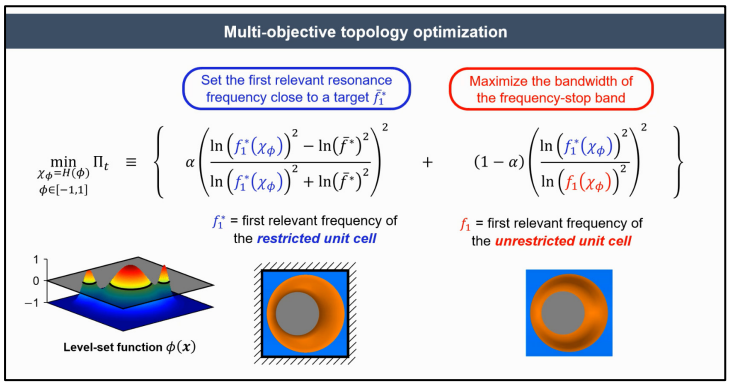

Description The video shows an animation of how the topology of the unit cell changes throughout each iteration of the optimization algorithm, providing a complementary more descriptive representation of the results in Fig. 13.

Link https://www.cimne.com/metacoustic/cvdata/cntr1/spc1/dtos/mdia/Demostrators/CompMetDesign/metamaterial-optim.mp4

Early 3D-printed prototype demonstrator

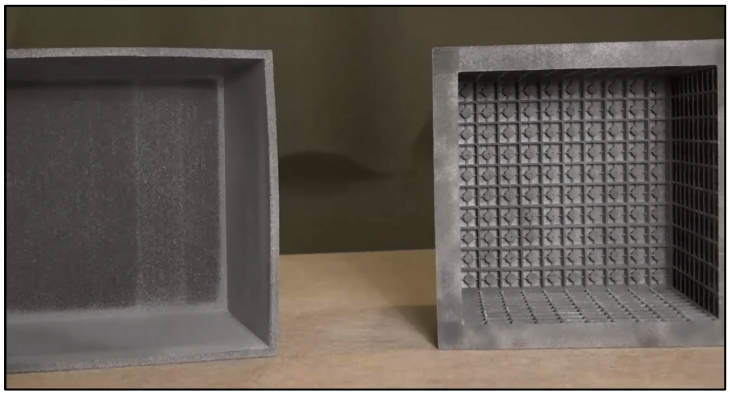

Description In this video, an early 3D-printed prototype in the shape of a box is tested in an acoustic laboratory and its performance is compared to an equivalent (same mass) homogeneous box. By covering a small speaker emitting a pure tone at 4100 Hz (frequency of operation of the metamaterial), one can clearly appreciate the improved attenuation capabilities of the acoustic metamaterial design.

Link https://www.cimne.com/metacoustic/cvdata/cntr1/spc1/dtos/mdia/Demostrators/CompMetDesign/metamaterial-demo.mp4

Acknowledgments

The development of this thesis has been possible thanks to funding received by the Spanish Ministry of Education through the FPU program for PhD grants.

Additionally, in the context of the works derived from this thesis, the author would like to acknowledge the funding received from the European Research Council under the European Union's Seventh Framework Programme through the ERC AdG project "Advanced tools for computational design of engineering materials" (COMP-DES-MAT / ERC Advanced Grant agreement n. 320815) and under the European Union's Horizon 2020 Research and Innovation Programme through the ERC PoC project "Computational catalog of multiscale materials: a plugin library for industrial finite element codes" (CATALOG / Proof of Concept Grant agreement n. 779611) and the ERC PoC project "Computational design and prototyping of acoustic metamaterials for tailored insulation of noise" (METACOUSTIC / Proof of Concept Grant agreement n. 874481). Finally, the author would also like to acknowledge the funding received from the Spanish Ministry of Economy and Competitiveness through the project "Computational design of Acoustic and Mechanical Metamaterials" (METAMAT / Research Grant DPI2017-85521-P).